

---

# Growth of large single crystals from the Ga-Pd-Sn system for basic research in heterogeneous catalysis

Kristian Micheli Bader

---



München 2023



---

# **Growth of large single crystals from the Ga-Pd-Sn system for basic research in heterogeneous catalysis**

**Kristian Micheli Bader**

---

Dissertation  
an der Fakultät für Geowissenschaften  
der Ludwig-Maximilians-Universität  
München

vorgelegt von  
Kristian Micheli Bader  
aus Marquartstein

München, den 22.05.2023

Erstgutachter: Prof. Dr. Peter Gille

Zweitgutachter: PD Dr. habil. R. Radhakrishnan Sumathi

Tag der mündlichen Prüfung: 19.01.2024

# Abstract

In recent years, it became clear that intermetallic compounds may be superior in heterogeneous catalysis compared to commonly used catalysts, such as catalytically active elements or substitutional alloys, since intermetallics may combine high activity, selectivity and lifetime [1, 2]. They outmatch active elements like noble metals due to their sheer number of available compounds. According to the active-site isolation concept, substitutional alloys may show higher selectivity compared to catalysts of the pure active elements due to geometrically isolated active sites [3]. However, since substitutional alloys have no site preference in their structure they allow diffusion and segregation under operation conditions, eliminating their advantage towards elements during operation and restricting their life time [4]. Intermetallic compounds have defined atomic positions and therefore do not allow segregation. This makes them long term-stable, highly selective heterogeneous catalysts [1, 2]. Intermetallic compounds in the binary Ga-Pd system have been shown to be excellent catalysts for the semi-hydrogenation of acetylene [1, 5–9]. The phases GaPd and GaPd<sub>2</sub> have already been grown as centimeter-sized single crystals and studied in detail [10–17]. Furthermore, the phases GaPd<sub>2</sub> and SnPd<sub>2</sub> (sharing the space group *Pnma*) form the solid solution Ga<sub>1-x</sub>Sn<sub>x</sub>Pd<sub>2</sub>, which has already been investigated regarding its catalytic properties [18, 19]. It was found that the activity for the semi-hydrogenation of acetylene changes significantly with Sn substituting Ga, and has a maximum at the composition  $x = 0.28$ . The good selectivity is not affected by this substitution [19]. The substitution of Ga from the 3rd main group by Sn with four valence electrons, without an accompanying structure change of the solid solution, thus allows to distinguish electronic and structural effects on the catalytic properties. Due to its industrial importance as a decisive purification step in the production of polyethylene, the semi-hydrogenation of acetylene is a well suited model reaction of high interest [20].

In order to study these catalytic effects, or even to identify the active sites, surface calculations need to be compared with catalytic measurements. Since only single-crystalline surfaces can be calculated, large enough, well-oriented single-crystalline surfaces are necessary for experimental comparison. To grow single crystals of sufficient size, the present study investigates solid-liquid equilibria of the solid solution Ga<sub>1-x</sub>Sn<sub>x</sub>Pd<sub>2</sub>. It was found that Ga<sub>1-x</sub>Sn<sub>x</sub>Pd<sub>2</sub> can be grown from high-temperature solutions where up to 60 at.% of Ga can be replaced by Sn. At higher Sn contents an equilibrium between the solid and the liquid does not exist, and thus crystal growth from the liquid phase is not possible. In the crystals, grown from (Ga,Sn)-rich solutions, up to  $x_{max} = 0.54$  of Ga can be substituted by Sn. For the single crystal growth the Czochralski method [21] proved to be a well-suited method and crystals, several cm<sup>3</sup> in size, weighing up to 18 g were grown successfully. In order to cover the interesting compositions for catalytic investigations the compositions

$x = 0.08, 0.18, 0.29$  and  $0.40$  were grown [19]. The resulting crystals have been investigated in detail regarding their chemical composition, their structure and their “real” structure. Single crystalline surfaces with orientations parallel to the (100), (010), (001), (210) and (013) planes with at least  $10 \text{ mm}^2$  have been prepared and proper polishing conditions for the surfaces have been established. They are recently investigated under industry-close conditions on a so called fixed-bed reactor [22].

In an additional chapter the single crystal growth of  $\text{Ga}_3\text{Pd}_5$  from Ga-rich solution using the Czochralski technique is described for the first time. A single crystal with a mass of more than 3 g could be obtained despite of the narrow temperature window of the solid/liquid equilibrium ( $1030^\circ\text{C} \geq T \geq 980^\circ\text{C}$ ) in the binary Ga-Pd system [23]. The grown crystal shows a strong anisotropic growth morphology with extended  $\{010\}$  faces which is different from results with structurally related phases, such as  $\text{GaPd}_2$  [1, 11, 24]. Structure analyses using X-ray powder and single crystal diffraction correspond to the known structure model of  $\text{Ga}_3\text{Pd}_5$  in the space group  $Pbam$  [25]. Tiny effects found in thermal analysis led to further investigations of the grown crystal. Ongoing studies by X-ray diffraction, SEM and TEM examinations revealed the presence of coherent precipitates of  $\text{GaPd}$  ( $P2_13$ ) in annealed samples, indicating a retrograde solubility of Ga in  $\text{Ga}_3\text{Pd}_5$  at lower temperatures. The crystal growth process, structural details and ongoing studies on the thermodynamic stability of  $\text{Ga}_3\text{Pd}_5$  are reported.

# Zusammenfassung

In den letzten Jahren zeigte sich, dass in der heterogenen Katalyse intermetallische Phasen Vorteile gegenüber den klassischen Katalysatoren, wie katalytisch aktive Elemente oder Substitutionslegierungen, haben, weil sie oft wichtige Qualitätskriterien eines Katalysators, wie hohe Aktivität, Selektivität und Lebensdauer, vereinen. [1, 2]. Reinen aktiven Elementen, wie Edelmetallen, sind sie aufgrund der Anzahl an Kombinationsmöglichkeiten von zwei oder mehr Elementen überlegen, weil sich dadurch neue, teils bessere Eigenschaften ergeben. Legierungen und intermetallische Phasen erfüllen das Konzept der "Isolierten aktiven Zentren", woraus geometrisch bedingt eine höhere Selektivität als bei aktiven Elementen resultiert [3]. Dabei haben intermetallische Phasen den Vorteil, dass ihre Struktur durch feste Plätze im Atomgitter definiert ist, während bei Legierungen unter industriellen Reaktionsbedingungen Diffusion und Segregation auftritt. Dabei geht ihr Vorteil gegenüber reinen Elementen verloren und ihre Lebensdauer wird eingeschränkt [4]. Die dauerhafte Isolation der aktiven Zentren durch definierte Gitterplätze macht intermetallische Phasen deshalb zu langzeitstabilen, hoch selektiven heterogenen Katalysatoren [1, 2].

Intermetallische Phasen im binären Ga-Pd-System haben sich dabei als hervorragende Katalysatoren für die Semihydrierung von Acetylen erwiesen [1, 5–9]. Die Phasen GaPd und GaPd<sub>2</sub> wurden deshalb bereits als Einkristalle in der Größenordnung von mehreren Kubikzentimetern gezüchtet und eingehend auf ihre katalytischen und strukturellen Eigenschaften untersucht [10–17]. Außerdem bilden die isostrukturellen Phasen GaPd<sub>2</sub> und SnPd<sub>2</sub> die lückenlose Mischkristallreihe Ga<sub>1-x</sub>Sn<sub>x</sub>Pd<sub>2</sub> (Raumgruppe *Pnma*), bei der bereits katalytische Untersuchungen durchgeführt wurden [18, 19]. Dabei wurde festgestellt, dass sich die Aktivität für die Semihydrierung von Acetylen mit der Substitution von Ga durch Sn signifikant ändert und ein Maximum bei der Zusammensetzung  $x = 0,28$  auftritt. Die gute Selektivität wird dabei nicht beeinträchtigt [19]. Die Substitution von Ga aus der 3. Hauptgruppe durch Sn mit vier Valenzelektronen, bei gleichbleibender Struktur des Mischkristalls, erlaubt somit, elektronische und strukturelle Effekte auf die katalytischen Eigenschaften getrennt voneinander betrachten zu können. Aufgrund der industriellen Bedeutung als entscheidender Reinigungsschritt bei der Herstellung von Polyethylen ist die Semihydrierung von Acetylen eine vielversprechende Modellreaktion für katalytische Untersuchungen an der Mischkristallreihe Ga<sub>1-x</sub>Sn<sub>x</sub>Pd<sub>2</sub> [20].

Um die katalytischen Vorgänge zu verstehen oder sogar die aktiven Zentren zu identifizieren, müssen Oberflächenberechnungen mit katalytischen Messungen verglichen werden. Da nur einkristalline Oberflächen berechnet werden können, sind ausreichend große, gut orientierte einkristalline Oberflächen in der Größenordnung von mehreren Quadratmillimetern bis zu wenigen Quadratzentimetern für den experimentellen Vergleich erforderlich. Um die nötigen Informationen

für die Züchtung solcher Einkristalle zu erlangen, wurden in der vorliegenden Arbeit die Fest-Flüssig-Gleichgewichte der Mischkristallreihe  $\text{Ga}_{1-x}\text{Sn}_x\text{Pd}_2$  untersucht.  $\text{Ga}_{1-x}\text{Sn}_x\text{Pd}_2$  kann aus Hochtemperaturlösungen gezüchtet werden, bei denen bis zu 60 at.% Ga durch Sn ersetzt wurden. Bei höheren Sn-Anteilen existiert kein Gleichgewicht zwischen der flüssigen Phase und dem Mischkristall  $\text{Ga}_{1-x}\text{Sn}_x\text{Pd}_2$ , weshalb Einkristallzüchtung nicht möglich ist. In den Kristallen, die aus (Ga,Sn)-reichen Lösungen gezüchtet werden, kann bis zu  $x_{max} = 0,54$  Ga durch Sn ersetzt werden. Für die Einkristallzüchtung hat sich die Czochralski-Methode [21] als gut geeignet erwiesen, und es wurden erfolgreich Kristalle mit einer Größe von bis zu mehreren Kubikzentimetern und einem Gewicht von bis zu 18 g gezogen. Um die für die katalytischen Untersuchungen interessanten Zusammensetzungen abzudecken, wurden Zusammensetzungen mit  $x = 0,08, 0,18, 0,29$  und  $0,40$  gezüchtet [19]. Es wurden einkristalline Oberflächen mit Orientierungen (100), (010), (001), (210) und (013) mit mindestens  $10 \text{ mm}^2$  hergestellt und geeignete Polierbedingungen für die Oberflächen erarbeitet. Diese werden aktuell unter industrienahen Bedingungen in einem Festbettreaktor untersucht [22]. Außerdem werden Untersuchungen an den Kristallen hinsichtlich ihrer chemischen Zusammensetzung, ihrer Struktur und ihrer Realstruktur vorgestellt.

In einem weiteren Kapitel wird erstmals die Einkristallzüchtung von  $\text{Ga}_3\text{Pd}_5$  aus Ga-reicher Lösung mit der Czochralski-Technik beschrieben. Trotz des engen Fensters in dem die Phase mit der Schmelze im Gleichgewicht ist ( $1030^\circ\text{C} \geq T \geq 980^\circ\text{C}$  [23]), konnte ein Einkristall mit einer Masse von mehr als 3 g gezüchtet werden. Der Kristall zeigt eine stark anisotrope Wachstumsmorphologie mit ausgeprägten {010}-Facetten, die sich von der Morphologie strukturell verwandter Phasen, wie  $\text{GaPd}_2$ , deutlich unterscheidet [1, 11, 24].

Die Strukturanalyse und Verfeinerung mittels Röntgenpulver- und Einkristalldiffraktometrie bestätigen die bereits publizierte Struktur von  $\text{Ga}_3\text{Pd}_5$  mit der Raumgruppe *Pbam* [25]. Unregelmäßigkeiten, die bei der thermischen Analyse festgestellt wurden, führten zu weiteren Untersuchungen des Kristalls. Laufende Untersuchungen mittels Röntgenbeugung, Raster- und Transmissionselektronenmikroskop weisen auf eine ausgeprägte retrograde Löslichkeit von Ga in  $\text{Ga}_3\text{Pd}_5$  bei abnehmenden Temperaturen hin. Es werden der Züchtungsprozess, strukturelle Details und laufende Studien zur thermodynamischen Stabilität von  $\text{Ga}_3\text{Pd}_5$  vorgestellt.

# Contents

<b>Abstract</b>	<b>iv</b>
<b>Zusammenfassung</b>	<b>v</b>
<b>Abbreviations and important hints</b>	<b>xi</b>
<b>1 Introduction</b>	<b>1</b>
1.1 Project overview . . . . .	1
1.2 Thread . . . . .	1
1.3 Intermetallic compounds in heterogeneous catalysis . . . . .	2
1.4 Solid solutions by substitution of Ga by Sn in Ga-Pd phases . . . . .	3
<b>2 Methods</b>	<b>9</b>
2.1 Studies on the Ga-Pd-Sn system . . . . .	9
2.1.1 Sample preparation . . . . .	9
2.1.2 Equilibrium-cooling experiments . . . . .	9
2.1.3 Directional solidification experiments . . . . .	10
2.2 Czochralski growth of single crystals . . . . .	11
2.2.1 Experimental preparation . . . . .	11
2.2.2 Czochralski growth apparatus . . . . .	12
2.2.3 Growth strategy for the growth of $\text{Ga}_{1-x}\text{Sn}_x\text{Pd}_2$ . . . . .	13
2.2.4 Growth strategy for the growth of $\text{Ga}_{1-x}\text{Sn}_x\text{Pd}$ . . . . .	14
2.2.5 Crystal growth process . . . . .	15
2.3 Preparative methods . . . . .	18
2.3.1 Orientation of single-crystalline slices . . . . .	18
2.3.2 Surface preparation . . . . .	18
2.4 Analytical methods . . . . .	19
2.4.1 X-ray diffraction methods . . . . .	19
2.4.2 Electron microscopy . . . . .	22
2.4.3 Differential thermal analysis . . . . .	23
2.4.4 Phase diagram information . . . . .	23
<b>3 Results</b>	<b>24</b>
3.1 Phase diagram studies in the Ga-Pd-Sn system . . . . .	24
3.1.1 X-ray powder diffraction analysis . . . . .	25
3.1.2 Texture and phase content of samples in the vicinity of $\text{Ga}_{1-x}\text{Sn}_x\text{Pd}_2$ . . . . .	29
3.1.3 Thermal investigations . . . . .	54
3.1.4 Phase properties . . . . .	57

---

3.2	Single crystal growth . . . . .	68
3.2.1	Single crystal growth of $\text{Ga}_{1-x}\text{Sn}_x\text{Pd}_2$ . . . . .	68
3.2.2	Single crystal growth of $\text{Ga}_{1-x}\text{Sn}_x\text{Pd}$ . . . . .	79
3.3	X-ray investigations on Czochralski-grown $\text{Ga}_{1-x}\text{Sn}_x\text{Pd}_2$ . . . . .	80
3.3.1	Non-annealed powders . . . . .	80
3.3.2	Annealed powders . . . . .	81
3.3.3	Laue scans . . . . .	83
3.3.4	Rocking curve analysis . . . . .	85
3.3.5	X-ray topography . . . . .	86
3.4	Electron backscatter diffraction on single crystals . . . . .	93
3.5	Polishing of single-crystalline surfaces . . . . .	95
<b>4</b>	<b>Discussion</b> . . . . .	<b>98</b>
4.1	On the Ga-Pd-Sn system . . . . .	98
4.1.1	Primary crystallization areas . . . . .	98
4.1.2	Crystallization paths . . . . .	101
4.1.3	Sn substitution in the phase $\text{GaPd}_2$ . . . . .	107
4.1.4	Sn substitution in further phases . . . . .	108
4.2	Single crystal growth of $\text{Ga}_{1-x}\text{Sn}_x\text{Pd}_2$ . . . . .	109
4.2.1	Crystal growth and growth parameters . . . . .	109
4.2.2	Inclusion formation . . . . .	110
4.2.3	Growth interface . . . . .	111
4.2.4	Low-angle grain boundaries . . . . .	112
4.2.5	Segregation effects . . . . .	115
4.2.6	Striations or artefacts . . . . .	115
4.3	Conditions of prepared crystal slabs for catalytic experiments . . . . .	117
4.4	The preparation of powders for X-ray powder diffraction . . . . .	118
4.5	Single crystal growth of $\text{Ga}_{1-x}\text{Sn}_x\text{Pd}$ . . . . .	120
<b>5</b>	<b>Single crystal growth and characterization of <math>\text{Ga}_3\text{Pd}_5</math></b> . . . . .	<b>122</b>
5.1	Introduction . . . . .	122
5.2	Growth strategy . . . . .	123
5.3	Experimental section . . . . .	124
5.3.1	$\text{Ga}_3\text{Pd}_5$ single crystal growth . . . . .	124
5.3.2	Surface preparation . . . . .	125
5.3.3	Analysis . . . . .	126
5.4	Results . . . . .	128
5.4.1	Single crystal growth of $\text{Ga}_3\text{Pd}_5$ . . . . .	128
5.4.2	Thermal and chemical analyses of $\text{Ga}_3\text{Pd}_5$ . . . . .	130
5.4.3	TEM analyses . . . . .	134
5.4.4	Results from X-ray diffraction data analyses of $\text{Ga}_3\text{Pd}_5$ . . . . .	138
5.5	Discussion . . . . .	144
5.5.1	Crystal growth . . . . .	144
5.5.2	Stability of $\text{Ga}_3\text{Pd}_5$ . . . . .	144
5.5.3	Structure refinement of $\text{Ga}_3\text{Pd}_5$ . . . . .	148



---

<b>6</b>	<b>Conclusion</b>	<b>149</b>
6.1	Phase diagram studies and single crystal growth in the Ga-Pd-Sn system . . . . .	149
6.1.1	Phase diagram studies focussed on $\text{Ga}_{1-x}\text{Sn}_x\text{Pd}_2$ . . . . .	149
6.1.2	Single crystal growth of $\text{Ga}_{1-x}\text{Sn}_x\text{Pd}_2$ . . . . .	150
6.2	Single crystal growth of $\text{Ga}_3\text{Pd}_5$ . . . . .	151
	<b>Appendix</b>	<b>163</b>
A.1	Bragg-Brentano diffraction on slices of single crystals . . . . .	163
A.2	Annealing conditions of powders for X-ray powder diffraction . . . . .	167
A.3	X-ray powder diffraction patterns . . . . .	170
A.4	Experiments overview . . . . .	178
A.5	Images of Czochralski-grown crystals . . . . .	180
	<b>Danksagung</b>	<b>186</b>

# Abbreviations and important hints

## Abbreviations

ACRT	accelerated crucible rotation technique
BSE	backscattered electron
DTA	differential thermal analysis
EBSD	electron backscatter diffraction
EDX	energy-dispersive X-ray spectroscopy
EPMA	electron-probe microanalysis
FIB	focused ion beam
FSE	forescattered electron
FWHM	full width at half maximum
HRTEM	high-resolution transmission electron microscopy
HT	high temperature
HV	high vacuum
IPF <sub>Z</sub>	inverse pole figure Z
$k^*$	pseudobinary segregation coefficient $k^* = \frac{x}{x_L}$
LAGB	low-angle grain boundaries
PSD	position-sensitive semiconductor detector
RF	radio frequency
SAED	selected area electron diffraction
SE	secondary electron
SEM	scanning electron microscopy
SIM	scanning ion microscopy
SP	setpoint
SSD	sub-surface damage
TEM	transmission electron microscopy
$T_L$	liquidus temperature
$\omega$	weight fraction
WDX	wavelength-dispersive X-ray spectroscopy
WSP	working setpoint
XPD	X-ray powder diffraction
XSD	X-ray single crystal diffraction

**Important hints**

1. It is important to define a notation for the phases and the initial starting melts: The crystals are described as  $A_{n-x}B_xC_m$ . The formula means that B substitutes A while C has an independent mole fraction.  $x = \frac{n(B)}{n(A)+n(B)}$ .
2. The starting melts are written in  $(A_{1-x_L}B_{x_L})_{100-y_L}C_{y_L}$ . Here and also later in the solid A substitutes B while C is independent. In order to distinguish  $x_L$  and  $y_L$  clearly in the text,  $x_L$  is expressed in decimal numbers and  $y_L$  in atomic percent.
3. In some cases different phases appear where the same elements substitute each other. For example  $Ga_{1-x}Sn_xPd$  and  $Sn_{1-x}Ga_xPd$ . In such cases the order of the elements defines the phase. e. g.,  $Ga_{1-x}Sn_xPd$  refers to the Sn substitution of Ga in the cubic phase GaPd while  $Sn_{1-x}Ga_xPd$  refers to the Ga substitution of Sn in the orthorhombic phase SnPd (tab. 1.1).
4. In some phases it was possible to determine  $x$  in the solid from the lattice parameters measured by X-ray powder diffraction. In such a case, it is written  $x_{XPD}$ . The detailed determination process is described in the results.
5. Since some structures have been published in references with different setups, the setup used here always corresponds to the setup of the phases in tab. 1.1.
6. When peaks of DTA curves are discussed, the term “onset” describes the starting point of a signal measured chronologically earlier and “endset” describes the final point of a thermal effect, chronologically later. This is independent of whether or not thermal effects were measured upon heating or cooling. This nomenclature is different from the NETZSCH software.
7. So called “tie-lines” connect the composition of the melt with the solid being in equilibrium with it.

# Chapter 1

## Introduction

### 1.1 Project overview

This thesis is part of a DFG-funded project on basic research in heterogeneous catalysis. It is aimed to prepare single-crystalline samples of a few  $\text{cm}^3$  in size in order to enable studies to distinguish structural and electronic effects in intermetallic catalysts. The need of single-crystalline samples of this size results from the approach of comparing surface energy calculations with catalytic measurements on surfaces of the catalyst. Poly-crystalline surfaces do not allow *ab initio* surface energy calculations while single-crystalline models do. Therefore, the large specific surfaces that powders provide for precise catalytic measurements, have to be overcome by measurements on large single-crystalline areas, typically in the range of  $1 \text{ cm}^2$ . Furthermore, when catalytic properties need to be understood, single crystals allow investigations on specific crystallographic orientations which powders do not. The project is mainly based on the solid solution series  $\text{Ga}_{1-x}\text{Sn}_x\text{Pd}_2$  as model catalyst. While the structure of the solid solution does not change by substituting Ga by Sn, the catalytic properties do change with the electronic state. That allows to discriminate structural and electronic effects in catalysis. Additionally, the material is a catalyst for the semi-hydrogenation of acetylene, a very important industrial reaction in the production of polyethylene. The reaction can be easily performed under industry-close conditions in small scale and therefore, it is a suited model reaction [22].

### 1.2 Thread

The thread of this thesis contains three key contents:

The first one are phase diagram studies on the Ga-Pd-Sn system to work out the required thermodynamic basic information, needed for single crystal growth. This part concentrates on the (Ga,Sn)-rich side of the liquidus surface of  $\text{Ga}_{1-x}\text{Sn}_x\text{Pd}_2$ . Some additional relations to the surrounding of the liquidus surface of  $\text{Ga}_{1-x}\text{Sn}_x\text{Pd}$ , treated by Dorner, A. ([26–28]) are established additionally.

The second content covers the growth and the characterisation of the single crystals of  $\text{Ga}_{1-x}\text{Sn}_x\text{Pd}_2$ . Also results, that expand on Dorners work on the growth of  $\text{Ga}_{1-x}\text{Sn}_x\text{Pd}$  are presented briefly.

The third content are crystal growth and studies on  $\text{Ga}_3\text{Pd}_5$  displaying new results on the structure and the thermodynamic stability. This part was added

since several questions on binary  $\text{GaPd}_2$  as a reference material for  $\text{Ga}_{1-x}\text{Sn}_x\text{Pd}_2$  occurred, which are closely related to the precipitation of  $\text{Ga}_3\text{Pd}_5$  in  $\text{GaPd}_2$ .

## 1.3 Intermetallic compounds in heterogeneous catalysis

Heterogeneous catalysis in the common sense means that the catalyst is in the solid state, while the reactants are gaseous and/or liquid<sup>1</sup>. The importance of heterogeneous catalysis increased dramatically since the beginning of the last century and today more than 85 % of the large-scale chemical-technical processes run with solid catalysts. Especially since the necessity of environmental and climate protection and sustainable energy production and resource management has arrived in the heads, heterogeneous catalysis became a key tool to bring together economical and ecological strategies in material conversion industries [29]. Hence, understanding processes in heterogeneous catalysis is a future-oriented requirement.

It has been found that intermetallic catalysts have advantages towards common industrial catalysts that are either pure catalytically active elements like noble metals or substitutional alloys made from them [1]. To understand the advantages of intermetallic catalysts one needs to know three variables that define the catalyst's performance. These are the activity, the selectivity and the lifetime. The activity describes the increase of reaction velocity of one or more catalytic reactions compared to the same reaction without a catalyst. The selectivity of the catalyst describes its ability to favour only one desired reaction and to suppress the formation of unwanted by-products. The lifetime describes the time the catalyst is stable under operating conditions until it needs to be exchanged or renewed. A high-performance catalyst has high activity, high selectivity and high lifetime [30]. The highest activity can be expected from pure elements, mostly noble metals. However, according to the active-site isolation concept, catalysts with their active sites being spatially isolated by non-active elements may have better selectivity [3]. This is, because for a heterogeneous catalyst, there are two effects reasonable, the ligand effect and the structural (or geometric) effect. The first one describes the electronic structure of the material, the second one the atoms' arrangement [2]. Accordingly, in multi-atom materials different structures and arrangements, compared to the elemental material may influence the catalytic properties dramatically. This is shown in fig. 1.1, by the example of the semi-hydrogenation of acetylene on an elemental Pd catalyst and on a catalyst where the Pd atoms are well isolated by non-active elements. Due to increased interatomic distances of the isolated Pd atoms, only weak  $\pi$ -bonds between the active atoms and the acetylene molecules are possible, leading to a selective semi-hydrogenation to ethylene. On the elemental Pd, stronger di- $\sigma$ -bonded acetylene may be directly hydrogenated to ethane or carbonaceous deposits,  $\text{C}_4\text{H}_x$  [1].

Substitutional alloys in the first instance meet the active site isolation concept. Nevertheless, since there is no site preference of the atoms, under operation conditions temperature diffusion and segregation is a key problem, leading to a restricted lifetime [4]. This is not the case in intermetallic phases that are characterized by

---

<sup>1</sup>In the last few years also liquid metal films came up as heterogeneous catalysts.

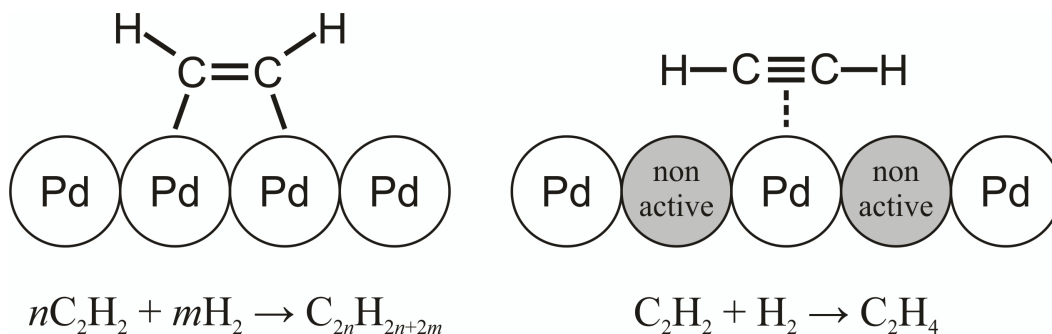


Figure 1.1: Catalytic reaction of C<sub>2</sub>H<sub>2</sub> and H<sub>2</sub> on the surface of a) a non-isolated Pd catalyst and b) a catalyst with well isolated Pd atoms. Drawn after [1] and [31]. Non-selective reaction from [6].

well defined atomic sites, allowing almost no diffusion and segregation. Several intermetallic catalysts therefore have come in the focus of research since they may combine high activity, selectivity and lifetime [1, 2].

Amongst these intermetallic catalysts especially phases of the Ga-Pd system have proved to be highly suited for the semi-hydrogenation of acetylene [1, 5–9]. The importance of the semi-hydrogenation of acetylene (fig. 1.1, b) is due to acetylene being a catalyst poison that has to be removed from the ethylene feedstock before the polymerisation to polyethylene. In the ethylene flow, after cracking, there are 0.5–2 % of acetylene that need to be lowered to the one-digit ppm regime, because otherwise acetylene-derived oligomers and polymers block the active sites on the Ziegler-Natta catalysts, lowering their activity significantly [20, 32]. During the semi-hydrogenation of acetylene high selectivity towards ethylene is required since (i) direct hydrogenation to ethane or further hydrogenation of ethylene is economically intolerable and (ii) oligomerization and resulting carbonaceous deposits lead to the deactivation of the catalyst [1, 32, 33]. Hence, since Ga-Pd catalysts meet those high requirements with respect to selectivity and also activity and long-term stability the phases GaPd and GaPd<sub>2</sub> have been studied in detail and have already been grown in cm<sup>3</sup>-sized crystals for this purpose [10–17]. These studies aimed to understand where the active centres for the catalytic reactions in the structure of the material are, by analysing specific crystallographic surfaces. So far, these centres or active sites, respectively, could not be understood completely.

## 1.4 Solid solutions by substitution of Ga by Sn in Ga-Pd phases

Trying to understand and to improve intermetallic catalysts, besides the geometric effect also the ligand effect needs to be taken into account. In most systems both effects are closely connected, making separate conclusions difficult. In order to isolate structural and electronic effects in catalysts, comparisons between the phases GaPd and GaPd<sub>2</sub> and isostructural compounds from the systems In-Pd and Al-Pd are already present. These studies reveal that InPd and InPd<sub>2</sub> do not show any difference in the catalytic behaviour compared to the Ga-Pd compounds. AlPd<sub>2</sub> has far lower selectivity that cannot be explained by intrinsic properties, but by the formation of a hydrate on the surface and therefore by geometrical effects [34, 35]. Accepting

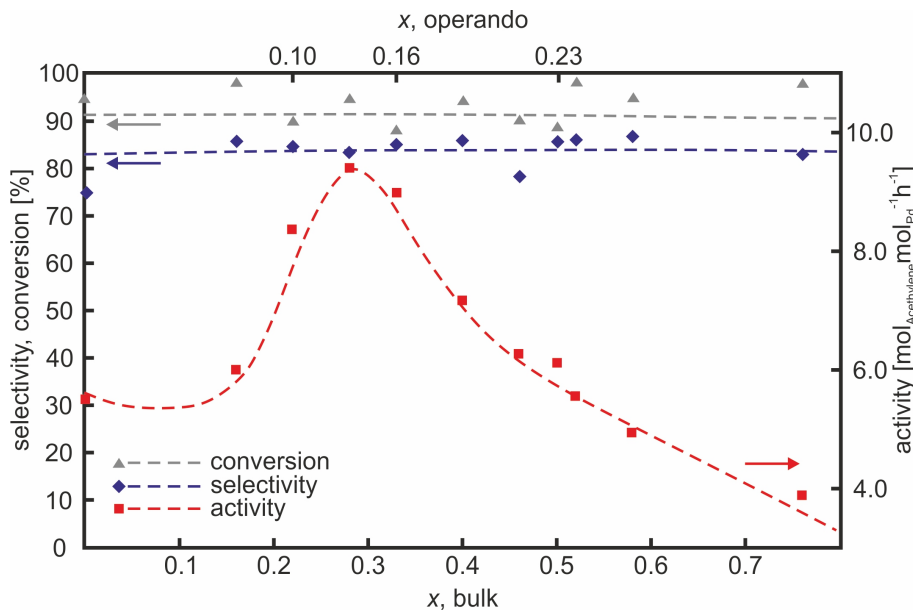


Figure 1.2: Behaviour of the activity and the selectivity of  $\text{Ga}_{1-x}\text{Sn}_x\text{Pd}_2$  with changing Sn substitution for Ga, measured on powders prepared by solid-state synthesis, drawn after [19].  $x$  refers to  $\text{Ga}_{1-x}\text{Sn}_x\text{Pd}_2$ .

these results, a different approach is necessary. One may be substituting electrons, i.e. replacing atoms from the structure by atoms of the neighbouring groups in the periodic table. Unfortunately, in most cases structural changes and transitions to different phases occur. Nevertheless, the numerous amount of intermetallics implies a variety of isostructural compounds with different electronic states that allow to address the ligand effect [2]. The compound  $\text{Ga}_{1-x}\text{Sn}_x\text{Pd}_2$  is such a new approach to discriminate electronic and structural effects. It proved to be very suitable due to several advantages compared to a Ga substitution by elements from the same period:

1. The catalytic properties are influenced by the substitution of Ga by Sn and weak changes in the Ga-Sn ratio cause significant changes in the catalytic behaviour (fig. 1.2). While the selectivity of the catalyst remains unchanged, the activity of  $\text{Ga}_{1-x}\text{Sn}_x\text{Pd}_2$  has an optimum when 30 % of Ga is substituted by Sn ( $x = 0.3$ ) [19]. The activity at  $x = 0.3$  doubles compared to  $x = 0$  and  $x = 0.5$ . Higher substitutions are not interesting from the catalytic point of view.
2. Still the two end members of the solid solution,  $\text{GaPd}_2$  and  $\text{SnPd}_2$ , are isostructural (tab. 1.1) and show total miscibility [18].
3. Compared to Ge, as the group IV neighbour of Ga in the periodic table, the difference in the atomic number between Ga and Sn is large enough to distinguish the two atoms in X-ray diffraction. That allows to understand the integration of Sn in the unit cell.

Summarizing, changing the electronic structure by incorporation of Sn, with an additional valence electron, results in a change of the catalytic properties but no change in the structure. Hence, the catalytic influence of the electronic state is

Phase	Structure type	Pearson symbol	Space group	Lattice parameter [ $\text{\AA}$ ]			Ref.
				$a$	$b$	$c$	
GaPd <sub>2</sub>	Co <sub>2</sub> Si	<i>oP12</i>	<i>Pnma</i>	5.4829(8)	4.0560(4)	7.7863(8)	[36]
SnPd <sub>2</sub>	Co <sub>2</sub> Si	<i>oP12</i>	<i>Pnma</i>	5.6505(8)	4.3125(7)	8.097(1)	[19]
GaPd	FeSi	<i>cP8</i>	<i>P2<sub>1</sub>3</i>	4.89695(6)			[12]
SnPd	MnP	<i>oP8</i>	<i>Pnma</i>	6.1388(4)	3.89226(3)	6.3377(4)	[37]

Table 1.1: Published crystal structure data of relevant phases, with respect to the solid solutions Ga<sub>1-x</sub>Sn<sub>x</sub>Pd<sub>2</sub> and Ga<sub>1-x</sub>Sn<sub>x</sub>Pd.

uncoupled from the structure, making the solid solution Ga<sub>1-x</sub>Sn<sub>x</sub>Pd<sub>2</sub> a highly interesting research object in order to understand the catalytic behaviour of intermetallic phases. Powdered or polycrystalline samples are relatively easy to synthesize and give precise information on the average catalytic properties of the material. Still, they have the disadvantage that always many crystallographic planes are exposed during experiments and the information is always an average of all participating surfaces ( $hkl$ ). This does not allow comparisons with surface-scientific investigations and surface calculations on specific surfaces. Therefore, catalytic effects cannot be associated with specific crystallographic surfaces. The active sites of most catalytic materials can therefore usually not be identified [22]. Conversely, surface investigations on single crystals in combination with quantum chemical calculations, in order to understand the ongoing processes, are a powerful tool [2]. The possibility to test single crystals catalytically under industry-close conditions in reactors has already been tested [22]. Still the high surface area that is provided by powders needs to be overcome by a large enough surface, when using single-crystalline slabs. This can only be achieved by well advanced crystal growth techniques, providing inclusion free, oriented single crystals of several cm<sup>3</sup> in size. The reported growth of single crystals of the Ga-Pd system and the unique possibility of experimental observation qualifies the Czochralski technique as preferred method for single crystal growth in the Ga-Pd-Sn system as well. The focus of this research is the single crystal growth of Ga<sub>1-x</sub>Sn<sub>x</sub>Pd<sub>2</sub>. For that it is necessary to investigate the Ga-Pd-Sn phase diagram, with respect to the feasibility of growing the desired compositions from the liquid phase and the corresponding growth parameter.

When discussing electron doping of GaPd<sub>2</sub> by Sn, Ge as the neighbour of Ga cannot be ignored. Here no pretests concerning its catalytic properties are present. For the primary crystallisation region and the range of the miscibility of Ga<sub>1-x</sub>Ge<sub>x</sub>Pd<sub>2</sub> first results have been published by Püschel (2020) [38]. However, the vast disadvantage of substituting Ga by Ge compared to the substitution of Ga by Sn is the difficulty to distinguish Ga and Ge by X-ray methods. Accordingly, statements about the distribution of the Ga and Ge atoms in the unit cell are almost impossible and accordingly the solid solution Ga<sub>1-x</sub>Ge<sub>x</sub>Pd<sub>2</sub> of minor importance for understanding catalysts.

GaPd was proved to be a highly selective long-term stable catalyst for the semi-hydrogenation of acetylene [13], similar to GaPd<sub>2</sub>. Accordingly, the partial substitution of Ga by Sn in GaPd may also be a powerful approach to discriminate electronic and structural effects in the catalyst. Despite, here also no catalytic pretests are present, however information about the primary crystallisation region of Ga<sub>1-x</sub>Sn<sub>x</sub>Pd have been made within the context of the present project [26, 27].



Regarding the structures of SnPd and GaPd the two phases do not form a total solid solution in contrast to  $\text{Ga}_{1-x}\text{Sn}_x\text{Pd}_2$  [12, 37]. Hence, total miscibility can be excluded, but a partial solid solution may be enough for uncoupling structural and electronic effects and to study the materials in this context. For example, regarding  $\text{Ga}_{1-x}\text{Sn}_x\text{Pd}_2$ , according to [19] a substitution of 40 % would be enough to gain samples with the maximum selectivity and also samples with higher and lower Sn substitution before and after the peak with maximum selectivity (fig. 1.2). Hence, no total solid solution is needed for proper studies on the effect of the Ga substitution by Sn.

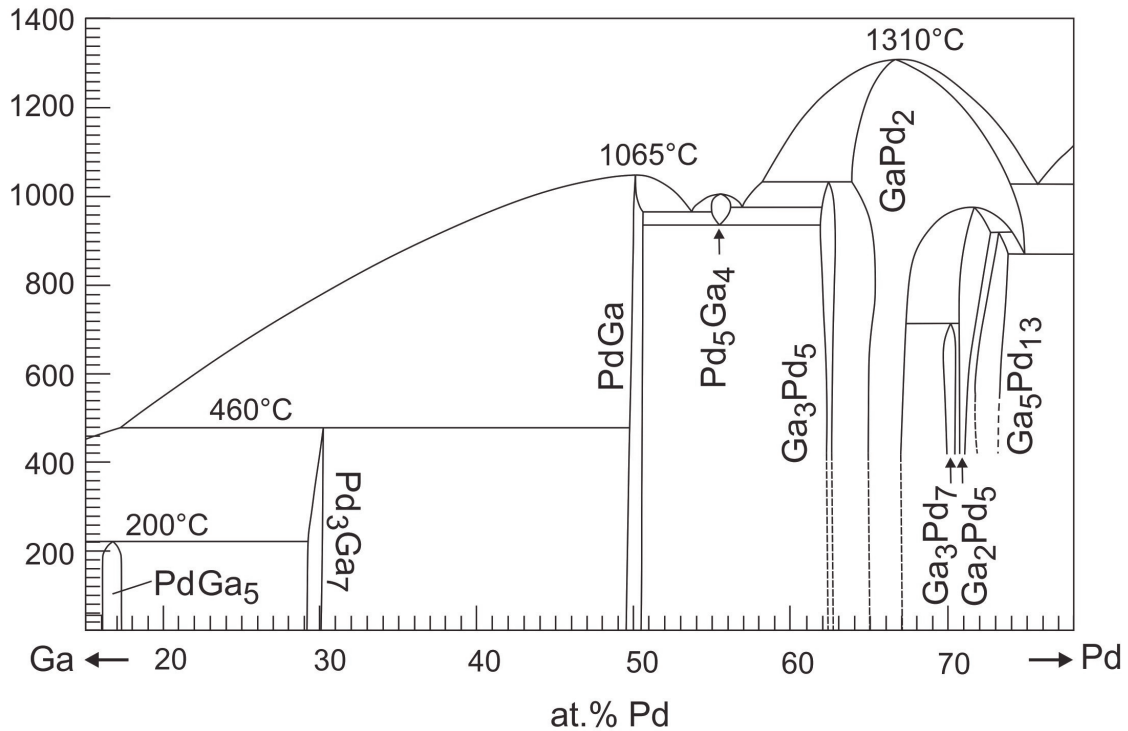


Figure 1.3: Important section of the Ga-Pd phase diagram. Drawn after [23].

According to the well accepted Ga-Pd phase diagram, GaPd and GaPd<sub>2</sub> both can be crystallized either congruently from melt or incongruently from high-temperature solutions (fig. 1.3) [23]. However, regarding the Sn-Pd phase diagram, SnPd<sub>2</sub> has no equilibrium with a liquid phase but is formed by a peritectoid decomposition (fig. 1.4) [39]. Accordingly, for  $\text{Ga}_{1-x}\text{Sn}_x\text{Pd}_2$  it has to be expected that only a partial substitution of Ga by Sn can be achieved by crystal growth from the liquid phase. Consequently, the substitution limits that are expected are structural for  $\text{Ga}_{1-x}\text{Sn}_x\text{Pd}$  and a vanishing equilibrium of solid and liquid for  $\text{Ga}_{1-x}\text{Sn}_x\text{Pd}_2$ . The presence of these limits is aggravated by the fact that only minor information concerning the ternary phase diagram is present. Only a 500°C isothermal section is published from the Ga-Pd-Sn system [18] and shown in fig. 1.5. It can be seen that amongst the phases listed in tab. 1.1, there is also a ternary phase,  $\text{Ga}_{2+p+q}\text{Sn}_{4-p}\text{Pd}_9$ , present in the vicinity of  $\text{Ga}_{1-x}\text{Sn}_x\text{Pd}_2$  (tab. 3.1) [40]. Furthermore, fig. 1.5 shows the total miscibility of GaPd<sub>2</sub> and SnPd<sub>2</sub> at 500°C and further studies in this context confirmed the validity of the total miscibility also at room

temperature [18].

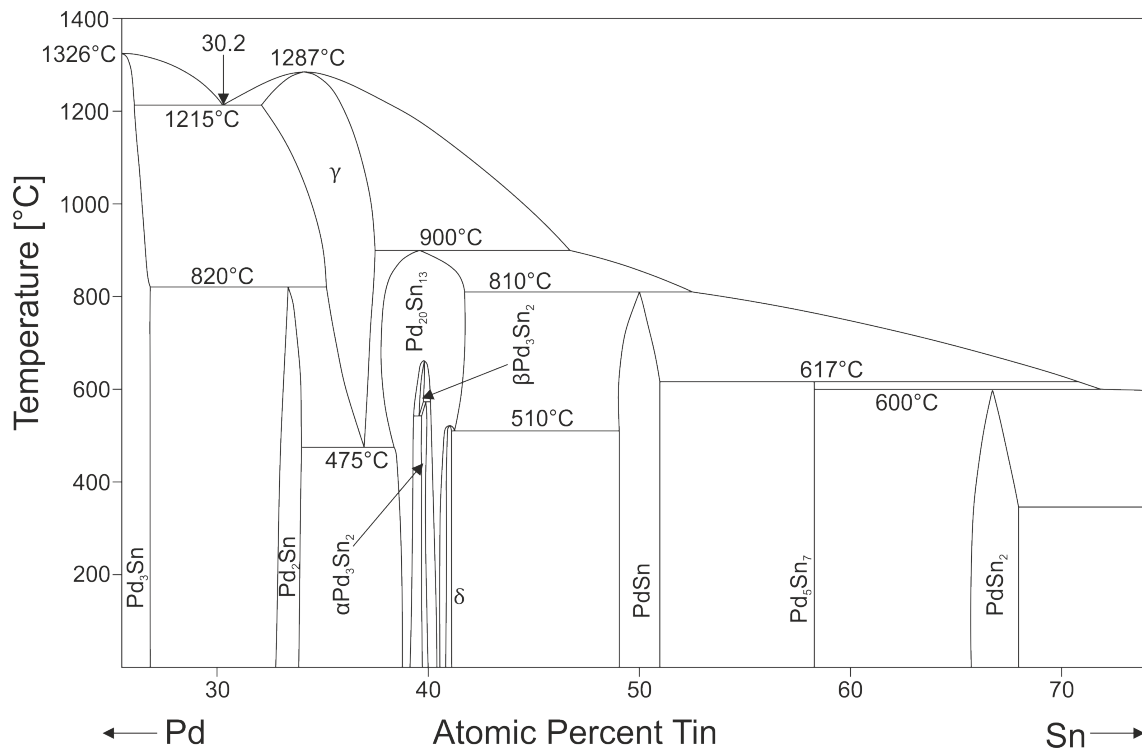


Figure 1.4: Important section of the Pd-Sn phase diagram. Drawn after [39].

All binary phase diagrams of the Ga-Pd-Sn system are known [23, 39, 41], however information regarding the liquidus surface of the ternary system with respect to crystal growth are unknown and can only be found experimentally since unknown high-temperature phases are present in the system and accordingly phase diagram calculations are not possible.

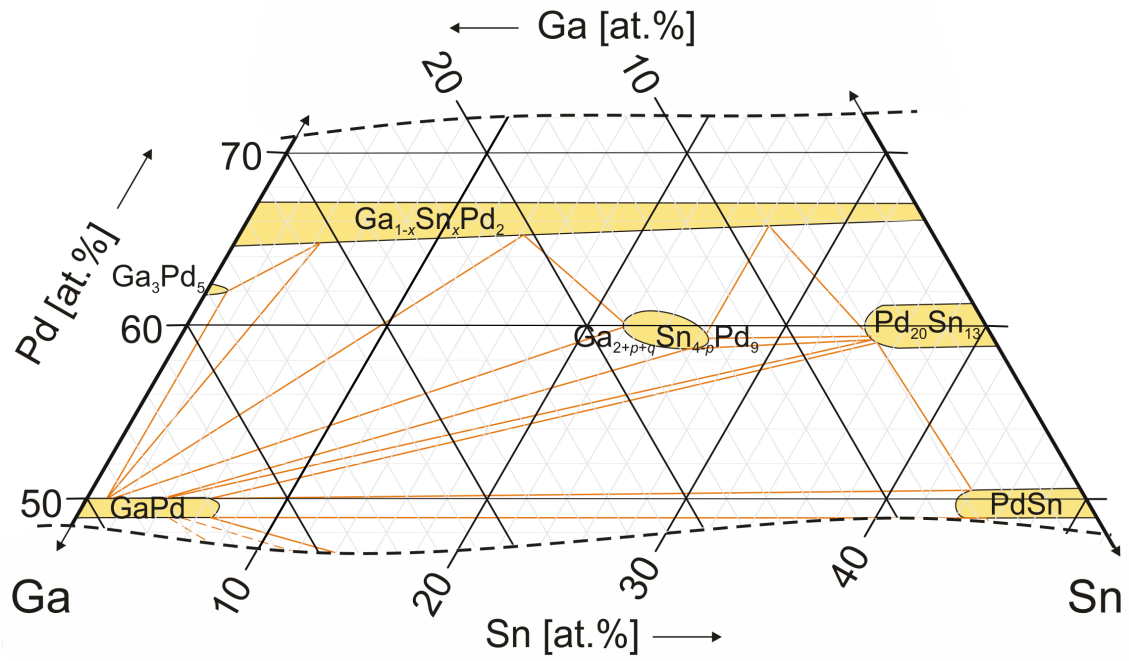


Figure 1.5: Isothermal section of the Ga-Pd-Sn Gibbs triangle at 500°C, in the vicinity of the Pd-poor side of  $\text{Ga}_{1-x}\text{Sn}_x\text{Pd}_2$ . Yellow fields are the stability regions of the phases and orange lines are the 500°C tie-triangles<sup>2</sup>. Drawn after [18].

<sup>2</sup>Tie-triangles connect the three phases that are in equilibrium [42].

# Chapter 2

## Methods

### 2.1 Studies on the Ga-Pd-Sn system

#### 2.1.1 Sample preparation

To avoid large specific surfaces the starting materials for the melts were synthesized from pieces of pure elements only. In order to remove traces of impurities from the surfaces (e.g. from cutting), the Pd bars (3N5 grade, Degussa) were etched wet-chemically in an ultrasonic bath using aqua regia. To remove traces of the acid the pieces were cleaned in distilled water in three steps, where the last one was performed in an ultrasonic bath. Water traces were removed in two washing-steps of technical acetone and a final step of acetone p.a. in the ultrasonic bath. The Ga granules (5N grade, ChemPur) and the Sn granules (5N grade, Spuremetalle Freiberg) received no further treatment for the phase diagram studies. The elements were placed either in an alumina crucible (Alsint 99.7, Haldenwanger) and then in a silica glass ampoule or directly in a pyrolytically graphitised silica glass ampoule. The ampoules were evacuated to high vacuum for oxygen-free conditions, filled with about 200 mbar Ar (5N grade) in order to achieve ambient pressure at operation conditions and then fused. Since temperatures will later be higher than 1220°C, which is close to the glass transition temperature of silica glass, a pressure close to ambient pressure must be ensured at temperatures that high, in order to avoid deformation of the ampoules. Then the fused silica glass ampoules were placed in a RF heater. The aim was to dissolve Pd in the (Ga, Sn)-rich solution while mixing strongly, to assure a homogeneous liquid. Slow heating was necessary since strong exothermic reactions between Ga and Pd can be observed, leading to the cracking of alumina crucibles or to spalling off the pyrolytic graphite layer. After heating, the synthesis was kept at high temperature for about one hour to ensure total mixing. By switching off the power of the RF generator, the synthesis was quenched to a fine-grained ingot, that can easily be dissolved later without stirring.

#### 2.1.2 Equilibrium-cooling experiments

The absence of thermodynamic information on several binary phases of the two ternary phase diagrams and all ternary phases makes experimental investigations on the ternary systems necessary. Since Pd is expensive, the main conditions for these phase diagram studies are that a low Pd mass must be sufficient and the experimental

time should be as low as possible. Quenching is a frequently used approach in former comparable works, but the information on the crystallization path is relatively poor. Therefore, to understand the spatial order of the crystallization paths, Bridgman experiments were performed here. Those were carried out in alumina crucibles with 7 mm inner diameter, fused in silica glass ampoules, with melt masses of typically around 10 g. Besides the relatively high amounts of necessary Pd (which is unfavourable due to its high price) the high crucible diameter led to ingot heights of less than 12 mm, resulting in a very low thermal gradient. Thinner diameters were not possible, since the pieces of the elements can separate due to their surface tension during heating into droplets, sticking to the rough alumina crucible wall, preventing mixing of the melt. The low thermal gradient made the main principle of a Bridgman experiment, i.e. a thermal gradient in the crucible, worthless. Still, it was possible to reproduce the crystallization path in such experiments. In order to reduce the starting mass of Pd, an approach was to use lower amounts in a smaller alumina crucible with 6 mm inner diameter. Since the thermal gradient is minimal in such small amounts of melt anyway (typically 2 g), these experiments are carried out in muffle furnaces by slow cooling. In order to further improve these experiments, the alumina crucible was replaced by a thin layer of graphite in the silica glass ampoule (7 mm inner diameter). Pyrolytic graphite layer reduce the wetting of the metallic melt to the ampoule to a minimum and accordingly sticking of melt droplets to the ampoule wall can be excluded [43]. Furthermore, the silica glass ampoules can be shaped before graphitising, for example with a tip at the bottom. Examples for the ampoules are shown in fig. 2.1. The total mass from which it was possible to extract valuable information was 0.5-1 g. This was taken as the standard setup for the phase diagram studies. Those equilibrium-cooling experiments were heated in muffle furnaces in charges of 3-6 ampoules, kept at high temperatures for 12 h to assure proper melting and then were cooled with 1-2 K/h to temperatures where everything is solidified.

An exception was the quenching of few special experiments after a certain time of equilibrium-cooling at specific temperatures, taken from the DTA curves. The purposes of these quenching experiments were either to get a better evidence which phase crystallized first, to clarify if solid-solid phase transitions occurred or to preserve a high temperature phase to room temperature. For quenching, flowing water or liquid nitrogen were used.

After the ampoules were cracked, the small solid droplets were cut into sections for further investigations. Cutting was carried out through the sample centre, parallel to the vertical axis of the sample during cooling. Early experiments revealed that usually the earlier crystallized material is at lower positions of the droplet causing a chronological order along the experiments vertical axis. Accordingly, if the samples are cut in a plane that is localized in the experiments axis, each part contains approximately the same composition, i.e. the same crystallization sequence. The compositions of the starting charges as well as the resulting first-to-freeze phases are summarized in tab. A.1 in the appendix.

### 2.1.3 Directional solidification experiments

The equilibrium-cooling experiments, described above, were in most cases suitable to get the majority of information regarding a certain composition. Still in some

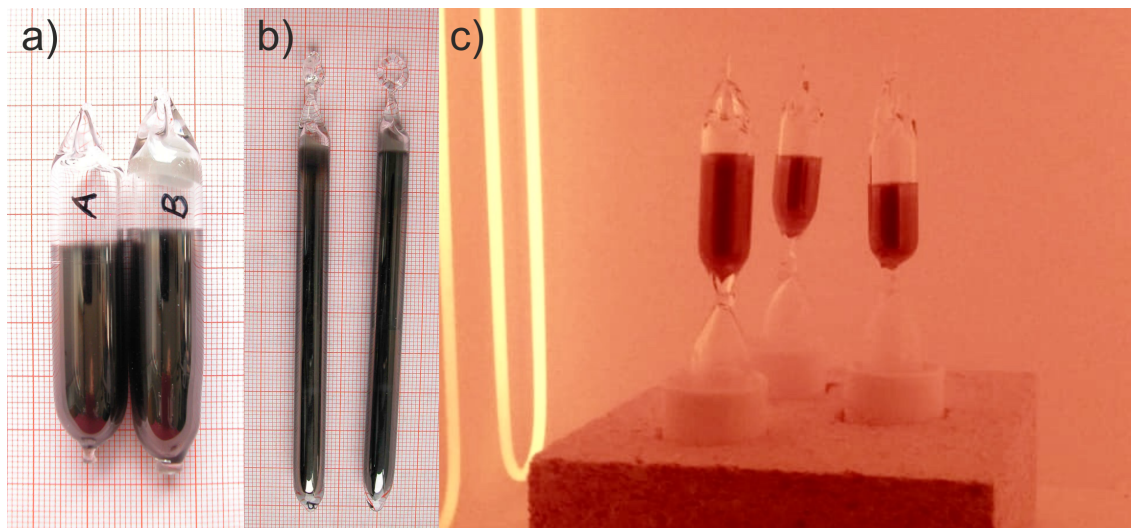


Figure 2.1: a) Pyrolytically graphitised ampoules in which the equilibrium cooling experiments were carried out. b) Pyrolytically graphitised ampoules for Bridgman experiments. c) Ampoules in the muffle furnace standing on a silica base in order to keep the ampoules off the refractory of the furnace to avoid damages of the ampoules at temperatures higher than 1200°C.

cases the time sequence of a crystallization path may be difficult to interpret. In such cases Bridgman experiments can be carried out, additionally. For these, the starting material is synthesized in a graphitised fused silica ampoule, exactly as described above. After the synthesis in the RF generator the ingot of typically around 5 g was crushed and then filled in a graphitised silica glass ampoule with 5 mm inner diameter (fig. 2.1, b). The ampoule was evacuated to high vacuum, then filled with around 200 mbar Ar (5N grade) and fused. The ampoules were placed in a Bridgman furnace, overheated and then lowered at constant temperature profile depending on the expected solidus of the specific composition with a rate of 3.5 mm/d, corresponding to a cooling rate of 1.5 K/h. The ingot of such a Bridgman experiment was 35–40 mm in length.

## 2.2 Czochralski growth of single crystals

### 2.2.1 Experimental preparation

For the Czochralski experiments the Pd was treated as described in section 2.1.1. Ga and Sn were further treated after weighing, to remove surface oxide layers. Both were reduced by heating under H<sub>2</sub> (5N grade) atmosphere, placed either directly in the 15 ml synthesis alumina crucible (Alsint 99.7, Haldenwanger) or in a glassy carbon crucible. Since Ga and Sn form an eutectic mixture that can be liquid at room temperature [41], the reduction was carried out separately. Typical melt masses were in the region of 45–55 g with an accuracy of at least 0.02 at.%. Subsequently, all elements were loaded in the alumina synthesis crucible, placed in the fully metal sealed system and after evacuating set under Ar (5N grade) atmosphere. The synthesis with a RF heater was performed as described above. Even short-term storage

was done under vacuum. The melt ingot was transferred in a 10 ml alumina growth crucible (Alsint 99.7, Haldenwanger) and placed in the growth apparatus.

### 2.2.2 Czochralski growth apparatus

The Czochralski apparatus is described in [44] and shown in fig. 2.2. The growth chamber of the Czochralski apparatus is fully metal sealed by Cu gaskets. The pulling rod is vacuum tight by a magnetofluid rotary feed-through. The crucible rotation feed-through is a magnetic coupling. The translation, i.e the pulling mechanism, is placed in a metal bellow seal. The seed is mounted onto a ceramic seed holder (fig. 2.2, b) that rotates during growth. A step motor allows very low pulling rates, below 25  $\mu\text{m}/\text{h}$ , which are necessary during incongruent growth from solution (explanation in chapter 2.2.5). The melt is rotating reverse. Before the growth the chamber is evacuated to a low  $10^{-7}$  mbar regime and then filled with Ar (5N grade) so that the pressure later equals ambient pressure at growth temperatures. The heater is a graphite meander resistance heater. To minimise the control loop and thermal fluctuations, the thermocouple is placed in contact to the resistance heater. Therefore, it must be kept in mind that the real temperature in the solution stays unknown. During homogenization of the melt, ACRT<sup>1</sup> can be applied to improve mixing [45]. A viewport with a glass window allows the observation of every step during the whole process with a stereoscopic microscope. Since no automatic diameter control of the crystal is known for such low pulling rates, the temperature program can only be adapted based on visual changes and the operator's judgement. Unfortunately, with increasing temperatures the melt and the crystal emit thermal radiation with increasing intensity and decreasing wavelength of the intensity maximum, according to the Planck's radiation law [46]. Therefore, above 1100°C the growth chamber is that bright that almost no contrast is visible. This problem is reduced by using shortpass filters that have an absorption edge in the region of 525–550 nm cutting off the most intense wavelengths.

---

<sup>1</sup>Accelerated crucible rotation technique is a stirring method by alternating accelerating and decelerating of the crucible rotation [45].



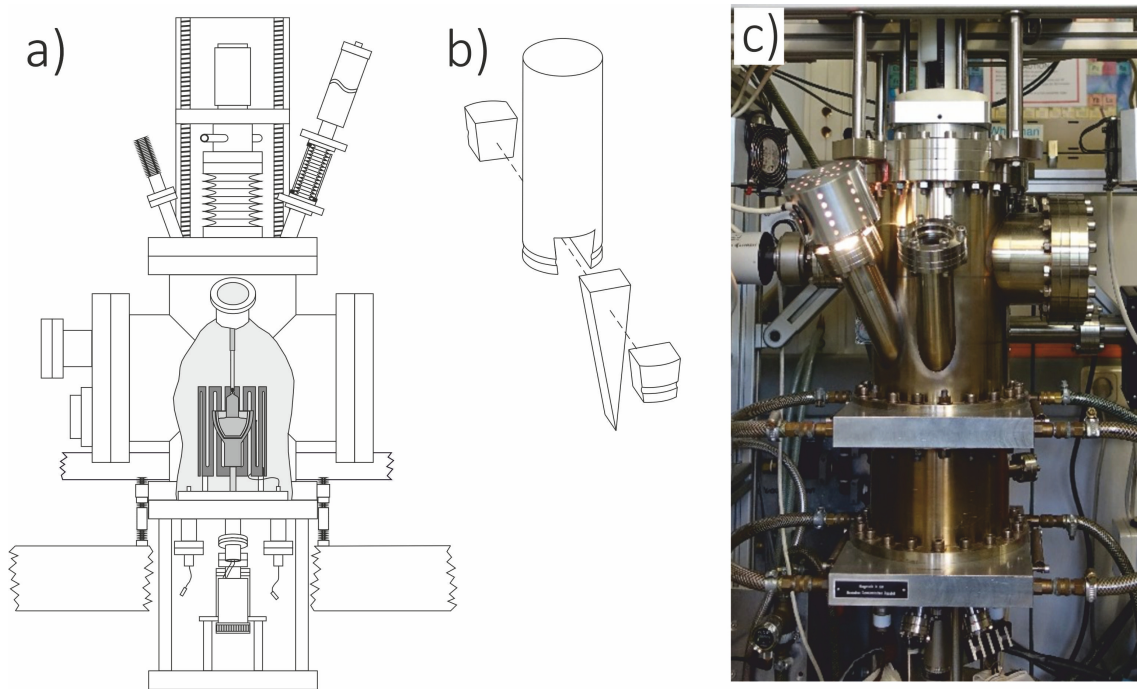


Figure 2.2: a) Schematic sketch of the growth chamber of the Czochralski apparatus and b) sketch of the seed holder (Both changed after [44]. c) Image of the whole apparatus

### 2.2.3 Growth strategy for the growth of $\text{Ga}_{1-x}\text{Sn}_x\text{Pd}_2$

$\text{GaPd}_2$  can be grown either congruently or incongruently<sup>2</sup> from Ga- or Pd-rich solutions at temperatures below  $1310^\circ\text{C}$  in a range between 58.3 to 76.0 at.% Pd [23, 47]. A congruent growth was not suitable for  $\text{Ga}_{1-x}\text{Sn}_x\text{Pd}_2$  with a series of different compositions ( $x = 0.1, 0.2, 0.3, 0.4$ ), since in a ternary system the liquidus surface has only one congruent composition. Therefore, growth will end up incongruently anyway with a different composition than the only congruently melting one. The aimed compositions regarding the Sn content have to cover the regions shown in fig. 1.2, between the onset and the endset of the activity peak caused by Sn. One important argument to grow incongruently from solution are lower growth temperatures. Temperatures exceeding  $1200^\circ\text{C}$  on the one hand make pre-experiments significantly more difficult, leading to the loss of their main purpose to get a large amount of information based on a fast, cheap and easy method. On the other hand, the Czochralski growth gets challenging at temperatures that high. The optical conditions, that are necessary for visual observation of the growth process get worse and the diameter control becomes a guessing game. High temperatures at long duration will lead to a loss of the elements with higher vapour pressures and therefore to shifted and unknown starting compositions. In this case, a loss of Ga with the higher vapour pressure is likely. A shift to a Pd-rich solution may even be possible. Therefore,

<sup>2</sup>Often there is confusion about the terms congruent and incongruent. Congruent crystal growth means that the crystal and the melt have the same composition. In contrast, incongruent crystal growth means that the crystal is grown from a solution of different composition than its own. This is also described as solution growth, since a high melting component (in this case Pd) is dissolved in a very low melting component (in this case Ga and Sn).



in these studies the growth from Ga-rich solutions was favourable over congruent growth. Lowering the growth temperatures can be achieved besides from Ga-rich solution also from Pd-rich solution. This approach is too risky, since in the binary Ga-Pd system, GaPd<sub>2</sub> grown from Pd-rich solution has a retrograde solubility of Pd at temperatures below 1000°C, leading to complicated peritectoid decompositions of the initial phase (fig. 1.3) [23]. Hence, the only option is a Ga-rich solution. The growth from solution brings along another underestimated advantage, discussed in [48, 49]. Stable crystal growth needs a limiting factor that ensures a stable diameter or at least the dampening of changes. In industrial large-scale crystal growth with growth rates of 10<sup>1</sup>-10<sup>2</sup> cm<sup>3</sup> per minute, the released latent heat from crystallization is the limiting factor making stable diameter control possible. In the scales of single crystal growth of intermetallic phases with growth rates sometimes lower than 25 μm/h, the latent heat is neglectable. Nevertheless, Ga as an excess component from incongruent growth is such a limiting factor and makes the crystal growth slow, but well controllable. Pd contents in the melt of  $y_L = 61-62$ <sup>3</sup> were suitable with growth temperatures around 1200°C offering still a good yield. Applying the lever rule [50] in the binary Ga-Pd system results in a crystal mass of 40–55 m.% of the initial melt mass. Even though this may be different in the ternary system, there is no more precise approximation yet. The initial Sn content was based on the pre-experiments. The pseudobinary segregation coefficient  $k^*$  measured in the pre-experiments was decisive here. Hence, only starting compositions were used for Czochralski crystal growth where experimental success was already ensured, concerning the melt composition. The pre-experiments revealed that in the case of Sn substitution for Ga in the region between  $0.1 \leq x \leq 0.4$ ,  $k^* \approx 1$  [26]. Hence, segregation with respect to the Ga/Sn ratio can be neglected. For proper crystal growth a native seed is the best option. Since no native seeds for the different Sn or Ge contents were present, binary GaPd<sub>2</sub> seeds were suitable, since the lattice mismatch between GaPd<sub>2</sub> and Ga<sub>1-x</sub>Sn<sub>x</sub>Pd<sub>2</sub> is low. Regarding SnPd<sub>2</sub> the mismatch of the end members of the solid solution is 3 % along *a*, 6 % along *b* and 4 % along *c* [36, 51] (tab. 1.1). Since substitution was planned only up to  $x \leq 0.4$  it was expected to be even lower, according to Vegard's law [52]. The GaPd<sub>2</sub> seed crystal was cut oriented in one of the crystallographic main directions and shaped to a wedge with a 10° opening angle and a basis of 1.5 · 1.5 mm<sup>2</sup> (fig. 2.2, b).

### 2.2.4 Growth strategy for the growth of Ga<sub>1-x</sub>Sn<sub>x</sub>Pd

GaPd can also be grown congruently or incongruently from Pd-rich or from Ga-rich solution at temperatures below 1065°C [10] in a range between 17.5 to 53.5 at.% Pd [23]. In this case the crystallization path on the Pd-rich side reaches an eutectic point early, lowering the yield on this side. Therefore, also in this case incongruent growth from Ga-rich solution is the method of choice. Again, lower temperatures and increased growth stability by Ga excess as a limiting factor were the decisive arguments against congruent growth. Since no pre-tests were present on the influence of Sn substitution for Ga on the catalytic behaviour of GaPd, the Sn content for single crystal growth was chosen with constant increasing substitution steps to the maximum possible substitution which is  $x = 0.16$  [26]. In contrast to the Ga<sub>1-x</sub>Sn<sub>x</sub>Pd<sub>2</sub> solid solution, strong segregation with respect to the Ga/Sn

<sup>3</sup>According to the description (Ga<sub>1-x<sub>L</sub></sub>Sn<sub>x<sub>L</sub></sub>)<sub>100-y<sub>L</sub></sub>Pd<sub>y<sub>L</sub></sub>.

ratio with a pseudobinary segregation coefficient of  $k^* \approx 0.3$  was revealed in the  $\text{Ga}_{1-x}\text{Sn}_x\text{Pd}$  partial solid solution. Accordingly, from solutions with starting Sn contents of  $x_L = 0.2$  and  $0.4$  crystals with Sn contents of  $x = 0.06$  and  $0.12$  are expected. As seed material binary GaPd was used. The lattice parameter mismatch is reported to be below 1% for the highest possible substitution case and therefore neglectable for seeding [26]. The seeds were cut as described in section 2.2.3 but with the pulling axis either parallel to the [110] or the [111] direction.

### 2.2.5 Crystal growth process

Before growth can be started, the melt needs to be mixed homogeneously and the seeding temperature needs to be found. After heating with 500 K/h to a temperature that is at least 50 K above the estimated seeding temperature, ACRT was applied for at least 12 h. As described in section 2.2.2 the thermocouple is placed next to the heater, while the actual melt temperature is unknown. Accordingly, the seeding temperature needs to be determined alternatively as described hereafter. When the melt is slowly cooled, at some temperature supercooling of the melt collapses, leading to a sudden appearance of several crystallites in the melt at once. When the melt is heated again, the crystallites start to dissolve. The temperature, where the last crystallite dissolves is the solidus temperature of that crystallite and therefore the liquidus temperature of the melt and accordingly the seeding temperature. Crystallites are usually visible as small tips on the metallic melt surface. Sometimes, enabled ACRT is helpful to see if crystals are still present. Two difficulties had to be handled during this process: The very high supercooling rates in Ga-rich solutions (supercooling of 165 K was observed in Ga-Pd-Sn solutions) and the slow dissolution of crystals (To get an accurate seeding temperature heating ramps of 2 K/h are appropriate). Accordingly, heating slow enough to ensure complete dissolution may be extremely time consuming. To accelerate the heating process, high heating ramps were applied at the beginning (200 K/h) together with permanent ACRT. The ramps were then reduced in an approximately exponential way, depending on the amount of crystals still present. In the last stage, where the heating ramps are 2 K/h the melt is kept at constant rotation since better observation is possible and ACRT is enabled only temporary since movement in the melt increases the visibility of crystallites, i.e. small tips in the melt. When the last crystallite disappears, seeding conditions are found and a short overheating of the melt is applied as a precaution. The melt is cooled again to seeding temperature and the seed is lowered to the melt. Seed and crucible are kept in constant counter rotation of 10 rpm (crystal) and 5 rpm (melt). When the seed touches the surface of the melt, the melt usually snaps to the seed, wetting it and forming the meniscus being typically for Czochralski growth. After reaching stable conditions, the crystal and crucible rotation can be carefully increased. The typical crucible rotation during growth was 8 rpm and the typical crystal rotation was 20–30 rpm.

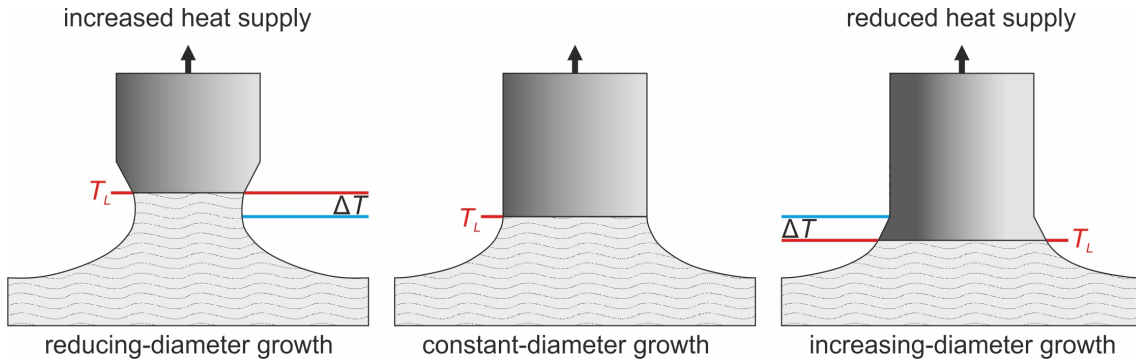


Figure 2.3: Diameter development in Czochralski growth from solution. The main factor for the diameter evolution is the state of the three-phase coexistence line (crystal, solution, Ar atmosphere), that is affected by the position of the liquidus temperature  $T_L$ . Changed after [49].

To test if the seeding temperature is correct, fast test pulling of 2 mm/h was applied. Too low or too high temperatures lead either to a rapid diameter increase or a separation of the seed and the melt, respectively. If the temperature is correct, after the test pulling process the grown crystal and the first millimeters of the seed are dissolved again. This is because the abrupt snapping of the slightly warmer melt to the seed may cause dislocations due to stresses induced by a thermal shock [53] and a larger diameter at the upper part of the wedge-shaped seed increases its stability and lowers the risk of losing a grown crystal. Then the actual growth process starts. First, the diameter is increased, forming the shoulder of the crystal. After that the aim is to keep the diameter constant and pull a crystal of cylindrical shape. According to fig. 2.3 the diameter control in Czochralski growth works by increased or decreased heat supply. This may either be achieved by controlling the pulling rate and therefore change the latent heat by crystallization or it may be achieved by changing the power of the heater. Both methods shift the liquidus temperature  $T_L$ . Increased heat supply will shift  $T_L$  upwards, changing the angle between crystal and melt at the three-phase coexistence line as shown in fig. 2.3, a: The amount of melt in the meniscus increases and an interplay of surface tension and adhesion causes a constriction of the meniscus. Accordingly, the next layer of the crystal will be narrower than the previous one and the diameter of the crystal will be reduced. In opposite an increasing diameter (for example during the growth of the crystal's shoulder) will be achieved by reduced heat supply, lowering  $T_L$  [49]. The scale of growing intermetallics for basic research is by far too small that the released latent heat has an influence on the heat supply at the growth interface. Therefore, diameter control can be only achieved by power supply of the heater.

Because growth is carried out from solution, the temperature has to be adapted all the time to the liquidus surface of the melt. Consequently, continuous cooling of the melt is necessary, with cooling ramps adapted to the steepness of the liquidus curve. The diameter increases when the cooling ramp is steeper than the liquidus curve and consequently decreases vice versa. Theoretically, the temperature program can be run automatically, programmed after the steepness of the liquidus curve. In practical operation the unknown ternary liquidus surfaces and factors like increased thermal transport with increasing crystal mass and its dependence on the

crystal shape do not allowed this. Thus, the temperature program is only based on the operator's evaluation, leading to slight fluctuations of the crystal diameter. Especially, because of the slow growth rates, changes in the diameter get visible hours to days later.

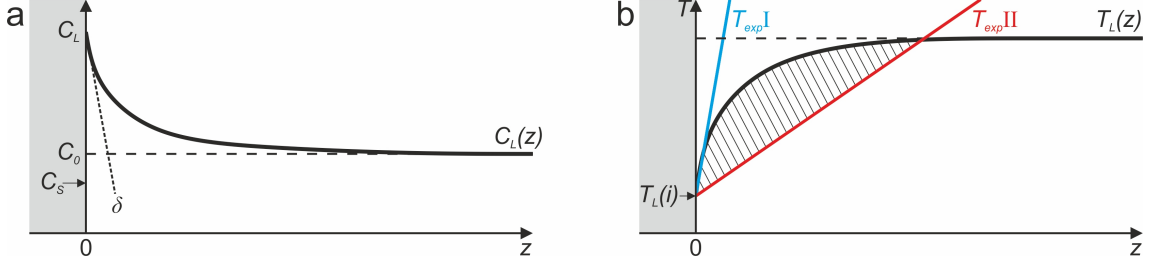


Figure 2.4: Sketch of the growth interface (grey: crystal) regarding a) the concentration curve of an excess component and b) the corresponding liquidus temperature curve in the solution.  $T_{exp I}$  displays a non-critical experimental temperature gradient and  $T_{exp II}$  displays a critical experimental temperature gradient where constitutional supercooling occurs. Drawn after [49] and [54].

Incongruent crystal growth implies another difficulty. Regarding fig. 2.4, a, the excess component (in this case the solvents Ga and Sn) is enriched next to the interface of a constantly growing crystal since the crystal has a different composition than the melt. This leads to a concentration gradient in the solution. The transport in the layer next to the interface is diffusion driven only. Since diffusion is the slowest transport mechanism in the fluid, incongruent crystal growth is a diffusion-limited, slow process. As a result, there is always a region in the melt below the interface where the liquidus temperature in the bulk melt,  $T_L(z)$ , is higher than the liquidus temperature at the actual growth interface,  $T_L(i)$  (fig. 2.4, b). Meaning, that regions in the bulk of the melt have better conditions to crystallize than those directly next to the growth interface. In the case of a high experimental temperature gradient ( $T_{exp I}$ ) in the melt, conditions for crystallization are only fulfilled directly next to the crystal. However, if the experimental temperature gradient is low ( $T_{exp II}$ ) temperatures in the melt may be below the liquidus temperature and a supercooled region next to the growth interface is formed (fig. 2.4, b, hatched area). This effect, called constitutional supercooling, may lead to growth interface instabilities that appear in practice as dendritic growth, cellular growth, or trapping of solution in the crystal [55–57]. Hence, a high experimental temperature gradient ( $T_{exp I}$ ) is important for incongruent crystal growth. However, naturally metallic melts have an excellent thermal conductivity (at least in the dimension of two digit  $W/mK$ ) and therefore a low thermal gradient is expected. Tiller's equation describes the conditions that must be fulfilled to achieve a stable growth interface [58].

$$\frac{G}{v} \geq \frac{mC_0(1 - k_0)}{Dk_0} \quad (2.1)$$

Accordingly, to avoid constitutional supercooling and ensure a stable growth interface the quotient of the temperature gradient,  $G$ , and the growth rate,  $v$ , needs to be larger than a certain value depending on the slope of the liquidus curve,  $m$ , the

initial concentration,  $C_0$ , the diffusion coefficient,  $D$ , and the equilibrium segregation coefficient,  $k_0$ . Therefore, since  $G$  is low naturally, a slow growth rate is the only influenceable variable to achieve a stable growth interface. If growth rates are slow enough, diffusion-driven transport of the excess component away from the melt may be sufficient, causing a lower concentration gradient  $\frac{dC_L}{dz}$  according to Fick's first law [59]. It holds

$$(C_L - C_S)v = -D \left( \frac{dC_L}{dz} \right)_{z=0} \quad (2.2)$$

where  $C_L$  is the concentration at the growth interface,  $C_S$  is the concentration in the crystal,  $v$  the growth rate,  $D$  the diffusion coefficient and  $z$  the distance from the growth interface. A lower concentration gradient implies a lower change of the liquidus temperature of the solution next to the growth interface (fig. 2.4, b) and therefore low experimental temperature gradients are feasible.

During the progressing crystal growth experiment it holds furthermore that the concentration difference between crystal and solution ( $C_L - C_S$ ) increases (due to Pd depletion and Ga, Sn enrichment in the solution) while the conditions for diffusion get worse with decreasing liquidus temperatures [60]. Accordingly, the pulling rates have to be continuously decreased to maintain a stable growth interface. As a result, the cooling program has to be adapted to the pulling rate. The pulling rates were usually in the range of 100  $\mu\text{m}/\text{h}$  for the first mm and were continuously lowered in steps until 25  $\mu\text{m}/\text{h}$  in the last part of the crystal. After finishing the crystal growth, the crystal was removed from the melt by fast pulling (20 mm/h).

## 2.3 Preparative methods

### 2.3.1 Orientation of single-crystalline slices

Since the basis of the project are catalytic measurements on surfaces of well-oriented crystallographic planes ( $hkl$ ), the orientation of single-crystalline slabs was necessary. Prior to cutting, the slices were fixed on a goniometer with the Logitech 0CON-200 wax and then brought to a Laue camera with backscattering mode. The accuracy of the adjustment of the slices was within  $0.1^\circ$ .

### 2.3.2 Surface preparation

After orienting, the slabs were transferred with the goniometer onto a WS 22, (KD UNIPRESS) wire lapping saw and cut with a 50  $\mu\text{m}$  tungsten wire and a slurry made of 800 mesh boron carbide and glycerol. Cutting by lapping allows a minimum surface damage and material loss. After cutting, the slabs were transferred to a polishing head without further correction. The angular error was typically below  $0.5^\circ$ . According to the trigonometrical tangent function a deviation of the desired crystallographic plane and the real surface of  $0.5^\circ$  results in a step of approximately one unit cell every 100–200 unit cells and is therefore acceptable.

Before the polishing, lapping with 3–5  $\mu\text{m}$  corundum water suspension was applied for approximately 15 minutes. Then polishing with diamond paste of decreasing grain size with 9, 6, 3, 1 and 0.25  $\mu\text{m}$  for 1–2 h for each step with a moderate pressure of 1–2 kPa was applied. Finally, if necessary, a 10-minute chemo-mechanical

polishing step with Syton OP-S (*Struers*) was carried out. Problems arising and the evaluation of the polished surfaces are explained closer in section 2.4.1.2.

## 2.4 Analytical methods

### 2.4.1 X-ray diffraction methods

#### 2.4.1.1 X-ray powder diffraction (XPD)

X-ray powder diffraction (XPD) was used to analyse the phase content in the pre-experiments and to study the lattice parameters of different phases. The samples were ground in an agate mortar and later sieved with a 20  $\mu\text{m}$  polyamide sieve. It turned out that phases of the Ga-Pd system are very sensitive to stress, induced from grinding. Therefore, annealing of the powders was necessary before X-ray diffraction measurements. Single crystal samples, or the powders of single crystals, respectively from the Ga-Pd-Sn system were annealed at 800°C for 12 h. Multi-phase samples from the Ga-Pd-Sn system were annealed at 580°C for 24 h. These conditions are further explained below. The data collection was carried out, depending on the specific material or purpose of the measurement, either in reflection with Bragg-Brentano geometry on quartz zero-background sample holders or in transmission with Debye-Scherrer geometry in glass capillaries. Bragg-Brentano geometry with higher wavelength was superior for phase analysis or lattice parameter fitting. Debye-Scherrer geometry reduces texture effects like preferred orientation and therefore was mainly used for the Rietveld refinement of powders of single crystals. In most cases a Bragg-Brentano diffractometer (XRD3003 TT) with Cu- $K\alpha_1$  radiation and a Ge(111) monochromator was used. High-resolution data were collected on a 1D position-sensitive semiconductor detector (PSD, 1D Meteor) with a resolution of  $2\theta = 0.013^\circ/\text{step}$ . For lattice parameter fitting, an internal  $\text{LaB}_6$  standard (NIST 660a) was used. Since complicated platy-like cracking behaviour was observed in several samples, a STOE KRISTALLOFLEX Debye-Scherrer diffractometer, equipped with a Mo- $K\alpha_1$  radiation, a Ge(111) monochromator and a PSD with a resolution of  $2\theta = 0.1^\circ/\text{step}$ , was used in order to suppress preferred orientation/texture effects. Measurements almost free from preferred orientation were achieved by using 0.5 mm capillaries and 30 % internal  $\alpha\text{-Al}_2\text{O}_3$  standard (NBS 674a) as supporting material.  $\alpha\text{-Al}_2\text{O}_3$  was chosen since its lower structure factor, compared to the phases of the Ga-Pd-Sn-system allowed such high amounts of Standard as supporting material. Phase analysis as well as lattice parameter refinement was done by Rietveld refinement. Le Bail fitting was applied for phase analysis and lattice parameter refinement since the influence on Sn on the structure of several phases is unknown yet. For both models the program package *FullProf* was used [61]. For Rietveld refinement and phase analysis the pseudo-Voigt function as a linear combination of the Gaussian and the Lorentzian function was used. The FWHM, the maximum intensity and the peak position are equal for both, the Gaussian and the Lorentzian profile proportion. It is written as

$$pV(x) = \eta L(x) + (1 - \eta)G(x), 0 \leq \eta \leq 1 \quad (2.3)$$

where  $L$  is the Lorentzian function and  $G$  the Gaussian function. For crystallite size and microstrain refinement the Thompson-Cox-Hastings function (also a

pseudo-Voigt function) was used [62]. The instrument parameters were refined on diffraction patterns of measured  $\text{LaB}_6$  standard (NIST 660a).

In the Ga-Pd-Sn system, different eutectoid or spinodal decompositions occurred, resulting in grain sizes that cannot be resolved with EDX or WDX. Hence, XPD was in many samples the only possibility to analyse the phase content. After the first XPD measurements, it emerged that annealing was necessary as the samples are partly very sensitive to stress, induced by grinding, resulting in extremely broad peaks. (figs. A.10 and A.11). To find proper annealing conditions, series of annealing experiments on identical sieved powders ( $< 20 \mu\text{m}$ ) of (i) a multiphase sample (QX647-B) and (ii) a former single crystal were carried out. Before annealing, all powders were evacuated to HV in silica ampoules, then filled with 130 mbar Ar (5N grade) and fused. The multiphase specimen was chosen since it contained the most common phases: Two generations of  $\text{Ga}_{1-x}\text{Sn}_x\text{Pd}_2$ ,  $\text{Ga}_{1-x}\text{Sn}_x\text{Pd}$  and  $\text{Ga}_{2+p+q}\text{Sn}_{4-p}\text{Pd}_9$ . The temperature series of the multiphase sample were  $580^\circ\text{C}$ ,  $680^\circ\text{C}$  and  $780^\circ\text{C}$  for 24 h each. The lowest  $T$  of  $580^\circ\text{C}$  was chosen 50 K below the lowest detected DTA signal at  $630^\circ\text{C}$ . Also, temperatures 100 K and 200 K higher were tested since better results were expected at higher  $T$ . The results showed changes in the phase content for the sample annealed at  $780^\circ\text{C}$ . Annealing at  $580^\circ\text{C}$  or  $680^\circ\text{C}$  did not show any differences (fig. A.10). Therefore,  $580^\circ\text{C}$  was considered the best annealing temperature since it is below the lowest DTA signal. A second series of annealing was carried out with the most proper  $T = 580^\circ\text{C}$  for 12 h, 24 h, and 120 h annealing time. While the 12 h run still showed broad peaks, the 24 h run exhibited the best patterns. Longer annealing times resulted in a change of the phase content, remarkably at 120 h (fig. A.11).

Quenched samples were very difficult to analyse since annealing undid the results of quenching. One attempt of analysing the phase content of quenched samples were XPD measurements in Bragg-Brentano geometry on polished transversal sections of the ingots from the equilibrium-cooling experiments. The idea was to ablate the disrupted interface layer and hoping for a grain size low enough and evenly distributed orientation. However, the problem was poor statistics resulting in either extreme intensities or missing peaks for specific lattice planes. Furthermore, it was observed that many of the equilibrium-cooling droplets had a very uniform orientation of specific phases, resulting additionally in texture effects, i.e. preferred orientation in diffraction patterns.

As a single-phase model material a piece of a Czochralski-grown single crystal with the composition  $\text{Ga}_{0.7}\text{Sn}_{0.3}\text{Pd}_2$  was used. It was milled and sieved as described above. In single-phase materials of the Ga-Pd-Sn system, that were handled within this project ( $\text{Ga}_{1-x}\text{Sn}_x\text{Pd}_2$ ,  $\text{Ga}_{1-x}\text{Sn}_x\text{Pd}$ ) no changes in the phase content were expected or observed at temperatures lower than  $900^\circ\text{C}$ . Annealing was tested at  $800^\circ\text{C}$  for 12 h and 24 h and under the same condition as the multiphase powders for comparison ( $580^\circ\text{C}$  for 24 h). Furthermore, having quenched polycrystalline powders in mind, crushing the material in liquid  $\text{N}_2$  was tested since a more brittle cracking behaviour and less deformation, i.e. strain was expected at temperatures as low as  $-196^\circ\text{C}$ . However, only minor improvement could be achieved. An analysis of the FWHM revealed a slight improvement of powders crushed in liquid N compared to powders crushed at room temperature but the effect was too small for proper Rietveld refinement (fig. A.9). Also different grain sizes were tested for their quality in XPD measurements. The idea was that less milling would damage the stress

sensitive material less. Here the grain size ranges  $< 20 \mu\text{m}$ ,  $20\text{--}50 \mu\text{m}$  and  $50\text{--}100 \mu\text{m}$  were compared (fig. A.9). As expected, larger grain size samples had improved FWHM, but pronounced preferred orientation occurred (see the comparison between the diffraction patterns displayed in fig. A.8). Annealing at  $800^\circ\text{C}$  improved the FWHM remarkably compared to annealing at  $580^\circ\text{C}$  for 24 h (fig. A.9). Since the difference between  $800^\circ\text{C}$  for 12 h or 24 h was marginal, 12 h was chosen.

Summarizing, the best annealing conditions for multiphase samples were  $580^\circ\text{C}$  for 24 h, for single-phase samples  $800^\circ\text{C}$  for 12 h and quenched samples were difficult to analyse.

#### 2.4.1.2 X-ray diffraction on single-crystalline slabs

First results of catalytic measurements by S. Barth, TU Chemnitz on the surfaces of slabs of the three crystallographic main directions revealed results that cannot be explained with a single-crystalline surface: (i) The conversion on all crystallographic planes was the same. (ii) The conversion on the slabs was as high as in powdered samples while it should be lower on single-crystalline surfaces. (iii) The selectivity on the single-crystalline slabs was low while it should be high compared to powders or polycrystalline material [63]. Furthermore, during quick orientation checks of single-crystalline polished slices on a powder diffractometer in Bragg-Brentano geometry, there were peaks present which are not connected to the plane being currently in diffraction condition. According to Bragg's equation  $n\lambda = 2d\sin\theta$ , on a diffractometer with Bragg-Brentano geometry, only lattice planes being parallel to the diffractometer's zero plane can be in diffraction condition [64, 65]. Accordingly, only one peak (or its higher orders) is allowed to appear in the diffractogram. In the case of different slabs of  $\text{Ga}_{1-x}\text{Sn}_x\text{Pd}_2$  different peaks occurred. These circumstances gave rise to further investigations of the surfaces.

To investigate the condition of the surface of the single crystal slices, a sample holder was constructed to take up the polishing head (fig. 2.5). Hence, after every polishing step, control of the surface was possible. The slices were fixed with Logitech 0CON-200 wax on the polishing head. To shield signals from the polishing head or the diffractometer sample holder, a Pb aperture with a hole was designed to absorb X-rays scattered from anything else than the crystal. In consequence of the Pb shield Pb reflexes were present but did not interfere with peak positions of the crystals. Figs. A.2, A.4 and A.6 in the appendix show that the intensity of the undesired peaks decreases with every polishing step. Furthermore, the intensities of the peaks decrease with longer polishing time and with lower polishing pressure. The optimum polishing pressure was in the order of  $1\text{--}2 \text{ kPa}$ . It was adjusted by measuring the force with a load cell and adapting it to the crystal's surface being polished. Slices with different crystallographic orientations behave different. Regarding the (100) surface after polishing with  $6 \mu\text{m}$  diamond polish, the signal

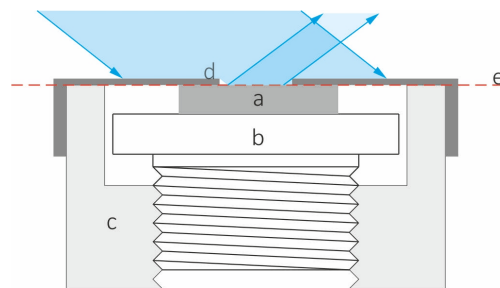


Figure 2.5: Schematic sketch of a diffractometer sample holder for testing the polishing quality: a) crystal, b) polishing head, c) sample holder, d) Pb aperture, e) diffractometer zero plane.



cannot be distinguished from the background any more, while in the case of the (001) surface, polishing down to 1  $\mu\text{m}$  diamond polish was necessary. The signals did not disappear at all on the (010) surface by mechanical polishing down to 0.125  $\mu\text{m}$  and chemo-mechanical polishing with Syton OP-S could not be avoided.

#### 2.4.1.3 Laue diffraction

Laue X-ray diffraction in backscattering geometry was used for orienting the single crystals prior to cutting crystal slabs for catalytic investigations or seeds for growth experiments. Additionally, crystals were checked for their single-crystallinity by scanning with the Laue camera on different positions on the crystal.

#### 2.4.1.4 X-ray topography

X-ray topography (XRT) was carried out at the Fraunhofer-Institut für Integrierte Systeme und Bauelementetechnologie (IISB) in Erlangen. A Rigaku XRTmicron using Cu- $K\alpha$  radiation and on some subgrains also Cr- $K\alpha$  at 40 kV and 30 mA in reflection mode in Lang geometry with a XTOP high-resolution CCD detector with a pixel size of 5.4  $\mu\text{m}$  was used. One single-crystalline (100) slab of  $\text{Ga}_{0.6}\text{Sn}_{0.4}\text{Pd}_2$  was measured using the 412 reflection. By  $\omega$  scans with  $\Delta\omega = 0.1^\circ$  an orientation map was created and by composing topographs with different  $\omega$  a maximum intensity map was created.

### 2.4.2 Electron microscopy

Electron microscopy was carried out for imaging, chemical analysis and detailed orientation checks.

On a Cameca SX-100 EPMA system backscattered electron (BSE) imaging and chemical analyses by wavelength-dispersive X-ray spectroscopy (WDX) were carried out. The EPMA was equipped with five wavelength-dispersive X-ray spectrometers and a  $\text{LaB}_6$  cathode. An accelerating voltage of 15 keV and a current of 40 nA was used and the calibration was carried out on standards of binary GaPd and elemental Sn. Later a Czochralski-grown externally certified single crystal of  $\text{Ga}_{0.7}\text{Sn}_{0.3}\text{Pd}_2$  was used as standard material [66]. Pd- $L_\alpha$  and Sn- $L_\alpha$  were measured on a PET crystal and Ga- $K_\alpha$  was measured on a LiF crystal. For matrix correction the PAP model was used [67].

A Hitachi Schottky field emission scanning electron microscope (FE SEM SU5000) in both, secondary electron (SE) and BSE mode at 20 kV acceleration voltage was used for imaging in few cases, due to its better resolution compared to the EPMA.

For electron backscatter diffraction EBSD the Kikuchi patterns were acquired using a Bruker Quantax EBSD system with a  $e^- \text{Flash}^{HR}$  detector and the software package *Esprit*, version 2.2. The resolution for the Kikuchi patterns was 320 x 240 pixels, the acceleration voltage was 15 kV, the sample distance was 18 mm and the samples were tilted  $70^\circ$ . The EBSD system is mounted to a scanning electron microscope (Jeol JSM 7800 F) with an ARGUS<sup>TM</sup> imaging system, equipped with two BSE and three foreshattered electron (FSE) detectors.

### 2.4.3 Differential thermal analysis

Differential thermal analysis (DTA) was mainly used in order to understand crystallization paths and phase transitions and to get information about the liquidus temperature of specific compositions. Usually segments cut out of ingots from the normal freezing experiments were analysed by DTA. Since a representative part of a sample was necessary to get valuable data in order to interpret its crystallization path, the segments were cut through their vertical axis. Experiments have shown that crystallization typically starts from the bottom, or primarily crystallized phases sink to the ground, causing a segregation along the vertical axis, but not perpendicular to it. For the measurements a Netzsch DTA (404/3/F) system was used. The measurements were carried out under stationary Ar atmosphere of ambient pressure in open alumina crucibles (30  $\mu\text{l}$ ) with typical sample masses of around 50–100 mg.  $\text{Al}_2\text{O}_3$  powder was used as reference. The heating and cooling rates were 5 K/min. The DTA was calibrated using the melting points of Ag ( $T_m = 961.8^\circ\text{C}$ ) and Au ( $T_m = 1064^\circ\text{C}$ ) under the same conditions. The onset<sup>4</sup> temperature was defined as the intercept of the baseline of the DTA curve and the tangent in the first turning point of the peak. For the endset it was the intersect of the baseline and the last turning point.

### 2.4.4 Phase diagram information

It is worth to mention how the information, necessary to grow single crystals were processed. The most important information are the tie-lines<sup>5</sup> and boundaries of the primary crystallization areas in the phase diagram as well as rough estimations of the growth temperatures. An idea of the ternary phase diagram in the vicinity of the phases that need to be grown, is necessary. The information was gained from analysing the experiments described in the chapters 2.1.3 and 2.1.2. The approach of evaluating and interpreting BSE and SE images, XPD, DTA, WDX and EDX data and combining the information has proven to be the method of choice.

---

<sup>4</sup>In hint 6 the use of the terms “onset” and “endset” is explained.

<sup>5</sup>Tie-lines connect the composition of the melt with the solid being in equilibrium with it.

# Chapter 3

## Results

### 3.1 Phase diagram studies in the Ga-Pd-Sn system

Fig. 3.1 shows some examples for the resulting solid bodies of equilibrium-cooling and Bridgman experiments that were analysed for the phase diagram studies. The equilibrium-cooling experiments can be grouped according to their initial melt composition, phase content, their structural appearance and their DTA curves. Accordingly, regions with samples that have similarities can be described that are shown in fig. 3.2. The most abundant phases are listed in tabs. 1.1 and 3.1. In the following sections characteristic examples are described closer for each of such a region. The Sn or Ga substitution behaviour in the binary phases is not always clarified. Usually, Ga and Sn substitute each other, like in  $\text{Ga}_{1-x}\text{Sn}_x\text{Pd}_2$ . The lack of single crystals has not allowed structure refinement by X-ray methods, yet. Therefore, assumptions on the incorporation of the third component into binary phases can only be made, based on the measured chemical compositions.

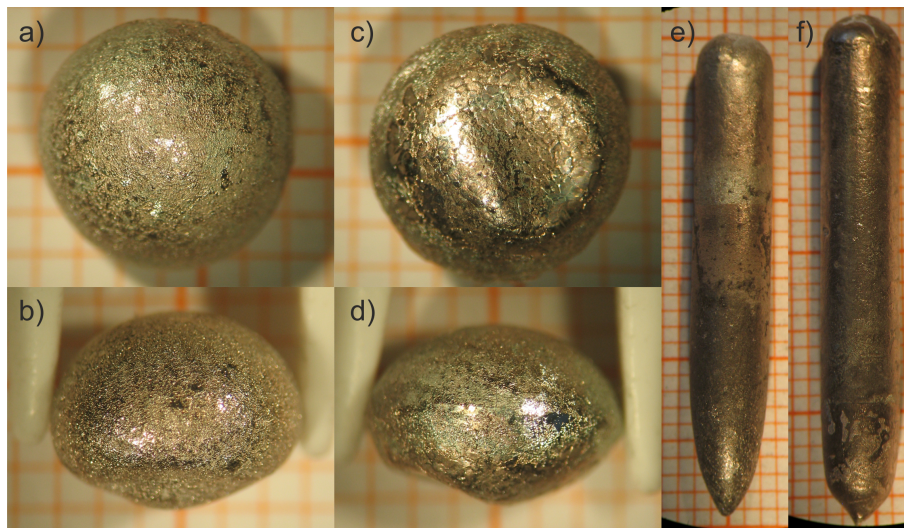


Figure 3.1: a-d) Resulting solid droplets from equilibrium-cooling experiments. In c and d it is visible that there are grains (of  $\text{Ga}_{1-x}\text{Sn}_x\text{Pd}_2$ ) accumulated at the bottom. e,f) Resulting ingots from the Bridgman experiments.

Phase	Structure type	Pearson symbol	Space group	Lattice parameter [Å]			Ref.
				<i>a</i>	<i>b</i>	<i>c</i>	
$\text{Ga}_{2+p+q}\text{Sn}_{4-p}\text{Pd}_9$	$\text{Ti}_2\text{N}^*$	<i>cF120</i>	<i>Fd\bar{3}m</i>	12.4048(9)			[40]
$\text{Ga}_3\text{Pd}_5$	$\text{Ge}_3\text{Rh}_5$	<i>oP16</i>	<i>Pbam</i>	5.41(1)	10.49(1)	4.02(1)	[25]
$\text{Pd}_{20}\text{Sn}_{13}$	$\text{Ni}_{13}\text{Ga}_3\text{Ge}_6$	<i>hP66</i>	<i>P3_121</i>	8.7985(11)		16.984(3)	[68] <sup>†</sup>

Table 3.1: Published crystal structure data of further phases that occur in the vicinity of the solid solutions  $\text{Ga}_{1-x}\text{Sn}_x\text{Pd}_2$  and  $\text{Ga}_{1-x}\text{Sn}_x\text{Pd}_2$ .\*) Related to the structure type with additional Pd atoms in octahedral and tetrahedral voids. †) Later revisited with the inverted space group  $P3_221$  [69].

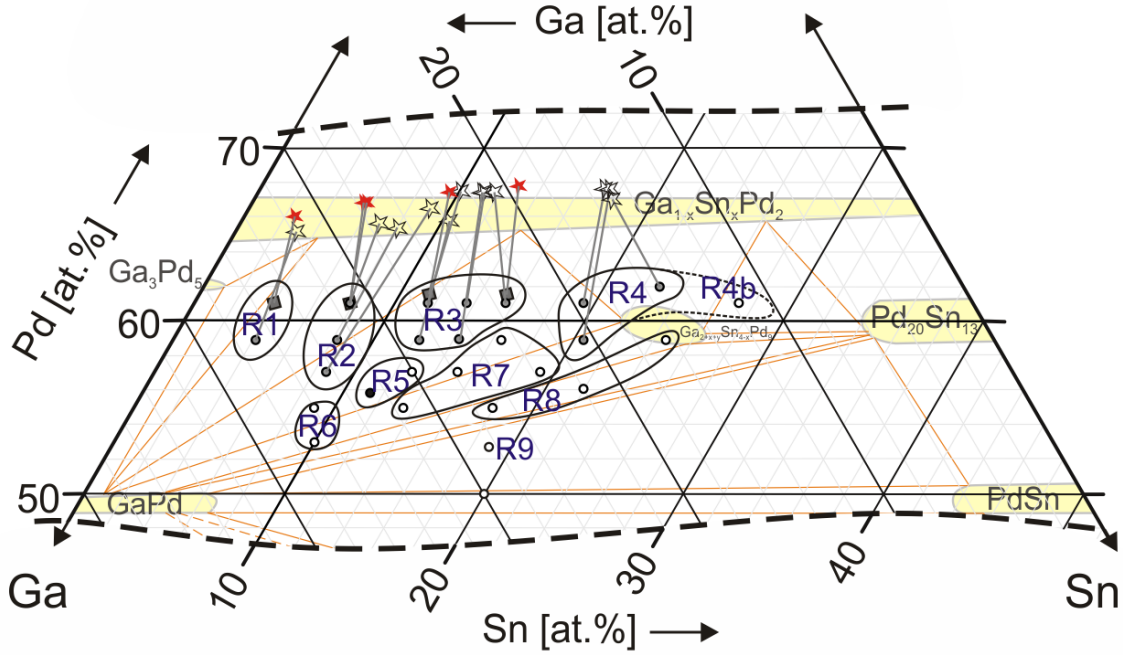


Figure 3.2: Regions R1–R9 that have specific phase contents (listed in tab. A.3), related crystallization paths and textures. The dots represent the initial compositions of the experiments. Grey-filled experiments result in the primary crystallization of  $\text{Ga}_{1-x}\text{Sn}_x\text{Pd}_2$ . The corresponding grey lines are the tie-lines<sup>1</sup> while the first-to-freeze compositions are shown as stars. Red stars are Czochralski experiments. The stability regions of the different phases drawn in yellow as well as their orange tie-triangles<sup>2</sup> are published by [18] and refer to the temperature of 500°C. The boundary lines of the regions are only a help for the viewer.

### 3.1.1 X-ray powder diffraction analysis

First results concerning the methodology of the X-ray powder diffraction (XPD) measurements were presented in chapter 2.4.1.1 especially with focus on annealing of the samples. In polycrystalline samples the Bragg-Brentano geometry diffractometer with  $\text{Cu-K}\alpha_1$  radiation and accordingly higher wavelength, showed to be the more

<sup>1</sup>Tie-lines connect the composition of the melt with the solid being in equilibrium with it.

<sup>2</sup>Tie-triangles connect the three phases that are in equilibrium [42].

suiting option compared to the Mo- $K\alpha_1$  radiation with shorter wavelength. Most phases of the Ga-Pd system are closely related in their structure according to the intergrowth concept [24]. Accordingly, the peaks of the different phases with closely related structures are in very similar positions. This also holds for the substitution of Ga by Sn and also the only ternary phase  $\text{Ga}_{2+p+q}\text{Sn}_{4-p}\text{Pd}_9$ . Therefore, the short Mo wavelength causes massive peak overlapping in the diffraction patterns, while Cu- $K\alpha_1$ -measured patterns allow proper differentiation of the peaks. Phases with minor proportions may be still hidden by other ones. However, occasional texture effects due to crystals with platy or needle-like habitus proved to be a disadvantage here, caused by the sample preparation necessary for the Bragg-Brentano geometry. In those cases preferred orientation was refined with the March-Dollase function but not systematically quantified. A rough tendency showed that  $\text{Ga}_{3-x}\text{Sn}_x\text{Pd}_5$  shows a platy habitus while  $\text{Ga}_{1-x}\text{Sn}_x\text{Pd}_2$  and  $\text{Pd}_{20}\text{Sn}_{13-x}\text{Ga}_x$  tend to have a needle-like habitus.

All samples from the pre-experiments were examined via XPD regarding their weight fractions and their lattice parameters of the individual phases. Their phase content is given in tabs. 3.2 to 3.12 and further details like the distribution of the phases in the samples as well as their lattice constants are presented in the sections 3.1.2 and 3.1.4. As an overview, representative diffraction patterns of different samples from each region are shown in fig. 3.3.

More detailed and typically occurring properties of the patterns are shown in fig. 3.4.  $\text{Ga}_{1-x}\text{Sn}_x\text{Pd}$  and  $\text{Ga}_{2+p+q}\text{Sn}_{4-p}\text{Pd}_9$  always have sharp and symmetrical peaks (regardless of the instrumental parameters). In the case of fig. 3.4, a,  $\text{Ga}_{1-x}\text{Sn}_x\text{Pd}_2$  also occurs in sharp symmetric peaks. This is only the case for samples with lower Pd and lower Sn content, settled around the regions R5, R6 and R7. The pattern shown in fig. 3.4, b, clearly contains two generations of  $\text{Ga}_{1-x}\text{Sn}_x\text{Pd}_2$ , one with larger and one with lower lattice parameters, resulting in lower and higher diffraction angles, respectively. Such samples are typical for higher Pd contents in the regions R2 and R3. The pattern in fig. 3.4, c, shows very asymmetric peaks for  $\text{Ga}_{1-x}\text{Sn}_x\text{Pd}_2$ . This displays a gradient in the lattice parameters and accordingly a chemical gradient (this will be elaborated later). The low-angle part of the individual peaks has a higher weight proportion than the high-angle part. Also in other experiments, this distribution occurs more frequently than the other way round however plateaus or broad peaks display that the proportions may be approximately equally, too. Such asymmetric or broadened peaks are mostly abundant in the regions R4 and R8. Between the case with two clearly distinguishable peaks of the two  $\text{Ga}_{1-x}\text{Sn}_x\text{Pd}_2$  generations (fig. 3.4, b) and the gradient within the peaks (fig. 3.4, c) mixed variations occur regularly. Fig. 3.4, d, shows a slight asymmetry in the peaks of  $\text{Pd}_{20}\text{Sn}_{13-x}\text{Ga}_x$ , with tails more pronounced on the left side of the peaks. In many cases the proportion of a specific phase is too low for a proper evaluation of the peak profiles. For example,  $\text{Ga}_{1-x}\text{Sn}_x\text{Pd}_2$  is often only present in small amounts in the sample. Then it is difficult to distinguish whether one or more generations are present or whether the lattice parameters of the phase show a gradient.



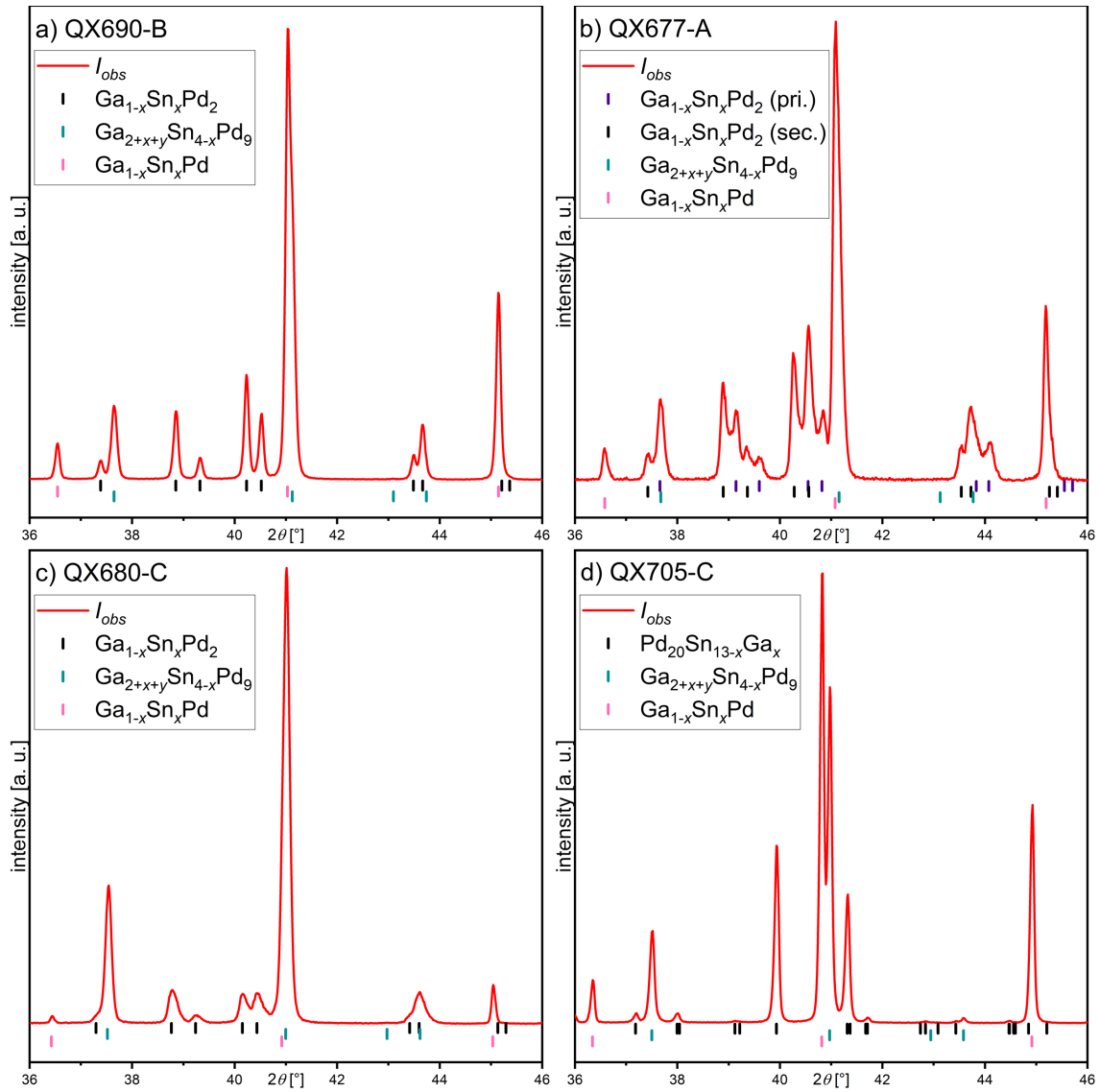


Figure 3.4: Exemplary diffraction patterns, measured with Cu- $K\alpha_1$  radiation, showing different typically occurring peak profiles. a) All phases have sharp individual peaks. b) The phase  $Ga_{1-x}Sn_xPd_2$  occurs two times, with lower and higher  $2\theta$  position for each individual peak. c) The phase  $Ga_{1-x}Sn_xPd_2$  occurs with highly asymmetrical peak profiles, with higher intensities for each individual peak at lower  $2\theta$  angles. d) The phase  $Pd_{20}Sn_{13-x}Ga_x$  occurs with asymmetrical peak profiles, but this time with higher intensities at higher  $2\theta$  angles for each individual peak.



### 3.1.2 Texture and phase content of samples in the vicinity of $\text{Ga}_{1-x}\text{Sn}_x\text{Pd}_2$

The description of the textures is based on BSE images gained by EPMA or SEM, meaning that the terms “darker”/“brighter” refer to a lower/higher average atomic number  $Z$  of the specific measured phases. In the case of  $\text{Ga}_{1-x}\text{Sn}_x\text{Pd}_2$ ,  $\text{Ga}_{2+p+q}\text{Sn}_{4-p}\text{Pd}_9$  and  $\text{Pd}_{20}\text{Sn}_{13-x}\text{Ga}_x$ , WDX measurements show that sometimes the orientation contrast of individual grains can be greater than the contrast between the different phases because the average atomic numbers are similar. In such cases, phases can only be distinguished by WDX/EDX measurements.  $\text{Ga}_{1-x}\text{Sn}_x\text{Pd}$  has the highest Ga content and the lowest Pd and Sn contents and therefore can be easily identified as a darker phase. The chronological order of crystallization is discussed later in detail. In the following paragraphs, the discussed regions R1–R9 of the phase diagram are numbered consecutively according to fig. 3.2

#### 3.1.2.1 Region R1

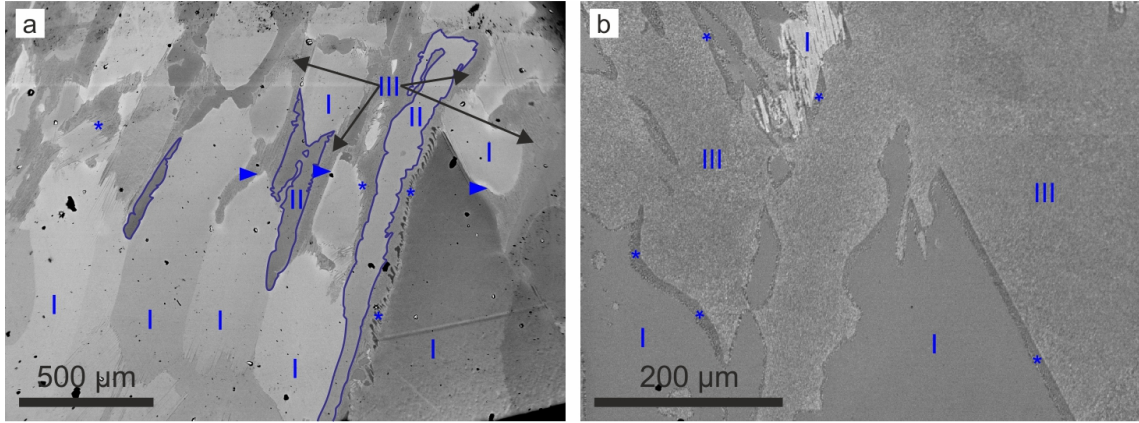


Figure 3.5: BSE images of QX642-A as an example for experiments of starting melt compositions in region R1 (fig. 3.2, R1). The Roman numerals I-III mark different repeating paragenetic sequences (or phases) of the texture.

Solids crystallized from melts according to region R1 (fig. 3.2, R1, tab. 3.2) contain the phases  $\text{Ga}_{1-x}\text{Sn}_x\text{Pd}_2$ ,  $\text{Ga}_{3-x}\text{Sn}_x\text{Pd}_5$  and  $\text{Ga}_{1-x}\text{Sn}_x\text{Pd}$ .  $\text{Ga}_{1-x}\text{Sn}_x\text{Pd}_2$  exists in two generations, one primarily solidified and one finely distributed in the matrix. Region R1 includes experiments with a low Sn content of  $x_L \leq 0.1$  and a Pd content of  $59 \leq y_L \leq 61$  in the initial composition<sup>3</sup>. The texture in region R1 consists of large grains of  $\text{Ga}_{1-x}\text{Sn}_x\text{Pd}_2$  (fig. 3.5, phase I), followed by elongated grains of  $\text{Ga}_{3-x}\text{Sn}_x\text{Pd}_5$  (blue-framed phase, II, in fig. 3.5). The spaces are filled with a dispersed, fine-grained material with grain sizes smaller than 1–2  $\mu\text{m}$  (fig. 3.5, sequence III). The  $\text{Ga}_{1-x}\text{Sn}_x\text{Pd}_2$  grains (I) show a slight increase in the Sn content from the inner to the outer part or from the bottom to the top, i.e. always in the direction of the growth. The Sn content rises sharply at the edge of the grains, which is clearly visible in the light-coloured rim in the BSE images (blue arrows, fig.

<sup>3</sup>According to the description  $(\text{Ga}_{1-x_L}\text{Sn}_{x_L})_{100-y_L}\text{Pd}_{y_L}$ .



3.5, a). The brightness difference within these grains may be even larger than the brightness contrast between grains of the phases  $\text{Ga}_{1-x}\text{Sn}_x\text{Pd}_2$  and  $\text{Ga}_{3-x}\text{Sn}_x\text{Pd}_5$ . Both indicates segregation during the crystallization. As a result, these phases can only be distinguished by WDX measurements. The average composition of most  $\text{Ga}_{3-x}\text{Sn}_x\text{Pd}_5$  grains is  $\text{Ga}_{2.86(3)}\text{Sn}_{0.11(3)}\text{Pd}_{5.03(3)}$ . The measured composition with the highest Sn content was  $\text{Ga}_{2.81(3)}\text{Sn}_{0.16(3)}\text{Pd}_{5.03(3)}$  and an increase of the Sn content from earlier to later-crystallized areas could also be observed in this phase. Some grains of  $\text{Ga}_{1-x}\text{Sn}_x\text{Pd}_2$  show lamellae. The stars in fig. 3.5 mark rims next to the primarily grown  $\text{Ga}_{1-x}\text{Sn}_x\text{Pd}_2$  grains that consist of parallelly grown  $\text{Ga}_{1-x}\text{Sn}_x\text{Pd}_2$  and  $\text{Ga}_{3-x}\text{Sn}_x\text{Pd}_5$  lamellae. In some cases a fine-grained, decomposed material, with a major content of  $\text{Ga}_{1-x}\text{Sn}_x\text{Pd}$  is present in these lamellae. The fine-grained matrix (fig. 3.5, sequence III) contains the phases  $\text{Ga}_{1-x}\text{Sn}_x\text{Pd}$  and  $\text{Ga}_{1-x}\text{Sn}_x\text{Pd}_2$  according to the XPD results. WDX measurements in the same area give averaged compositions resulting from different phases due to the excitation volume of the electron beam exceeding the size of individual grains. XPD refinements of the fine-grained  $\text{Ga}_{1-x}\text{Sn}_x\text{Pd}_2$  fraction allow the calculation of Sn contents from refined lattice parameters according to the equations given in section 3.3.2. While the first solidified part of primarily grown  $\text{Ga}_{1-x}\text{Sn}_x\text{Pd}_2$  grains has a measured Sn content of  $0.08(3) \leq x \leq 0.09(3)$ , rising slightly to the last grown ends of the grains, the calculated Sn content of the secondary formed generation of  $\text{Ga}_{1-x}\text{Sn}_x\text{Pd}_2$  is  $0.27(5) \leq x_{XPD} \leq 0.28(5)$ .

The only DTA curve measured from a sample in region R1 (fig. 3.6) has three endothermic signals in the heating curve. The first onset<sup>4</sup> is at  $\approx 860^\circ\text{C}$ , the second one at  $\approx 930^\circ\text{C}$  with a shoulder at higher temperatures and the third signal is a smooth rise with a sudden drop back to the base line at  $\approx 1230^\circ\text{C}$ , indicating the end of a long-lasting dissolution process. The cooling curve has only two peaks. The first is a sharp exothermic heat signal at  $1180^\circ\text{C}$  and the second one is a smaller signal at  $\approx 950^\circ\text{C}$ . The difference between the first cooling signal at  $\approx 1180^\circ$  and the last heating signal at  $\approx 1230^\circ\text{C}$  displays supercooling. The extreme sharp signal furthermore shows the sudden collapse of the supercooling.

sample	$y_L$	$x_L$	$\text{Ga}_{1-x}\text{Sn}_x\text{Pd}_2$		$\text{Ga}_{3-x}\text{Sn}_x\text{Pd}_5$ $\omega[\text{wt.}\%]$	$\text{Ga}_{1-x}\text{Sn}_x\text{Pd}$ $\omega[\text{wt.}\%]$
			primary $\omega[\text{wt.}\%], x$	secondary $\omega[\text{wt.}\%], x_{XPD}$		
QX642-A	59	0.10	12, 0.09(3)	34, 0.27(5)	7	47

Table 3.2: Phase content of the equilibrium-cooling experiments of starting melt compositions in region R1, based on Rietveld refinement. Additional information is gained from the residual melt of the Czochralski experiment QX649-II.  $y_L$  and  $x_L$  define the melt composition<sup>5</sup>.  $x_{XPD}$  is the calculated Sn content determined from the lattice parameters as described in section 3.3.2.

<sup>4</sup>In hint 6 the use of the terms “onset” and “endset” is explained.

<sup>5</sup>According to the description  $(\text{Ga}_{1-x_L}\text{Sn}_{x_L})_{100-y_L}\text{Pd}_{y_L}$ .

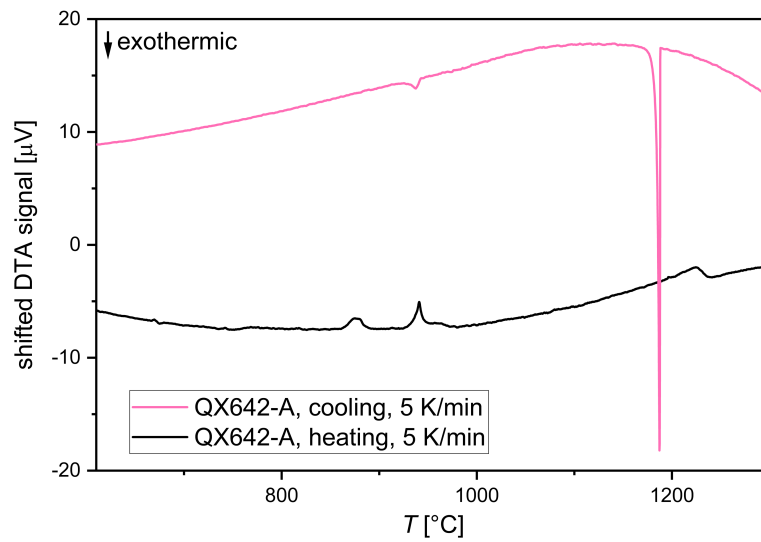


Figure 3.6: DTA curves of QX642-A from region R1.

### 3.1.2.2 Region R2

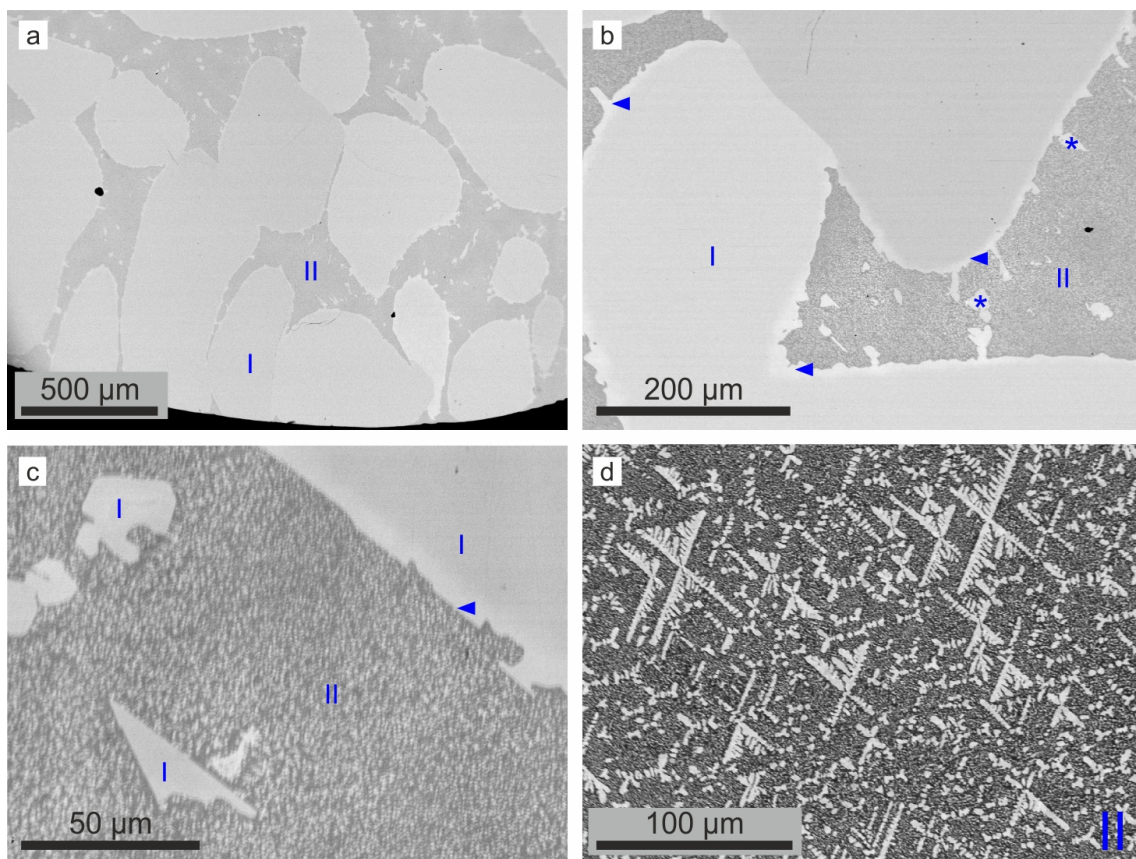


Figure 3.7: BSE images of samples from region R2 (fig. 3.2, R2). a-c) QX663-B, d) QX690-A. The Roman numerals I and II mark different repeating paragenetic sequences (or phases) of the texture.

Solids crystallized from melts according to region R2 (fig. 3.2, R2, tab. 3.3) contain only  $\text{Ga}_{1-x}\text{Sn}_x\text{Pd}_2$  and  $\text{Ga}_{1-x}\text{Sn}_x\text{Pd}$ . Again,  $\text{Ga}_{1-x}\text{Sn}_x\text{Pd}_2$  is present in two generations, one is primarily crystallized (fig. 3.7, sequence I), the other one is fine-grained in the matrix (fig. 3.7, sequence II). Experiments from region R2 have initial melts with a Sn content of  $x_L = 0.2$  and a Pd content of  $57 \leq y_L \leq 61$ <sup>6</sup>. The content of primarily grown  $\text{Ga}_{1-x}\text{Sn}_x\text{Pd}_2$  decreases from higher to lower  $y_L$  (61–57 at.%) from  $\omega = 76$  wt.% to below  $\omega = 1$  wt.%. At the rim of the  $\text{Ga}_{1-x}\text{Sn}_x\text{Pd}_2$  grains a strong increase in the Sn content is recognizable by the bright rim in the BSE images (blue arrows). The blue stars mark fine dendritic tails of  $\text{Ga}_{1-x}\text{Sn}_x\text{Pd}_2$ . The matrix is dispersed and fine-grained (smaller than 1–2  $\mu\text{m}$ ) with larger dendritic star-like grains of  $\text{Ga}_{1-x}\text{Sn}_x\text{Pd}_2$ . These may be oriented randomly (figs. 3.7, a-c) or in a crystallographic relation to each other (fig. 3.7, d). The dendrites may be up to 100  $\mu\text{m}$  in size and have a higher Sn content ( $x \approx 0.4$ ) than the first-crystallized part of  $\text{Ga}_{1-x}\text{Sn}_x\text{Pd}_2$ . The calculated Sn content  $x_{XPD}$  of  $\text{Ga}_{1-x}\text{Sn}_x\text{Pd}_2$  in the fine-grained material is uniform in all experiments with values of  $0.43(5) \leq x_{XPD} \leq 0.45(5)$ .

The DTA heating curves from these experiments (fig. 3.8) contain three endothermic signals. The first peaks have common onsets at  $\approx 850^\circ\text{C}$  and are double peaks. The second peaks also share common onset temperatures at  $910\text{--}920^\circ\text{C}$ . The third signals are smoothly rising and fall back abruptly to the background line, displaying long-lasting dissolution processes. The endset correlates with the initial Pd melt content  $y_L$ . Samples with higher  $y_L$  show higher endset temperatures, displaying that the initial Pd content has the major influence on the liquidus temperature. The DTA cooling curves contain three exothermic signals for all experiments. The first one (at high temperatures) corresponds to the endset of the last endothermic signal during heating, i.e. to the liquidus temperature. However, there are also exceptions, mostly to lower temperatures in the cooling curves, that are assigned to supercooling of the melt. In the case of one DTA curve (QX647-A) the cooling curve onset is at slightly lower temperature than the heating curve endset. Accordingly, in this experiment, the cut sample does not exactly display the initial composition and the endset of the heating signal must be taken as the correct solidus/liquidus temperature. The second exothermic signals during cooling are shared signals at  $\approx 920^\circ\text{C}$  for all experiments and the last exothermic signal during cooling varies slightly between  $650^\circ\text{C}$  and  $620^\circ\text{C}$ .

sample	$y_L$	$x_L$	$\text{Ga}_{1-x}\text{Sn}_x\text{Pd}_2$		$\text{Ga}_{1-x}\text{Sn}_x\text{Pd}$ $\omega[\text{wt.}\%]$
			primary $\omega[\text{wt.}\%], x$	secondary $\omega[\text{wt.}\%], x_{XPD}$	
QX663-B	61	0.20	76, 0.20(3)	9, 0.43(5)	15
QX647-A	59	0.20	5, 0.23(5)	45, 0.45(5)	50
QX690-A	57	0.20	< 1, 0.27(3)	45, 0.45(5)	55

Table 3.3: Phase content of the equilibrium-cooling experiments of starting melt compositions in region R2, based on Rietveld refinement.  $x_{XPD}$  is calculated from the refined lattice parameters according to the equations in section 3.3.2.  $x_L$  and  $y_L$  correspond to the melt composition<sup>6</sup>.

<sup>6</sup>According to the description  $(\text{Ga}_{1-x_L}\text{Sn}_{x_L})_{100-y_L}\text{Pd}_{y_L}$ .

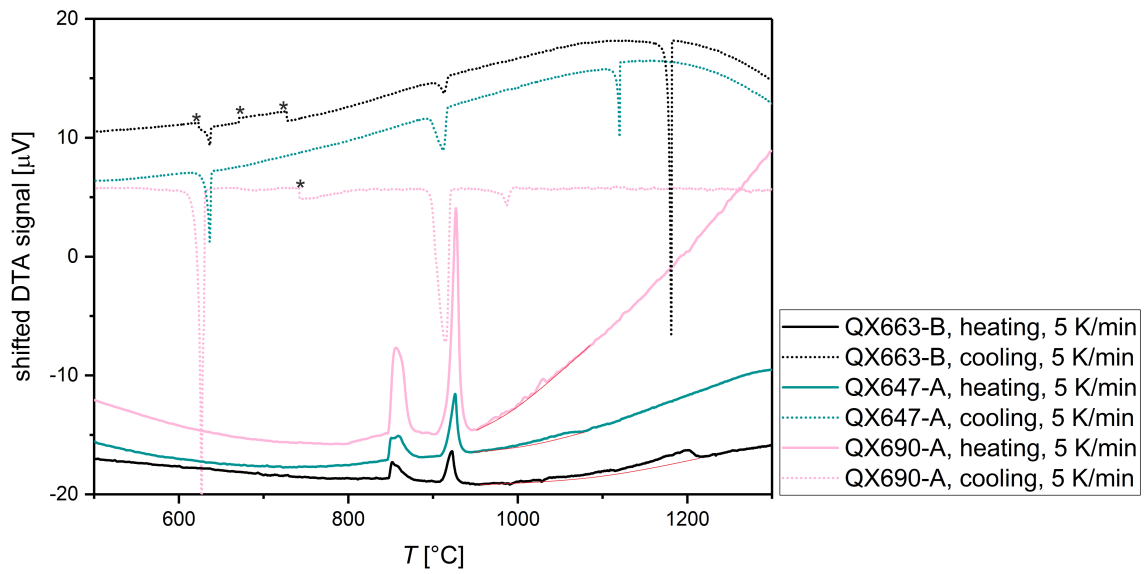


Figure 3.8: DTA curves of different samples from region R2. The stars mark artefacts, known from the instrument. Addition of thin red constructed background lines allows better visibility of dissolution processes. For the cooling curve of QX690-A a background subtraction by a manual B-spline fit was performed, due to its slope.



## 3.1.2.3 Region R3

## Equilibrium-cooling experiments in region R3

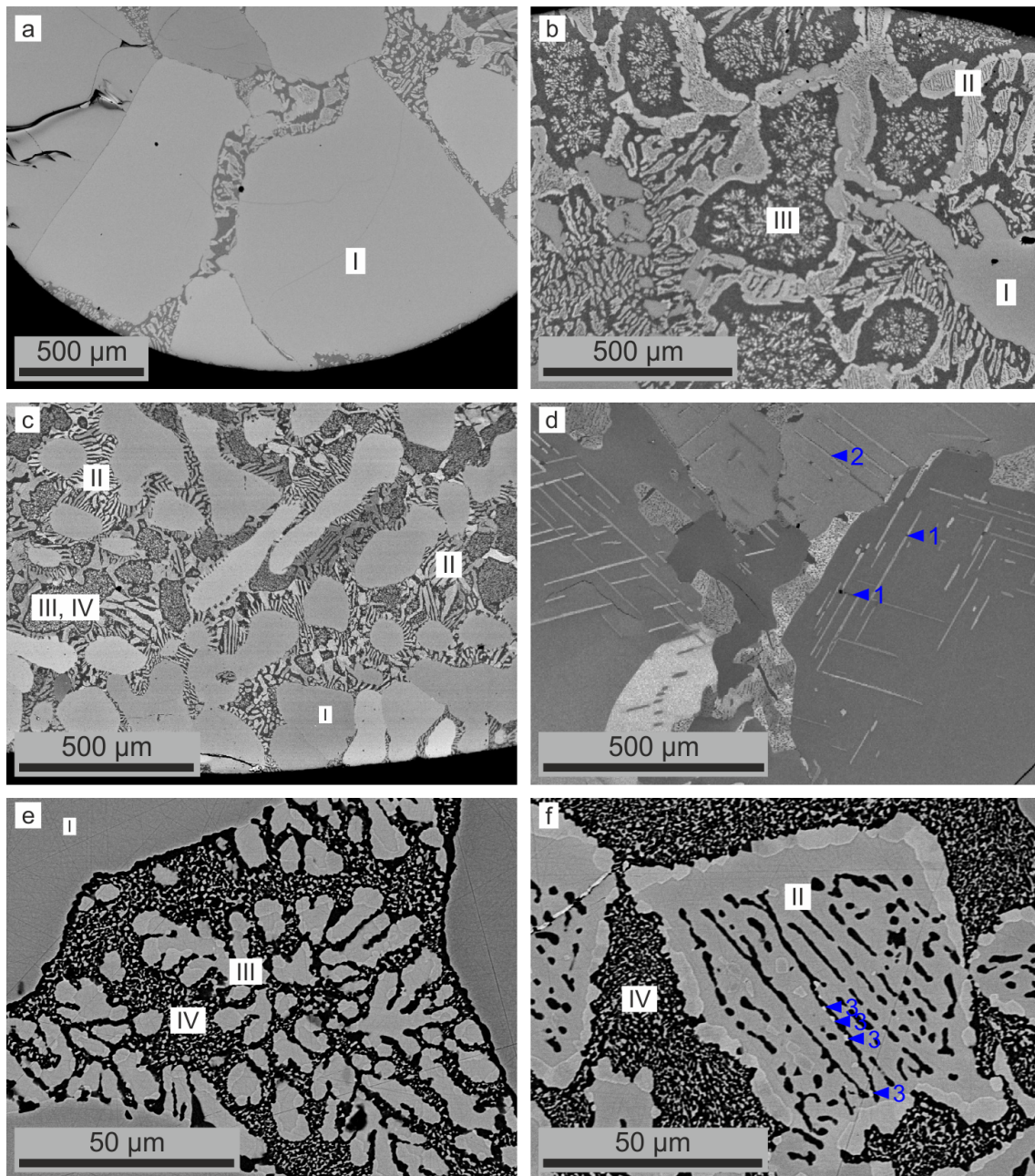


Figure 3.9: BSE images of different examples of samples from region R3 (fig. 3.2, R3), a–c), measured with the Cameca EPMA, d) with the Hitachi SEM. a,b,e,f) QX677-A, c) QX647-B, d) QX675-A. The Roman numerals I–IV mark different repeating paragenetic sequences (or phases) of the texture.

Solids crystallized from melts according to region R3 (fig. 3.2, R3, tab. 3.4) contain the phases  $\text{Ga}_{1-x}\text{Sn}_x\text{Pd}_2$ ,  $\text{Ga}_{1-x}\text{Sn}_x\text{Pd}$  and  $\text{Ga}_{2+p+q}\text{Sn}_{4-p}\text{Pd}_9$  while  $\text{Ga}_{1-x}\text{Sn}_x\text{Pd}_2$  is grown primarily. Those samples have initial melts with a Sn con-

tent of  $0.3 \leq x_L \leq 0.4$  and a Pd content of  $59 \leq y \leq 61$ <sup>7</sup>. The primarily grown  $\text{Ga}_{1-x}\text{Sn}_x\text{Pd}_2$  grains (fig. 3.9, sequence I) sometimes contain grid systems of precipitated  $\text{Ga}_{2+p+q}\text{Sn}_{4-p}\text{Pd}_9$  needles (fig. 3.9, d). Those grid systems sometimes contain fine-grained  $\text{Ga}_{1-x}\text{Sn}_x\text{Pd}$  (arrow 1). Arrow 2 shows that the  $\text{Ga}_{2+p+q}\text{Sn}_{4-p}\text{Pd}_9$  needles are sometimes accompanied by  $\text{Ga}_{1-x}\text{Sn}_x\text{Pd}$  precipitates over the full length. The second sequence (fig. 3.9, II) is formed of striped areas. Large-grained stripes of  $\text{Ga}_{2+p+q}\text{Sn}_{4-p}\text{Pd}_9$  alternate with fine-grained (smaller than 1–2  $\mu\text{m}$ ) multiphase stripes. The multiphase stripes consist of fine dispersed grains of predominantly  $\text{Ga}_{1-x}\text{Sn}_x\text{Pd}$  and also  $\text{Ga}_{2+p+q}\text{Sn}_{4-p}\text{Pd}_9$ . In Sn-rich samples the brighter  $\text{Ga}_{2+p+q}\text{Sn}_{4-p}\text{Pd}_9$ -rich stripes are more abundant and thicker while  $\text{Ga}_{1-x}\text{Sn}_x\text{Pd}$ -rich stripes may be thinner. In fig. 3.9, f, it can be seen that the brighter regions may contain  $\text{Ga}_{1-x}\text{Sn}_x\text{Pd}_2$  (arrow 3). The third feature of the samples is dendritically grown  $\text{Ga}_{2+p+q}\text{Sn}_{4-p}\text{Pd}_9$  (fig. 3.9, III). The matrix (fig. 3.9, sequence IV) is a multiphase, fine-grained (smaller than 1–2  $\mu\text{m}$ ) eutectoid-like system, dominated by  $\text{Ga}_{1-x}\text{Sn}_x\text{Pd}$  also containing  $\text{Ga}_{2+p+q}\text{Sn}_{4-p}\text{Pd}_9$  and  $\text{Ga}_{1-x}\text{Sn}_x\text{Pd}_2$ .

The DTA heating curves from these experiments (fig. 3.10) contain four endothermic signals. The first three peaks have shared onsets at approx. 800°C, 850°C and 900°C in all measured samples. The third peaks have shoulders at higher temperatures. The fourth signals are long, smoothly rising signals with sharp ending that display dissolution processes. The DTA cooling curves contain four exothermic signals for all experiments. The first one (at high temperatures) is related to the endset of the last endothermic signal during heating i.e, liquidus and solidus correspond to each other. It should be mentioned that the onset of the first signal during cooling is higher than the endset of the last signal during heating in some cases. The second and the third exothermic signals are shared signals at  $\approx 920^\circ\text{C}$  and  $\approx 780^\circ\text{C}$  and the last signals vary between 650°C and 620°C.

sample	$y_L$	$x_L$	$\text{Ga}_{1-x}\text{Sn}_x\text{Pd}_2$		$\text{Ga}_{1-x}\text{Sn}_x\text{Pd}$ $\omega[\text{wt.}\%]$	ternary* $\omega[\text{wt.}\%]$
			primary $\omega[\text{wt.}\%], x$	secondary $\omega[\text{wt.}\%], x_{XPD}$		
QX677-A	61	0.30	19, 0.31(3)	35, 0.46(5)	29	17
QX675-A	61	0.35	19, 0.35(3)	32, 0.46(5)	26	23
QX677-C	61	0.40	18, 0.34(3)	28, 0.47(5)	21	33
QX647-B	59	0.30	28, 0.30(3)	29, 0.47(5)	31	12
QX677-B	59	0.35	< 1, 0.34(3)	33, 0.47(5)	31	36
QX696-A	59	0.35	39, 0.33(3)		33	29
QX693-B	59	0.35	2, 0.33(3)	29, 0.45(5)	35	33

Table 3.4: Phase content of the equilibrium-cooling experiments of starting melt compositions in region R3, based on Rietveld refinement of the X-ray powder diffraction (XPD) data.  $x_{XPD}$  is calculated from the refined lattice parameters according to the equations in section 3.3.2. ternary\* =  $\text{Ga}_{2+p+q}\text{Sn}_{4-p}\text{Pd}_9$ .  $x_L$  and  $y_L$  correspond to the melt composition<sup>7</sup>.

<sup>7</sup>According to the description  $(\text{Ga}_{1-x_L}\text{Sn}_{x_L})_{100-y_L}\text{Pd}_{y_L}$ .

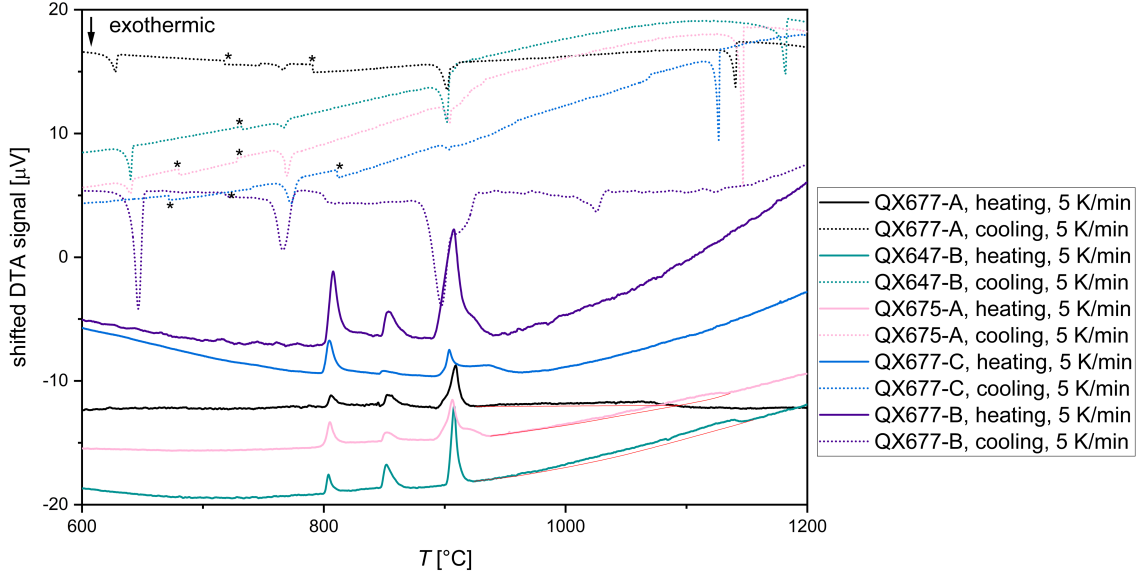


Figure 3.10: DTA curves of different samples from region R3. The stars mark artefacts, known from the instrument. Thin red, constructed background lines allow better visibility of dissolution processes. For the cooling curves of QX677-A and B and the heating curve of QX677-A a background subtraction by a manual B-spline fit was performed, due to its slope.

### Bridgman experiment in region R3

A special experiment located in this region, was the Bridgman experiment QX689-B ( $x_L = 0.35$ ,  $y_L = 59$ )<sup>8</sup>, which aimed to transfer the time sequence of the crystallization path into a spatial sequence (fig. 3.11). The ingot can be divided into four sections (I–IV), intersected by clear transitions. The phases occurring in the different sections, found by XPD are given in tab. 3.5 and visualized in fig. 3.12. The first part (up to 6.5 mm, fig. 3.11, I) is almost a single-phase material of  $\text{Ga}_{1-x}\text{Sn}_x\text{Pd}_2$ . Still, this area is not single-crystalline but consists of several grains and small amounts of  $\text{Ga}_{1-x}\text{Sn}_x\text{Pd}$  can be found in the XPD analysis, most likely in inclusions. The second area (fig. 3.11, II), with a length of about 4.2 mm contains needles of  $\text{Ga}_{1-x}\text{Sn}_x\text{Pd}_2$  (fig. 3.11, II, a) in a matrix of  $\text{Ga}_{2+p+q}\text{Sn}_{4-p}\text{Pd}_9$  (fig. 3.11, II, b).  $\text{Ga}_{2+p+q}\text{Sn}_{4-p}\text{Pd}_9$  occurs with different brightness in the BSE images. However, a chemical contrast could not be found by WDX measurements and an orientation contrast is likely. Furthermore, fine-grained (smaller than 1–2  $\mu\text{m}$ ) polycrystalline phases of mainly  $\text{Ga}_{1-x}\text{Sn}_x\text{Pd}$  and few amounts of  $\text{Ga}_{1-x}\text{Sn}_x\text{Pd}_2$  or  $\text{Ga}_{2+p+q}\text{Sn}_{4-p}\text{Pd}_9$  are precipitated or trapped in  $\text{Ga}_{2+p+q}\text{Sn}_{4-p}\text{Pd}_9$ . Both, the brightness contrasts and the precipitates appear in lines, following a specific orientation. The next area (fig. 3.11, III) contains dendrite-like structures of mainly  $\text{Ga}_{2+p+q}\text{Sn}_{4-p}\text{Pd}_9$  (f. 3.11, III, b) with the same properties described for II, b. Those are alternating with dispersed, fine-grained (lower than 1–2  $\mu\text{m}$ ) darker structures (f. 3.11 III, c) of  $\text{Ga}_{1-x}\text{Sn}_x\text{Pd}$ , with  $\text{Ga}_{2+p+q}\text{Sn}_{4-p}\text{Pd}_9$  and ( $\text{Ga}_{1-x}\text{Sn}_x\text{Pd}_2$ ) containing spotted to dendritic structures of  $\text{Ga}_{2+p+q}\text{Sn}_{4-p}\text{Pd}_9$ , 2–20  $\mu\text{m}$  in size. In this area needles of  $\text{Ga}_{1-x}\text{Sn}_x\text{Pd}_2$  of up to 100  $\mu\text{m}$  (f. 3.11, III, a) are intersecting the brighter and darker striped structures. The last 10 mm (f. 3.11, IV) consist of a fine-grained

<sup>8</sup>According to the description  $(\text{Ga}_{1-x_L}\text{Sn}_{x_L})_{100-y_L}\text{Pd}_{y_L}$ .



structure of  $\text{Ga}_{1-x}\text{Sn}_x\text{Pd}$  and  $\text{Ga}_{2+p+q}\text{Sn}_{4-p}\text{Pd}_9$  (IV, b), with either dendrites of  $\text{Ga}_{2+p+q}\text{Sn}_{4-p}\text{Pd}_9$ , up to several mm in length, or smaller (up to 50  $\mu\text{m}$ ) star- and needle-like crystallites of the same phase. Fig. 3.13 shows the development of the lattice parameters of the individual phases over the length of the ingot, or rather in the different analysed sections. For  $\text{Ga}_{1-x}\text{Sn}_x\text{Pd}_2$  the lattice parameters of the primarily grown part differ strongly from the secondarily grown ones. For all other phases, there is either a slight increase or a slight decrease (for  $\text{Ga}_{2+p+q}\text{Sn}_{4-p}\text{Pd}_9$ ) from section II to the end of section III.

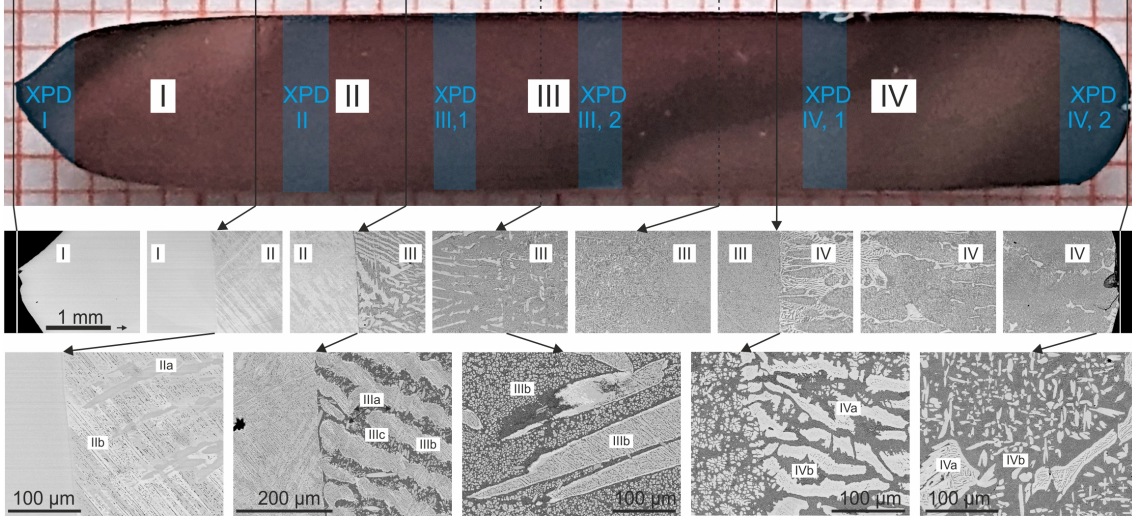


Figure 3.11: Bridgman experiment QX689-B ( $y_L = 59$ ,  $x_L = 0.35$ ). The upper part is a polished longitudinal section of the whole ingot. The middle part shows BSE images showing the different textures and boundaries in-between. The bottom part shows magnified BSE images of characteristic positions. The arrows mark the positions of the BSE images. The blue sections have been analysed by XPD and the results are displayed in tab. 3.5.

area according to fig.3.11	$\text{Ga}_{1-x}\text{Sn}_x\text{Pd}_2$ $\omega[\text{wt.}\%], x_{XPD}$	$\text{Ga}_{2+p+q}\text{Sn}_{4-p}\text{Pd}_9$ $\omega[\text{wt.}\%]$	$\text{Ga}_{1-x}\text{Sn}_x\text{Pd}$ $\omega[\text{wt.}\%]$
I	97, 0.36(3) (WDX)		3
II	32, 0.46(5)	49	20
III, 1	38, 0.48(5)	22	39
III, 2	32, 0.49(5)	25	44
IV, 1	10, 0.48(5)	53	36
IV, 2	1, 0.5(1)	62	37

Table 3.5: Phase content of the Bridgman experiment QX689-B ( $y_L = 59$ ,  $x_L = 0.35$ ), based on Rietveld refinement. The samples are cut from the marked positions in fig. 3.11.  $x_{XPD}$  is calculated from the refined lattice parameters according to the equations in section 3.3.2. For section I  $x$  was measured by WDX and not calculated, since  $\text{Ga}_{1-x}\text{Sn}_x\text{Pd}_2$  crystallized primarily in large grains.  $x_L$  and  $y_L$  correspond to the initial melt composition<sup>9</sup>.

<sup>9</sup>According to the description  $(\text{Ga}_{1-x_L}\text{Sn}_{x_L})_{100-y_L}\text{Pd}_{y_L}$ .



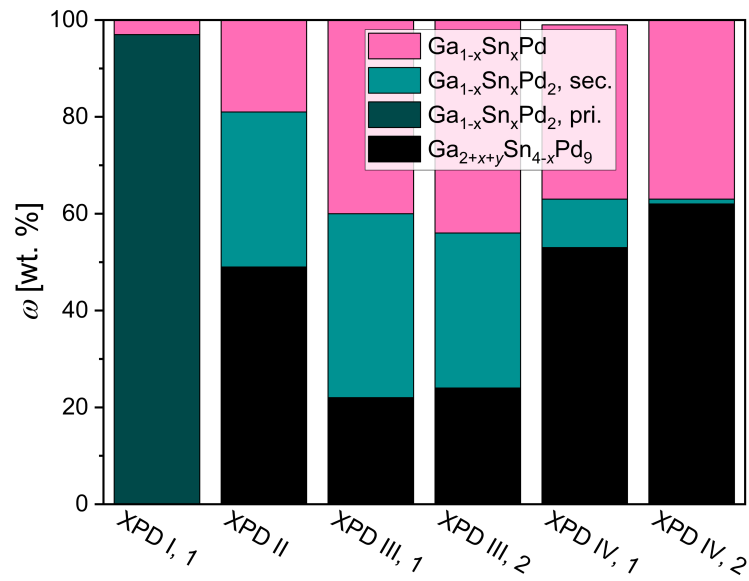


Figure 3.12: Visual phase distribution of the XPD analysis from the sections marked in fig. 3.11. The values are listed in tab. 3.5.

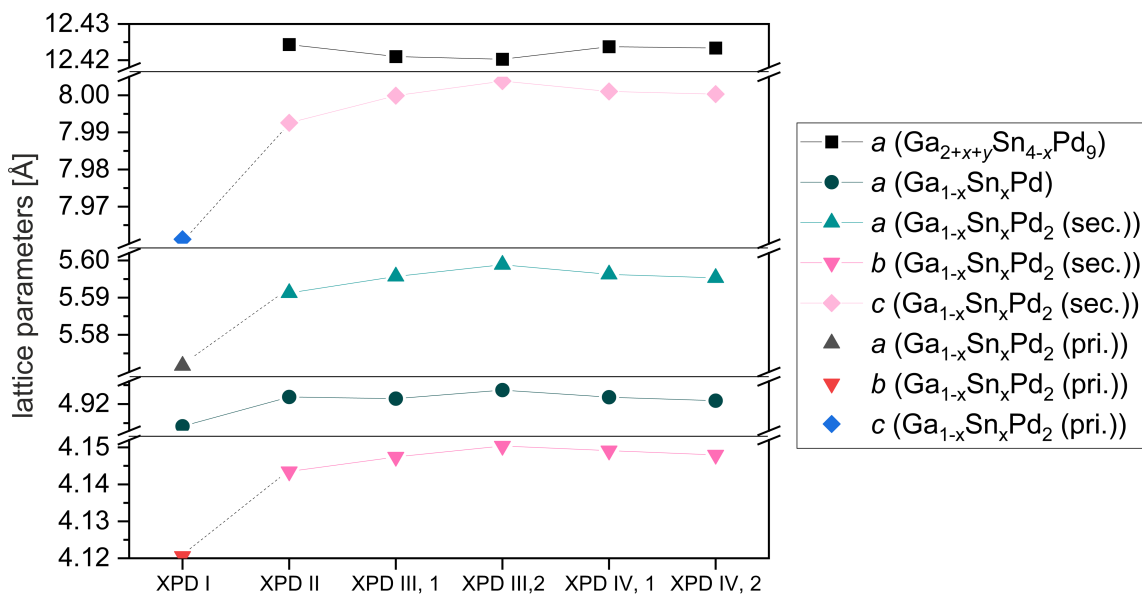


Figure 3.13: Lattice parameters of the different phases gained from XPD analysis of the sections marked in fig. 3.11.

## 3.1.2.4 Region R4

## Equilibrium-cooling experiments in region R4

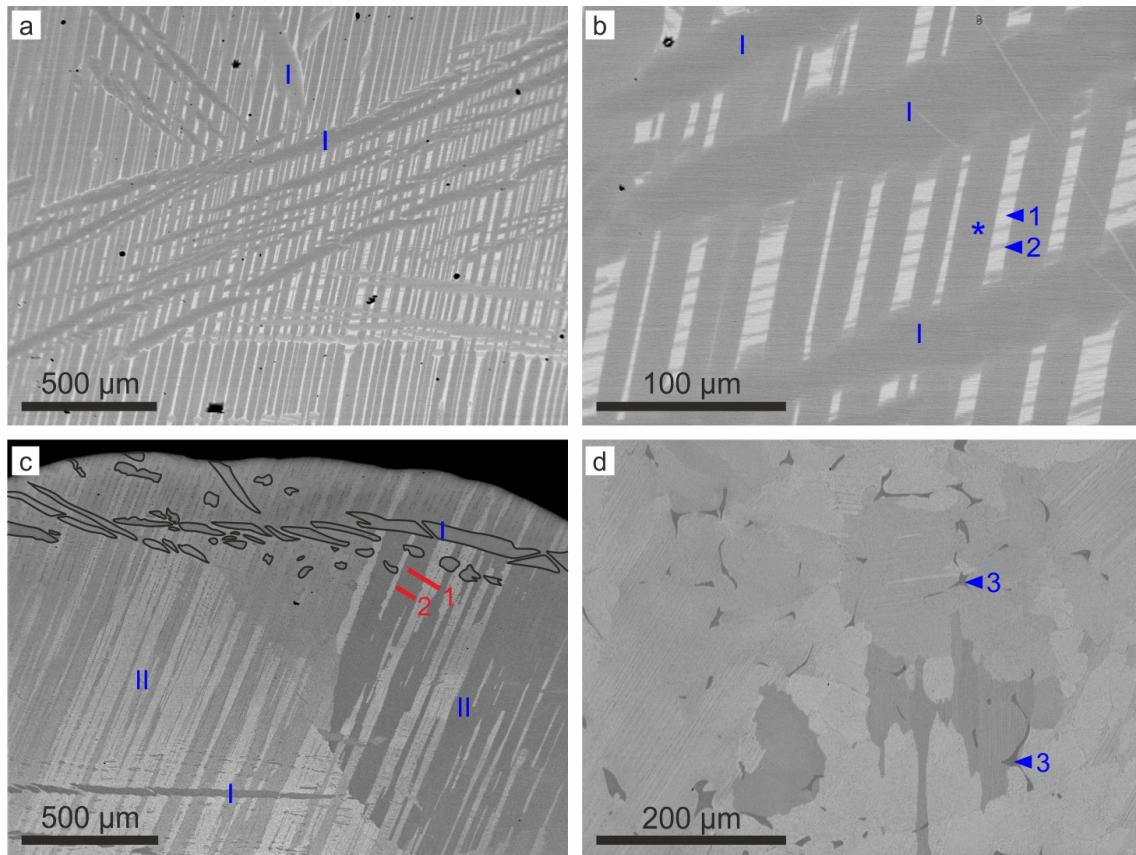


Figure 3.14: BSE images of different examples of samples from region R4 (fig. 3.2, R4). In image c (QX680-C) some needles of  $\text{Ga}_{1-x}\text{Sn}_x\text{Pd}_2$  are framed black for better visualisation. The two red lines in c indicate the tracks of the line measurements displayed in fig. 3.15. a,b) QX690-C, c) QX680-C, d) QX671-B. The numbers I and II mark different repeating paragenetic sequences (or phases) of the texture.

Solids crystallized from melts according to region R4 (fig. 3.2, R4, tab. 3.6) contain the phases  $\text{Ga}_{1-x}\text{Sn}_x\text{Pd}_2$ ,  $\text{Ga}_{1-x}\text{Sn}_x\text{Pd}$ ,  $\text{Ga}_{2+p+q}\text{Sn}_{4-p}\text{Pd}_9$  and  $\text{Pd}_{20}\text{Sn}_{13-x}\text{Ga}_x$ . The samples have initial melt compositions with a Sn content of  $0.4 \leq x_L \leq 0.6$  and a Pd content  $61 \leq y \leq 62$ <sup>10</sup>.  $\text{Ga}_{1-x}\text{Sn}_x\text{Pd}_2$  is present as large primarily grown single-phase needles (3.14, sequence I). In earlier described samples from regions R1, R2 and R3 the Sn content  $x$  was strongly related to  $x_L$  in the single-phase  $\text{Ga}_{1-x}\text{Sn}_x\text{Pd}_2$  grains. In contrast, the  $\text{Ga}_{1-x}\text{Sn}_x\text{Pd}_2$  crystallites seem to have a constant Sn content of  $x = 0.53(3) - 0.54(3)$ .

<sup>10</sup>According to the description  $(\text{Ga}_{1-x_L}\text{Sn}_{x_L})_{100-y_L}\text{Pd}_{y_L}$ .

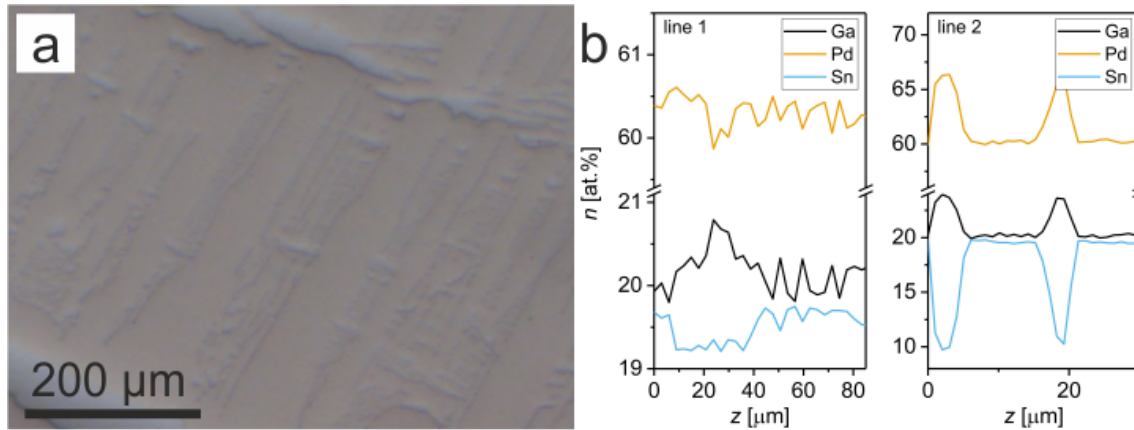


Figure 3.15: a) Incident light microscope image of QX680-C. b) WDX line measurements (position marked in fig. 3.14).

The primarily grown  $\text{Ga}_{1-x}\text{Sn}_x\text{Pd}_2$  needles are embedded in a texture that contains lamellae or bands of  $\text{Ga}_{2+p+q}\text{Sn}_{4-p}\text{Pd}_9$  (fig. 3.14, b, star),  $\text{Ga}_{1-x}\text{Sn}_x\text{Pd}_2$  (fig. 3.14, b, arrow 1) and  $\text{Pd}_{20}\text{Sn}_{13-x}\text{Ga}_x$  (fig. 3.14, b, arrow 2). Different stripes of  $\text{Ga}_{2+p+q}\text{Sn}_{4-p}\text{Pd}_9$  vary in their chemical composition (fig. 3.15, b, line 1). The Pd content remains approximately constant while Sn and Ga differ by 0.5–1 at.%. Furthermore, some stripes contain fine structures of  $\text{Ga}_{1-x}\text{Sn}_x\text{Pd}_2$  that are visible in the incident light microscope and in line measurements (fig. 3.15, a and b, line 2). Line 1 in figs. 3.14 and 3.15 shows a lower Ga and higher Sn content in the lamellae that contain  $\text{Ga}_{1-x}\text{Sn}_x\text{Pd}_2$  ( $\text{Ga}_{17.8(2)}\text{Sn}_{20.82(18)}\text{Pd}_{61.35(19)}$ ) compared to the pure  $\text{Ga}_{2+p+q}\text{Sn}_{4-p}\text{Pd}_9$  lamellae ( $\text{Ga}_{20.03(18)}\text{Sn}_{19.72(17)}\text{Pd}_{60.24(16)}$ ). XPD measurements indicate low contents of  $\text{Pd}_{20}\text{Sn}_{13-x}\text{Ga}_x$  are present in these structures even if they could not be found by WDX measurements, probably due to a low amount and grain size. The orientation of these lamellae structures is consistent either over the whole sample or within large areas. The amount of  $\text{Pd}_{20}\text{Sn}_{13-x}\text{Ga}_x$  varies strongly within the samples. Fine-grained (lower than 1–2  $\mu\text{m}$ ) eutectoid-like structures can be found in some samples (fig. 3.14, d, arrow 3).

sample	$y_L$	$x_L$	Ga <sub>1-x</sub> Sn <sub>x</sub> Pd <sub>2</sub>		1-1 $\omega$ [wt.%]	ternary $\omega$ [wt.%]	20-13 $\omega$ [wt.%]
			primary $\omega$ [wt.%], $x$	secondary $\omega$ [wt.%], $x_{XPD}$			
QX680-C	61	0.50	7, 0.39(3)	12, 0.45(5)	10	71	
QX693-A	61	0.50	7, 0.53(3)	20, 0.46(5)	11	62	
QX690-C	62	0.60	20, 0.54(3)	*		80	< 1
QX671-B	59	0.50	†	6, 0.47(5)	12	82	†
QX696-B	59	0.50	†	10, 0.48(5)	13	77	†
QX675-B	61	0.70		22, 0.6(1)		59	20

Table 3.6: Phase content of the equilibrium-cooling experiments of starting melt compositions in region R4, based on Rietveld refinement.  $x_{XPD}$  is calculated from the refined lattice parameters according to the equations in section 3.3.2. Abbreviations: 1-1 = Ga<sub>1-x</sub>Sn<sub>x</sub>Pd; ternary = Ga<sub>2+p+q</sub>Sn<sub>4-p</sub>Pd<sub>9</sub>; 20-13 = Pd<sub>20</sub>Sn<sub>13-x</sub>Ga<sub>x</sub>. \*In this sample the lattice parameters of the primarily and the secondarily grown Ga<sub>1-x</sub>Sn<sub>x</sub>Pd<sub>2</sub> are quite similar, why the peaks overlap and accordingly the weight fractions of the two generations cannot be distinguished. †In these samples primary Ga<sub>1-x</sub>Sn<sub>x</sub>Pd<sub>2</sub> as well as Pd<sub>20</sub>Sn<sub>13-x</sub>Ga<sub>x</sub> was not detected. Nevertheless, in the Bridgman experiment QX689-A with exactly the same composition it could be proofed in low amounts (see below and fig. 3.18).  $x_L$  and  $y_L$  correspond to the melt composition<sup>11</sup>.

The DTA heating curves of the experiments with starting melt compositions in region R4 (fig. 3.16) contain two endothermic signals. The first onsets are in the region of 780°C to 810°C. These exhibit in some samples sharp signals and in others a gradually increasing signals. The second kind of signals are in all measurements long-lasting plateaus over a range of 150 K to 200 K. Differently from the long, smoothly rising signals of the dissolution processes in the former regions, these plateaus are characterized by a clear onset. The onset and the endset temperatures seems to depend on the initial Sn and Pd contents. Experiments with higher  $x_L$  and  $y_L$ <sup>11</sup> tend to be related to higher temperatures. The DTA cooling curves of experiments with starting melt compositions in region R4 differ slightly. The first exothermic signal is a sharp peak either merging into a longer plateau-like signal or being followed by a broad flattened signal, partly with sharp onset, partly with direct transition or with additional exothermic bulges in the plateau. According to the texture, it is likely that these signals correspond to peritectoid decompositions, resulting in the lamella structure that these experiments share. It seems that the primary crystallization signal is merged with the peritectoid decomposition signal in some cases, i.e. decomposition may follow directly after crystallization. Another exothermic signal can be found in all curves at temperatures between 800°C (QX680-C and QX671-B with sharp peaks) and 650°C (with flat bulges).

<sup>11</sup>According to the description (Ga<sub>1-x<sub>L</sub></sub>Sn<sub>x<sub>L</sub></sub>)<sub>100-y<sub>L</sub></sub>Pd<sub>y<sub>L</sub></sub>.

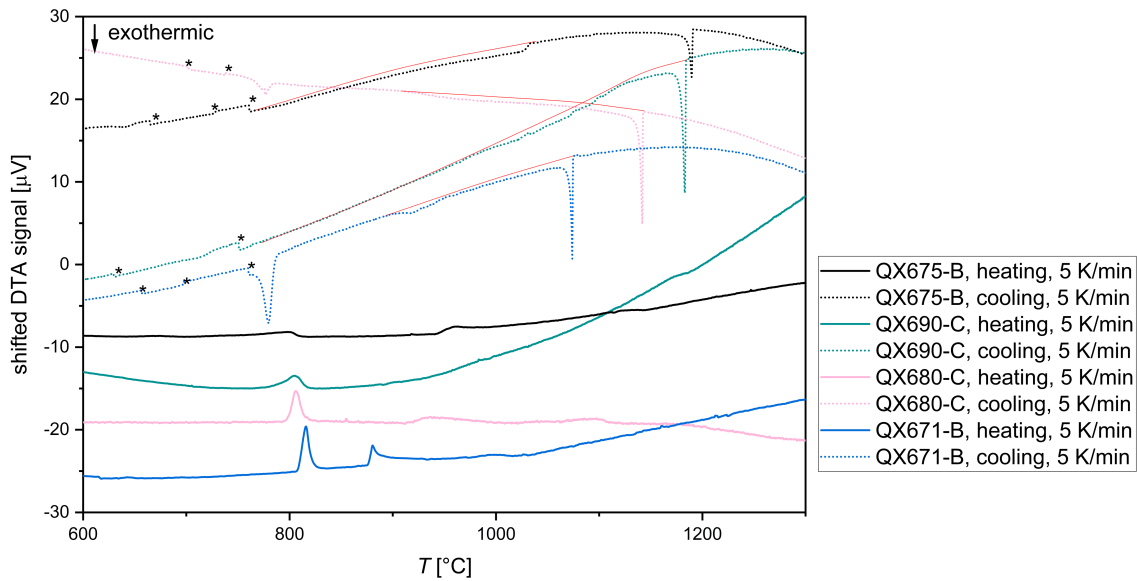


Figure 3.16: DTA curves of different samples from region R4. The stars mark artefacts, known from the instrument. Thin red constructed background lines allow better visibility of minor smooth deviations of the signal from the background.

In QX675-B (fig. 3.2, R4b) primary  $\text{Ga}_{1-x}\text{Sn}_x\text{Pd}_2$  could not be proven. Still, since the texture and the DTA curve is similar to the other samples, with starting melt compositions in region R4, it is listed here.

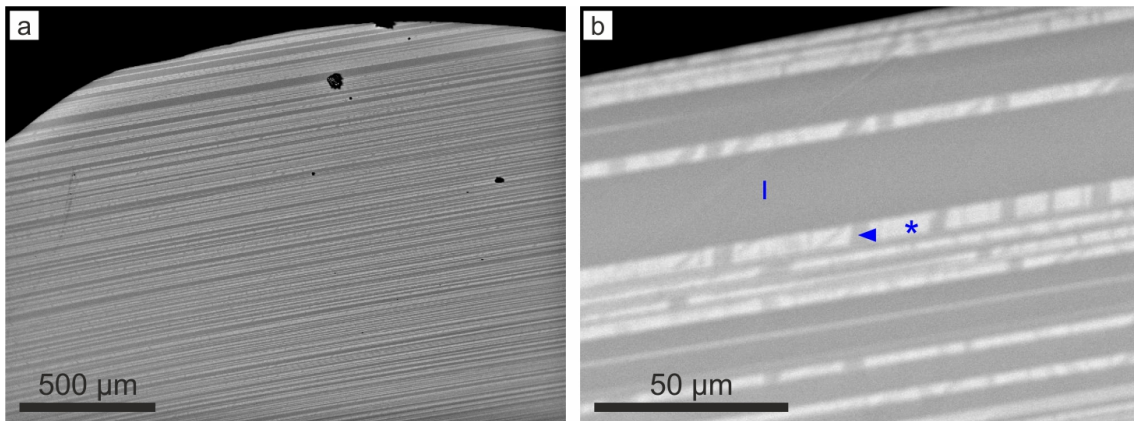


Figure 3.17: BSE images of QX675-B (region R4b, fig. 3.2, R4b).

#### Bridgman experiment in region R4

In this region the Bridgman experiment QX689-A ( $x_L = 0.50$ ,  $y_L = 59$ )<sup>12</sup> was located (fig. 3.18, tab. 3.7). The first two thirds (I) of the ingot display the same structure described above: large single-crystalline needles of  $\text{Ga}_{1-x}\text{Sn}_x\text{Pd}_2$  (Ia) are placed in homogeneously oriented lamellae of Sn-rich  $\text{Ga}_{1-x}\text{Sn}_x\text{Pd}_2$ ,  $\text{Ga}_{2+p+q}\text{Sn}_{4-p}\text{Pd}_9$  and  $\text{Pd}_{20}\text{Sn}_{13-x}\text{Ga}_x$  (Ib). The single-crystalline needles are only abundant in the first few millimeters and the amount of  $\text{Ga}_{1-x}\text{Sn}_x\text{Pd}_2$  is reduced within the first-crystallized

<sup>12</sup>According to the description  $(\text{Ga}_{1-x_L}\text{Sn}_{x_L})_{100-y_L}\text{Pd}_{y_L}$ .



to the later-crystallized part.  $\text{Pd}_{20}\text{Sn}_{13-x}\text{Ga}_x$  is present in the first part only. A sharp cut marks the transition to the next region (II) consisting of dendrites with the same texture as the first part but with numerous, small, homogeneously distributed  $\text{Ga}_{1-x}\text{Sn}_x\text{Pd}$  inclusions (IIa) and fine-grained eutectic-like structures (IIb) of mainly  $\text{Ga}_{1-x}\text{Sn}_x\text{Pd}$  and  $\text{Ga}_{2+p+q}\text{Sn}_{4-p}\text{Pd}_9$  in-between. From these the  $\text{Ga}_{1-x}\text{Sn}_x\text{Pd}$ -rich part is very fine-grained, eutectoid-like. After 1.5 mm another sharp cut follows. The last part (III) does not display major changes of texture and phase content. Sections II and III show a high similarity to the sections III and IV of the Bridgman experiment QX689-B of region R3, regarding the phase content, the texture and the chronology of the different sequences. Accordingly a shared crystallization path in the later part of both experiments is likely.

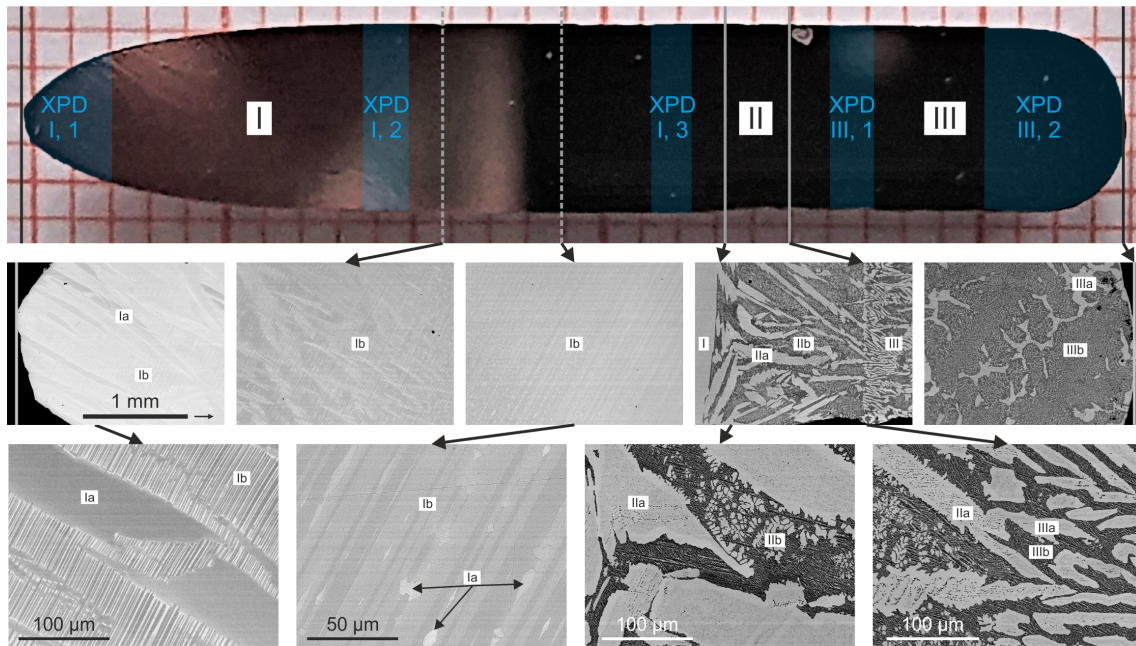


Figure 3.18: Bridgman experiment QX689-A. The upper part is a polished longitudinal section of the whole ingot. The middle part are BSE images showing the different textures and boundaries in-between. The bottom part shows magnified BSE images of characteristic positions. The arrows mark the positions of the BSE images. The blue sections have been measured by XPD and the results are displayed in tab. 3.7.

area according to fig. 3.18	$\text{Ga}_{1-x}\text{Sn}_x\text{Pd}_2$		1-1 $\omega$ [wt.%]	ternary $\omega$ [wt.%]	20-13 $\omega$ [wt.%]
	primary $\omega$ [wt.%], $x$	secondary $\omega$ [wt.%], $x_{XPD}$			
I, 1	32, 0.53(3)	27, 0.63(8)		33	7
I, 2		25, 0.49(5)			
I, 3		9, 0.44(5)			
III, 1			40	60	
III, 2			40	58	2

Table 3.7: Phase content of the Bridgman experiment QX689-A ( $y_L = 59$ ,  $x_L = 0.50$ ) of the samples marked in fig. 3.18, based on Rietveld refinement. The samples are cut from the marked positions in fig. 3.18.  $x_{XPD}$  is calculated from the refined lattice parameters according to the equations in section 3.3.2.  $x$  was measured by WDX. Abbreviations: 1-1 =  $\text{Ga}_{1-x}\text{Sn}_x\text{Pd}$ ; ternary =  $\text{Ga}_{2+p+q}\text{Sn}_{4-p}\text{Pd}_9$ ; 20-13 =  $\text{Pd}_{20}\text{Sn}_{13-x}\text{Ga}_x$ .  $x_L$  and  $y_L$  correspond to the melt composition<sup>13</sup>.

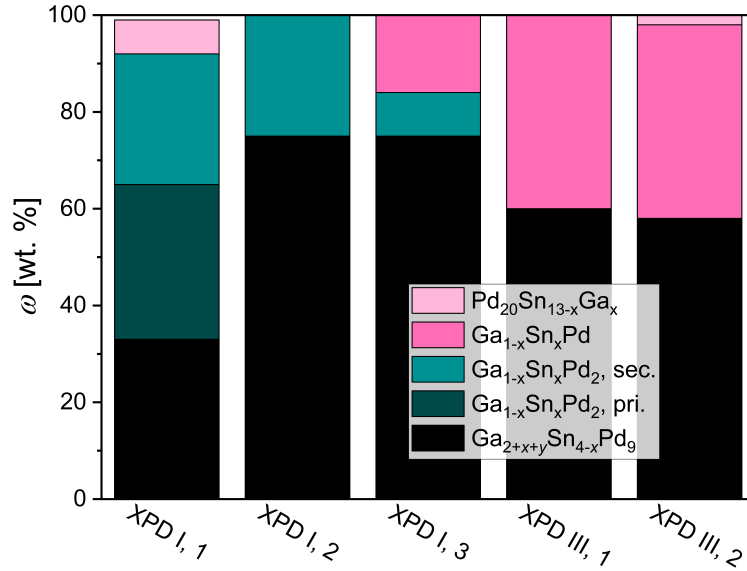


Figure 3.19: Visual phase distribution of the XPD analysis from the sections marked in fig. 3.18. The values are listed in tab. 3.7.

<sup>13</sup>According to the description  $(\text{Ga}_{1-x_L}\text{Sn}_{x_L})_{100-y_L}\text{Pd}_{y_L}$ .

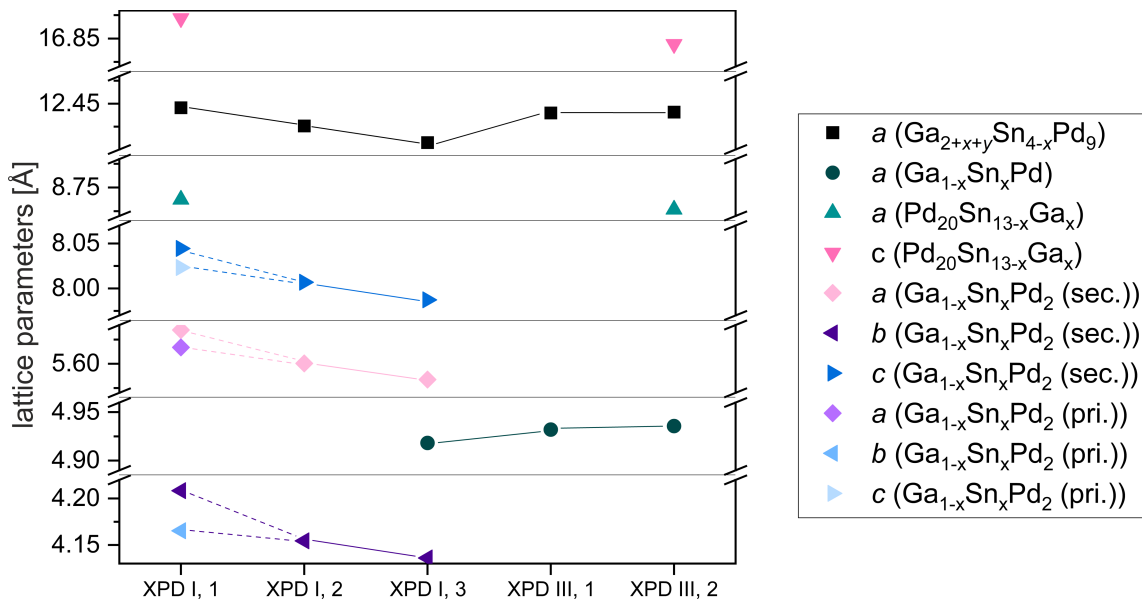


Figure 3.20: Lattice parameters of the different phases of the XPD analysis from the sections marked in fig. 3.18.

### 3.1.2.5 Region R5

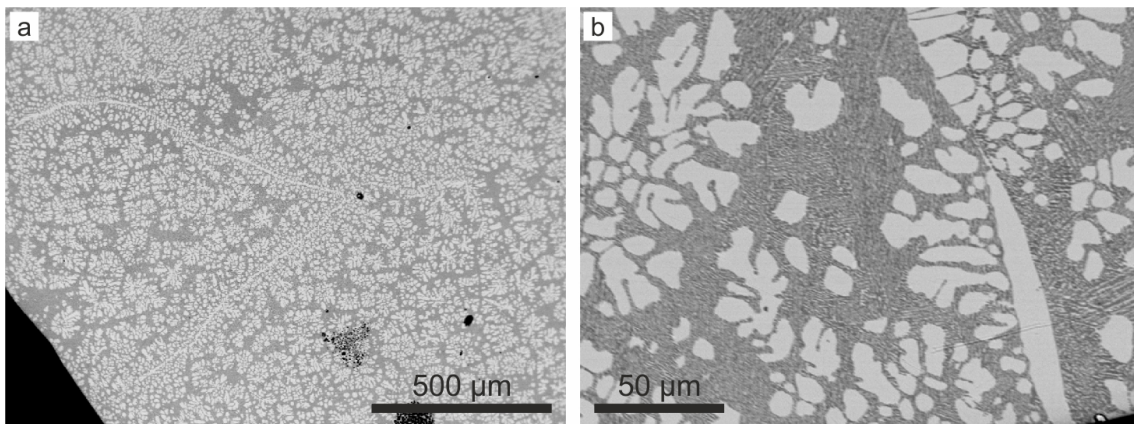


Figure 3.21: BSE images of different examples of samples from region R5 (fig. 3.2, R5).

Solids crystallized from melts according to region R5 (fig. 3.2, R5, tab. 3.8) contain the phases  $\text{Ga}_{1-x}\text{Sn}_x\text{Pd}$ ,  $\text{Ga}_{1-x}\text{Sn}_x\text{Pd}_2$  and  $\text{Ga}_{2+p+q}\text{Sn}_{4-p}\text{Pd}_9$ . The samples differ from other ones with comparable phase content because of their fine-grained texture without signs of primary crystallization (fig. 3.21). They contain eutectic-like structures of  $\text{Ga}_{2+p+q}\text{Sn}_{4-p}\text{Pd}_9$  and a very fine-grained (smaller than 1–2  $\mu\text{m}$ ) eutectoid-like fraction.



experiment	$y_L$	$x_L$	$\text{Ga}_{1-x}\text{Sn}_x\text{Pd}_2$ (sec.) $\omega$ [wt.%], $x_{XPD}$	$\text{Ga}_{1-x}\text{Sn}_x\text{Pd}$ $\omega$ [wt.%]	$\text{Ga}_{2+p+q}\text{Sn}_{4-p}\text{Pd}_9$ $\omega$ [wt.%]
QX690-B	57	0.30	28, 0.47(5)	46	26
QX723	56.16	0.25	-	-	-

Table 3.8: Phase content of the equilibrium-cooling experiments of starting melt compositions in region R5, based on Rietveld refinement.  $x_{XPD}$  is calculated from the refined lattice parameters according to the equations in section 3.3.2. For the experiment QX723 only a DTA measurement was carried out.  $x_L$  and  $y_L$  are related to the initial melt composition<sup>14</sup>.

The DTA heating curves from the experiments with starting melt compositions in region R5 (fig. 3.22) have the lowest detected solidus and liquidus temperatures. They are strongly related to that of region R3 with the difference that the last dissolution signal in the heating curve is missing and analogously the first exothermic crystallization signal. Accordingly, the heating curves contain three endothermic signals at  $\approx 800^\circ\text{C}$ ,  $\approx 850^\circ\text{C}$  and  $880\text{--}900^\circ\text{C}$  where signs of a double peak can be found. The DTA cooling curves contain three exothermic signals for both experiments. The first onset is at  $\approx 900^\circ\text{C}$  in the curves of both experiments. The second exothermic signals are flat bulges, differing for both experiments and occurring at  $\approx 770^\circ\text{C}$  (QX690-B) and  $\approx 730^\circ\text{C}$  (QX723), respectively. The last exothermic cooling peaks are sharp strong signals occurring at  $\approx 680^\circ\text{C}$  (QX723) and  $\approx 640^\circ\text{C}$  (QX690-B).

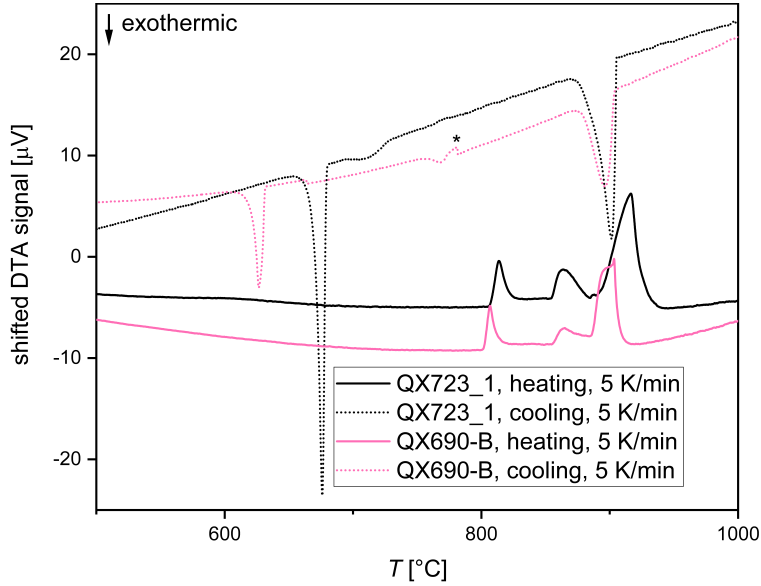


Figure 3.22: DTA curves of different samples from region R5. The stars mark artefacts, known from the instrument.

<sup>14</sup>According to the description  $(\text{Ga}_{1-x_L}\text{Sn}_{x_L})_{100-y_L}\text{Pd}_{y_L}$ .

## 3.1.2.6 Region R6

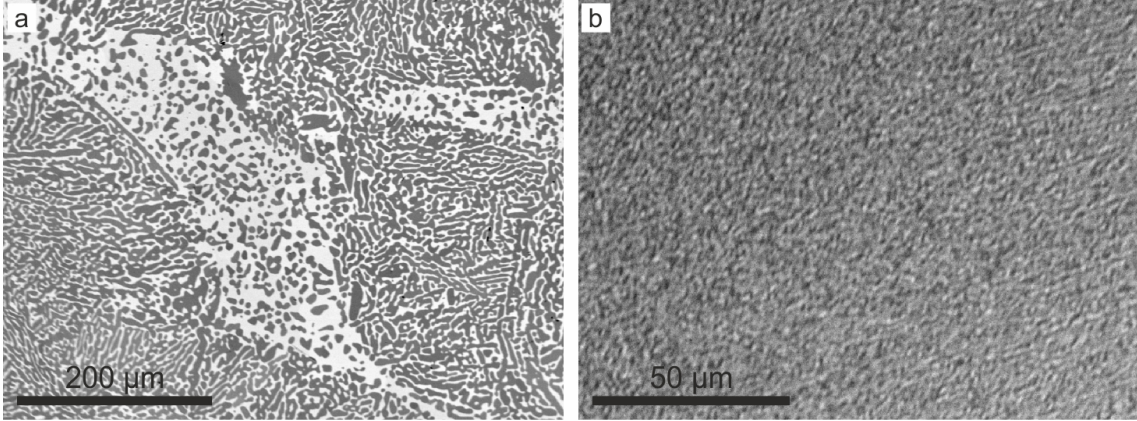


Figure 3.23: BSE images of examples of samples from region R6 (fig. 3.2, R6). a) QX705-A, b) QX642-B.

Solids crystallized from melts according to region R6 (fig. 3.2, R6, tab. 3.9) contain the phases  $\text{Ga}_{1-x}\text{Sn}_x\text{Pd}_2$ ,  $\text{Ga}_{1-x}\text{Sn}_x\text{Pd}$  and  $\text{Ga}_{2+p+q}\text{Sn}_{4-p}\text{Pd}_9$ . Their texture (fig. 3.23) is uniform throughout the samples. QX705-A has a very disperse, fine-grained texture with grain sizes smaller than 1–2  $\mu\text{m}$ . QX642-B also has a fine-grained structure, but with grains of several micrometers in size, large enough to be measured by WDX. Although  $\text{Ga}_{1-x}\text{Sn}_x\text{Pd}_2$  was detected by XPD, it could not be found by BSE imaging or WDX measurements. However, since the BSE image display only a cross section, phases/grains might be hidden in another part of the sample, especially if being present only in small amounts.

experiment	$y_L$	$x_L$	$\text{Ga}_{1-x}\text{Sn}_x\text{Pd}_2$ (sec.) $\omega[\text{wt.}\%], x_{XPD}$	$\text{Ga}_{1-x}\text{Sn}_x\text{Pd}$ $\omega[\text{wt.}\%]$	$\text{Ga}_{2+p+q}\text{Sn}_{4-p}\text{Pd}_9$ $\omega[\text{wt.}\%]$
QX642-B	53.1	0.21	3, 0.36(5)	64	33
QX705-A	55	0.20	27, 0.48(5)	62	11

Table 3.9: Phase content of the equilibrium-cooling experiments of starting melt compositions in region R6, based on Rietveld refinement.  $x_{XPD}$  is calculated from the refined lattice parameters according to the equations in section 3.3.2.  $y_L$  and  $x_L$  relate to the melt composition<sup>15</sup>.

The DTA heating curves of the two experiments of region R6 (fig. 3.24) differ, so that a relation of the crystallization paths cannot be assumed.

<sup>15</sup>According to the description  $(\text{Ga}_{1-x_L}\text{Sn}_{x_L})_{100-y_L}\text{Pd}_{y_L}$ .

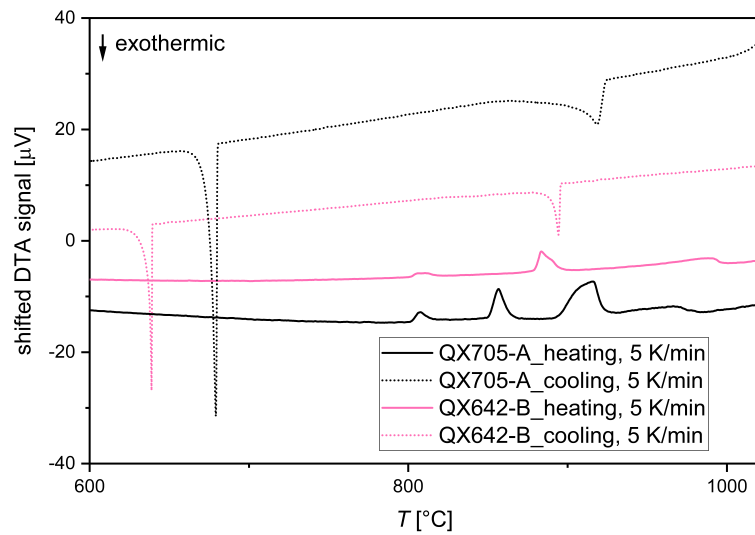


Figure 3.24: DTA curves of different samples from region R6. The stars mark artefacts, known from the instrument.

### 3.1.2.7 Region R7

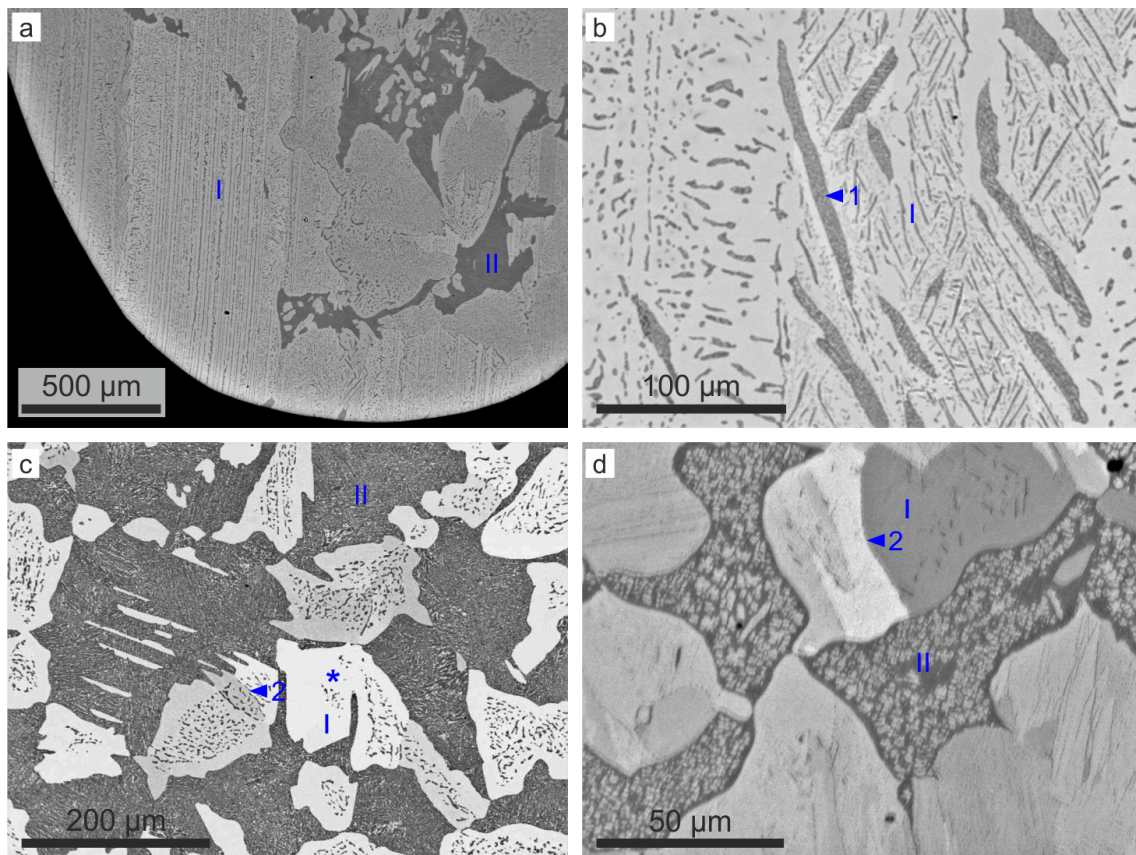


Figure 3.25: BSE images of different examples of samples from region R7 (fig. 3.2, R7). The Roman numerals I and II mark different repeating paragenetic sequences (or phases) of the texture.

Solids crystallized from melts according to region R7 (fig. 3.2, R7, tab. 3.10) contain the phases  $\text{Ga}_{1-x}\text{Sn}_x\text{Pd}_2$ ,  $\text{Ga}_{1-x}\text{Sn}_x\text{Pd}$  and  $\text{Ga}_{2+p+q}\text{Sn}_{4-p}\text{Pd}_9$ . The main feature of these experiments are large (50  $\mu\text{m}$  up to 2 mm), primarily grown grains of  $\text{Ga}_{2+p+q}\text{Sn}_{4-p}\text{Pd}_9$  (fig. 3.25, sequence I). These grains are strongly perforated, most likely by peritectoid decomposition. It is clearly visible that the decompositions are arranged in a coherent manner with respect to the initial grain. The precipitates contain different fine-grained phases (visible in fig. 3.25, b, arrow 1). An eutectoid decomposition of the phase that previously formed in a peritectic may be possible. The  $\text{Ga}_{2+p+q}\text{Sn}_{4-p}\text{Pd}_9$  main grains show brightness contrasts (3.25, b, arrow 2). Nevertheless, WDX measurements show no chemical contrasts, and accordingly orientation contrasts must be visible. The grains of  $\text{Ga}_{2+p+q}\text{Sn}_{4-p}\text{Pd}_9$  are embedded in a fine-grained, dispersed matrix, hinting at an eutectic solidification at the end of the crystallization path (fig. 3.25, sequence II).

experiment	$y_L$	$x_L$	$\text{Ga}_{1-x}\text{Sn}_x\text{Pd}_2$ (sec.) $\omega[\text{wt.}\%], x_{XPD}$	$\text{Ga}_{1-x}\text{Sn}_x\text{Pd}$ $\omega[\text{wt.}\%]$	$\text{Ga}_{2+p+q}\text{Sn}_{4-p}\text{Pd}_9$ $\omega[\text{wt.}\%]$
QX671-A	59	0.40	25, 0.47(5)	25	50
QX705-B	55	0.30	2, 0.48(5)	49	49
QX680-A	57	0.35	12, 0.48(5)	36	52
QX680-B	57	0.45	2, 0.47(5)	19	79
QX696-C	57	0.45	< 1	29	71

Table 3.10: Phase content of the equilibrium-cooling experiments of starting melt compositions in region R7, based on Rietveld refinement.  $x_{XPD}$  is calculated from the refined lattice parameters according to the equations in section 3.3.2. In the case of QX696-C “< 1” means that the highest peaks at the typical positions of  $\text{Ga}_{1-x}\text{Sn}_x\text{Pd}_2$  are present, but in such low intensity that adequate refinement is not possible.  $y_L$  and  $x_L$  relate to the melt composition<sup>16</sup>.

The DTA heating curves from these experiments (fig. 3.26) contain two endothermic signals (QX671-A has additional peaks). The first and the second endothermic signals are shared by all curves at  $\approx 800^\circ\text{C}$  and  $\approx 870^\circ\text{C}$ . The second merges into a longer dissolution process over a range of 50–100 K. In the case of QX671-A an additional signal at  $850^\circ\text{C}$  is present. Furthermore, at  $\approx 940^\circ\text{C}$ , another endothermic peak arises in the above-mentioned plateau. The DTA cooling curves from the experiments in this region differ and exhibit between two and four exothermic signals. The first cooling signals vary (according to the respective liquidus temperature). The measured curves of all experiments share a signal in the range between  $890^\circ\text{C}$  and  $870^\circ\text{C}$  (here is the onset of the second peak during heating). Furthermore, signals of different curves accumulate at temperatures of  $\approx 760^\circ\text{C}$  and  $\approx 630^\circ\text{C}$ .

<sup>16</sup>According to the description  $(\text{Ga}_{1-x_L}\text{Sn}_{x_L})_{100-y_L}\text{Pd}_{y_L}$ .

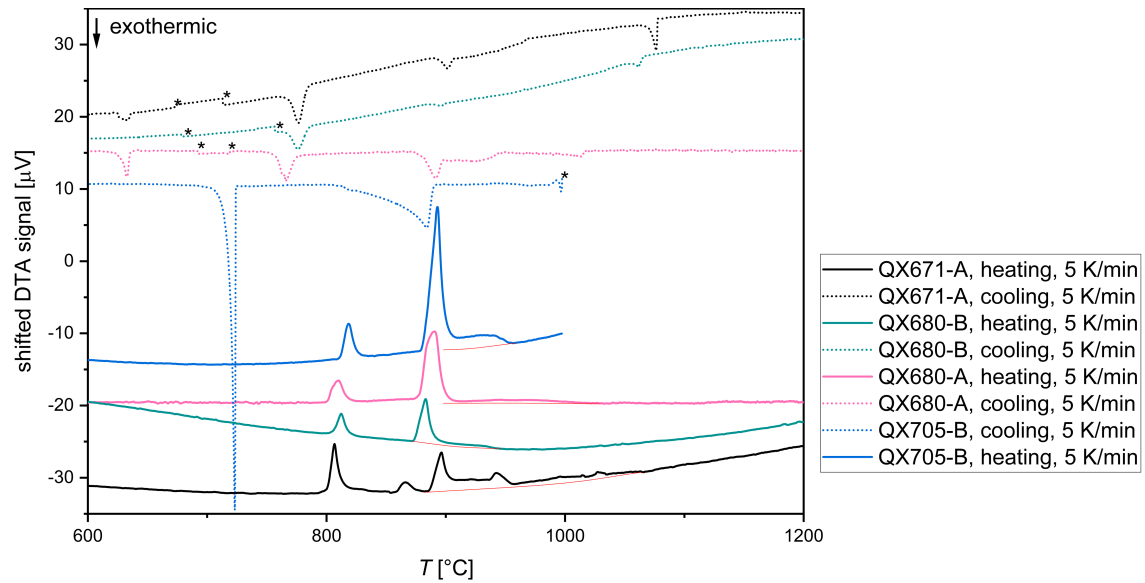


Figure 3.26: DTA curves of different samples from region R7. The stars mark artefacts, known from the instrument. Thin red constructed background lines allow better visibility of dissolution processes. For the cooling curve of QX705-B a background subtraction by a manual B-spline fit was performed since the curve was very steep.



## 3.1.2.8 Region R8

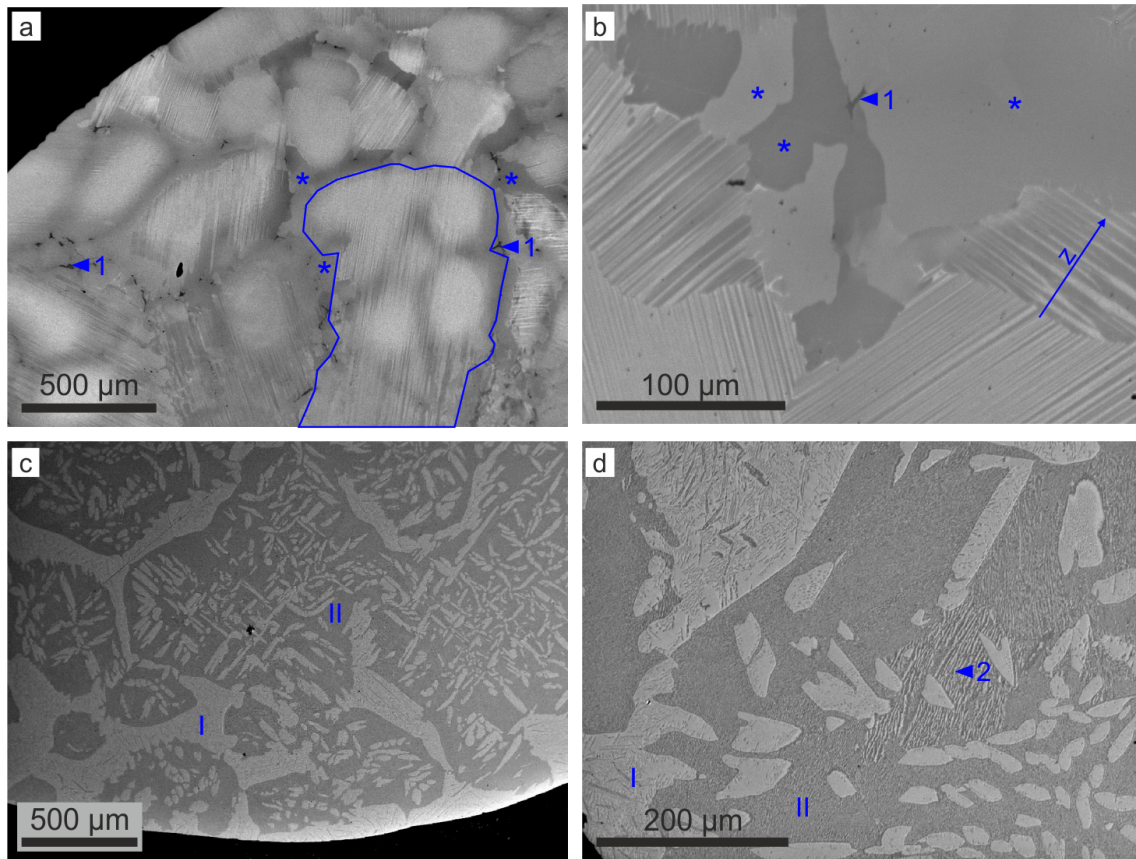


Figure 3.27: a,b) BSE images of QX671-C and c,d) BSE images of QX705-C from region R8 (fig. 3.2, R8). The Roman numerals I and II mark different repeating paragenetic sequences (or phases) of the texture.

Region R8 (fig. 3.2, R8, tab. 3.11) is a rather inconsistent group, which is mainly constituted by the phase content and by the DTA curves to a lesser extent. The textures of the different experiments differ from each other. All experiments from region R8 contain the phases  $\text{Ga}_{1-x}\text{Sn}_x\text{Pd}$ ,  $\text{Ga}_{2+p+q}\text{Sn}_{4-p}\text{Pd}_9$  and  $\text{Pd}_{20}\text{Sn}_{13-x}\text{Ga}_x$ . Consequently, these are experiments that are not related to the primary crystallization area of  $\text{Ga}_{1-x}\text{Sn}_x\text{Pd}_2$ . The sample QX671-C contains grains of primarily grown  $\text{Ga}_{2+p+q}\text{Sn}_{4-p}\text{Pd}_9$  (up to 1 mm). These grains may be strongly striped but also homogeneous single-phase grains of  $\text{Ga}_{2+p+q}\text{Sn}_{4-p}\text{Pd}_9$  occur (fig. 3.27, stars). Different homogeneous grains may have differences in their respective chemical composition. Darker grains have the average composition  $\text{Pd}_{59.6(2)}\text{Sn}_{20.6(2)}\text{Ga}_{19.8(3)}$  while lighter grains have the composition  $\text{Pd}_{59.9(1)}\text{Sn}_{23.7(9)}\text{Ga}_{16.4(8)}$ . The framed area in fig. 3.27, a, shows striped zones, extending over lighter and darker areas with the stripes following a uniform orientation. WDX measurements show chemical contrasts within the stripes (fig. 3.28). While changes in the Pd content are minor, the Sn and Ga contents differ strongly. The bright stripes have a average composition of  $\text{Pd}_{61.3(3)}\text{Sn}_{30.1(4)}\text{Ga}_{8.6(8)}$ , while the dark stripes are composed of  $\text{Pd}_{59.8(3)}\text{Sn}_{24.4(2)}\text{Ga}_{15.8(5)}$ . Consequently, the brighter phase can be assigned to  $\text{Pd}_{20}\text{Sn}_{13-x}\text{Ga}_x$  while the darker one is  $\text{Ga}_{2+p+q}\text{Sn}_{4-p}\text{Pd}_9$ . The gaps between the

grains, or the striped areas, are filled with fine-grained, dispersed multiphase material (fig. 3.27, arrow 1). The sample QX705-C has large (up to 1 mm), partly strongly dendritically grown grains of  $\text{Ga}_{2+p+q}\text{Sn}_{4-p}\text{Pd}_9$ . Those are strongly perforated by precipitates (fig. 3.27, sequence I). The spacings consist of a multiphase, dispersed matrix (fig. 3.27, sequence II), which is mostly very fine-grained, but sometimes also shows coarser regulated structures that remind more of an eutectic (fig. 3.27, arrow 2). The experiment QX675-C (fig. 3.29) has a texture from which information on the crystallization path is difficult to draw. The complete sample shows no single-crystalline area.

experiment	$y_L$	$x_L$	$\text{Ga}_{1-x}\text{Sn}_x\text{Pd}$ $\omega$ [wt. %]	$\text{Ga}_{2+p+q}\text{Sn}_{4-p}\text{Pd}_9$ $\omega$ [wt. %]	$\text{Pd}_{20}\text{Sn}_{13-x}\text{Ga}_x$ $\omega$ [wt. %]
QX705-C	55	0.40	47	31	22
QX671-C	59	0.60	12	67	21
QX675-C	56	0.50	35	28	37

Table 3.11: Phase content of the equilibrium-cooling experiments of starting melt compositions in region R8, based on Rietveld refinement.  $y_L$  and  $x_L$  relate to the melt composition<sup>17</sup>.

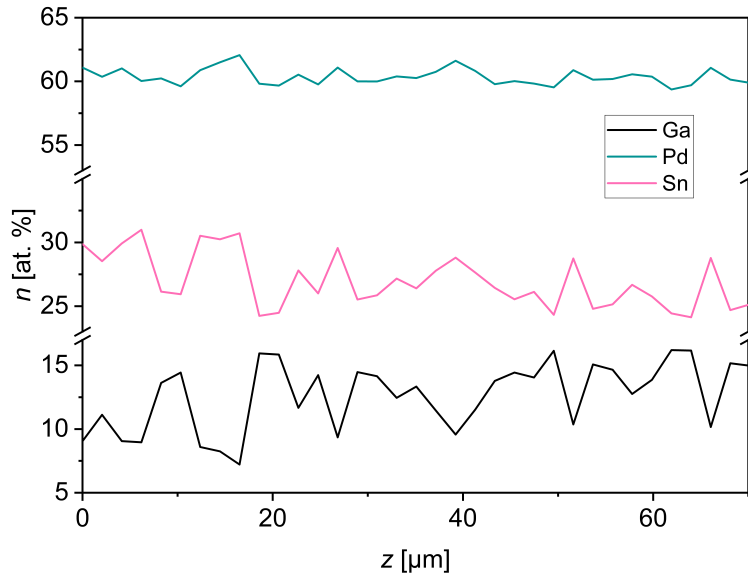


Figure 3.28: WDX line measurement in QX671-C (position marked in fig. 3.27, b).

<sup>17</sup>According to the description  $(\text{Ga}_{1-x_L}\text{Sn}_{x_L})_{100-y_L}\text{Pd}_{y_L}$ .

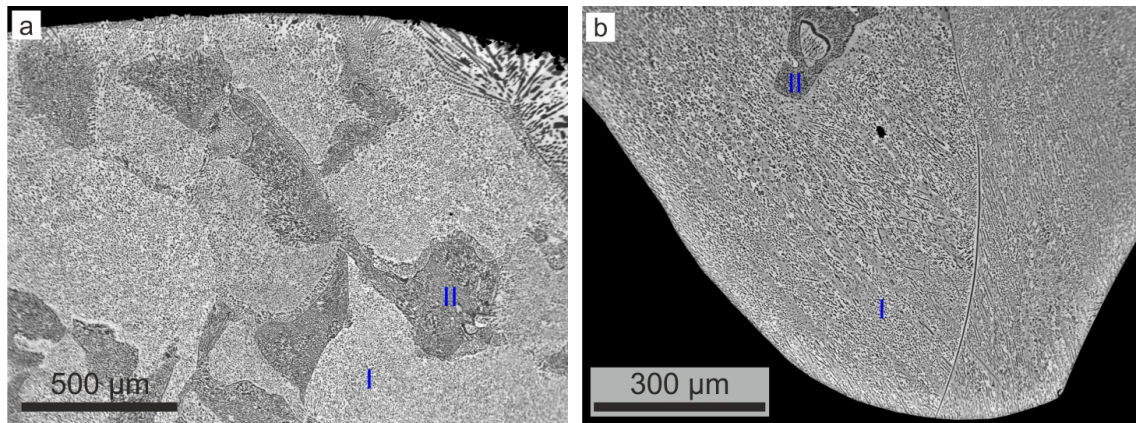


Figure 3.29: BSE images of QX675-C.

The DTA heating curves of all experiments in region R8 (fig. 3.30) are roughly similar and each contains two prominent signals. The first endothermic onset shared by all experiments is at  $\approx 780^\circ\text{C}$ . At onsets between  $850^\circ\text{C}$  and  $860^\circ\text{C}$  the second, larger peaks appear. These transition into dissolution processes, ending at different temperatures. In contrast to the heating curves, the DTA cooling curves have few similarities.

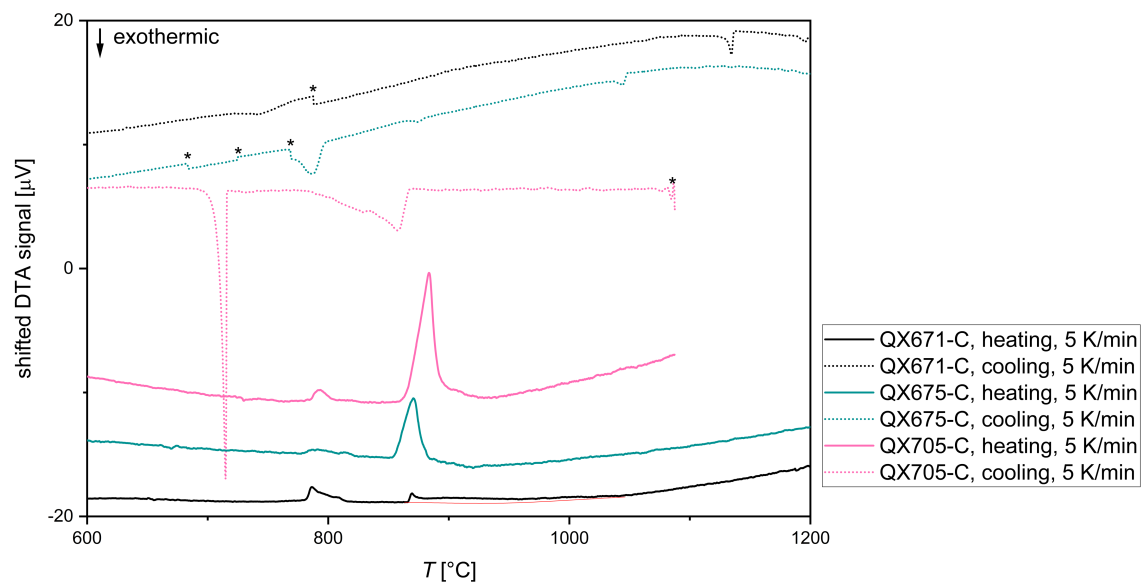


Figure 3.30: DTA curves of different samples from region R8. The stars mark artefacts, known from the instrument. Thin red constructed background lines allow better visibility of dissolution processes. For the cooling curve of QX705-C a background subtraction by a manual B-spline fit was performed since the curve was very steep.



## 3.1.2.9 Region R9

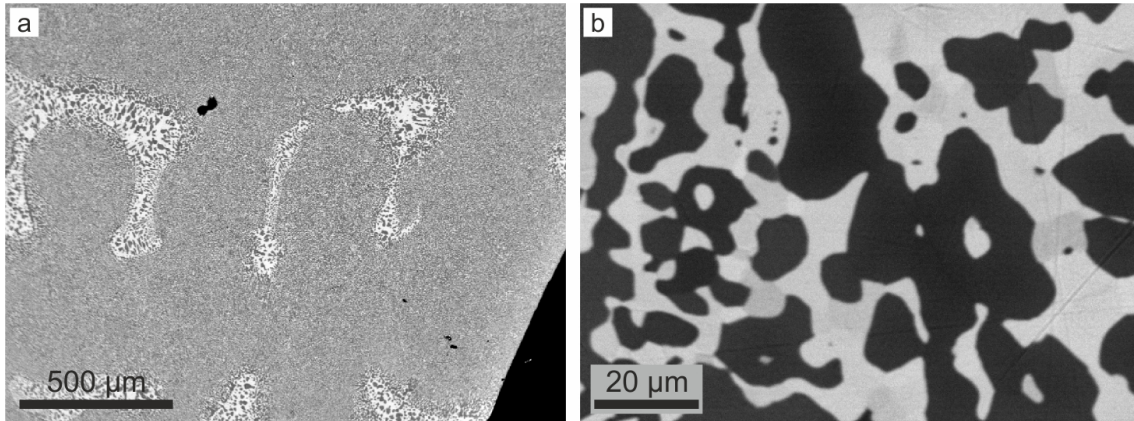


Figure 3.31: BSE images of QX681-F from Region R9.

The experiment QX681-F is the only one that solidified from a melt according to region R9 (fig. 3.2,R9). The ingot contains the phases  $\text{Ga}_{1-x}\text{Sn}_x\text{Pd}$ ,  $\text{PdSn}_{1-x}\text{Ga}_x$  and  $\text{Pd}_{20}\text{Sn}_{13-x}\text{Ga}_x$  (tab. 3.12). Accordingly, it is the only sample from this series containing  $\text{PdSn}_{1-x}\text{Ga}_x$ . The texture is likely to be eutectic. Regarding the phase content, the experiment has no relationship to the earlier regions R1-R8.

experiment	$y_L$	$x_L$	$\text{Ga}_{1-x}\text{Sn}_x\text{Pd}$ $\omega[\text{wt.}\%]$	$\text{PdSn}_{1-x}\text{Ga}_x$ $\omega[\text{wt.}\%]$	$\text{Pd}_{20}\text{Sn}_{13-x}\text{Ga}_x$ $\omega[\text{wt.}\%]$
QX681-F	52.75	0.40	64	10	26

Table 3.12: Phase content of the equilibrium-cooling experiments of region R9, based on Rietveld refinement.  $y_L$  and  $x_L$  relate to the melt composition<sup>18</sup>.

## 3.1.3 Thermal investigations

The main aim, to acquire the liquidus temperatures for certain compositions, i.e. to get an idea of the liquidus surface of primary crystallization region of  $\text{Ga}_{1-x}\text{Sn}_x\text{Pd}_2$ , could be achieved successfully. The knowledge about the liquidus surface reduces time and effort when the seeding temperature in the Czochralski apparatus is determined as described in section 2.2.5. Fig. 3.32 shows the temperatures where certain compositions start to solidify, measured by Differential thermal analysis (DTA). From these data points a liquidus surface is constructed. In addition, data points from the literature were plotted on the binary Ga-Pd line. It can be summarised that the Pd content has the greatest influence on the liquidus temperature, but the overall relationship cannot be simplified and depends significantly on the Sn content. Furthermore, there are two temperature minima in the investigated area. One is between the compositions  $\text{Ga}_{32.76}\text{Pd}_{56.16}\text{Sn}_{11.07}$  and  $\text{Ga}_{30.1}\text{Pd}_{57}\text{Sn}_{12.9}$  and the other one is close to the composition  $\text{Ga}_{27}\text{Pd}_{55}\text{Sn}_{18}$ . Possible solidification areas and crystallization paths will be discussed later.

<sup>18</sup>According to the description  $(\text{Ga}_{1-x_L}\text{Sn}_{x_L})_{100-y_L}\text{Pd}_{y_L}$ .

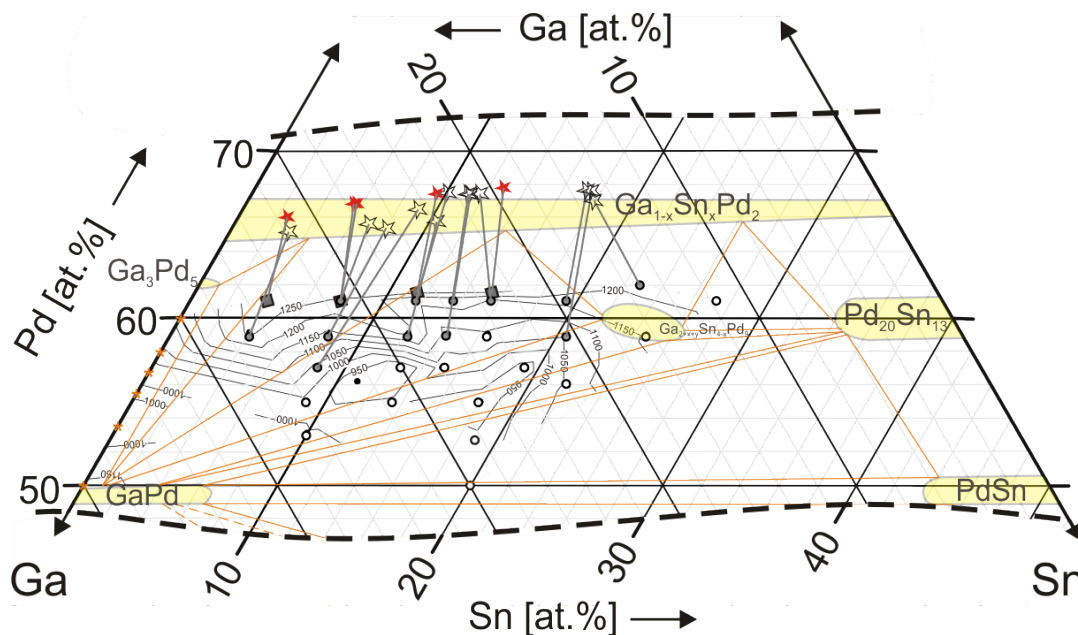


Figure 3.32: Constructed liquidus surface of all samples, measured by DTA in the vicinity of the (Ga,Sn)-rich side of the primary solidification area of  $\text{Ga}_{1-x}\text{Sn}_x\text{Pd}_2$ . The points show the starting compositions of the experiments. Experiments with melt compositions that are marked in grey, result in the primary crystallization of  $\text{Ga}_{1-x}\text{Sn}_x\text{Pd}_2$ . The grey lines show the tie-lines<sup>19</sup>. The stability regions of the different phases (yellow) as well as their tie-triangles<sup>20</sup> (orange) are published by [18] and refer to the temperature of 500°C. The liquidus temperatures on the binary Ga-Pd line, marked with yellow stars, are taken from [23].

The figs. 3.33 and 3.34 show the data points of the onsets (and if useful also endsets) of the DTA signals of all evaluated DTA heating and cooling curves around the presumed primary solidification area of  $\text{Ga}_{1-x}\text{Sn}_x\text{Pd}_2$ . In the heating curves (fig. 3.33) the last endsets correspond to the temperatures where the sample was completely dissolved, i.e. the respective solidus temperatures. Most of these “last endset” signals are the end of long-lasting dissolution processes, starting up to 200 K earlier, as shown in the DTA curves of the previous sections 3.1.2.1-3.1.2.8 (e.g. figs 3.6, 3.8 and 3.10).

Signals called “first onsets” in the cooling curves (fig. 3.34) correspond to the liquidus temperatures of the respective composition. Most onsets of further signals in the heating and cooling curves at lower temperatures except those corresponding to the liquidus or the solidus temperatures are not randomly distributed but are accumulated at certain temperatures or in lines. This indicates that many compositions share specific events at certain temperatures in the crystallization paths. Such events may be invariant points like eutectics and eutectoids or in the case of accumulations with temperature gradients peritectoid reactions. During heating of the DTA samples a first endothermic reaction takes place at  $\approx 800^\circ\text{C}$  for experiments with initial Sn content of  $0.2 \leq x_L \leq 0.6$ <sup>21</sup> indicating that most of these

<sup>19</sup>Tie-lines connect the composition of the melt with the solid being in equilibrium with it.

<sup>20</sup>Tie-triangles connect the three phases that are in equilibrium [42].

<sup>21</sup>According to the description  $(\text{Ga}_{1-x_L}\text{Sn}_{x_L})_{100-y_L}\text{Pd}_{y_L}$ .

experiments share the same event in the phase diagram. Heating further a second shared exothermic reaction takes place at temperatures of  $\approx 900\text{-}950^\circ\text{C}$  and finally the dissolution process of the first-to-freeze phase starts. Exceptions are eutectic compositions, indicated by sharp singular peaks.

During cooling, after the crystallization of the first phase, most experiments share endothermic reactions in the region of  $\approx 900\text{-}950^\circ\text{C}$ . At  $\approx 900^\circ\text{C}$  the eutectic is expected. Events above  $900^\circ\text{C}$  and below  $950^\circ\text{C}$  are either peritectic or quasi-peritectic reactions or peritectoid decompositions. Details are discussed in section 4.1.2. During further cooling, accumulated exothermic reactions take place at  $\approx 800^\circ\text{C}$  in experiments with initial Sn contents of  $0.3 \leq x_L \leq 0.5$ . In the case of experiments with  $x_L \leq 0.3$ , the onset temperatures decrease with decreasing  $x_L$  until  $\approx 620^\circ\text{C}$ .

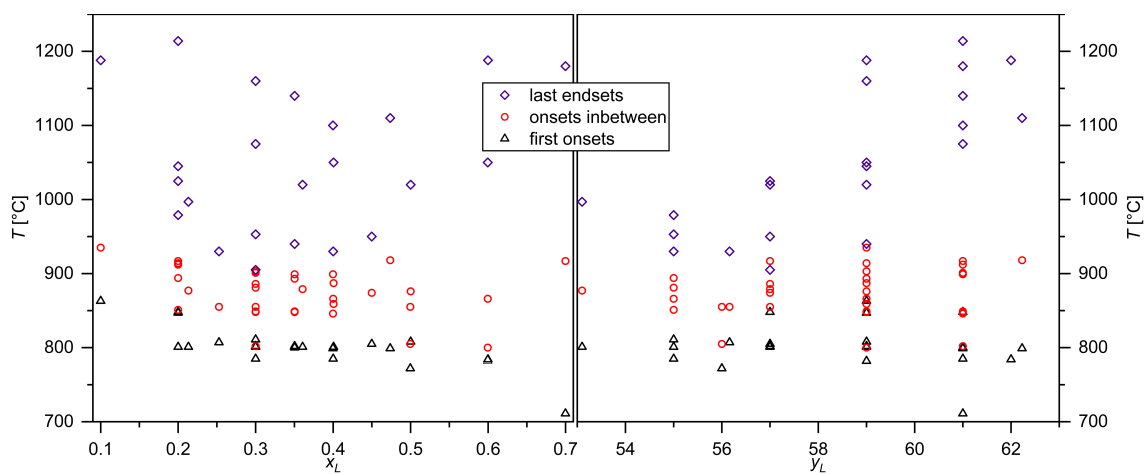


Figure 3.33: Onsets and the last endsets of all endothermic signals of all evaluated DTA heating curves.

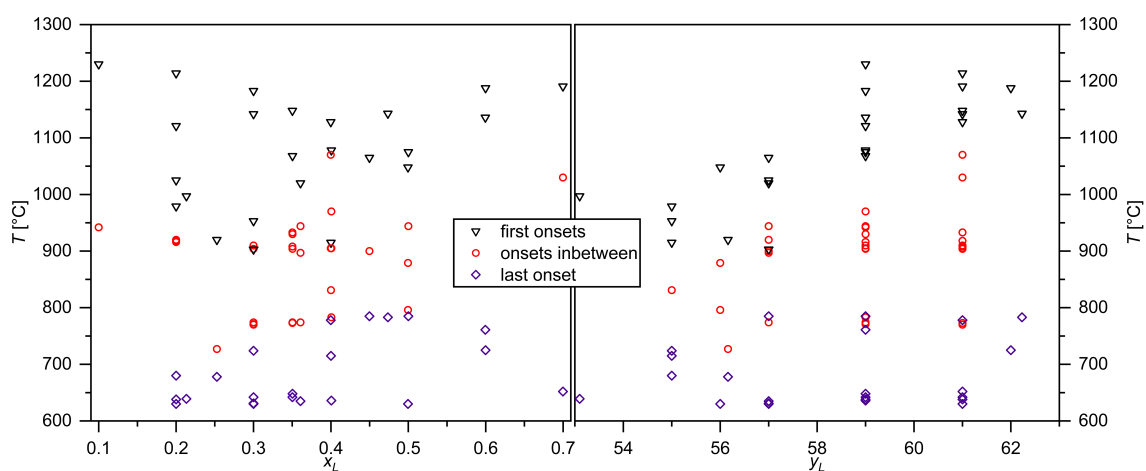


Figure 3.34: Onsets of all exothermic signals of all evaluated DTA cooling curves.

### 3.1.4 Phase properties

#### 3.1.4.1 $\text{Ga}_{1-x}\text{Sn}_x\text{Pd}_2$

##### Primarily crystallized $\text{Ga}_{1-x}\text{Sn}_x\text{Pd}_2$

$\text{Ga}_{1-x}\text{Sn}_x\text{Pd}_2$  crystallizes primarily in melts with initial Sn contents of  $x_L \leq 0.6$ <sup>22</sup>. The Pd-rich boundary of the primary solidification area was not investigated for practical reasons. The Pd-poor limit varies between  $55 \leq y_L \leq 59$ <sup>22</sup> in the initial melt. The melt compositions of experiments with primarily crystallized  $\text{Ga}_{1-x}\text{Sn}_x\text{Pd}_2$  can be seen in the figs. 3.2 and 3.32 where tie-lines<sup>23</sup> are shown. The maximum crystallized weight fraction  $\omega$  of the phase varied in the studied region ( $55 \leq y_L \leq 62$ ) is between  $\omega = 76$  wt.% (QX663-B) and  $\omega = 0$  wt.% at the edge of the primary solidification region. This shows that small changes in the Pd content in the initial melt cause large changes in the amount of  $\text{Ga}_{1-x}\text{Sn}_x\text{Pd}_2$  crystallizing.

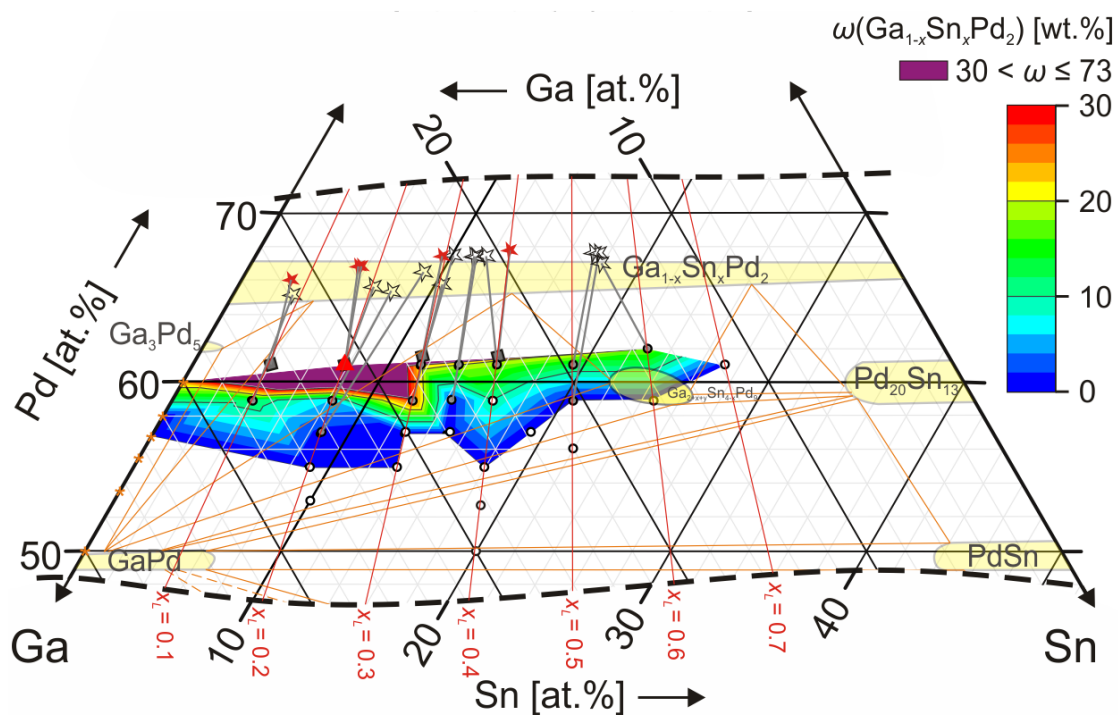


Figure 3.35: Part of Gibbs triangle, showing the distribution of the weight fraction,  $\omega$ , of primarily crystallized  $\text{Ga}_{1-x}\text{Sn}_x\text{Pd}_2$ , depending on the initial melt composition. In order to make the scale more descriptive, the purple area with very high  $\omega$  values has been separated graphically. The red triangle marks experiment QX663-B, which has the highest measured weight fraction,  $\omega$ , of  $\text{Ga}_{1-x}\text{Sn}_x\text{Pd}_2$  ( $\omega = 73$  wt.%) within these phase diagram studies. The points mark the starting compositions of the experiments. Grey-filled starting compositions result in the primary crystallization of  $\text{Ga}_{1-x}\text{Sn}_x\text{Pd}_2$ . The stability regions of the different phases drawn in yellow, are published by [18] and refer to the temperature of 500°C. The weight fractions on the binary Ga-Pd line, marked with yellow stars, are based on [23].

A crucial result for the estimation of the composition for the Czochralski crystal

<sup>22</sup>According to the description  $(\text{Ga}_{1-x_L}\text{Sn}_{x_L})_{100-y_L}\text{Pd}_{y_L}$ .

<sup>23</sup>Tie-lines connect the composition of the melt with the solid being in equilibrium with it.

growth of  $\text{Ga}_{1-x}\text{Sn}_x\text{Pd}_2$  is that  $x$  shows a linear dependence on  $x_L$ <sup>24</sup> and the pseudobinary segregation,  $k^*$  is approximately 1 in the equilibrium-cooling experiments (fig. 3.36). Additionally, the Pd content in the melt,  $y_L$ , has no significant influence on the segregation in the investigated region. Accordingly, for the calculation of the melt composition for later Czochralski experiments, no pseudobinary Ga-Sn segregation was taken into account, but only the ratio between (Ga,Sn) and Pd. Within the precision of the WDX measurements no clear relation between the Pd content in the crystal and in the melt,  $y$  and  $y_L$ , could be established.

In the polycrystalline pre-experiments, primarily grown  $\text{Ga}_{1-x}\text{Sn}_x\text{Pd}_2$  grains were analysed by XPD and WDX measurements. They prove that all lattice parameters  $a$ ,  $b$  and  $c$  increase with increasing Sn content,  $x$ , in the crystal. With more precise data of the Czochralski-grown crystals these values were refined (section 3.3.2). From the data gained in section 3.3.2 the Sn content,  $x$ , can be calculated from the lattice parameters. This is important to get information on  $x$  in crystals that are too small to be measured by WDX (e.g.  $\text{Ga}_{1-x}\text{Sn}_x\text{Pd}_2$ , formed in an eutectoid). In order to review the quality of the calculation procedure, the calculated Sn contents,  $x_{XPD}$ , were plotted against the measured  $x$  of the primarily formed  $\text{Ga}_{1-x}\text{Sn}_x\text{Pd}_2$  grains (fig. 3.38). The plot shows that the  $x_{XPD}$  values gained from XPD are correct within the range of the error, but tend to be slightly higher than those measured by WDX. Fig. 3.39 indicates a correlation of the measured amount of Sn substituting Ga in the crystal,  $x$ , and the measured amount of Pd,  $y$  meaning that crystals with higher Sn contents may contain higher Pd contents.

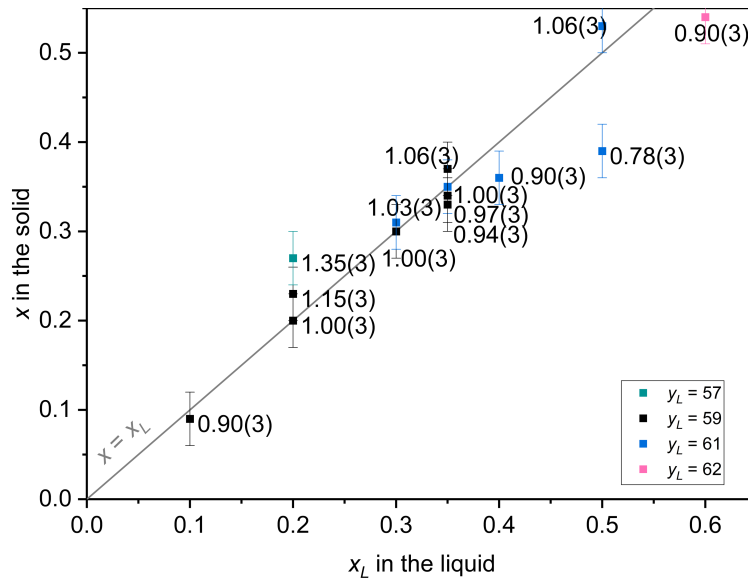


Figure 3.36: The Sn content in the crystal,  $x$ , plotted against the Sn content in the melt,  $x_L$ . The given values are the pseudobinary segregation coefficients  $k^* = \frac{x}{x_L}$ .

<sup>24</sup>According to the description  $(\text{Ga}_{1-x_L}\text{Sn}_{x_L})_{100-y_L}\text{Pd}_{y_L}$ .

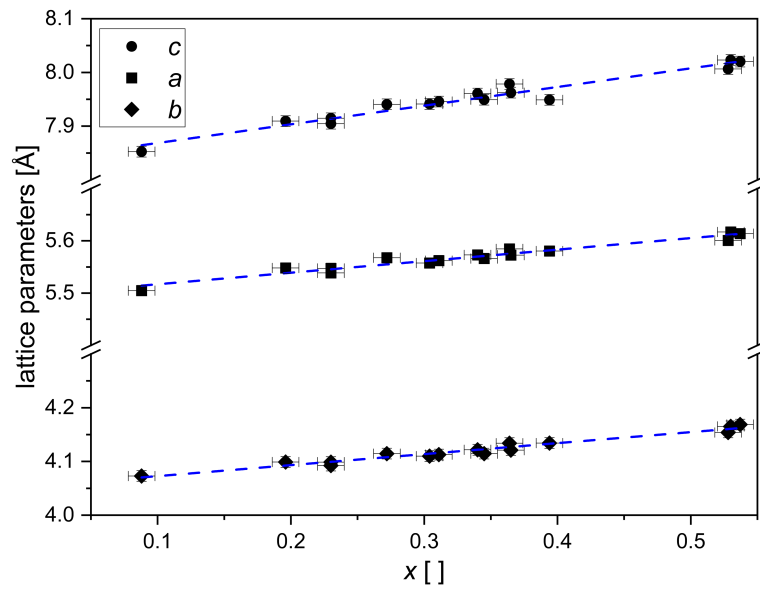


Figure 3.37: Lattice parameters,  $a$ ,  $b$  and  $c$ , of primarily crystallized  $\text{Ga}_{1-x}\text{Sn}_x\text{Pd}_2$ , in dependence of  $x$ .

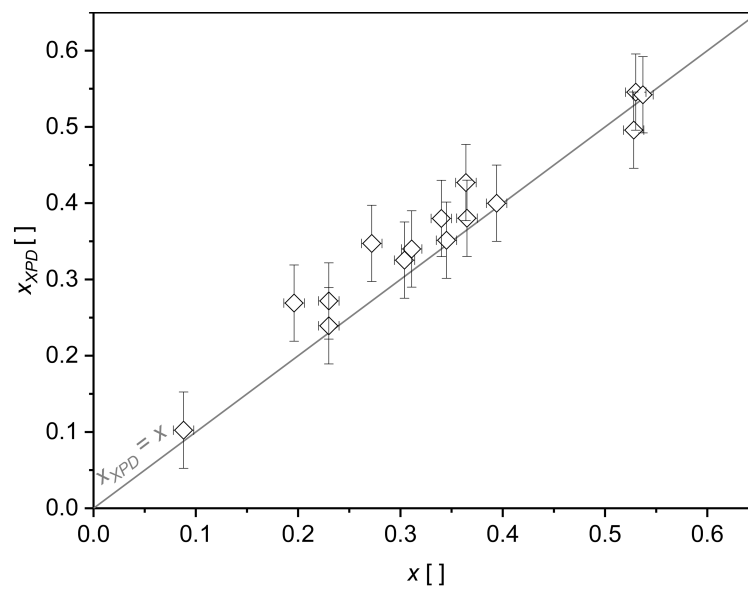


Figure 3.38: The calculated Sn content,  $x_{XPD}$ , from XPD data (as described in section 3.3.2), plotted against the measured Sn content,  $x$ , in the primarily crystallized grains. The plot is used to estimate the precision of the calculation of  $x_{XPD}$ .



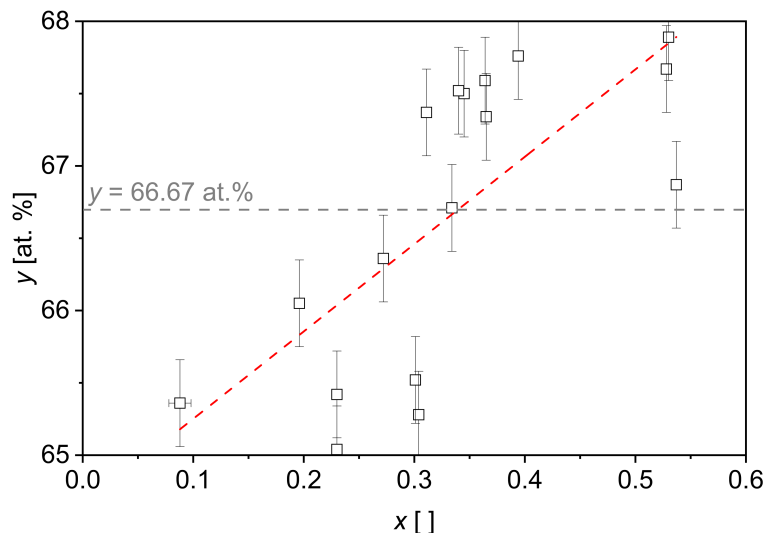


Figure 3.39: The Pd content in the crystal,  $y$ , measured by WDX and plotted against the Sn content in the crystal,  $x$ . The grey dotted line shows the Pd content in stoichiometric GaPd<sub>2</sub>.

### Secondarily crystallized Ga<sub>1-x</sub>Sn<sub>x</sub>Pd<sub>2</sub>

Secondarily formed Ga<sub>1-x</sub>Sn<sub>x</sub>Pd<sub>2</sub> is either finely distributed as a component of an eutectoid or, especially at higher  $x_L$ , it occurs as lamellae next to Ga<sub>2+p+q</sub>Sn<sub>4-p</sub>Pd<sub>9</sub> and Pd<sub>20</sub>Sn<sub>13-x</sub>Ga<sub>x</sub>. It is mostly present in experiments with starting compositions in the region of  $x_L = 0.2$  and  $y_L = 58$ <sup>25</sup> (fig. 3.40). The weight fraction,  $\omega$ , of secondary Ga<sub>1-x</sub>Sn<sub>x</sub>Pd<sub>2</sub> decreases to experiments with higher  $x_L$  and vanishes at  $x_L > 0.5$ . However, in experiments of melts with  $x_L = 0.7$  the phase is present again. In that region the above-mentioned lamellae with Ga<sub>2+p+q</sub>Sn<sub>4-p</sub>Pd<sub>9</sub> and Pd<sub>20</sub>Sn<sub>13-x</sub>Ga<sub>x</sub> occur. It can therefore be assumed that Ga<sub>1-x</sub>Sn<sub>x</sub>Pd<sub>2</sub>, has a different origin between melts with  $x_L \leq 0.5$  and  $x_L = 0.7$  with respect to the crystallization path.

<sup>25</sup>According to the description (Ga<sub>1-x<sub>L</sub></sub>Sn<sub>x<sub>L</sub></sub>)<sub>100-y<sub>L</sub></sub>Pd<sub>y<sub>L</sub></sub>.

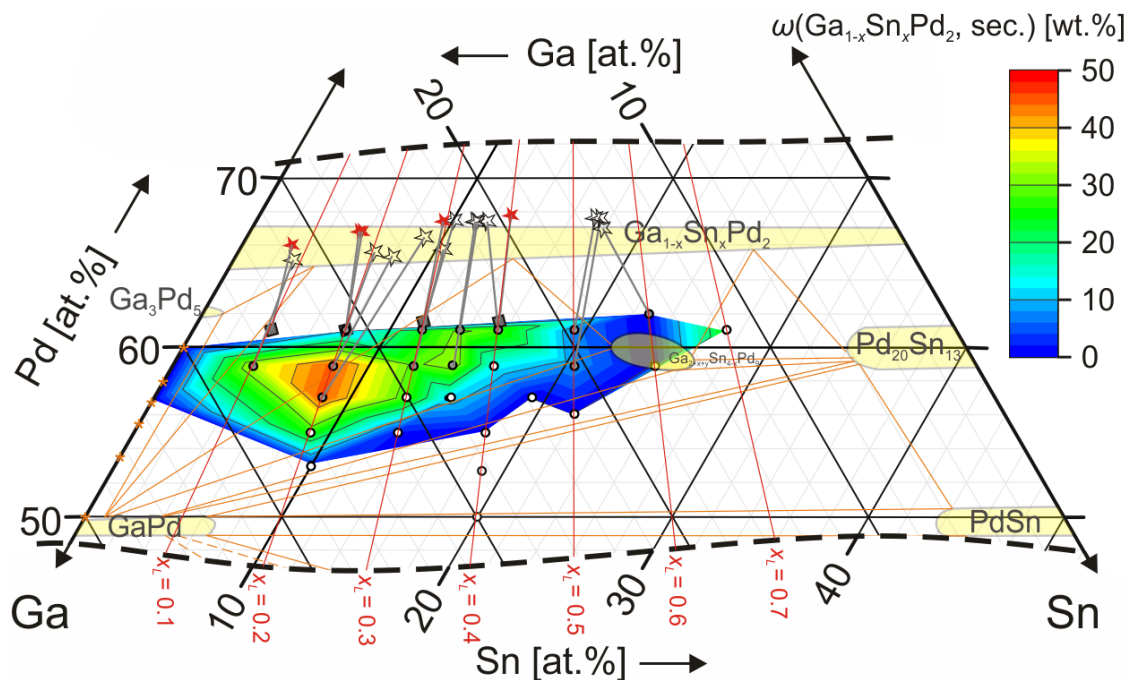


Figure 3.40: Part of Gibbs triangle, showing the distribution of the weight fraction,  $\omega$ , of secondarily formed  $\text{Ga}_{1-x}\text{Sn}_x\text{Pd}_2$ , depending on the initial melt composition. The grey and white points are the starting compositions of the experiments. Grey-filled experiments result in the primary crystallization of  $\text{Ga}_{1-x}\text{Sn}_x\text{Pd}_2$ . The stability regions of the different phases, drawn in yellow, are published by [18] and refer to the temperature of  $500^\circ\text{C}$ . The weight fractions on the binary Ga-Pd line, marked with yellow stars, are based on [23].

WDX measurements of the chemical composition of the individual grains of secondarily formed  $\text{Ga}_{1-x}\text{Sn}_x\text{Pd}_2$  are not possible in most cases since the phase is distributed finely. The diameter of the excitation volume of the electron beam exceeds the respective grain sizes, resulting in averaged compositions with the neighbouring phases. As mentioned in the previous section 3.1.4.1, the refinement of the lattice parameters and the calculation of  $x_{XPD}$  from these, according to the equations in section 3.3.2 was a powerful tool to estimate the composition of the secondary formed  $\text{Ga}_{1-x}\text{Sn}_x\text{Pd}_2$ . Fig. 3.41 shows that the calculated Sn content,  $x_{XPD}$ , occurs only in three values. Most experiments contain secondary  $\text{Ga}_{1-x}\text{Sn}_x\text{Pd}_2$  with the composition  $x_{XPD} = 0.47(5)$  with the lattice parameters  $a = 5.6(1) \text{ \AA}$ ,  $b = 4.1(1) \text{ \AA}$  and  $c = 8.0(1) \text{ \AA}$ . Due to the small number of values, other compositions ( $x_{XPD} = 0.27(5), 0.64(5)$ ) are not statistically reliable. Nevertheless, due to the texture and the large differences of  $x_{XPD}$ , it is clear that there must be three different origins for secondary  $\text{Ga}_{1-x}\text{Sn}_x\text{Pd}_2$ .



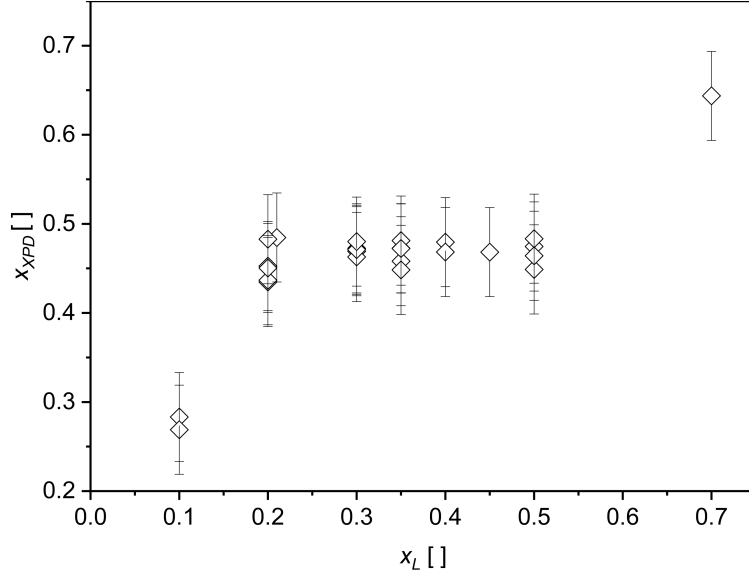


Figure 3.41:  $x_{XPD}$ , plotted against  $x_L$  of secondary  $\text{Ga}_{1-x}\text{Sn}_x\text{Pd}_2$ .  $x_{XPD}$  is calculated from the refined lattice parameters, according to the equations in section 3.3.2.

### 3.1.4.2 $\text{Ga}_{2+p+q}\text{Sn}_{4-p}\text{Pd}_9$

$\text{Ga}_{2+p+q}\text{Sn}_{4-p}\text{Pd}_9$  is very common in all experiments and shows the greatest differences in its textures. It occurs primarily grown as larger grains (usually decomposed) and dendrites, as fine dendrites and dendritic stars in eutectic textures and also fine-grained, dispersed as a component of an eutectoid. It frequently occurs in larger amounts, grown together with  $\text{Ga}_{1-x}\text{Sn}_x\text{Pd}_2$  on a three-phase coexistence line and also in a lamella-like decomposition structures together with  $\text{Ga}_{1-x}\text{Sn}_x\text{Pd}_2$  and  $\text{Pd}_{20}\text{Sn}_{13-x}\text{Ga}_x$ . Fig. 3.42 shows that the  $\text{Ga}_{2+p+q}\text{Sn}_{4-p}\text{Pd}_9$  contents in the experiments increase from low Sn and Pd to high Sn and Pd contents in the initial melts. The highest weight fractions of the phase can be observed in experiments with  $0.5 \leq x_L \leq 0.6$  and  $58 \leq y_L \leq 62$ <sup>26</sup> in the starting composition  $(\text{Ga}_{1-x_L}\text{Sn}_{x_L})_{100-y_L}\text{Pd}_{y_L}$ . The blue pentagons indicate that most of the measured compositions for this phase are located in this area as well. It can be seen that  $\text{Ga}_{2+p+q}\text{Sn}_{4-p}\text{Pd}_9$  was measured with a larger stability field, compared to the published one at 500°C [18]. The blue pentagons do not represent all present compositions, since eutectoid grain sizes are too small to be measured properly by WDX. Only compositions of grains large enough to be measured are shown. Fig. 3.43 shows that the lattice parameter  $a$  decreases with the measured Ga content and increases with the measured Sn content, while there is almost no relation to the Pd content. Ga and Sn accordingly substitute each other.

In some grains WDX measurements indicate a Sn gradient (also visible in plateau-like or asymmetric XPD peaks). The Sn content decreases along the growth directions of the individual grains, meaning there is a depletion of Sn in the melt, indicating the segregation coefficient for Sn being larger than 1.

<sup>26</sup>According to the description  $(\text{Ga}_{1-x_L}\text{Sn}_{x_L})_{100-y_L}\text{Pd}_{y_L}$ .

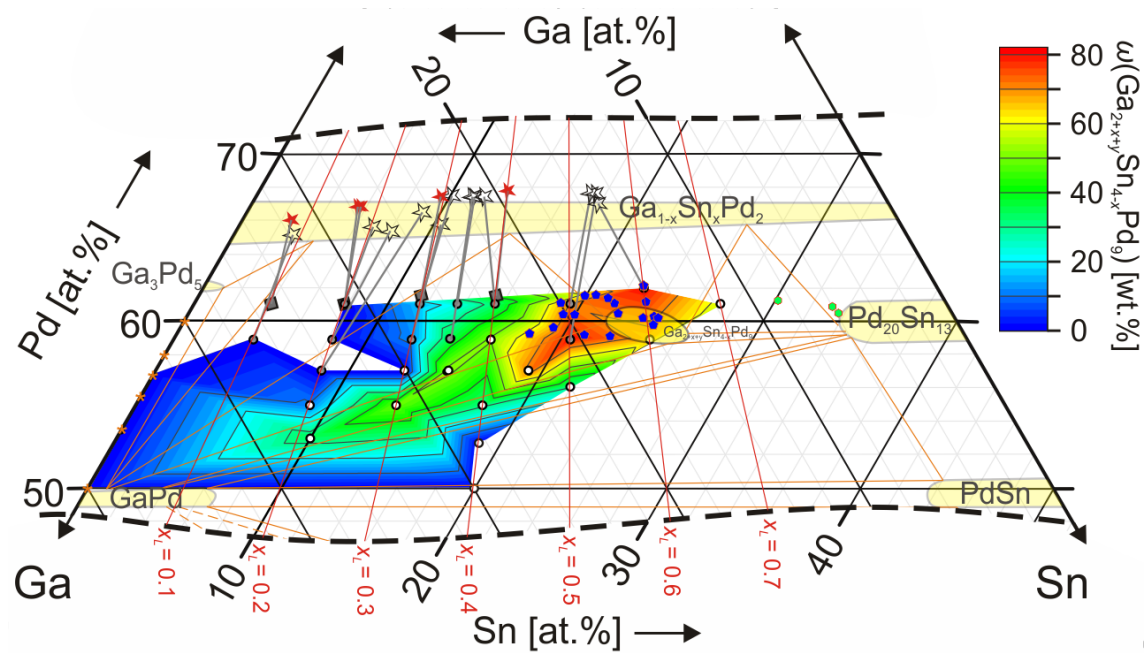


Figure 3.42: Part of Gibbs triangle, showing the distribution of the weight fraction,  $\omega$ , of  $\text{Ga}_{2+p+q}\text{Sn}_{4-p}\text{Pd}_9$ , depending on the initial melt composition. Blue pentagons show the measured compositions of  $\text{Ga}_{2+p+q}\text{Sn}_{4-p}\text{Pd}_9$ . The grey and white points are the starting compositions of the experiments. Grey-filled experiments result in the primary crystallization of  $\text{Ga}_{1-x}\text{Sn}_x\text{Pd}_2$ . The stability regions of the different phases drawn in yellow are published by [18] and refer to the temperature of  $500^\circ\text{C}$ . The weight fractions on the binary Ga-Pd line, marked with yellow stars, are based on [23].

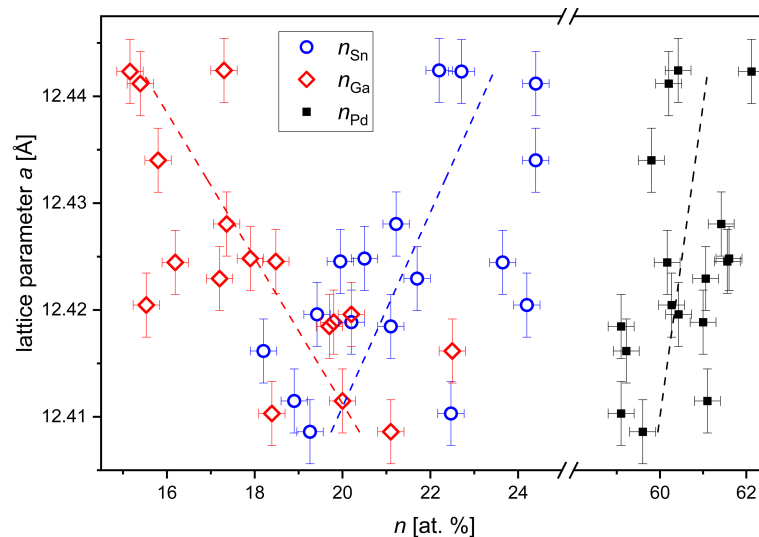


Figure 3.43: The refined lattice parameters of  $\text{Ga}_{2+p+q}\text{Sn}_{4-p}\text{Pd}_9$ , gained from XPD measurements, plotted against the Ga, Pd and Sn contents ( $n_{\text{Ga}}$ ,  $n_{\text{Pd}}$  and  $n_{\text{Sn}}$ ), measured by WDX. The dotted lines are linear trend lines

### 3.1.4.3 $\text{Ga}_{1-x}\text{Sn}_x\text{Pd}$

In these studies only  $\text{Ga}_{1-x}\text{Sn}_x\text{Pd}$  is regarded, that was formed secondarily in the vicinity of the (Ga,Sn)-rich primary crystallization region of  $\text{Ga}_{1-x}\text{Sn}_x\text{Pd}_2$ . Studies on primarily crystallized  $\text{Ga}_{1-x}\text{Sn}_x\text{Pd}$  have already been elaborated and published [26–28]. The following is a brief summary of the most important conclusions of these studies

- From melts with the composition  $(\text{Ga}_{1-x_L}\text{Sn}_{x_L})_{100-y_L}\text{Pd}_{y_L}$ ,  $\text{Ga}_{1-x}\text{Sn}_x\text{Pd}$  may crystallize primarily with Sn contents of  $x_L \leq 0.9$ . This applies to the Pd content  $45 \leq y_L \leq 50$ .
- The crystallization of  $\text{Ga}_{1-x}\text{Sn}_x\text{Pd}$  has a high pseudobinary segregation with Sn as the excess component and a low pseudobinary segregation coefficient of  $k^* = 0.3$ .
- The Pd content in the melt,  $y_L$ , influences the pseudobinary segregation coefficient,  $k^*$ . From melts with the same initial Sn content,  $x_L$ ,  $\text{Ga}_{1-x}\text{Sn}_x\text{Pd}$  crystallizes with higher Sn contents,  $x$ , if the initial Pd content,  $y_L$ , is higher.
- $\text{Ga}_{1-x}\text{Sn}_x\text{Pd}$  has a low structural limit for the substitution of Ga by Sn at  $x = 0.15$ , corresponding to initial melts with  $x_L = 0.4$ . That means from melts with  $0.4 \leq x_L \leq 0.9$  no larger Sn content than  $x = 0.15$  will be achieved, even though the limit for crystal growth is at  $x_L = 0.9$ .
- Below the structural limit,  $x = 0.15$ , for the substitution of Ga by Sn in  $\text{Ga}_{1-x}\text{Sn}_x\text{Pd}$ ,  $x$  rises linearly in dependence of the initial Sn content  $x_L$ .
- The lattice parameter  $a$  increases linearly with increasing  $x$ , from 4.90 Å to 4.95 Å, where the structural limit is reached (fig. 3.45).

In the area of the (Ga,Sn)-rich side of the primary solidification region of  $\text{Ga}_{1-x}\text{Sn}_x\text{Pd}_2$ , secondary  $\text{Ga}_{1-x}\text{Sn}_x\text{Pd}$  occurs in almost all experiments. Exceptions are only experiments with both, very high Sn and Pd fractions ( $x_L \geq 0.6$ ,  $y_L \geq 61$ ). In the investigated area  $\text{Ga}_{1-x}\text{Sn}_x\text{Pd}$  could not be observed to grow on a three-phase coexistence line, but is always formed either in an eutectic or even more often as a component of an eutectoid or by other solid-state decompositions of other phases. Since  $\text{Ga}_{1-x}\text{Sn}_x\text{Pd}$  grains are always fine-grained, chemical analyses by WDX were only possible in few cases.

Fig. 3.44, a shows the lattice parameters of secondary formed  $\text{Ga}_{1-x}\text{Sn}_x\text{Pd}$  gained from XPD measurements and Rietveld refinement. It is noticeable that the lattice parameters accumulate in three different sizes, at  $a_1 = 4.90(1)$  Å,  $a_2 = 4.92(1)$  Å and  $a_3 = 4.93(1)$  Å (The two data points with lattice parameters of 4.95(1) Å are from compositions where the phase crystallizes primarily). This indicates three different origins for the formation of secondary  $\text{Ga}_{1-x}\text{Sn}_x\text{Pd}$  in these experiments. Fig. 3.44, b, shows the deviation of the size of the lattice parameters, related to starting compositions of the experiments in the Gibbs triangle. Fig. 3.45 shows the lattice parameters, fitted against the Sn content,  $x$ , according to [26]. This allows a calculation of the Sn contents from the lattice parameters. From this fit  $a_1 = 4.90(1)$  Å is assigned to  $\text{Ga}_{0.98(2)}\text{Sn}_{0.02(2)}\text{Pd}$ ,  $a_2 = 4.92(1)$  Å to  $\text{Ga}_{0.93(2)}\text{Sn}_{0.07(2)}\text{Pd}$  and  $a_3 = 4.93(1)$  Å to  $\text{Ga}_{0.89(2)}\text{Sn}_{0.11(2)}\text{Pd}$ .

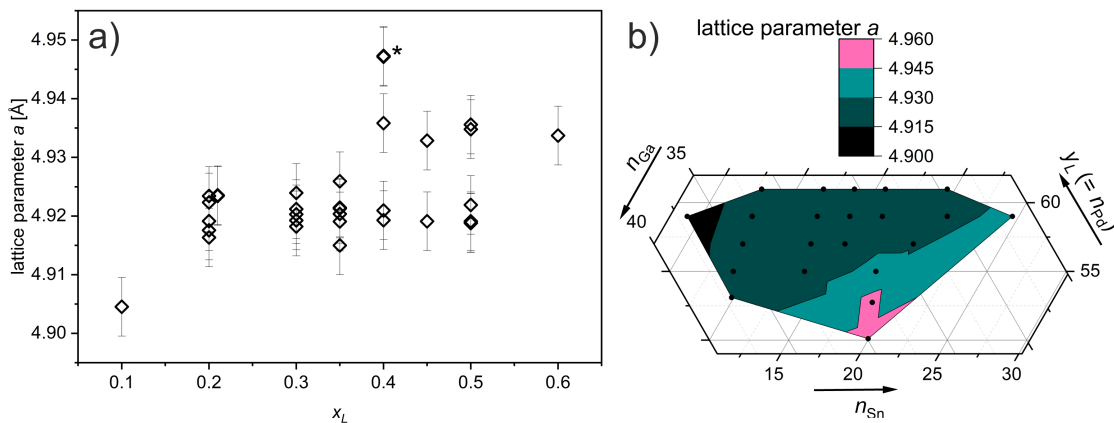


Figure 3.44: a) Lattice parameter  $a$  of secondarily formed  $\text{Ga}_{1-x}\text{Sn}_x\text{Pd}$ , plotted against the Sn contents of the initial melts,  $x_L$ <sup>27</sup>. The marked data point (\*) can be assigned to experiments that belong to the primary crystallization area of  $\text{Ga}_{1-x}\text{Sn}_x\text{Pd}$ . b) Part of Gibbs triangle, showing the deviation of the size of the lattice parameter  $a$ , depending on the initial melt composition from which the respective samples originate. The black dots give the composition of each experiment, containing secondary  $\text{Ga}_{1-x}\text{Sn}_x\text{Pd}$ .

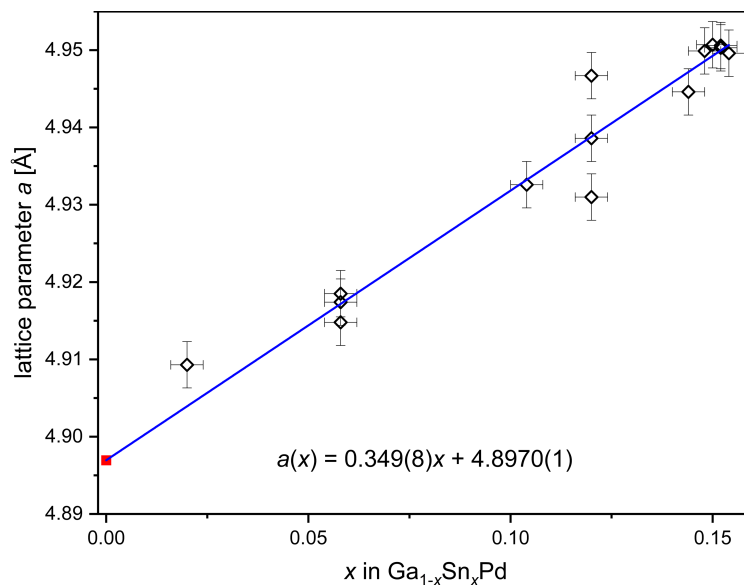


Figure 3.45: Lattice parameters of primarily grown  $\text{Ga}_{1-x}\text{Sn}_x\text{Pd}$  changed after [26]. The equation describes the added linear fit. The value for  $x = 0$  was taken from literature [12].

#### 3.1.4.4 $\text{Pd}_{20}\text{Sn}_{13-x}\text{Ga}_x$

In the investigated region,  $\text{Pd}_{20}\text{Sn}_{13-x}\text{Ga}_x$  appears secondarily in experiments with compositions shown in fig. 3.46. Only few compositions could be measured by WDX (indicated by green hexagons). Some of them are outside the 500°C stability

<sup>27</sup>According to the description  $(\text{Ga}_{1-x_L}\text{Sn}_{x_L})_{100-y_L}\text{Pd}_{y_L}$ .

region published by [18]. Fig. 3.47 shows an increase of the lattice parameter  $c$  with increasing lattice parameter  $a$ , indicating chemical differences in  $\text{Pd}_{20}\text{Sn}_{13-x}\text{Ga}_x$  between the measured samples. However, only a few compositions could be measured, from which conclusions must be handled carefully. A rough tendency is that both lattice parameters  $a$  and  $c$  increase with increasing measured Sn content,  $n_{\text{Sn}}$ , while they decrease with increasing Ga content,  $n_{\text{Ga}}$  (fig. 3.48). It can be seen that the Pd content,  $n_{\text{Pd}}$ , is roughly constant in the measured samples, and accordingly there is no relation between  $n_{\text{Pd}}$  and the lattice parameters.

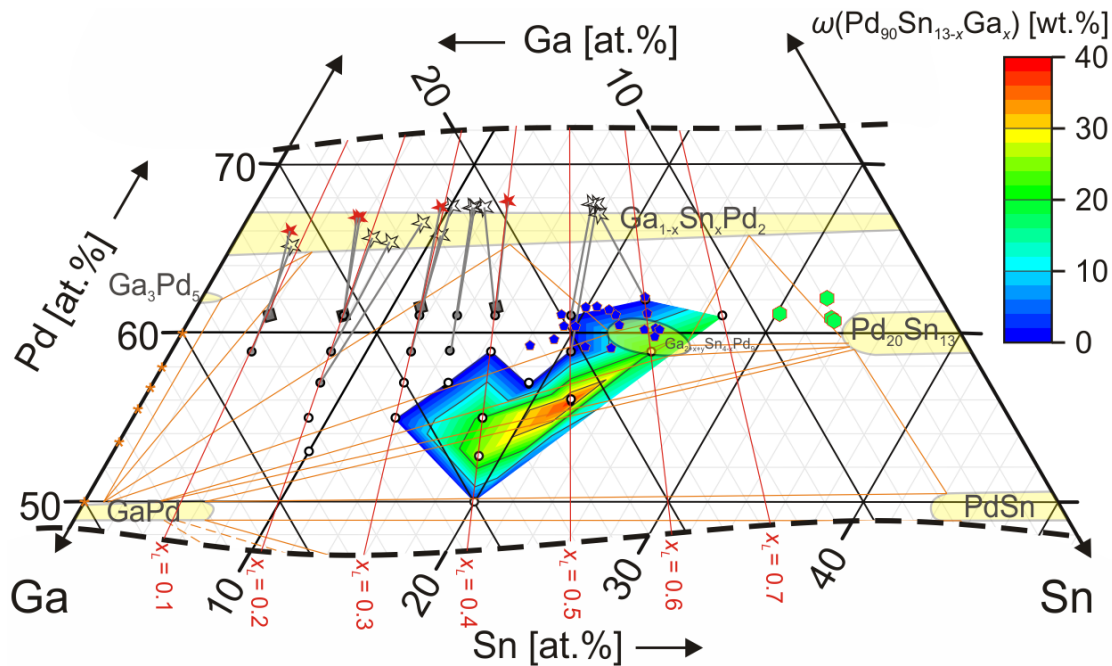


Figure 3.46: Part of Gibbs triangle, showing the distribution of the weight fraction  $\omega$  of  $\text{Pd}_{20}\text{Sn}_{13-x}\text{Ga}_x$ , depending on the initial melt composition. Green hexagons show the measured compositions of  $\text{Pd}_{20}\text{Sn}_{13-x}\text{Ga}_x$ . The grey and white points are the starting compositions of the experiments. Grey-filled experiments result in the primary crystallization of  $\text{Ga}_{1-x}\text{Sn}_x\text{Pd}_2$ . The stability regions of the different phases drawn in yellow are published by [18] and refer to the temperature of  $500^\circ\text{C}$ .

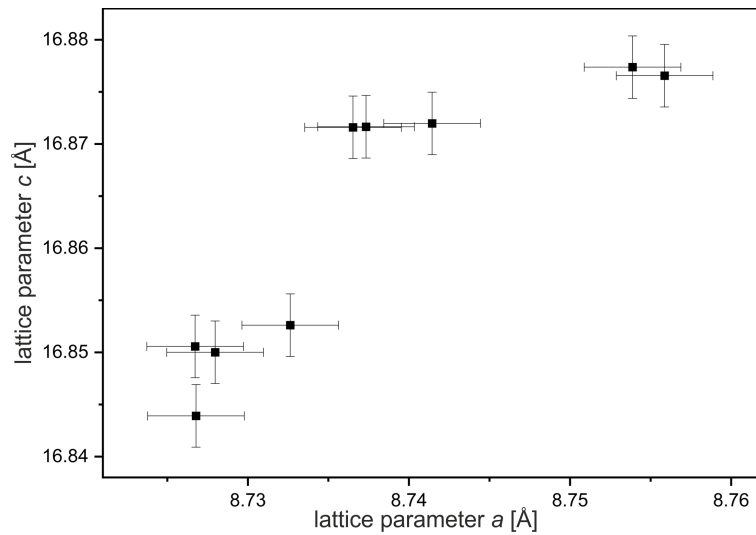


Figure 3.47: Lattice parameters  $a$  and  $c$  of  $\text{Pd}_{20}\text{Sn}_{13-x}\text{Ga}_x$  plotted against each other. The values are gained from Rietveld refinement of XPD measurements of the samples.

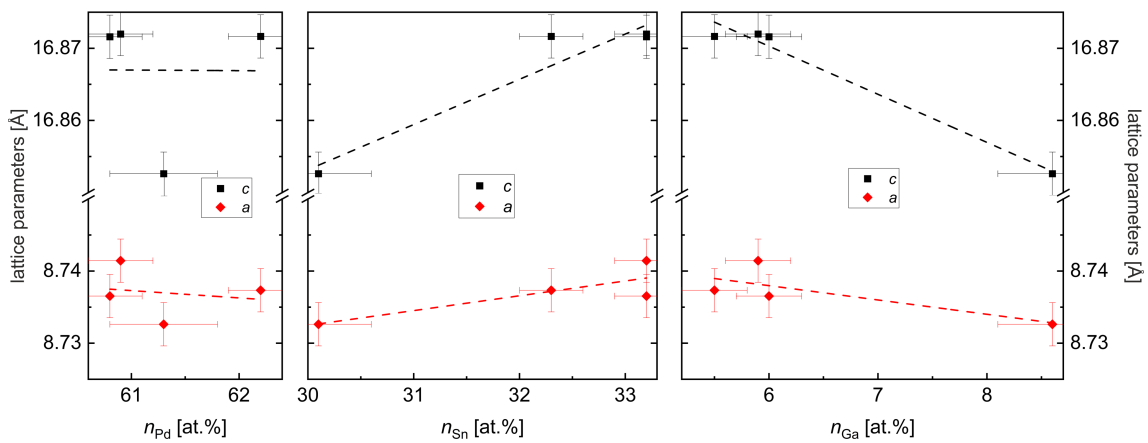


Figure 3.48: Lattice parameters  $a$  and  $c$  of  $\text{Pd}_{20}\text{Sn}_{13-x}\text{Ga}_x$ , plotted against the chemical composition, measured by WDX.

## 3.2 Single crystal growth

### 3.2.1 Single crystal growth of $\text{Ga}_{1-x}\text{Sn}_x\text{Pd}_2$

#### 3.2.1.1 Single crystal growth

During the experimental determination of the seeding temperature, as described in section 2.2.3, supercooling of typically 20 K and sometimes up to 45 K could be observed. The search for the seeding temperature proved to be challenging, as crystallites were not always visible and only small tips could be observed at the melt surface. It was found that the behaviour of the few oxide flakes, floating on the surface, was a good indicator for nucleation: When supercooling collapsed, they either suddenly moved to the outer part of the melt surface, or are fixed on the surface also when ACRT is applied. To find the seeding temperature slow heating until the last crystal is dissolved is the common procedure. However, strong supercooling did not allow slow heating rates, because otherwise hours or even days would be necessary to reach the seeding temperature. For this reason, after the supercooling had collapsed, heating was initially carried out at faster rates of up to 20 K/h and the ramp of the heating rate was reduced in stages until the usual rate of 2 K/h was finally achieved. If the heating ramp was reduced too early, the search went on for hours, or if it was reduced too late, the correct temperature for seeding was missed. During heating in stages shortly before the seeding temperature was reached, the few oxide flakes began to move freely on the surface. Furthermore, in the ACRT mode, small crystallites started to appear as tips on the surface. Both cases did not always occur, and therefore the seeding temperature was sometimes chosen too low. Since overheating was carried out between the search for the liquidus temperature and the actual seeding, the problem is minor because any spontaneously formed nuclei in the melt dissolve. If seeding is carried out with too low temperatures, the crystal starts to grow fast (mostly laterally). In such cases, the setpoint (SP) temperature was corrected manually in small steps, until the crystal was dissolved to the diameter of the seed tip.

The pre-treatment of the starting materials proved to be successful, allowing seeding on a shiny metallic surface without an oxide layer despite few oxide flakes. The metallic melts always snapped to the seed, wetting its tip properly (fig. 3.50, a). Compared to other intermetallic phases, the crystal growth of  $\text{Ga}_{1-x}\text{Sn}_x\text{Pd}_2$  behaved relatively stable. In accordance, reactions to changes of the  $T$  program were slow and late to be seen, which turned out to be a disadvantage. Especially during the first millimeters too high or too low temperatures could be noticed late. Usually a deviation of the equilibrium temperature leads either to visible lateral growth or a visible dissolution of the seed. In both cases, it can be reacted early enough. In the case of  $\text{Ga}_{1-x}\text{Sn}_x\text{Pd}_2$ , if the temperatures were too high, the separation between the crystal and the seed occurred after hours and unexpectedly, although a stable impression was obtained. A dissolution of the seed could never be observed and in some cases the separation between seed and crystal occurred during pulling even though in earlier stages the diameter of the seed had already increased slightly (fig. 3.50, c). This led to a time loss of days. If the temperature was too low, invisible lateral growth occurred. It is unclear whether the reflection of the crystal and the melt were identical so that the crystal could not be seen, or whether the melt wetted the crystal's surface in the initial stages. The lateral

growth only became apparent after some time, when tips (edges of facets or ridges) were visible in the melt, a few millimeters away from the seed or after the first few micrometers of pulling (fig. 3.50, b). In such cases, the crystal had to be dissolved back to an adequate diameter. As the growth proceeded, the optical conditions remained difficult and the phase boundary, the meniscus and the development of the diameter remained practically invisible (figs. 3.50, d–h). Therefore, it was difficult to get the crystal into the desired cylindrical shape, because diameter changes or the effects of temperature program adaptations became noticeable hours to days later. The use of shortpass filters improved the optical conditions at temperatures around 1050–1200°C significantly (figs. 3.50, h, i). Furthermore, the experience gained from previous experiments played an increasingly important role in successful crystal shapes of later experiments. The rotation of crystal and melt was kept low during the seeding process (crystal: 10 rpm, melt: counter rotating 5 rpm) and after equilibrium was established and growth was started, the rotation rates were increased to 20–30 rpm for the crystal and 8 rpm for the crucible.

The very first crystal (QX649-II,  $x = 0.1$ ) has trapped mother liquid inclusions already within the first millimeters (fig. 3.51) at a pulling rate of 100  $\mu\text{m}/\text{h}$ . Therefore, in later experiments the growth was started with 75  $\mu\text{m}/\text{h}$  and the pulling rates were decreased early in all later experiments after few millimeters and especially with increasing diameter. Typically, the pulling rates were reduced below 50  $\mu\text{m}/\text{h}$  after the diameter reached values of 8–10 mm and large parts of the growth process took place at pulling rates of 25  $\mu\text{m}/\text{h}$  (fig. 3.49) to avoid the trapping of mother liquid inclusions. Accordingly, a typical growth experiment lasted around 3 weeks. The cooling ramps were regularly corrected and adjusted in accordance with the developing diameter and adapted to changed pulling rates (visible in fig. 3.49, b). The cooling ramps reached maximum values of up to 0.4 K/h in the later growth process. The target setpoint (TSP) temperatures were reduced in a total range of approximately 100 K during a typical growth experiment. The real temperatures depend on factors, such as crystal shape (influencing the heat radiation from the crystal) and crystal length (with increasing crystal length and decreasing melt level the thermal transport changes significantly), and remain unknown, since the thermocouple is placed next to the heater. The end of the experiments was initiated by continuing the pulling and either keeping a constant SP temperature or continuing a constant ramp. Both methods (the first faster) lead to the temperature being higher than the liquidus temperature, causing first a diameter reduction and then a separation of the crystal from the melt. It was observed that the separation of melt and crystal always took place on a large area and that the diameter decrease was minor (fig. 3.56).



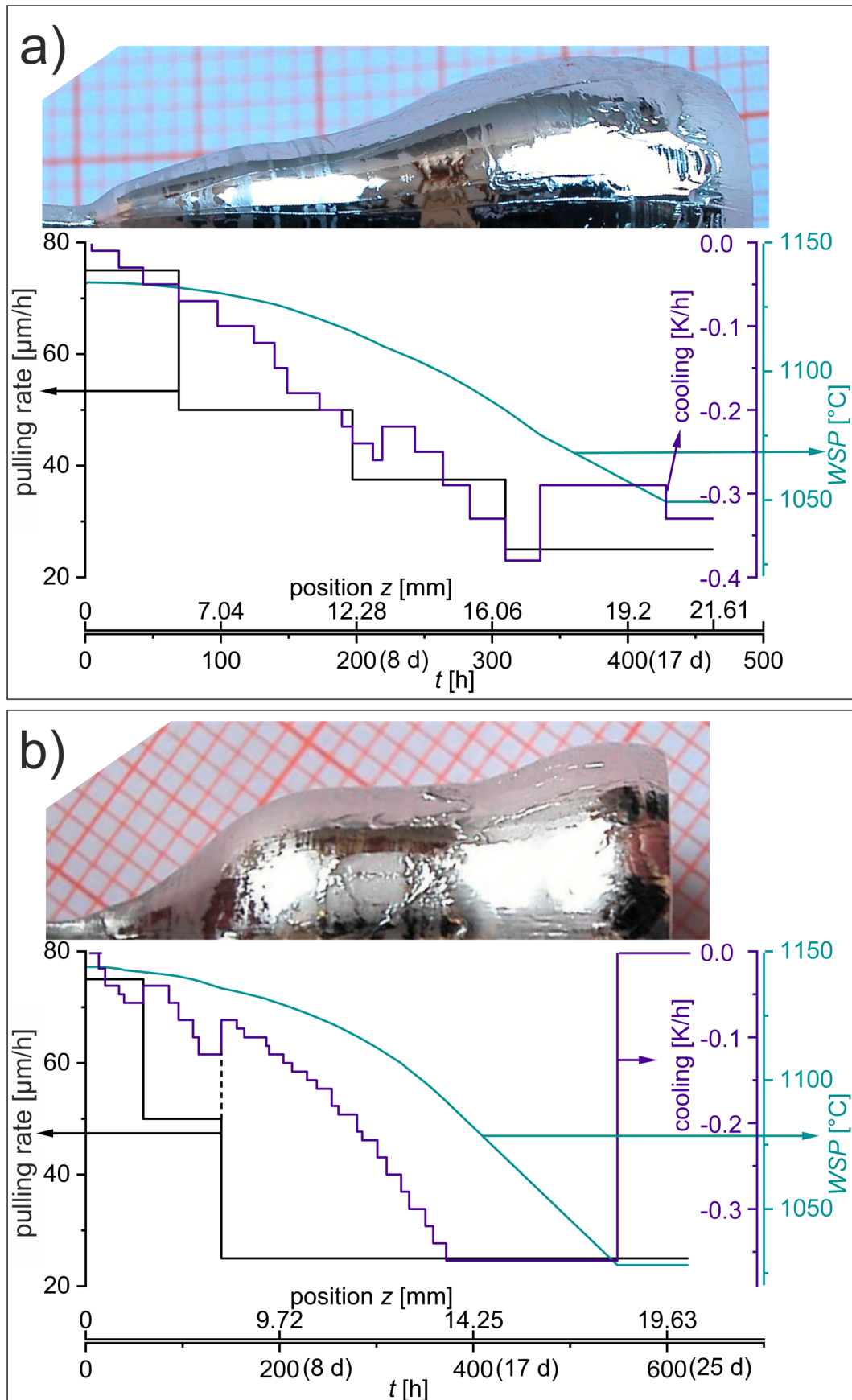


Figure 3.49: Growth parameters of a) QX703 and b) QX684. The pulling rates do not correspond to the growth rate, since the melt level decreases during growth. The working setpoint temperature (WSP) shows the temperature, measured by the thermocouple next to the heater.

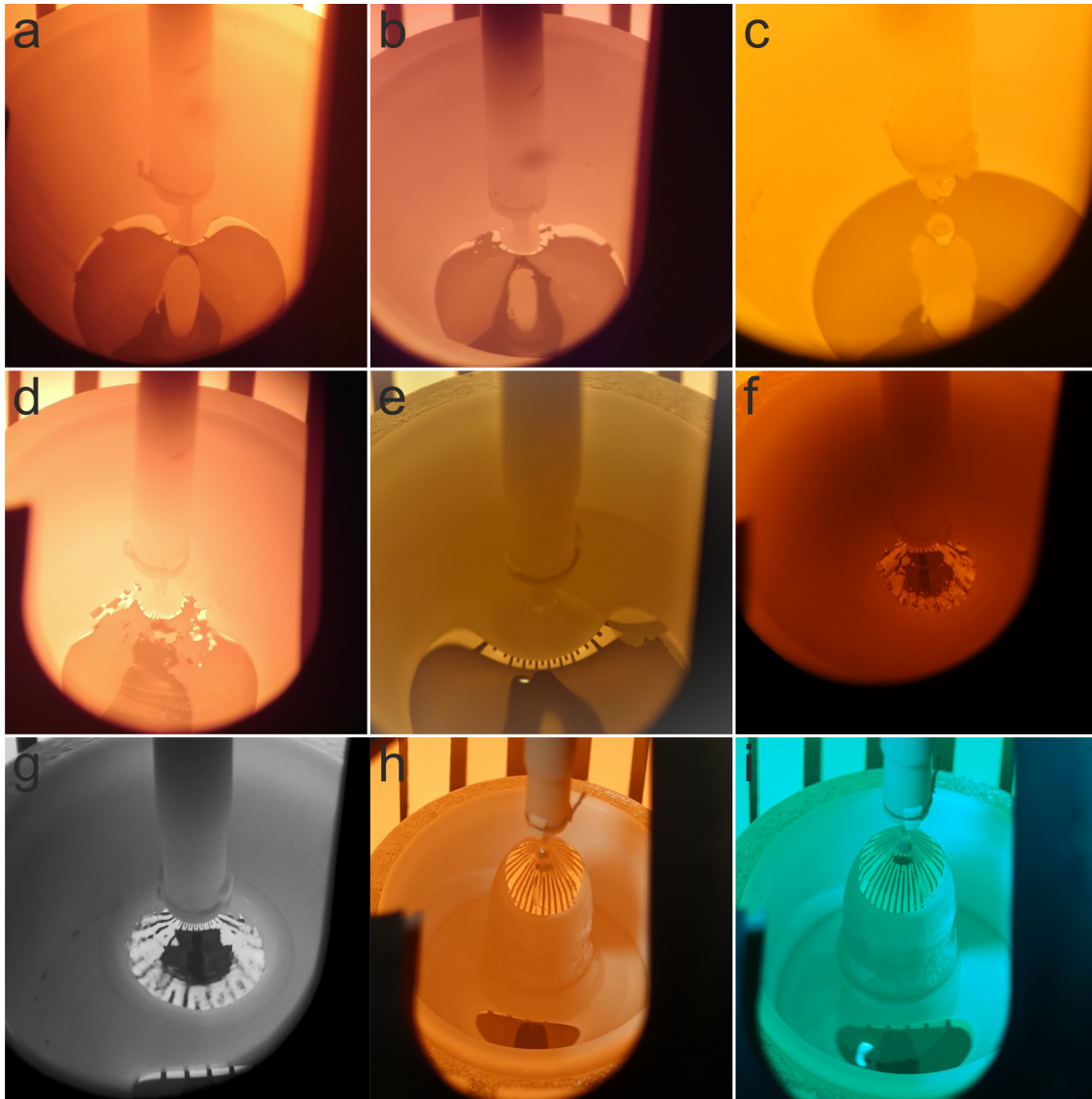


Figure 3.50: Typical situations occurring during crystal growth. a) QX674, seed, directly after wetting. b) QX674, first small tips around the seed on the melt indicate that the crystal is already growing laterally. c) QX649-III, after the first 75  $\mu\text{m}$  of growth, the crystal was separated from the melt because the growth temperature was too high. d) QX674, shiny tips show that the crystal is growing. In this case there is no visible contrast between melt and crystal. e) QX661, difficult visual conditions few days after seeding. f) QX667, after a few millimeters of growth, it becomes increasingly difficult to evaluate the development of the phase boundary. g) QX667, first attempts to make the phase boundary more visible were black and white images with increased contrast. An improvement compared to fig. f can be seen, but a photo must be taken for each insight. h) QX715. i) also QX715, for comparison a shortpass filter (in this case 525 nm cut-off wavelength) is placed in front of the viewport and shows a significant improvement in the optical conditions. General notes: The stripes on the crystals are the reflections of the glowing meander heater on the shiny metallic surface. In the lower part, the crystals seem to shine less because the ceramic crucible is reflected on the crystal. The same holds for the melt where only one dark spot shows the metallic shiny surface. The dark spot is the reflection of the hole in the heat shield where the seed holder is guided through on the curved melt surface. In c) the reflection with the seed holder is visible without curvature.

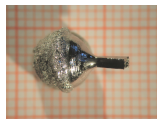

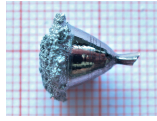





Crystal number		$m$ [g]	$x$	$x_L,$ $y_L$	$k^*$ (FTF)	Pulling direction	Growth interface
QX649-II		1.6	0.0757(13)	0.1, 61	0.76	[001]	-
QX649-III		6.7	0.0759(10)	0.1, 61	0.76	[001]	centre: concave, outer rim: convex
QX661		2.8	0.170(3)	0.2 <sup>†</sup> , 61 <sup>†</sup>	0.85 <sup>†</sup>	[001]	curved
QX667		11.7	0.1758(14)	0.2, 61	0.88	[010]	centre: concave
QX674		14.2	0.285(2)	0.3, 61.5	0.95	[010]	convex
QX703		14.1	0.290(3)	0.3, 61.5	0.97	[010]	concave
QX715		15.0	-	0.3, 61.5	-	[100]	concave
QX684		17.8	0.397(3)	0.4, 61.5	0.99	[010]	concave

Table 3.13: Czochralski-grown crystals. Larger images are shown in the appendix (figs. A.20-A.27). The Sn content,  $x$  in  $\text{Ga}_{1-x}\text{Sn}_x\text{Pd}_2$ , was measured by WDX. The value is always the average of at least 10 measuring points. The error is the standard deviation of these points. †) Because the melt of QX661 was refilled a low uncertainty for  $x_L$  has to be taken into account, which also affects the pseudobinary segregation coefficient,  $k^* = \frac{x}{x_L}$ .  $k^*$  was calculated from measurements at the first-to-freeze (FTF) parts of the crystals.  $x_L$  and  $y_L$  relate to the melt description,  $(\text{Ga}_{1-x_L}\text{Sn}_{x_L})_{100-y_L}\text{Pd}_{y_L}$ .

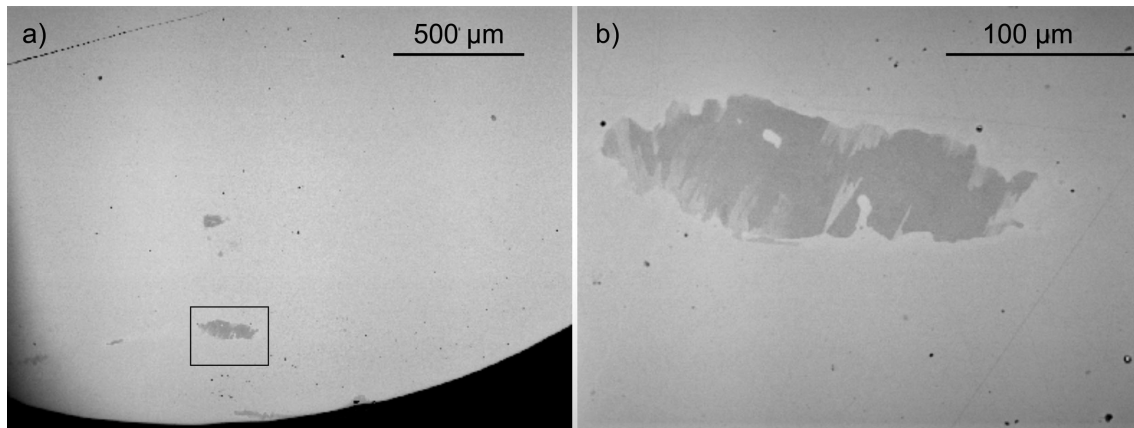


Figure 3.51: a) BSE images of a (001) slice (perpendicular to the growth direction [001]) of the very first grown single crystal QX649-II ( $x = 0.1$ ). The small box is enlarged in b) The rim of the inclusion is slightly brighter than the surrounding crystal due to Sn enrichment in the trapped melt and ongoing growth. The fine needles are  $\text{Ga}_{3-x}\text{Sn}_x\text{Pd}_5$ .

### 3.2.1.2 Basic investigations on the Czochralski-grown single crystals

Single crystals with the compositions of  $x = 0.1, 0.2, 0.3$  and  $0.4$  were achieved and their properties are listed in tab. 3.13. Systematic scans with a Laue camera revealed that all crystals are oriented like the seed crystal. Sn substitution for Ga slowly increases along the axial direction as measured by WDX on polished longitudinal cuts (fig. 3.53). Within the error of the microprobe no larger radial changes of the Sn content,  $x$ , could be measured. All crystals (except the first attempt, QX649-II, fig. 3.51) are inclusion-free.

Crystals pulled in [010] show an almost circular cross section, while crystals grown in [001] partly exhibit an elliptic cross section. QX649-III ( $x = 0.1$ ) has the most elliptic cross section with a ratio of 1 : 1.1 ([100] : [010]). The crystals show in most cases no facets. Only in the case of the crystal QX684 ( $x = 0.4$ , pulled in [010]) clear facets are visible. They are a pair of two appearing four times according to the orthorhombic symmetry (fig. 3.52). They have been indexed with a reflection goniometer being the {101} and the {102} facets. Additionally, a fine ridge can be observed along the whole length of the crystal facing towards the  $\langle 100 \rangle$  directions. Slight traces of facets and ridges are also visible on the crystal QX703 ( $x = 0.3$ , pulled in [010]).



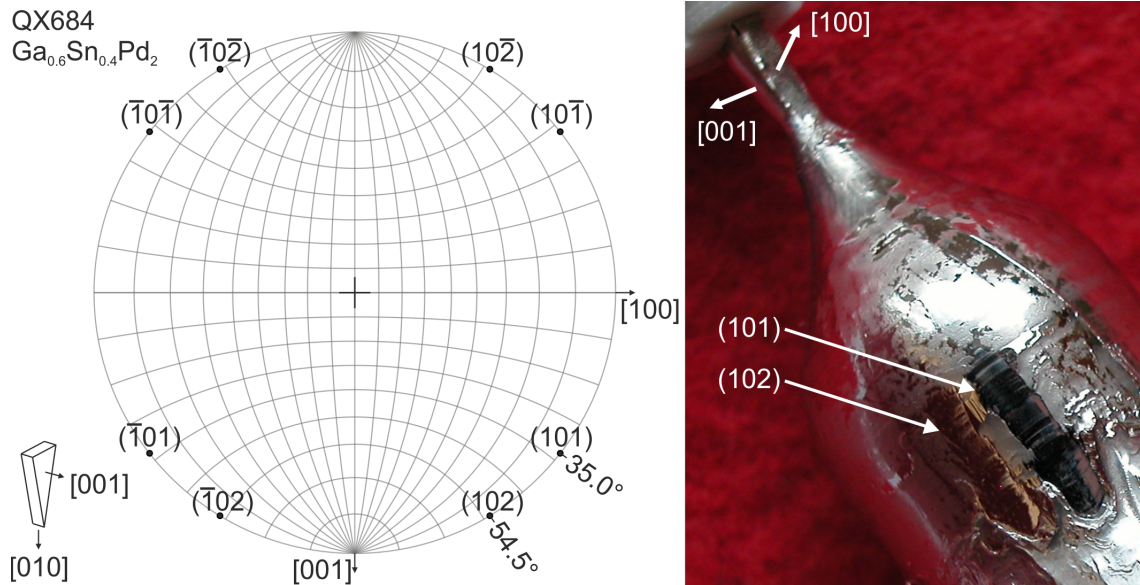


Figure 3.52: Stereographic projection and image of the  $\{101\}$  and the  $\{102\}$  facets of the crystal QX684. On the upper right part of the crystal a growth ridge is visible as a thin line.

Several crystals show brightness contrasts in BSE images of single-crystalline slabs. Fig. 3.56, d shows lines in the crystal which separate areas of different brightnesses. WDX line measurements across these lines do not indicate a chemical gradient or difference, why the only remaining reason can be an orientation contrast. Further investigations by Laue scanning, rocking curve analysis, EBSD and XRT are presented in later sections.

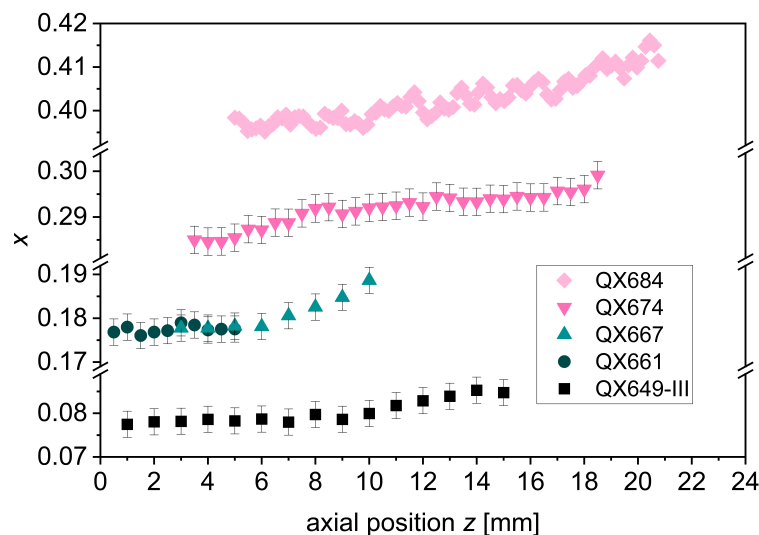


Figure 3.53: WDX measurements along the axis of different crystals.  $z$  describes the distance from the seed or the first-to-freeze part, respectively. The error bar for every point is the standard deviation of at least 10 measurement points. The QX684 curve is a line stage measurement, smoothed with a Savitzky–Golay filter.

In fig. 3.54 the segregation of Sn, measured in the first-to-freeze part of the

crystals is shown and compared to that of the pre-experiments. The pseudobinary segregation coefficient  $k^*$  seems to behave strictly linear for Czochralski experiments in the range of  $0.1 \leq x_L \leq 0.4$ .  $k^*$  rises from lower to higher  $x_L$  and is almost unity, for crystals with  $x_L = 0.4$ .  $k^*$  of the pre-experiments has a higher experimental error, which is why the Czochralski experiments, grown under near-equilibrium conditions and easier and more precise to measure, are considered more meaningful.

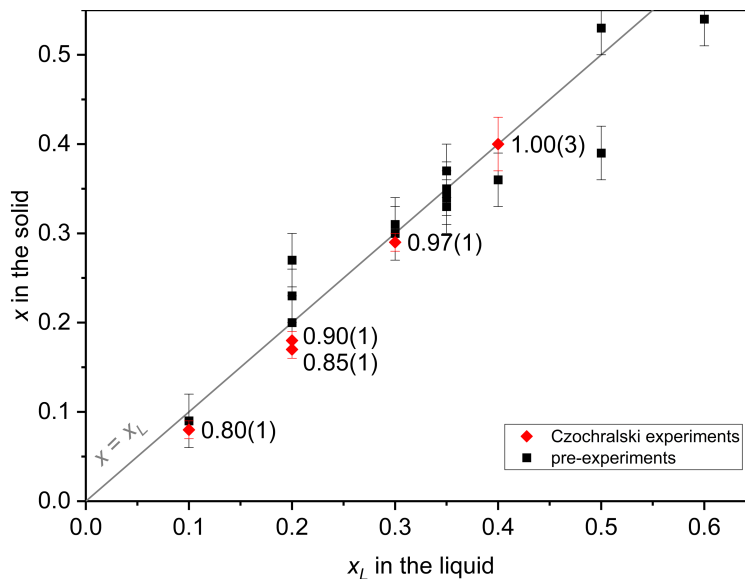


Figure 3.54: The Sn content in the crystal  $x$  plotted against the Sn content in the melt  $x_L$  as in fig. 3.36, but extended by the data of Czochralski-grown crystals. The grey line is unity and the values are the pseudobinary segregation coefficients  $k^* = \frac{x}{x_L}$ .  $x$  was measured by ICP-OES or WDX.

Fig. 3.55 shows the relation between the measured Pd contents  $y$  and the Sn contents,  $x$ , in the Czochralski-grown crystals, compared to the same relations in primarily grown grains of  $\text{Ga}_{1-x}\text{Sn}_x\text{Pd}_2$  in the pre-experiments. The positive linear correlation recognisable in the pre-experiments can also be found in the Czochralski-grown crystals. However, the Pd content in Czochralski grown crystals is generally higher compared to that of the pre-experiments. Since the initial Pd contents  $y_L$  have been chosen higher in the Czochralski experiments, it can be concluded that higher initial Pd contents in the melt lead to higher Pd contents in the crystals.

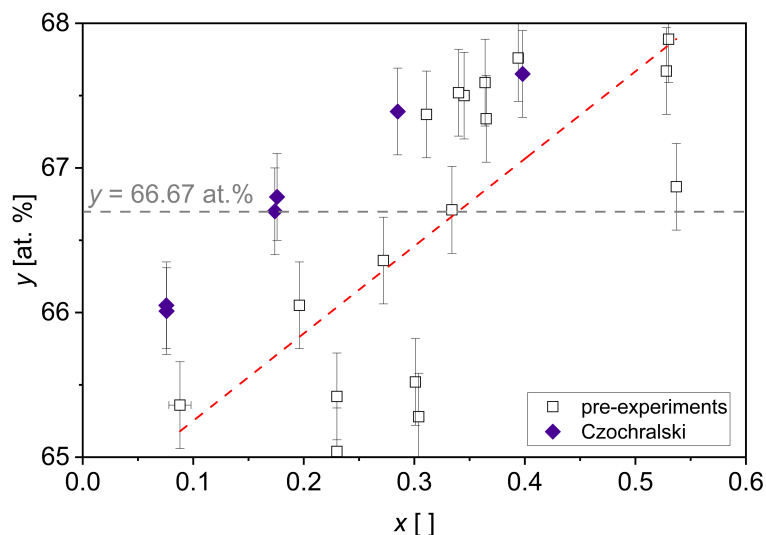


Figure 3.55: Relation between the measured Pd contents,  $y$ , and the Sn contents,  $x$ , in different crystals. The figure is similar to fig. 3.39, but extended by the measurement data from the Czochralski-grown crystals.

The growth interfaces are different, concave or convex or a combination of both (fig. 3.56). Their radius is determined graphically by analysing BSE images of longitudinal cuts of the crystals. The surface of a sphere was used to fit the growth interface of the crystals. The radius is only an approximation since the growth interface always deviates slightly from a spherical cap. Since some crystal slabs are not cut out of the centre of the crystal, a correction of the determined radius is applied. A dependence of the shape of the growth interface from the crystal's length, its total mass, its pulling direction, its pulling rate, the rotation speed and  $x_0$  or  $y_0$  was not found. Crystals with a larger diameter tend to have an increased tendency to a concave growth interface. Likely, the actual diameter development is related to the growth interface: Crystals separated from the melt in a state of increasing diameter always have a convex phase boundary (figs. 3.56, b, d), while crystals separated in the state of decreasing diameter have a concave interface (fig. 3.56, a, c, e). Furthermore, there are cases, where the interface is constructed of an convex outer part and a concave inner part (fig. 3.56, a) as well as cases of curved interfaces combining convex and concave elements (fig. 3.56, b). It can also be seen that cracks reach partially from the solidified residual melt sticking to the crystal up to 2 mm into the crystal (figs. 3.56, d, e, and 3.57). These images also show the presence of small pits, sometimes accompanied by small outgrowths, in the solidified growth interface. The BSE images show that lines with brightness contrasts, visible in the crystals, frequently are accompanied by these pits (fig. 3.57). These lines visible in the BSE images are further addressed in the sections 3.3.3-3.4.

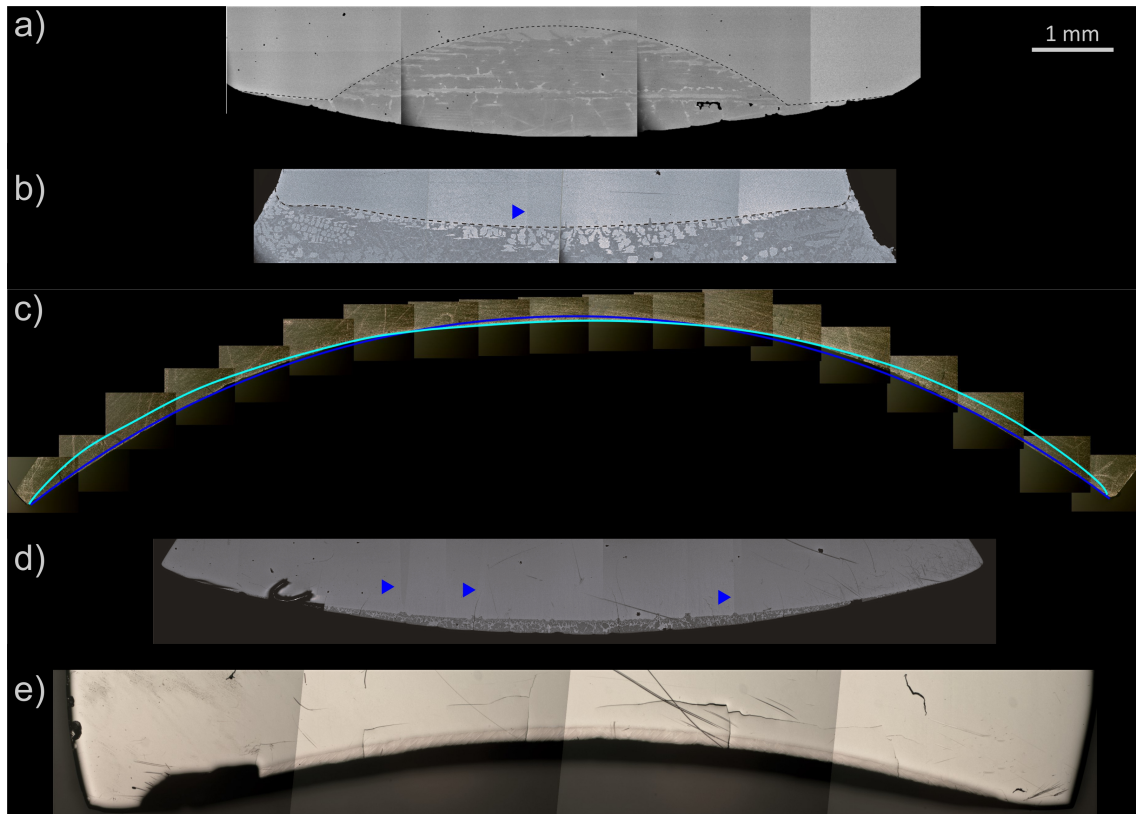


Figure 3.56: Composed images of the growth interfaces of the crystals a) QX649-III ( $x = 0.1$ , (010) slice), b) QX661 ( $x = 0.2$ , (010) slice), c) QX667 ( $x = 0.2$ , (001) slice), d) QX674 ( $x = 0.3$ , (100) slice) and e) QX684 ( $x = 0.4$ , (100) slice). a), b) and d) are BSE images, c) and e) are incident light microscope images. All crystals have a multi phase region attached to the growth interface, which is caused by residual melt, sticking to the crystal after separating it from the melt. e) Cracks starting from the multiphase area may reach 1–2 mm into the crystal (On the left side a piece broke off, due to these cracks). Lines in the crystals where a brightness contrast is visible in the BSE images, are marked with blue arrows. Lines that are not marked with blue arrows result from the assembling of different images.



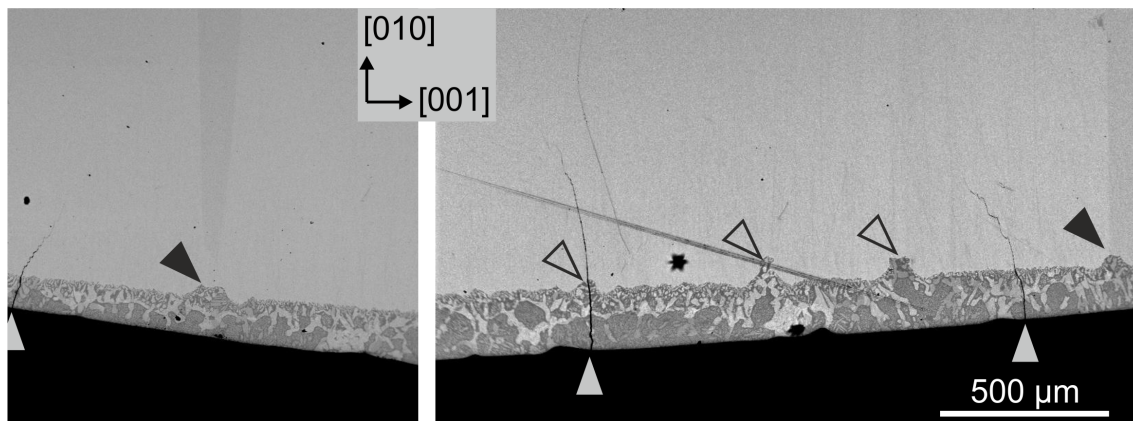


Figure 3.57: More detailed view of the pits and outgrowths in fig 3.56, d. The black arrows mark positions, where lines with brightness contrasts in BSE images clearly end in a pit in the growth interface. The black hollow arrows indicate further pits in the growth interface. The grey arrows mark cracks that reach from the polycrystalline residual melt up to 500  $\mu\text{m}$  into the crystal.

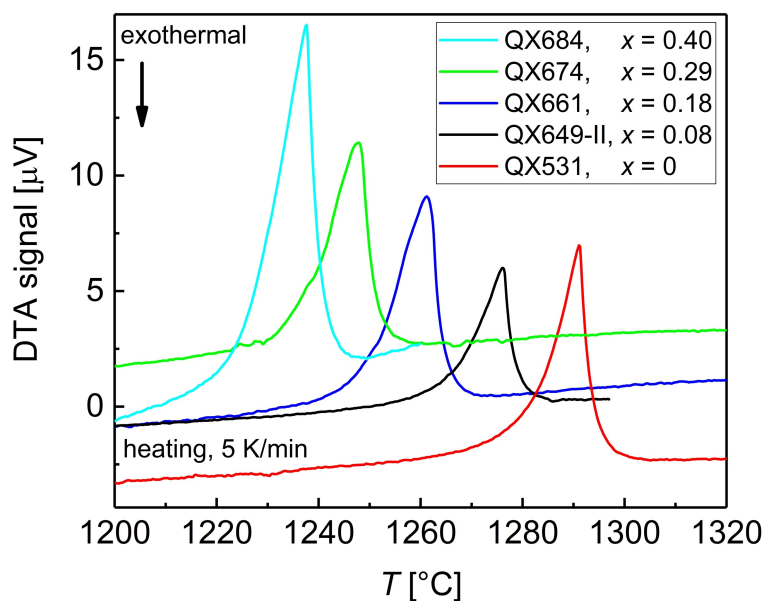


Figure 3.58: DTA heating curves of single-crystalline pieces with different Sn contents,  $x$ , grown from  $x_L = 0.1, 0.2, 0.3$  and  $0.4$  and almost constant Pd contents,  $61 \leq y_L \leq 61.5$  <sup>28</sup>.

DTA measurements with pieces of crystals with different Sn contents,  $x$ , show that the solidus temperatures decrease with increasing  $x$  (fig. 3.58). The intensities of the signals have no meaning here, since they depend on the masses of the measured samples.

<sup>28</sup>According to the description  $(\text{Ga}_{1-x_L}\text{Sn}_{x_L})_{100-y_L}\text{Pd}_{y_L}$ .

### 3.2.2 Single crystal growth of $\text{Ga}_{1-x}\text{Sn}_x\text{Pd}$

The crystal growth of  $\text{Ga}_{1-x}\text{Sn}_x\text{Pd}$  has already been described in detail [26, 27]. However, a further experiment was conducted after these studies and is presented in the following, in order to display the information, that was additionally gained. While the earlier described experiments had (Ga,Sn)-rich compositions ( $(\text{Ga},\text{Sn})_{55}\text{Pd}_{45}$ ) the experiment QX676 contained  $(\text{Ga}_{0.75}\text{Sn}_{0.25})_{51}\text{Pd}_{49}$  and accordingly was located closer to an almost congruent composition. The aim was to achieve a higher final crystal mass and to reduce the typical problems of growth from HT solution, such as constitutional supercooling. However, while the crystal growth with higher (Ga,Sn) contents proved to be as usual, the growth with lower Pd content turned out to be extremely tricky. Achieving an equilibrium situation, i.e. the seed being wetted by the melt without pulling for longer terms, could be only achieved after several attempts. Even though several times after seeding a diameter increase could be observed, a separation of the crystal from the melt occurred shortly after. The diameter increase was not a slow radial growth as known from earlier growth experiments of this system, but a fast radial growth of needles in a  $120^\circ$  angle, matching the threefold symmetry of the [111] pulling axis of the seed crystal with cubic space group  $P2_13$ . The needles grew to a length of 5–6 mm within a time scale of several minutes to few hours. However, when slightly increasing the temperatures to solve back in order to achieve a uniform diameter, the needles were relatively stable while the basis of the crystal already started to dissolve. While the dendrites were initially stable and almost unaffected at the beginning of the dissolution process, there was always a turning point at which the needles dissolved within minutes. As a result of the sudden dissolution, the separation of the crystal from melt took place. After several intervals of fast dendritic, lateral growth and subsequent separation of the seed from the melt while trying to get control of the diameter, the experiment was cancelled. A new approach with (Ga,Sn)-richer solution ( $(\text{Ga}_{0.75}\text{Sn}_{0.25})_{55}\text{Pd}_{45}$ ) resulted in the as-usual crystal growth procedure, known from earlier experiments and other intermetallic phases.

### 3.3 X-ray investigations on Czochralski-grown $\text{Ga}_{1-x}\text{Sn}_x\text{Pd}_2$

#### 3.3.1 Non-annealed powders

In section 2.4.1.1 the necessity of annealing the samples due to strong peak broadening has been stated. Rietveld refinement lead to poor fits why several models for refining strain and grain size were tested. The peak shape of the powders tended to be rather Lorentzian than Gaussian (with the parameter  $Shape1 \hat{=} \eta^\dagger$  approaching 1, using a pseudo-Voigt function in *Fullprof*). Size broadening models showed better fits than strain broadening models. Since no model could describe the powder as a homogenous single-phase material, a combination of two fractions, one with size broadening and one without size broadening (i.e. one nano-sized and one micro-sized fraction) proved to be the most appropriate approach. The best fitting model for the nano-sized fraction, proved to be the *Lorentzian isotropic size model* of the *Fullprof* package. Tab. 3.14 shows the results. The refinement of both fractions independently results in a fraction of 91 wt.% for the nano-sized phase and a particle size of 26 nm. Le Bail fitting results in an intermediate grain size of 23 nm. Due to complicated preferred orientation a Le Bail fit resulted in the best agreement factors by far. Rietveld refinement with preferred orientation was carried out, using the *March-Dollase Multi-axial function*. The most pronounced texture problems were peaks of the [010] zone, i.e. the  $h0l$  peaks. These showed increased intensities while the  $0k0$  peaks showed missing intensities. From that needle-like breaking behaviour perpendicular to the [010] direction can be concluded. Furthermore, the peaks 100 and 210 (and multiples) showed a platy-like habitus. Further texture effects seem to be present but could not be clearly identified due to their complicated manner.

Refinement	$R_p, R_{wp}, R_{exp}, \chi^2$	nano-sized fraction	size
Le Bail	7.06, 7.64, 6.51, 1.38.	*	23 nm
Rietveld	12.8, 14.7, 6.61, 4.96	91 m.%	26 nm

Table 3.14: Parameters of the different refinements. \*The fraction is not available in a Le Bail fit since it is calculated from the intensities.

<sup>†</sup> $pV(x) = \eta L(x) + (1 - \eta)G(x)$  (section 2.4.1.1, eq. 2.3).

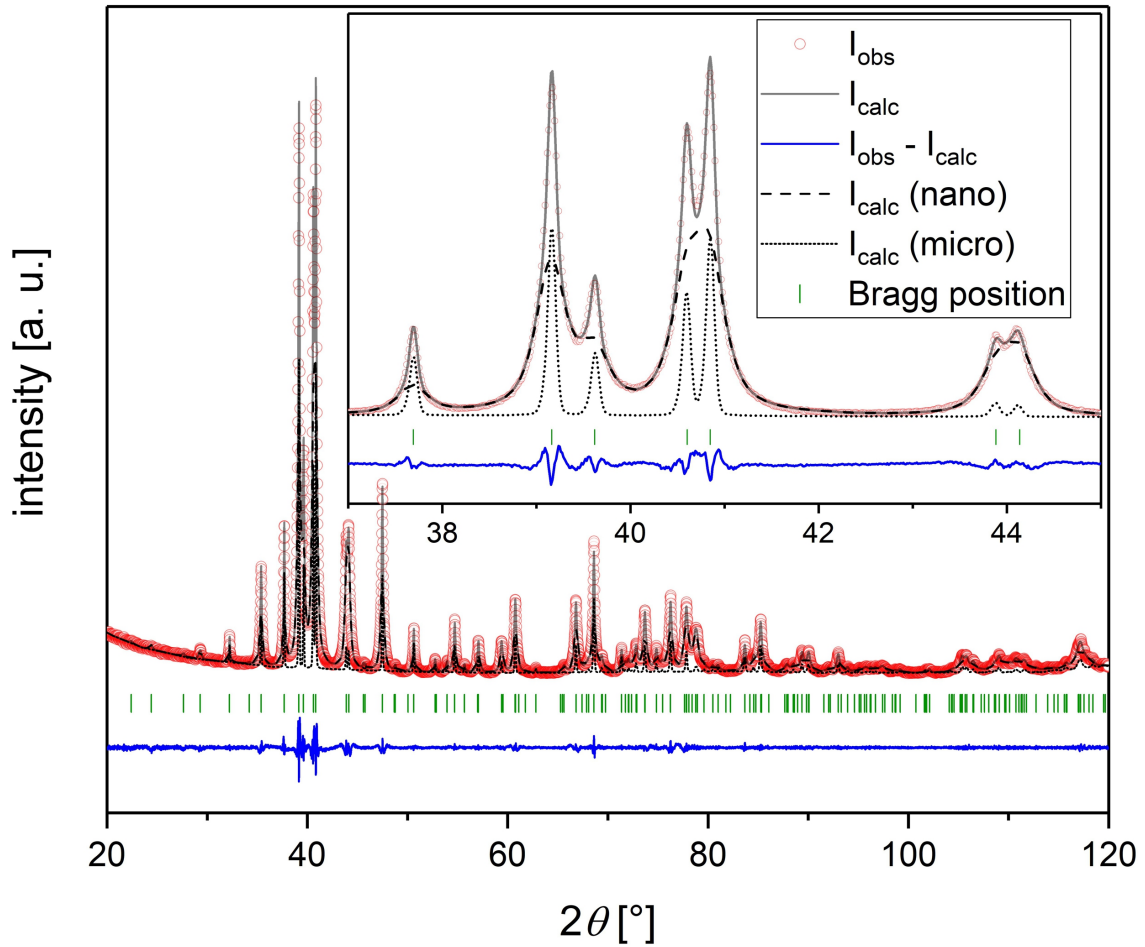


Figure 3.59: Le Bail fit of a non-annealed powder of the crystal QX674 ( $x = 0.3$ ). The red points are the measured points, the grey line is the overall calculated pattern, the blue line is the difference of the aforementioned patterns, the dashed line is the fraction of the powder, affected by size broadening. The dotted line is the fraction without size broadening and the green stripes mark the Bragg positions. Measured with  $\text{Cu-K}\alpha_1$  radiation. Agreement values:  $R_p$ : 7.06,  $R_{wp}$ : 7.64,  $R_{exp}$ : 6.51,  $\chi^2$ : 1.38.

### 3.3.2 Annealed powders

Annealed powders of single crystals with different compositions were measured by XPD. Cut crystal pieces were milled, sieved and annealed as described in section 2.4.1.1. The measurements were carried out with internal  $\text{LaB}_6$  standard (NIST660a) and were fitted with the Le Bail method in the *Fullprof* package for accurate lattice parameters. The fitted lattice parameters and published data of  $\text{GaPd}_2$  [36] and  $\text{SnPd}_2$  [19] then were plotted against the compositions measured by EPMA, i.e. the Sn content,  $x$ , in  $\text{Ga}_{1-x}\text{Sn}_x\text{Pd}_2$ . As shown in fig. 3.53, the crystals have a Sn gradient along their growth axes. Accordingly, pieces for XPD lattice parameter analysis need to be cut as small as possible and with a minimal extension in the direction of the growth axis. The lattice parameters increasing with increasing  $x$  in  $\text{Ga}_{1-x}\text{Sn}_x\text{Pd}_2$  does not meet Vegard's law [52] but a second order polynomial gives a good fit (fig. 3.60). The same holds for the unit cell volume (fig. 3.61). The

resulting equations turned out to be a powerful tool to estimate the Sn content of  $\text{Ga}_{1-x}\text{Sn}_x\text{Pd}_2$  in multi-phase samples where the compositions could not be measured by WDX, e.g. because grain sizes are smaller than the size of the excitation volume of the electron beam of the microprobe.

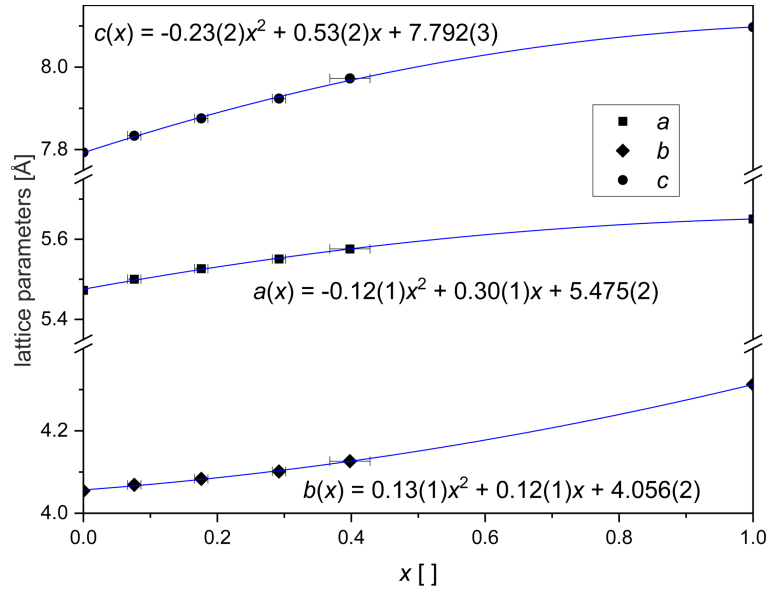


Figure 3.60: Le Bail-fitted lattice parameters of  $\text{Ga}_{1-x}\text{Sn}_x\text{Pd}_2$  and literature values for  $\text{GaPd}_2$  [36] and  $\text{SnPd}_2$  [19], plotted against  $x$ . The errors are within the size of the data points. The values of the lattice parameters and the agreement values are listed in tab. 3.15.  $x$  was measured with EPMA (WDX) or ICP-OES.

experiment	$x$	$a[\text{\AA}]$	$b[\text{\AA}]$	$c[\text{\AA}]$	$R_P, R_{WP}, R_{exp}, \chi^2$
QX649-II	0.08(1)	5.501(1)	4.068(1)	7.831(1)	9.22, 10.1, 6.56, 2.39
QX661	0.18(1)	5.527(1)	4.083(1)	7.876(1)	10.4, 11.2, 6.16, 3.29
QX674	0.29(1)	5.551(1)	4.102(1)	7.924(1)	8.85, 10.4, 4.85, 4.63
QX684	0.4(1)	5.576(1)	4.126(1)	7.973(1)	9.59, 11.0, 6.26, 3.07

Table 3.15: Lattice parameters of phase-pure powders from single crystals. The powders are measured with  $\text{Cu-K}\alpha_1$  radiation in Bragg-Brentano geometry with internal  $\text{LaB}_6$  standard (NIST660a).

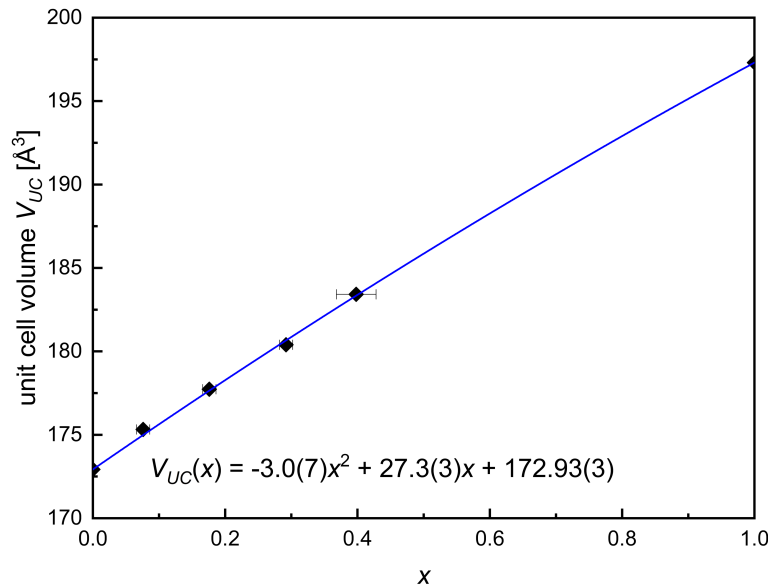


Figure 3.61: Unit cell volume  $V_{UC}$  plotted against  $x$  in  $\text{Ga}_{1-x}\text{Sn}_x\text{Pd}_2$ . Values for the calculation of the unit cell volumes are taken from tab. 3.15 and from literature for  $\text{GaPd}_2$  [36] and  $\text{SnPd}_2$  [19]. The errors are within the size of the data points.  $x$  was measured with EPMA (WDX) or ICP-OES.

### 3.3.3 Laue scans

Visible lines and contrasts on a (210) single crystalline surface in the stereo microscope (fig. 3.62) showed that the Czochralski-grown crystals contain grain boundaries. Those have also been investigated in BSE images of other crystals and on slices of different crystallographic orientations as shown in the figs. 3.56, b, d, and 3.57. First investigations with the Laue camera revealed that no larger tilts between the different measured patterns in the crystal occur and single-crystallinity is present. Accordingly, subgrain boundaries, i.e. low angle grain boundaries (LAGB), are visible. More systematic Laue scans on a raster (fig. 3.63) show the tilt and the rotation of each scanned position on the above-mentioned (210) surface. It is visible that there are numerous tilts and rotations between the Laue patterns at the different measured positions. All tilts are below  $1^\circ$  with the majority even below  $0.5^\circ$  with respect to each other. On some positions two Laue patterns, oriented differently have been measured in a single scan. This is expressed by two crosses on one scan position in fig. 3.63 and an example is shown in fig. 3.64.

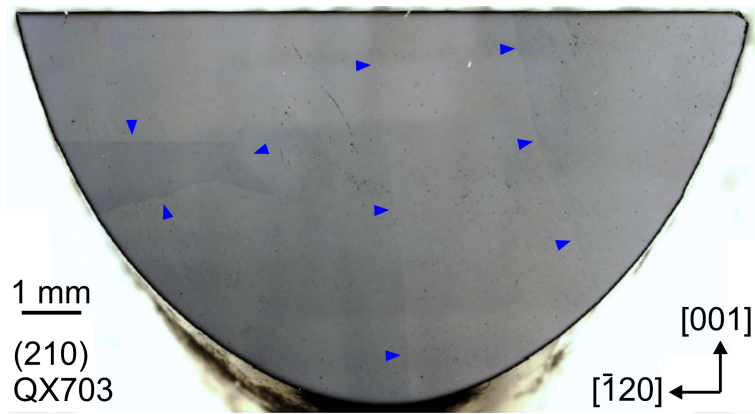


Figure 3.62: Stereomicroscopic image captured with a digital camera of a (210) single crystalline surface of QX703 ( $\text{Ga}_{0.7}\text{Sn}_{0.3}\text{Pd}_2$ ). The blue arrows mark subgrain boundaries visible on the surface.

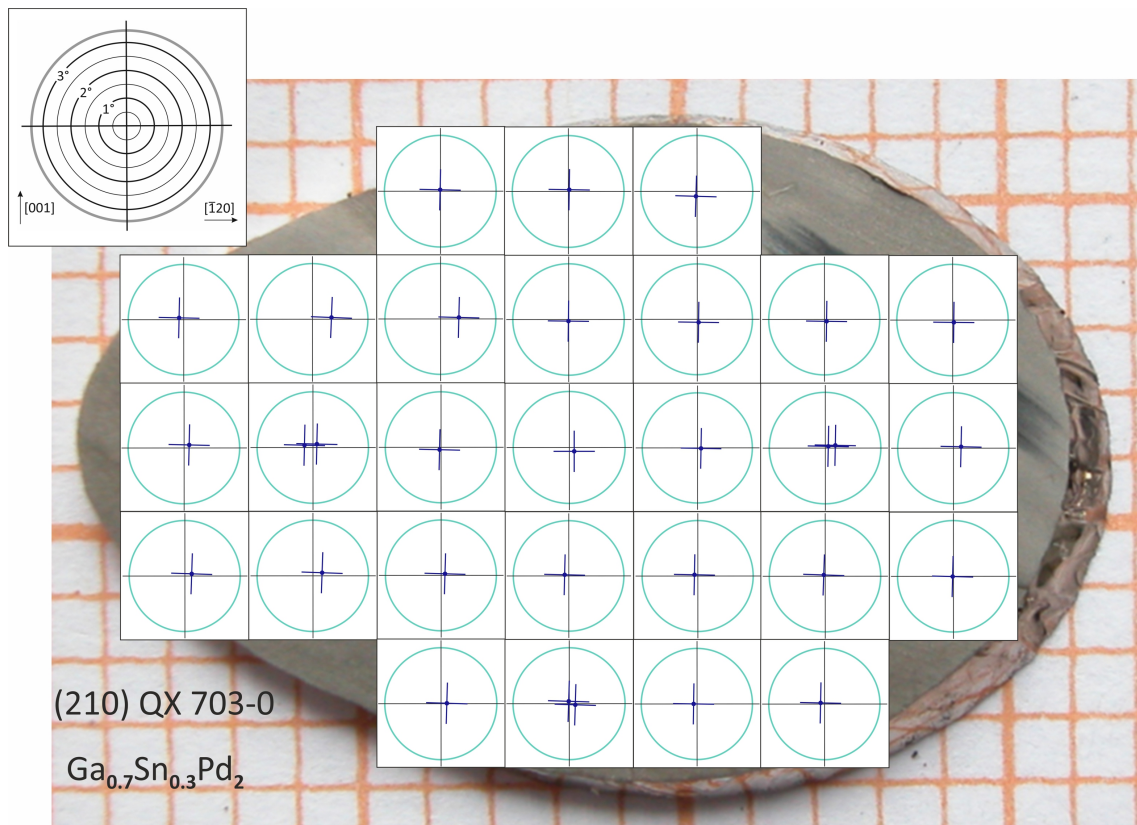


Figure 3.63: Scanning with the Laue camera on different spots on a (210) slab of QX703 ( $\text{Ga}_{0.7}\text{Sn}_{0.3}\text{Pd}_2$ ). The black crosses in the green circles represent the scanning point. The blue crosses show tilts and rotations of the subgrains. Some scans have two distinguishable Laue patterns and accordingly two blue crosses. Such a Laue pattern is shown in fig. 3.64 where all reflexes are present twice.



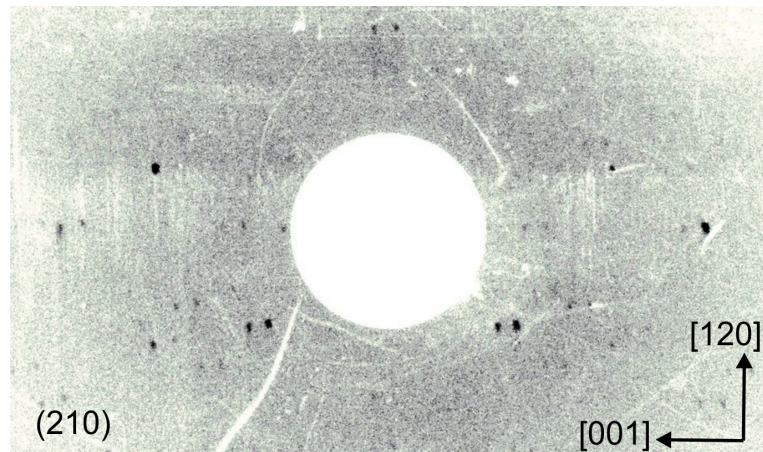


Figure 3.64: Laue image on a (210) surface of QX703 ( $\text{Ga}_{0.7}\text{Sn}_{0.3}\text{Pd}_2$ ) with two Laue patterns that are tilted  $0.7^\circ$  towards each other.

### 3.3.4 Rocking curve analysis

Systematic scans with the Laue camera and contrast lines in BSE images, shown in the figs. 3.56, b and d, gave reasons for further investigations on subgrains and mosaicity. Therefore, rocking curves were performed on crystals with  $x = 0.2$  and  $x = 0.4$ , shown in fig. 3.65. The measured curves confirmed tilts smaller than  $1^\circ$ . The largest tilt was observed on a (100) slice of a bottom part of QX684 ( $x = 0.4$ ) (fig. 3.65, a). Rocking curves on the 200 peak, with the goniometer axis of the diffractometer parallel to the growth direction, show two main domains with a tilt of  $\Omega = 0.7^\circ$ . Furthermore, if the curves of the first-to-freeze part and the last crystallized part are compared to each other, the shapes of the rocking curves seem to be related. Tilts parallel to the growth axis seem to increase from the first-to-freeze part to the later-crystallized part (fig. 3.65, a). Figs. 3.65, b–e, show the values of the tilt angle,  $\Omega$ , being independent from the Sn substitution,  $x$ . The rocking curve of the (100) slice of QX667 is a single peak with a FWHM of  $0.04^\circ$  (goniometer axis = [010]).

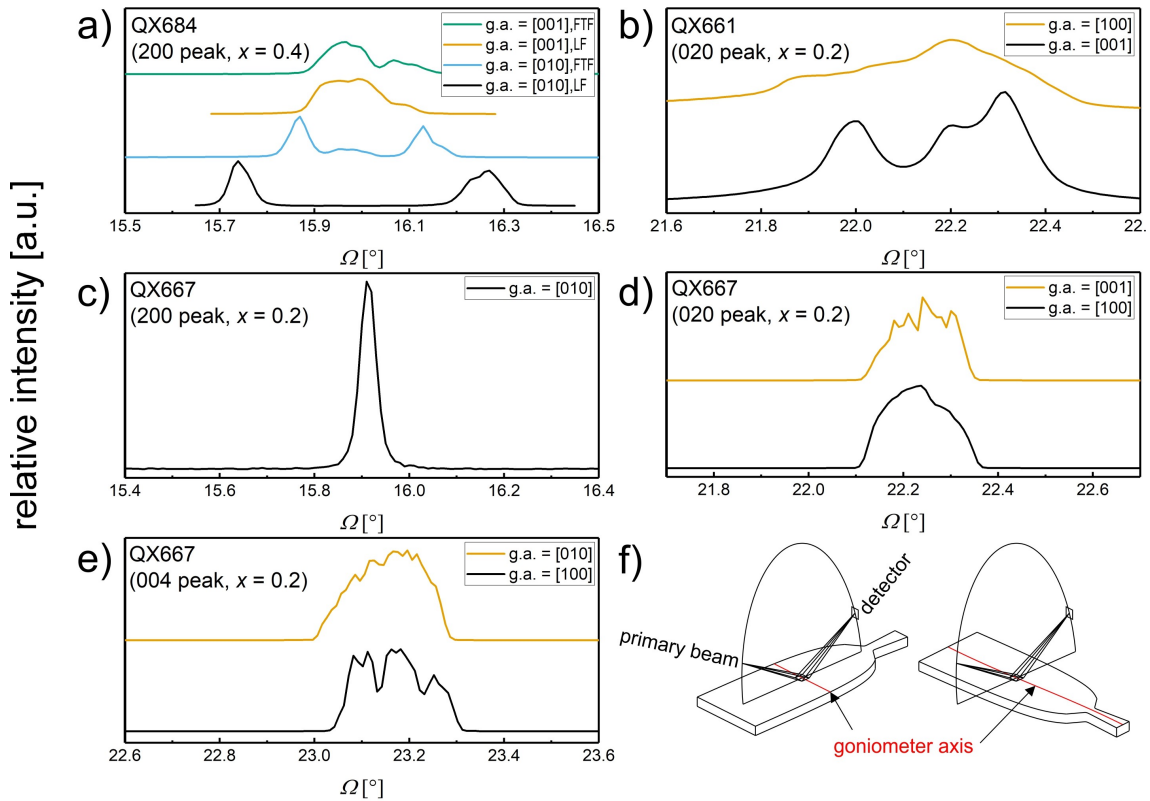


Figure 3.65: a) Rocking curves on the 200 peak of a single-crystalline slice of  $\text{Ga}_{0.60}\text{Sn}_{0.40}\text{Pd}_2$ . The measurement area was approximately  $4 \cdot 4 \text{ mm}^2$ . The curves were measured with the goniometer axis (g.a.) parallel and perpendicular to the growth axis, [010]. b) Measurements on the 020 peak of  $\text{Ga}_{0.82}\text{Sn}_{0.18}\text{Pd}_2$  parallel and perpendicular to the [001] growth axis. c-e) Measurements on three different slices of another  $\text{Ga}_{0.82}\text{Sn}_{0.18}\text{Pd}_2$  crystal grown in [010] direction. Explanation of the labelling: g.a. =  $[uvw]$  means that the goniometer axis is parallel to the  $[uvw]$  direction of the crystal (see f)). The crystal was measured at its top or close to the seed, respectively (FTF = first-to-freeze position) and at the last solidified part (LF).

### 3.3.5 X-ray topography

The individual rocking curves of the 412 peak, from which the X-ray topography (XRT) measurements were created, have a FWHM of  $0.05^\circ$  corresponding to approximately 20000 counts.  $\text{Cu-K}\alpha$  radiation was used. An  $\omega$  scan with constant  $2\theta$  angle was carried out in order to get an overview of possible tilts in the sample. The resulting maximum intensity map (fig. 3.66) shows numerous subgrains with orientation differences of up to  $2^\circ$ . Most subgrains are elongated parallel to the [010] growth axis of the crystal. Some subgrain boundaries are straight lines, either parallel to the [010] direction or often at an angle of  $\approx 20^\circ$  to the [010] direction. On the upper right part one subgrain ends at the shoulder of the crystal. Furthermore, it can be seen that the subgrains originate from the seed. The seed as well as the first-to-freeze part of the crystals are subdivided into numerous very small subgrains with tilts of up to  $2^\circ$  within the range of a few hundred micrometers. Within the first 5 mm of the crystal most smaller subgrains vanish and only few large subgrains

continue to grow. Furthermore, the scan shows increasing tilts within the subgrains from the first-to-freeze part near the seed to later grown parts within each subgrain. From each larger subgrain an individual topograph was measured. The individual topographs, exhibiting lighter and darker areas (e.g. fig 3.69), have been compiled to an overview (fig. 3.67). The light areas are regions where measured intensities are lower. Enlarged sections of fig. 3.67 show that the first-to-freeze area next to the seed is very disrupted (fig. 3.68, a) compared to the larger surrounding subgrains. In the larger grains, stripes perpendicular to the growth direction can be seen (figs. 3.67 and 3.68, b). Fig. 3.70 shows the topograph of a single subgrain (the same as in fig. 3.69, left) but measured with Cr- $K\alpha$  radiation on the 310 peak. The resolution of the measurement with the higher wavelength is clearly better. It can be seen that the stripes, visible in the topographs are identical in the Cr- $K\alpha$  and the Cu- $K\alpha$  measurements, which indicates that the stripes show intrinsic properties of the crystal.

A change of the lattice plane distance  $d$  causes a change of  $2\theta$  according to Bragg's equation  $n\lambda = 2d\sin\theta$  [64]. This can be observed in fig. 3.66, where the  $\omega$  map shows a strong tilt between the seed and the crystal. What seems to be a tilt at first, is actually a change of the lattice spacings changing the Bragg angle and accordingly the maximum position of  $\omega$ . Also the  $\omega$  shifts from the earlier to the later grown parts of the respective subgrains are likely to display the measured chemical gradient, shown in fig. 3.53.

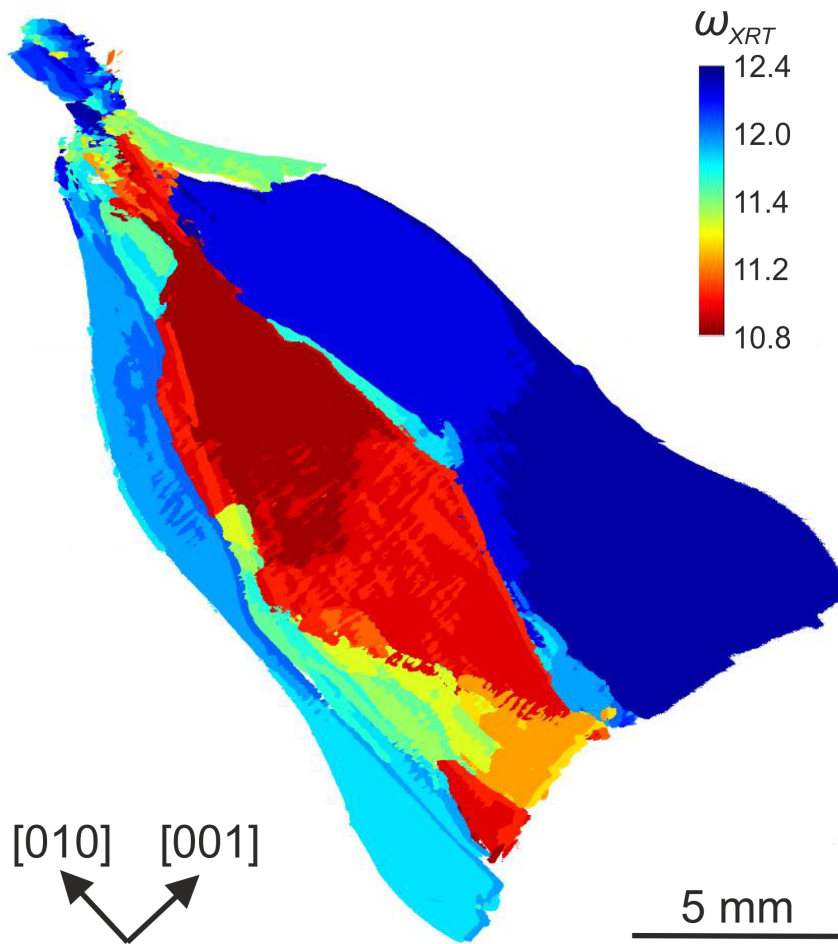


Figure 3.66: Orientation map of a (100) slab of  $\text{Ga}_{0.6}\text{Sn}_{0.4}\text{Pd}_2$  measured on the 412 peak (crystal QX684) with  $\text{Cu-K}\alpha$  radiation.  $2\theta$  was kept constant and  $\omega$  was changed in  $0.1^\circ$  steps to achieve the maximum intensity of each position.

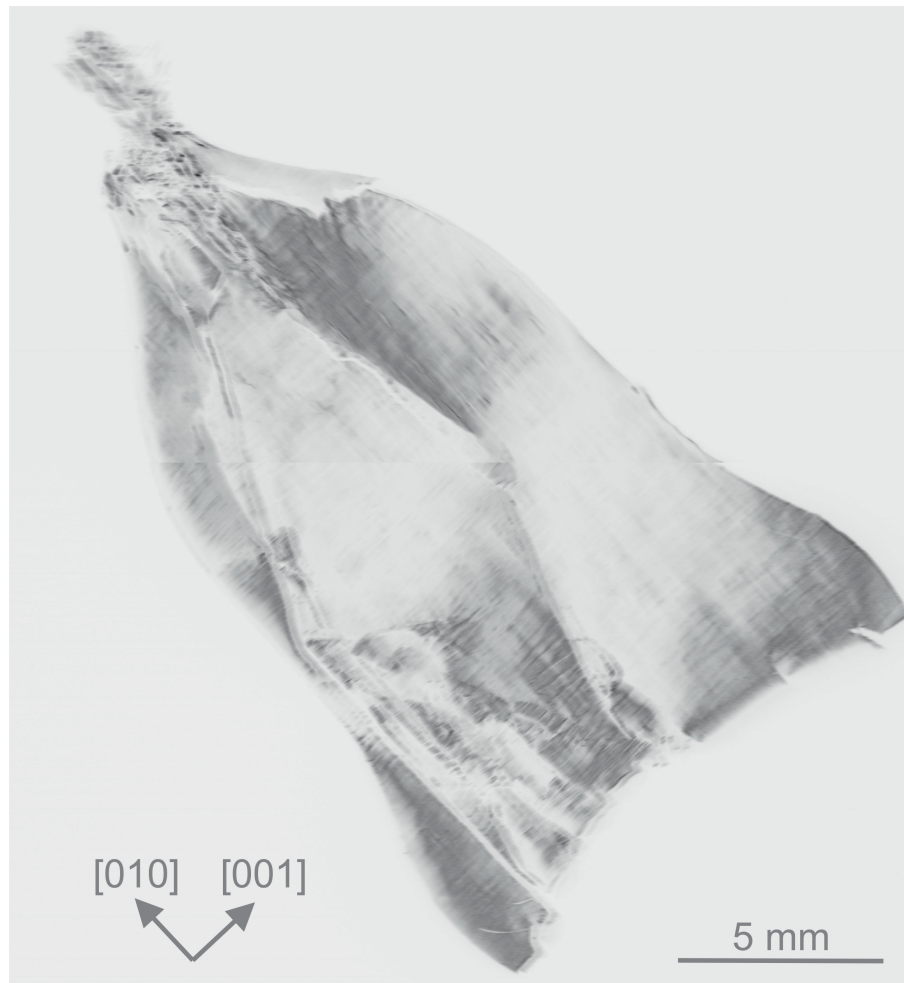


Figure 3.67: Compiled X-ray topography maximum intensity map of a (100) slab of  $\text{Ga}_{0.6}\text{Sn}_{0.4}\text{Pd}_2$  (crystal QX684). Each subgrain was measured independently. The map shows the measured intensity of the 412 peak, measured with  $\text{Cu-K}\alpha$  radiation.

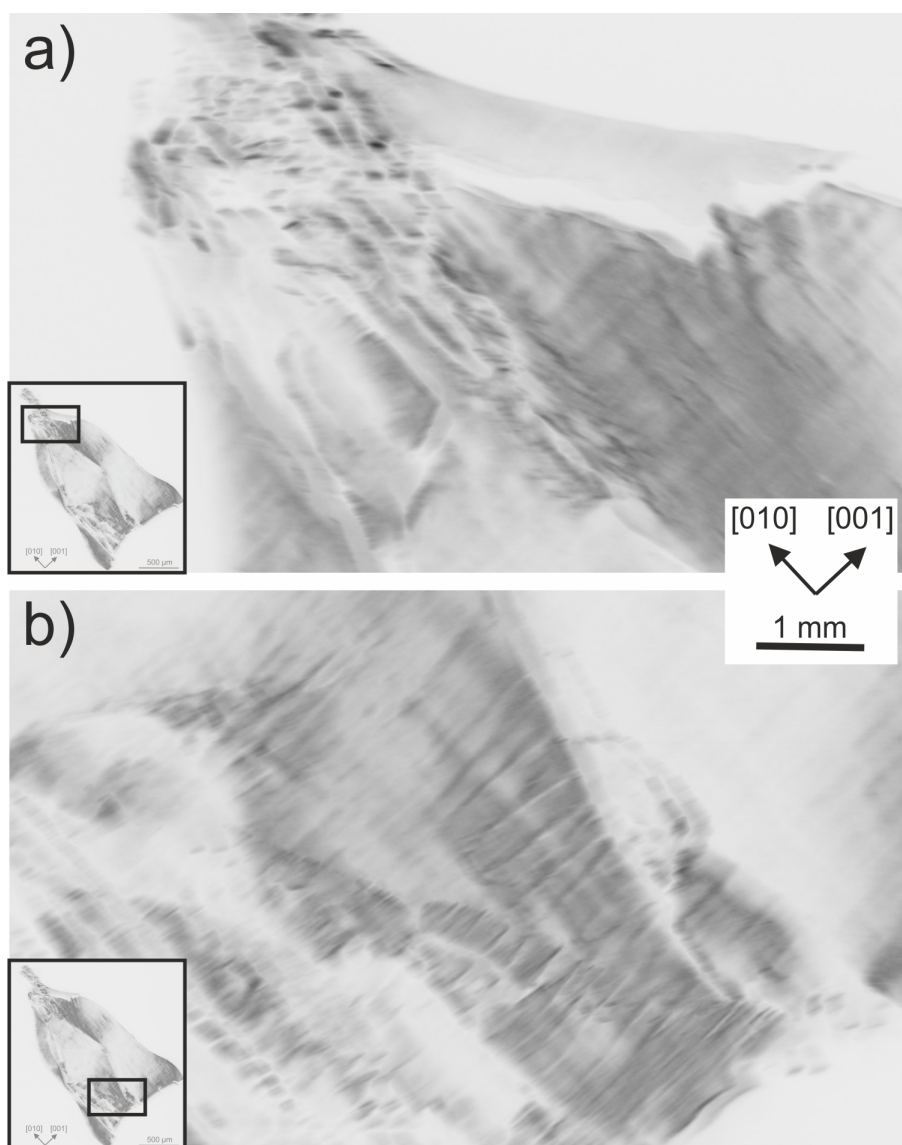


Figure 3.68: Magnified view of the topographs shown in fig. 3.67.

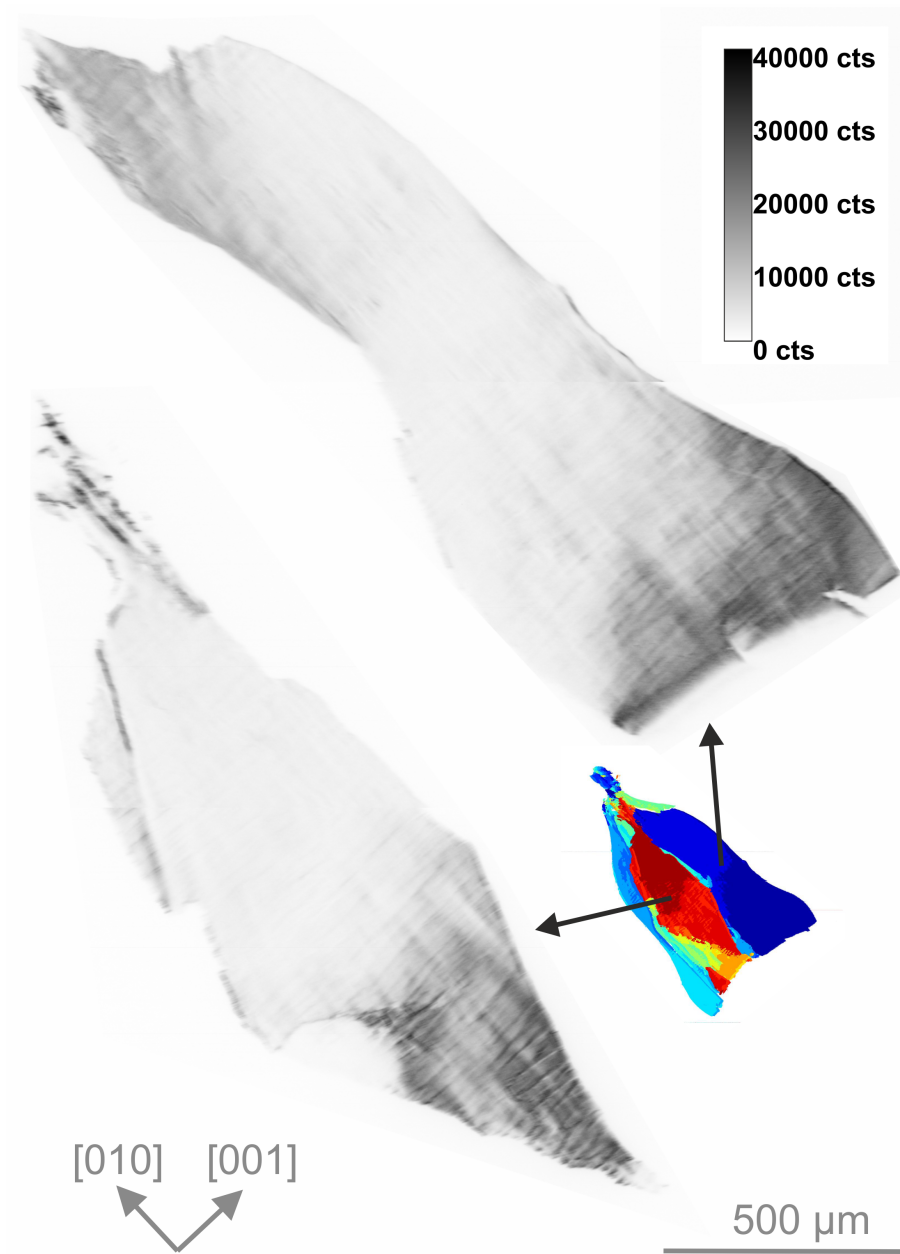


Figure 3.69: Two individual topographs, measured on the 412 peak with  $\text{Cu-K}\alpha$  radiation.



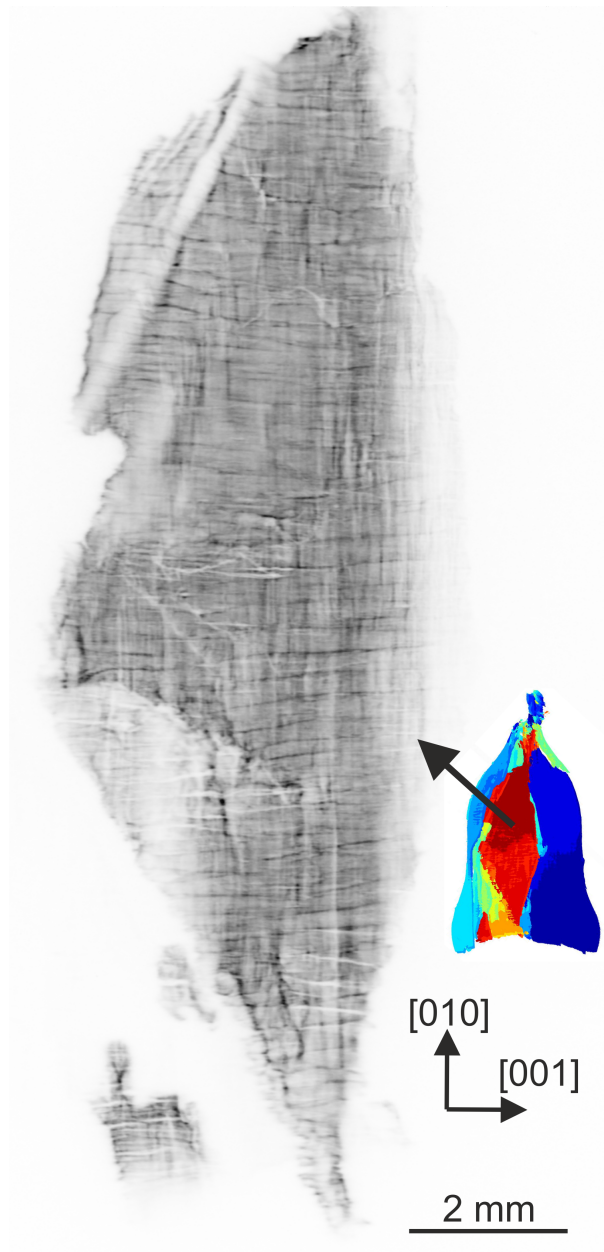


Figure 3.70: X-ray topograph of the same grain shown in fig. 3.69, left, but measured on the 310 peak, using  $\text{Cr-}K\alpha$  radiation.

## 3.4 Electron backscatter diffraction on single crystals

Electron backscatter diffraction (EBSD) measurements on slices perpendicular to the three main directions (QX674,  $x = 0.3$ , pulled in  $[010]$ ), as well as on a  $(210)$  surface (QX703,  $x=0.3$ , pulled in  $[010]$ ), were performed on a crystal by Ulrich Burkhardt, Max-Planck-Institut für Chemische Physik fester Stoffe Dresden. Fig. 3.71 shows the investigations on the  $(010)$  slice: The fore scattered electron (FSE) images show several subgrains with sizes in the range of several hundred micrometers. Smaller grains in the two digit micrometer range are also present (see b and c). The IPF\_Z maps show that the pole figures are quite close to the  $[010]$  direction but more detailed line measurements crossing the grain boundaries show tilts of typically  $0.3^\circ$ , but also up to  $1^\circ$ . Subgrains are also visible on the  $(210)$  slice, shown in fig. 3.72. Subgrains are clearly visible already in the SE and FSE images. The EBSD line measurements over the subgrain boundaries display tilts of up to  $2.5^\circ$ . These investigations could not proof tilts on the  $(100)$  and the  $(001)$  surfaces (figs. A.28 and A.29 in the appendix).

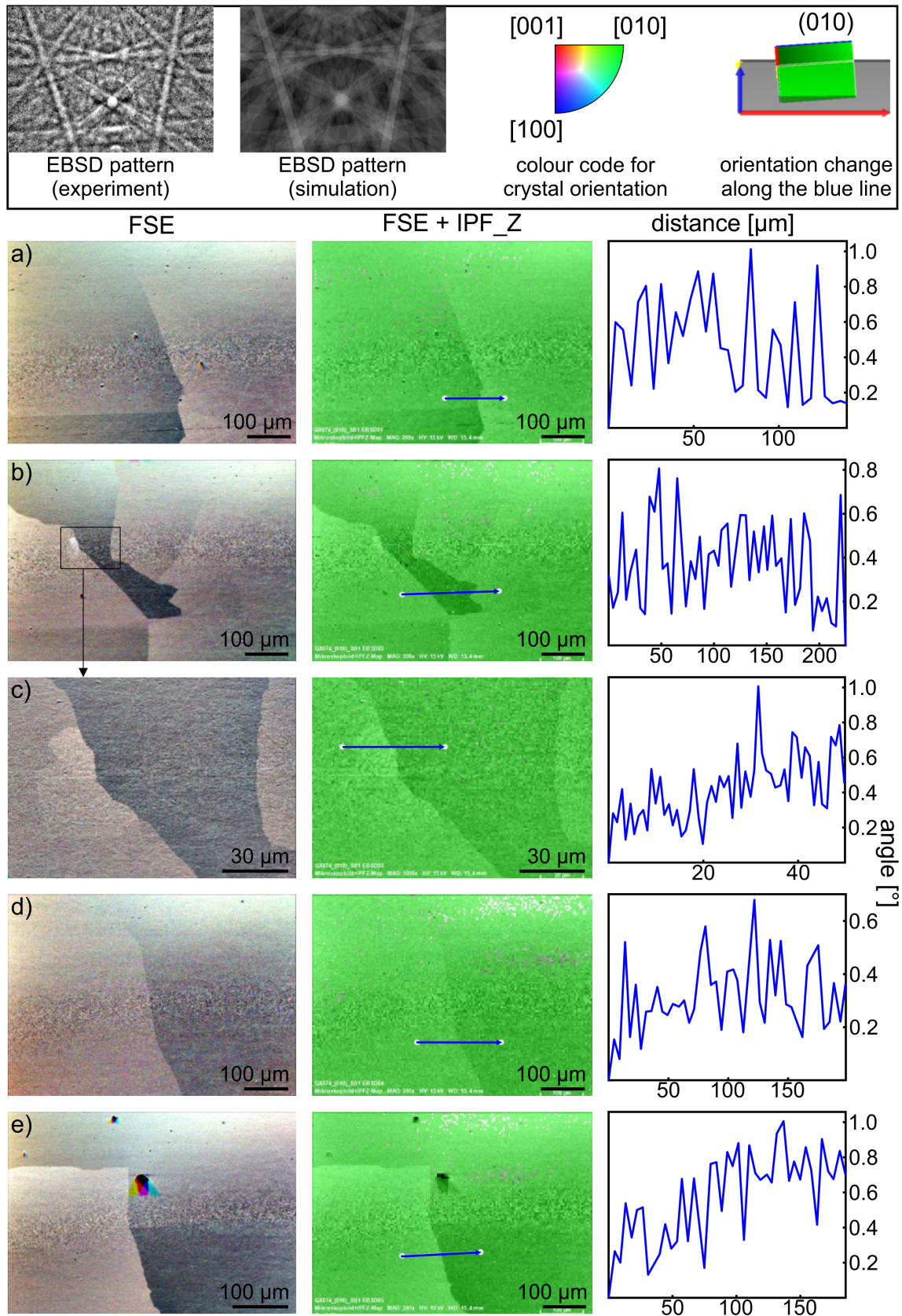


Figure 3.71: FSE, IPF\_Z maps and the orientation change along the blue lines of different positions on a (010) slice of a crystal with  $x = 0.3$  (QX674).

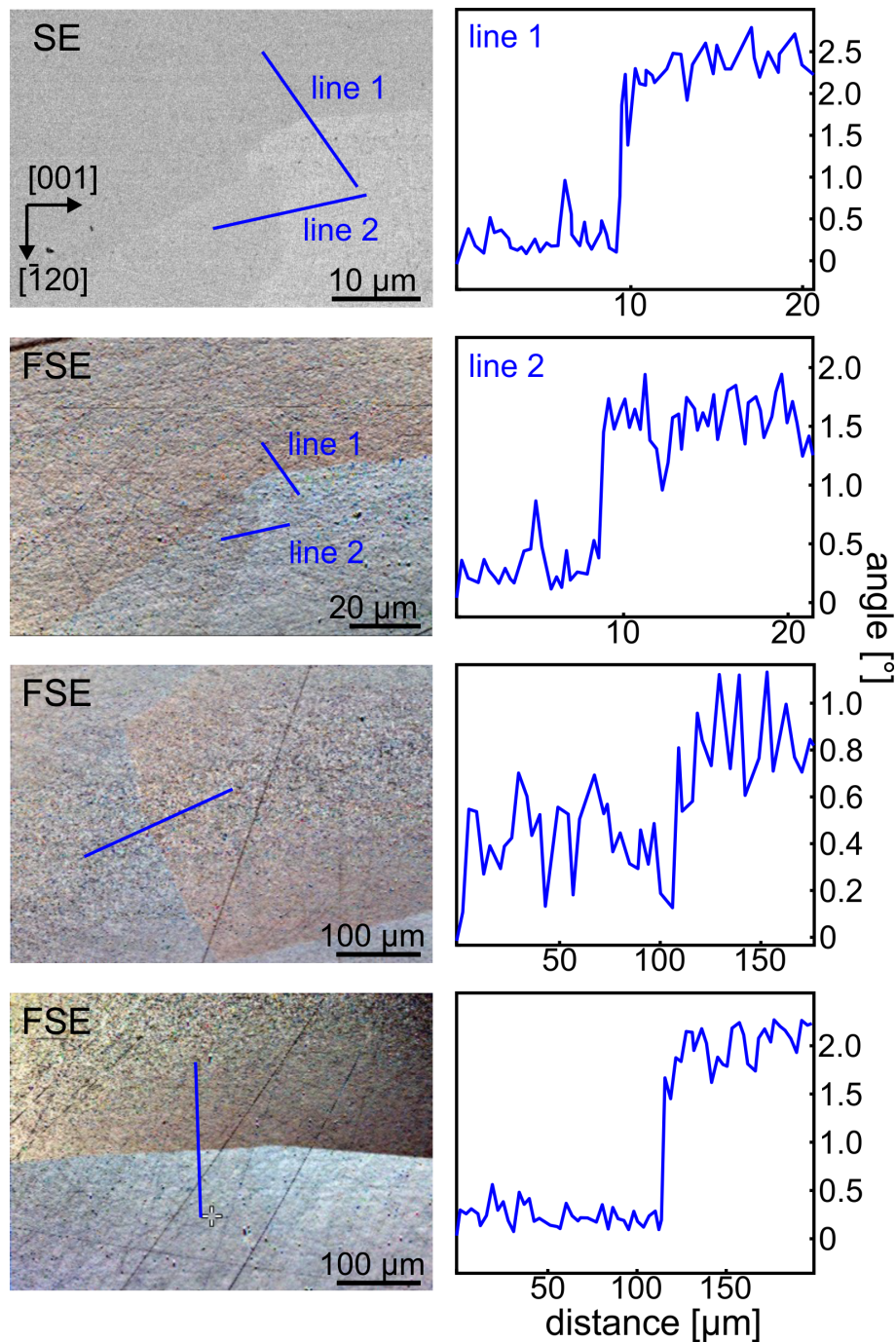


Figure 3.72: FSE and SE images of a (210) slice of a crystal with  $x = 0.3$  (QX703). The right pictures display the tilts along the lines on the left.

### 3.5 Polishing of single-crystalline surfaces

In section 2.4.1.2 it was already mentioned that unusual catalytic behaviour gave reason to further investigate the polishing of the slices in order to prepare suitable surfaces. In X-ray studies additional peaks occurred in the diffraction patterns of  $\theta$ - $\theta$  scans of single-crystalline slabs. The additional peaks appeared at the positions of the peaks of the lattice planes with the highest structure factor (210, 013, 211, and 020). There are always peaks present at the positions of the 211 and the 013 peaks



but depending on the crystallographic orientation of the crystal slice also the 210 and the 020 peaks may appear (figs. A.1, A.3 and A.5). The arising patterns have in common that they are independent of the Sn content, despite the peak position shift which is in very good agreement with refined lattice parameters of samples with the equivalent Sn contents. In contrast, the patterns measured on the single crystal slabs, strongly depend on the crystallographic orientation of the respective slab. They are always identical regarding the crystallographic orientation, independent of the crystal, its Sn content or the treatment (cutting, lapping and polishing). An exception was grinding where the intensities of the different individual peaks behave differently, compared to the other surface treatments (e.g. fig. A.2). In the case of all other treatments (cutting, lapping and polishing) the ratios between intensities of the different individual peaks are equal but the overall intensities decrease from corundum lapping to sawing to polishing. During polishing the intensities of the surface damage peaks decrease with decreasing grain size of the polish. On the (010) surface, the intensities of the surface damage peaks decrease continuously with decreasing polish grain size (fig. A.4). On the other two main directions the intensities of the surface damage peaks drop below the detection limit of XPD already after the first polishing steps. In the case of the (100) surface, the peaks are below the detection limit after the first polishing step with 6  $\mu\text{m}$  and on the (001) surface the same is the case after the polishing step with 1  $\mu\text{m}$  (figs. A.2 and A.6). In tab. 3.16 a measurement of the material erosion rates on a (210) surface shows an irregular erosion behaviour.

An additional example for the sensitivity towards surface treatment of  $\text{Ga}_{1-x}\text{Sn}_x\text{Pd}_2$  is the comparison of Laue images of an as-grown and an as-cut surface (fig. 3.73). At the same illumination time, the as-grown surface has sharper and more abundant reflexes. The as-cut surface has fewer and more diffuse reflexes, indicating surface damage, even though the wire lapping saw is considered as one of the most careful methods to cut crystals. The sensitivity of the material towards mechanical stress is also noticeable during the preparation of powders for XPD, where milling causes massive peak broadening (section 2.4.1.1).

Polishing step	$t$ [min]	material removal [ $\mu\text{m}$ ]
SiC 1200	30	35
diamond, 9 $\mu\text{m}$	60	94
diamond, 6 $\mu\text{m}$	60	4
diamond, 6 $\mu\text{m}$	60	17
diamond, 3 $\mu\text{m}$	120	55
diamond, 1 $\mu\text{m}$	150	25
diamond, 0.25 $\mu\text{m}$	90	1
Syton OP-S $\mu\text{m}$	12	3

Table 3.16: Exemplary measurement of the material removal during machine polishing of a (210) slab. The rotation rate was 36 rpm and the pressure 18 kPa. The final step with Syton OP-S was carried out manually. The polishing step with 6  $\mu\text{m}$  diamond polish was repeated after the erosion was low in the first attempt.

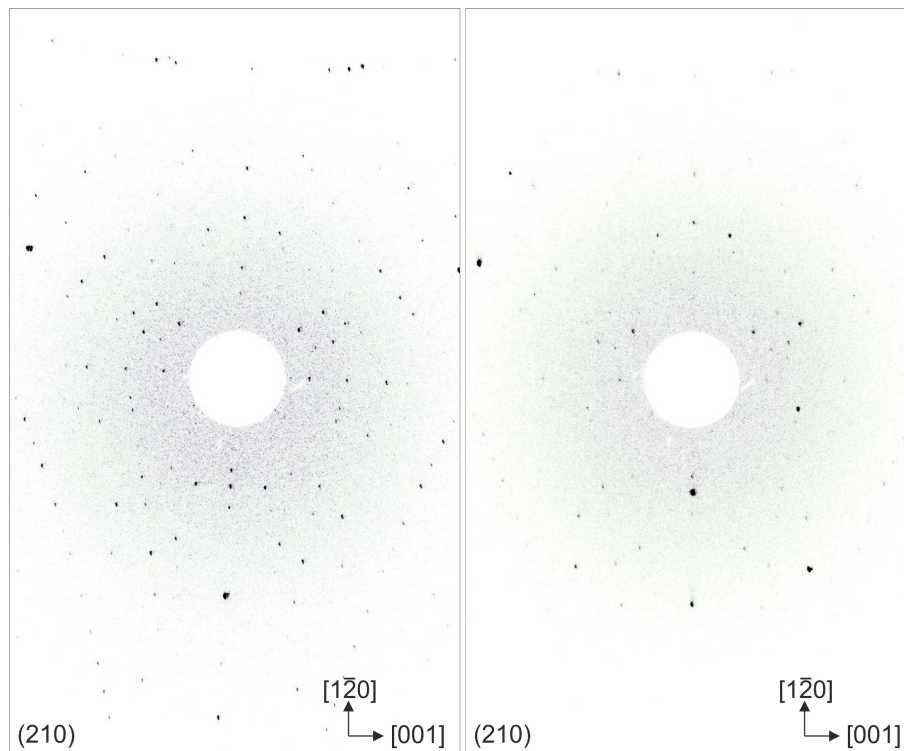


Figure 3.73: Comparison of two Laue images perpendicular to the (210) plane, on an as-grown surface (left) and on a surface that was cut with the wire lapping saw (right). It is clearly visible that reflexes on the as-grown surface are sharper and more abundant. Both images were taken under the same conditions with an illumination of 3 h. A shorter illumination of an as-cut surface results in only few reflexes making an evaluation difficult, while usually 15 minutes on as-grown surfaces are sufficient for proper evaluation of the orientation.

The polishing studies, already mentioned in section 2.4.1.2, are only for the purpose of obtaining perfect surfaces for catalytic measurements and cannot be considered as more extensive surface studies.

In section 4.3 the origin of these peaks is discussed and a polycrystalline sub-surface damage (SSD) layer is taken into account. The isolated 210 peak on a (100) slab was fitted with a pseudo-Voigt function in the X-ray diffraction software *Analyze* and the particle size was calculated, according to the Scherrer equation [70]. No other peak was fitted, since the other abundant peaks, 211 and 013, are very close to each other and appear as a single peak, due to the pronounced broadening. The method was applied at measurements of two stages of surface treatment. One was grinding with 1000 mesh SiC the other was lapping with 3–5  $\mu\text{m}$  corundum water slurry. The FWHM of around  $0.7^\circ$ – $0.8^\circ$  is equal for the two treatments even though the intensity of the 210 peak is almost twice in the case of grinding, compared to lapping. The calculated grain size of the crystallites of the SSD layer is 11–12 nm.

# Chapter 4

## Discussion

### 4.1 On the Ga-Pd-Sn system

The following chapter concentrates on the phase diagram studies. The focus is on numerous small equilibrium-cooling experiments as well as on several Bridgman experiments described, in chapter 2.1. In contrast to the Czochralski experiments, these experiments resulted usually in polycrystalline samples, typically containing the whole phase content of the respective crystallization path. These experiments were necessary and can be regarded as feasibility studies in order to get the information, needed for the growth of single crystals with the Czochralski technique. Due to the high effort and the costly material input, Czochralski experiments do not allow experimental uncertainties, especially since the growth itself is usually challenging enough. Accordingly, elaborating the boundaries for the crystal growth of  $\text{Ga}_{1-x}\text{Sn}_x\text{Pd}_2$  from (Ga,Sn)-rich solution, especially for the desired compositions,  $0.1 \leq x \leq 0.4$ , was necessary and could be achieved. The crystal growth was incongruent and additionally a segregation coefficient of Sn had to be expected. Therefore, precise estimations of melt compositions for the desired crystal compositions were gained from the pre-experiments. Another advantage were estimations of the growth temperatures.

As a side effect the surrounding liquidus surface around the primary crystallization region of  $\text{Ga}_{1-x}\text{Sn}_x\text{Pd}_2$  could be shown partially and the primary crystallization area of further phases could be estimated. Additionally, first results regarding the Sn incorporation in these phases could be shown.

#### 4.1.1 Primary crystallization areas

Defining the boundaries of the primary crystallization regions of the different phases proved to be non-trivial and several difficulties occurred: (i) Different primary crystallization areas can be very close to each other, in a very narrow chemical range. This is already visible in the binary systems Ga-Pd and Pd-Sn, where multiple phases may solidify primarily within a range of few at.% Pd. Regarding the Ga-Pd system, four primary solidification areas of the phases GaPd,  $\text{Ga}_4\text{Pd}_5$ ,  $\text{Ga}_3\text{Pd}_5$  and  $\text{GaPd}_2$  are settled within a composition range of less than 6 at.% [23]. (ii) Most likely at least one high-temperature (HT) phase is abundant. Such phases decompose into eutectoid mixtures, visible by fine-grained multiphase areas. (iii) Phases are present, that have a retrograde solubility of at least one of the components at lower temper-



atures, leading to peritectoid decompositions during cooling. Particularly affected is  $\text{Ga}_{2+p+q}\text{Sn}_{4-p}\text{Pd}_9$ , which occurs in the shape of primarily solidified grains which are always strongly perforated or have lamellae.  $\text{Ga}_{1-x}\text{Sn}_x\text{Pd}_2$  was also found to be primarily solidified, with subsequently formed lamellae of  $\text{Ga}_{2+p+q}\text{Sn}_{4-p}\text{Pd}_9$  and  $\text{Ga}_{1-x}\text{Sn}_x\text{Pd}$ . In some cases, it is therefore difficult to determine whether a respective phase is a decomposed HT phase or if it is one of the phases that only partly decomposed in a peritectoid reaction during cooling.

#### 4.1.1.1 Primary crystallization area of $\text{Ga}_{1-x}\text{Sn}_x\text{Pd}_2$

The (Ga,Sn)-rich side of the primary solidification area of  $\text{Ga}_{1-x}\text{Sn}_x\text{Pd}_2$  was narrowed down and is shown in fig. 4.1. In the present studies the tie-lines<sup>1</sup> of several compositions at the (Ga,Sn)-rich side of the primary solidification area of  $\text{Ga}_{1-x}\text{Sn}_x\text{Pd}_2$  could be determined (fig. 4.1). This was the fundamental information for numerous successful Czochralski single crystal growth experiments. The experiments show that the replacement of Ga by Sn in the melt results in almost the same substitution of Ga by Sn in the crystal and the pseudobinary segregation can be neglected (A detailed specification can be found in section 4.2.5). Accordingly, the Sn content in the melt,  $x_L$ <sup>2</sup>, almost equals the Sn content in the crystal,  $x$  (fig. 3.36). However, in experiments with higher Sn contents in the melt,  $x_L \geq 0.5$ , the first-to-freeze compositions are decoupled from the initial Sn contents in the melt, resulting in strong segregation between Sn and Ga. This might indicate that an upper boundary is approached, where  $\text{Ga}_{1-x}\text{Sn}_x\text{Pd}_2$  has no equilibrium with the liquid phase any more.  $\text{Ga}_{1-x}\text{Sn}_x\text{Pd}_2$  can be grown from (Ga,Sn)-rich solution of up to  $x_L \leq 0.6$  and the resulting Ga substitution by Sn in the crystals is up to  $x_{max} = 0.54$ .

<sup>1</sup>Tie-lines connect the composition of the melt with the solid being in equilibrium with it.

<sup>2</sup>According to the description  $(\text{Ga}_{1-x_L}\text{Sn}_{x_L})_{100-y_L}\text{Pd}_{y_L}$ .

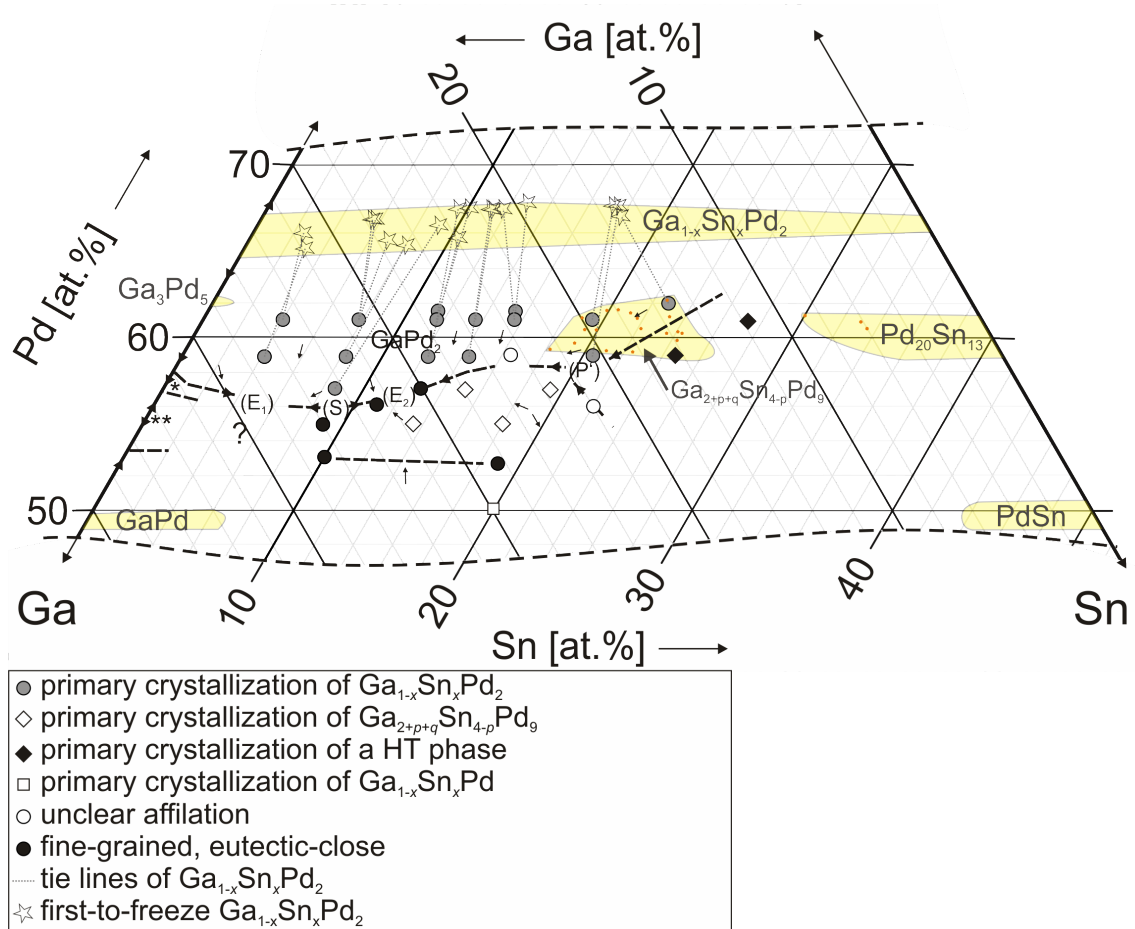


Figure 4.1: Primary solidification areas of the different phases in the investigated region. The dashed lines display estimated boundaries between primary crystallization areas of different phases. S is a saddle point and  $E_1$  and  $E_2$  are the estimated positions of eutectics.  $P'$  is the estimated position of a quasi-peritectic. The arrows on dashed lines show the tendency in which the crystallization paths proceed. \* marks the primary crystallization field of  $\text{Ga}_3\text{Pd}_5$  and \*\* marks the primary crystallization area of  $\text{Ga}_4\text{Pd}_5$  after [23]. The  $500^\circ\text{C}$  stability regions, published in [18], have been extended by measured compositions at room temperature, indicated by orange markers.

#### 4.1.1.2 Primary crystallization areas of further phases

Adjacent to the primary crystallization area of  $\text{Ga}_{1-x}\text{Sn}_x\text{Pd}_2$ , with lower  $y_L$  and  $0.2 \leq x_L < 0.5$ <sup>3</sup>, primary crystallization of  $\text{Ga}_{2+p+q}\text{Sn}_{4-p}\text{Pd}_9$  has been proven for the first time (experiments with such compositions are marked with white diamonds in fig. 4.1). Even though the grains of  $\text{Ga}_{2+p+q}\text{Sn}_{4-p}\text{Pd}_9$  are always at least partly decomposed, large-grown grains prove the primary crystallization of the phase (e.g. fig. 3.25). The grains contain precipitates of mostly  $\text{Ga}_{1-x}\text{Sn}_x\text{Pd}$ , showing a retrograde solubility of Ga in  $\text{Ga}_{2+p+q}\text{Sn}_{4-p}\text{Pd}_9$  with decreasing temperatures. The grains partly exhibit intact outer shells indicating that later-crystallized parts of the phase may have a higher tolerance towards Ga incorporation with decreasing

<sup>3</sup>According to the description  $(\text{Ga}_{1-x_L}\text{Sn}_{x_L})_{100-y_L}\text{Pd}_{y_L}$ .

temperatures. Comparing the stability region of the phase  $\text{Ga}_{2+p+q}\text{Sn}_{4-p}\text{Pd}_9$  and its primary crystallization area, it becomes clear that the phase crystallizes exclusively incongruently.

In Sn-richer areas (experiments with melt compositions, marked with black diamonds in fig. 4.1) it is uncertain, whether  $\text{Ga}_{2+p+q}\text{Sn}_{4-p}\text{Pd}_9$  or an unknown high-temperature (HT) phase crystallizes primarily. Such experiments contain grains with decomposition structures, showing spotted or mostly lamellae structures of the phases  $\text{Ga}_{2+p+q}\text{Sn}_{4-p}\text{Pd}_9$  and  $\text{Pd}_{20}\text{Sn}_{13-x}\text{Ga}_x$  (partly the phase  $\text{Ga}_{1-x}\text{Sn}_x\text{Pd}$  is included). It is not clear from the textures, whether one of the two phases crystallizes primarily at higher temperatures. The primary crystallization of a HT phase is therefore possible. In the binary Pd-Sn system, the phase  $\text{Pd}_{20}\text{Sn}_{13}$  has an equilibrium with the liquid. Depending on the melt composition, several different peritectoid decompositions are possible, containing always  $\text{Pd}_{20}\text{Sn}_{13}$  and either  $\alpha\text{-Pd}_3\text{Sn}_2$ ,  $\beta\text{-Pd}_3\text{Sn}_2$  (HT phase that transitions into  $\alpha\text{-Pd}_3\text{Sn}_2$  at lower temperatures) or a  $\delta$ -phase [39].

## 4.1.2 Crystallization paths

In the following, an overview of the crystallization paths, based on the interpretation of the collected data, is presented. Mainly, those crystallization paths are discussed, which end at the (Ga,Sn)-rich edge of the primary crystallization area of the phase  $\text{Ga}_{1-x}\text{Sn}_x\text{Pd}_2$ . In a limited range also the primary crystallization area of the phase  $\text{Ga}_{2+p+q}\text{Sn}_{4-p}\text{Pd}_9$  is addressed, since it is adjacent to that of  $\text{Ga}_{1-x}\text{Sn}_x\text{Pd}_2$  and common crystallization paths exist.

In the region where  $\text{Ga}_{1-x}\text{Sn}_x\text{Pd}_2$  crystallizes primarily from melts with a low initial Sn content of  $x_L \leq 0.1$ <sup>4</sup> (this corresponds to region R1 in fig. 3.2), two-phase crystallization of  $\text{Ga}_{1-x}\text{Sn}_x\text{Pd}_2$  and  $\text{Ga}_{3-x}\text{Sn}_x\text{Pd}_5$  follows. It can be concluded that the two phases crystallize on the univariant line in an eutectic channel<sup>5</sup>. The crystallization paths end in an eutectic point. This can be seen from the fine-grained matrix and the final signal of the DTA cooling curve at 942°C. The detailed composition of the eutectic was not further specified.

In experiments where  $\text{Ga}_{1-x}\text{Sn}_x\text{Pd}_2$  crystallizes primarily with the initial Sn content of  $x = 0.2$  (this corresponds to region R2 in fig. 3.2), only the phases  $\text{Ga}_{1-x}\text{Sn}_x\text{Pd}$  and  $\text{Ga}_{1-x}\text{Sn}_x\text{Pd}_2$  can be found.  $\text{Ga}_{1-x}\text{Sn}_x\text{Pd}_2$  occurs as a primarily crystallized phase and in the form of two secondarily solidified phases, one being of eutectic origin and the other of eutectoid origin.  $\text{Ga}_{1-x}\text{Sn}_x\text{Pd}$  exists exclusively finely distributed in an eutectoid. The primary crystallization DTA signal is followed by a common signal at about 919(2)°C in the DTA cooling curves of all experiments. Therefore, and due to the fine-grained matrix, an eutectic solidification of the residual melt can be concluded at that temperature. In fig. 4.1, E<sub>1</sub> displays the estimated position of this eutectic. Since the eutectic composition of the experiments of re-

<sup>4</sup>According to the description  $(\text{Ga}_{1-x_L}\text{Sn}_{x_L})_{100-y_L}\text{Pd}_{y_L}$ .

<sup>5</sup>In ternary systems univariant lines are the boundaries between two primary solidification areas. Accordingly, they have one degree of freedom and according to the Gibbs phase rule,  $F = 4 - P$  (ternary, isobaric system), three phases are in equilibrium, which are the melt and the two neighbouring solid phases. After the crystallization paths leave the primary solidification areas of the initially crystallizing phases and enter an univariant line, the crystallization in an eutectic channel will occur. In this case the univariant line is a valley and the two neighbouring phases crystallize simultaneously [42].

gion R1 was not further specified, it is possible that the crystallization paths of both regions R1 and R2 end in the same eutectic. However, this should be further investigated. In  $E_1$  the phases  $\text{Ga}_{1-x}\text{Sn}_x\text{Pd}_2$  (as a second generation) and  $\text{Ga}_{1-x}\text{Sn}_x\text{Pd}$  are present, in grain shapes being typical for eutectic textures. According to the Gibbs phase rule, in an eutectic, i.e. in an invariant point, three solid phases need to be in equilibrium with the melt<sup>6</sup> [42]. Accordingly, a third phase needs to be present in the eutectic. However, besides the aforementioned grains of the phases  $\text{Ga}_{1-x}\text{Sn}_x\text{Pd}_2$  and  $\text{Ga}_{1-x}\text{Sn}_x\text{Pd}$  a finer distributed mixture of  $\text{Ga}_{1-x}\text{Sn}_x\text{Pd}_2$  and  $\text{Ga}_{1-x}\text{Sn}_x\text{Pd}$  is present in large amounts hinting at a decomposition of the third phase of the former eutectic reaction. XPD measurements showing multiple peaks of  $\text{Ga}_{1-x}\text{Sn}_x\text{Pd}_2$  proof that there are different sets of the same phase with different lattice parameters<sup>7</sup>, i.e. different generations of the same phase. The DTA signal at 620–630°C, shared by all experiments, is attributed to a solid-solid phase transition, since the presence of a liquid in the investigated area at temperatures that low was excluded by melt observations in the Czochralski apparatus. In binary systems it is common that HT phases decompose into an eutectoid, consisting of the two adjacent phases. An example from the Ga-Pd binary system would be  $\text{Ga}_4\text{Pd}_5$  which decomposes into a fine eutectoid of the two neighbouring phases, GaPd and  $\text{Ga}_3\text{Pd}_5$ , during cooling [23].

In the central part of the investigated region in the Ga-Pd-Sn system at Sn contents between  $0.25 \leq x \leq 0.4$ , the phases  $\text{Ga}_{1-x}\text{Sn}_x\text{Pd}_2$  and  $\text{Ga}_{2+p+q}\text{Sn}_{4-p}\text{Pd}_9$  crystallize primarily. This corresponds to the regions R3, R5, and R7 in fig. 3.2 and accordingly to most of the experiments of the present phase diagram studies. These experiments share similar DTA cooling curves, phase contents, textures and closely related crystallization paths that end in a shared eutectic ( $E_2$  in fig. 4.1). Experiments with initial compositions located in region R3 are in the primary crystallization region of phase  $\text{Ga}_{1-x}\text{Sn}_x\text{Pd}_2$ . Experiments with compositions located in region R7 belong to the primary crystallization area of phase  $\text{Ga}_{2+p+q}\text{Sn}_{4-p}\text{Pd}_9$ . Experiments with initial compositions located in region R5 cannot be clearly assigned to one of the two primary crystallization areas since no primary solidified phase could be clearly identified. However, they clearly belong to one of the two areas. The first peaks of the DTA cooling curves differ between the above-mentioned experiments since they depend on the respective position on the liquidus surface. All other events in the DTA curves are largely similar. Experiments from region R5 do not show peaks above the prominent signal, at 905(1)°C, which all experiments share. All lower temperature signals in the DTA curves again have a high similarity with region R3 and R7. Based on the shape and the intensity of the signals at 905°C in the DTA cooling curves and the common fine-grained texture between the earlier primarily solidified regions, it can be assumed that a shared eutectic occurs here at 905°C. All experiments of these regions (R3, R5, R7) share the phases  $\text{Ga}_{1-x}\text{Sn}_x\text{Pd}$ ,  $\text{Ga}_{1-x}\text{Sn}_x\text{Pd}_2$  and  $\text{Ga}_{2+p+q}\text{Sn}_{4-p}\text{Pd}_9$ , exhibiting a fine-grained texture. However, it is not expected that these three phases form the eutectic, since they show pronounced differences in their grain sizes: For example  $\text{Ga}_{1-x}\text{Sn}_x\text{Pd}$  and a second generation of

<sup>6</sup>The Gibbs phase equation in a ternary isobaric system becomes  $F = 4 - P$  [42].

<sup>7</sup>Because precise correlations between the lattice parameters and the compositions of  $\text{Ga}_{1-x}\text{Sn}_x\text{Pd}_2$  could be established in section 3.3.2, fig. 3.60, it is easy to distinguish different generations with different Sn contents,  $x$ , by their lattice parameters in the diffractogram and even to calculate their composition.

$\text{Ga}_{2+p+q}\text{Sn}_{4-p}\text{Pd}_9$  occur in much finer grain sizes compared to  $\text{Ga}_{1-x}\text{Sn}_x\text{Pd}_2$  and the earlier generation of  $\text{Ga}_{2+p+q}\text{Sn}_{4-p}\text{Pd}_9$ . Accordingly, it is likely that a third phase decomposes later in an eutectoid reaction. Such solid-solid phase transitions are confirmed by the DTA curves showing peaks below the eutectic temperature. It can be seen in fig. 4.2 that between the phases  $\text{Ga}_{2+p+q}\text{Sn}_{4-p}\text{Pd}_9$  (II) and  $\text{Ga}_{1-x}\text{Sn}_x\text{Pd}_2$  (I), forming the eutectic, a finely distributed eutectoid mixture of  $\text{Ga}_{1-x}\text{Sn}_x\text{Pd}$  together with another generation of the phase  $\text{Ga}_{2+p+q}\text{Sn}_{4-p}\text{Pd}_9$  (III) occurs. This leads to the assumption that  $\text{Ga}_{1-x}\text{Sn}_x\text{Pd}$  and the other generation of  $\text{Ga}_{2+p+q}\text{Sn}_{4-p}\text{Pd}_9$  are simultaneously formed by the decomposition of a HT phase. Consequently, this HT phase, together with the earlier generation  $\text{Ga}_{2+p+q}\text{Sn}_{4-p}\text{Pd}_9$  and  $\text{Ga}_{1-x}\text{Sn}_x\text{Pd}_2$ , must have formed the eutectic in the first place. Since  $\text{Ga}_{2+p+q}\text{Sn}_{4-p}\text{Pd}_9$  can be proven as eutectic phase in  $E_2$  but not in  $E_1$ , there must be a saddle point in-between the rough position, which is marked by S in fig. 4.1.

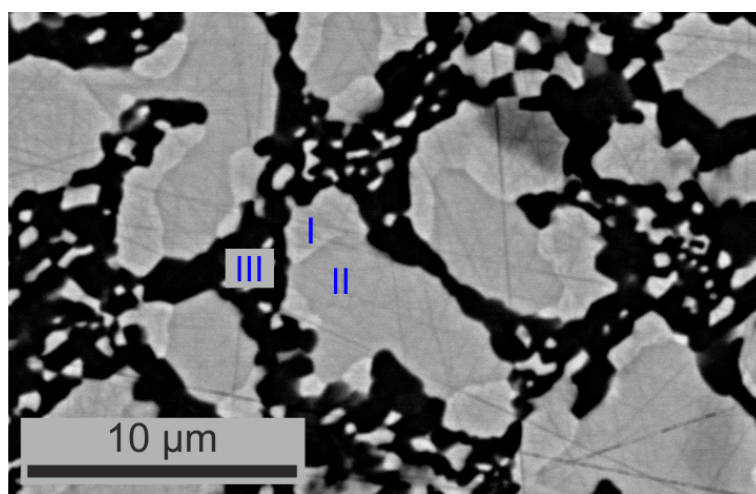


Figure 4.2: BSE image of the eutectic texture ( $E_2$  in fig. 4.1). I is eutectic  $\text{Ga}_{1-x}\text{Sn}_x\text{Pd}_2$ , II is eutectic  $\text{Ga}_{2+p+q}\text{Sn}_{4-p}\text{Pd}_9$  and III is eutectoid  $\text{Ga}_{1-x}\text{Sn}_x\text{Pd}$  and  $\text{Ga}_{2+p+q}\text{Sn}_{4-p}\text{Pd}_9$ .

According to the Gibbs phase rule, the HT phase must decompose into three low-temperature phases, since an eutectoid is an invariant point and therefore no degree of freedom is available [42]. However no further phase, besides  $\text{Ga}_{1-x}\text{Sn}_x\text{Pd}$  and  $\text{Ga}_{2+p+q}\text{Sn}_{4-p}\text{Pd}_9$  was found. Due to the fine-grained texture of the eutectoid, direct EPMA measurements of the individual grains were difficult, and the phases could sometimes only be detected by XPD measurements and indirect assignment by comparing XPD data and microprobe data. However, in the present case  $\text{Ga}_{1-x}\text{Sn}_x\text{Pd}$  and  $\text{Ga}_{2+p+q}\text{Sn}_{4-p}\text{Pd}_9$  can be proven to be a constituent of the eutectoid, since sufficiently large single-phase regions are present (fig. 4.2). A third phase may either be below the XPD detection limit or the adjacent HT phase decomposes into the neighbouring phases  $\text{Ga}_{1-x}\text{Sn}_x\text{Pd}$ ,  $\text{Ga}_{2+p+q}\text{Sn}_{4-p}\text{Pd}_9$  and  $\text{Ga}_{1-x}\text{Sn}_x\text{Pd}_2$ , which could be identified in the XPD refinements, but could hardly be assigned to any grains in the eutectoid texture. The experiments of region R5 are very close to the eutectic composition, since here the lowest liquidus temperatures (just above  $900^\circ\text{C}$ ) were measured and typical fine-grained textures, as described above, are present (fig. 3.21). In experiments with starting compositions in the regions R3 and R7, additional signals occur in the DTA cooling curves between the onset of

the primarily solidified phase and the eutectic. These may either be connected to a peritectoid decomposition or to the crystallization path reaching the univariant line, between two primary solidification fields. In that case nucleation of the neighbouring phase would cause an exothermic signal. Evidence exists for both and it is assumed that both occur. The first, peritectoid decomposition of formerly crystallized grains, occurs especially in region R7 in the form of polycrystalline lamellae in the phase  $\text{Ga}_{2+p+q}\text{Sn}_{4-p}\text{Pd}_9$  (fig. 3.25: peritectoid decomposition in primarily solidified grains. Fig. 3.11, section II: peritectoid decomposition of secondarily solidified grains). Evidence for the second (the crystallization path reaching the univariant line) can be found as two-phase (striped or dotted) textures between the primarily solidified grains and the eutectic gap fillings (well visible in fig. 3.9, c, as well as in fig. 3.11 at the transition between sequence I and II). The difference whether such an univariant two-phase region (eutectic channel) is striped or dotted depends on the cutting angle of the investigated surface since the real texture is typically either dendritic, rod-like or lamella-like and accordingly typically shaped comparable to directionally solidified eutectic textures [71, 72].

In the Bridgman experiment QX689-B, the crystallization path can be understood well in the first part: After the crystallization of the primary phase  $\text{Ga}_{1-x}\text{Sn}_x\text{Pd}_2$  on the liquidus surface (fig. 3.11, I), the crystallization path reaches the univariant line between the primary solidification areas of the phases  $\text{Ga}_{1-x}\text{Sn}_x\text{Pd}_2$  and  $\text{Ga}_{2+p+q}\text{Sn}_{4-p}\text{Pd}_9$ . A striped, lamellar sequence follows where the crystallization of the two phases occurs parallel, in the eutectic channel.  $\text{Ga}_{2+p+q}\text{Sn}_{4-p}\text{Pd}_9$  shows peritectoid decomposition, which appears in the form of  $\text{Ga}_{1-x}\text{Sn}_x\text{Pd}$  precipitates (dark in the BSE image in fig. 3.11, II). In the later-crystallized section, the crystallization path is more difficult to explain: Parallel structures of  $\text{Ga}_{1-x}\text{Sn}_x\text{Pd}_2$  and  $\text{Ga}_{2+p+q}\text{Sn}_{4-p}\text{Pd}_9$  continue to occur, but this time they form large dendrites. Their internal lamellae structure continues like in the sequence before. However, in-between the dendrites, the texture is fine-grained, eutectic-like. This cannot be explained by the chronological sequence of an equilibrium crystallization path, since the eutectic texture should only appear in the end (the upper part) of the ampoule. The following scenario explains the experimental finding: After having started with stable growth conditions, crystallization reached the eutectic channel (fig. 3.11, section II) and the average melt composition changed to higher (Ga,Sn)-contents leading to progressively lower liquidus temperatures. In the special geometry of the Bridgman ampoules with narrow diameters, effective material transport is hindered making complete mixing impossible. Instead, (Ga,Sn)-rich melt accumulates in a narrow region adjacent to the growth interface. This is the typical situation that has been described as constitutional supercooling by Tiller (section 2.2.5, equation 2.1) [58]. The risk of a morphologically unstable growth front is even higher in metallic melts with high thermal conductivity, leading to low thermal gradients. The consequence is an unstable growth interface and dendritic growth [56, 57]. Two-phase dendritic growth in an eutectic channel, from incongruent metallic three-phase systems is known and characterized. It shows comparable problems as single crystal growth from incongruent solution, such as constitutional supercooling [73]. Bridgman growth of metallic compounds tends to constitutional supercooling even more, since the setup is convection-stable. That prevents mixing in the ampoule and limits transport processes to diffusion only [74]. Especially in low-diameter vertical ampoules buoyancy-driven convection

is hindered while forced convection can only be carried out with high effort. As a result, the excess component is always enriched at the growth interface, leading to constitutional supercooling and consequently unstable dendritic growth may occur and the melt tends to be trapped between the dendrites. This process can be seen in section III in fig. 3.11, where fine-grained residual melt solidified between long-ranging dendrites. The phase distribution shows that the component  $\text{Ga}_{1-x}\text{Sn}_x\text{Pd}_2$  is depleted during crystallization in the eutectic channel, compared to  $\text{Ga}_{2+p+q}\text{Sn}_{4-p}\text{Pd}_9$ . As crystallization proceeds, another clear change occurs in the melt (fig. 3.11, transition between sections III and IV). A striped two-phase texture of  $\text{Ga}_{2+p+q}\text{Sn}_{4-p}\text{Pd}_9$  and  $\text{Ga}_{1-x}\text{Sn}_x\text{Pd}$  appears (the phase  $\text{Ga}_{1-x}\text{Sn}_x\text{Pd}_2$  is also present to a small extent), where the crystallization in the eutectic channel reaches the eutectic point. The directional solidification of eutectics is well known and typically forms rod- or lamella-like structures. Since the temperature in the ampoule is not isothermal, the eutectic does not solidify at once at the eutectic temperature, but theoretically proceeds with the lowering of the ampoule, along with the isotherms. As reported, lower solidification rates create larger inter-lamellar spacing, i.e. thicker rods or lamellae since there is more time for separation by diffusion [75–78]. Furthermore, different solidification rates create also different textures. It is reported that ternary intermetallic eutectics may even form a pseudo-two-phase structure at certain low growth rates, where one compound may crystallize spatially separated from the other two phases, exhibiting larger grain sizes and forming rods or hopper crystals [79]. In the present directionally solidified eutectic structure it may be seen very well that partially low crystallization rates created large rod structures as well as spatially slightly different textures (fig. 3.11, section IV). In the further crystallization process, a randomly oriented eutectic texture (with comparably smaller grain sizes) is dominating again. From the above-mentioned literature, it must be concluded that in this region the crystallization rate must have been increased and that fluctuating growth rates are present. Fig. 4.3 from another Bridgman experiment<sup>8</sup> gives an example of an eutectic structure that can only be explained by fluctuating crystallization rates, which results in fluctuating grain sizes. The lack of mixing in the convection-stable Bridgman ampoule might cause fluctuations in the melt concentrations due to diffusion-limited transport, meaning that the system could alternate between reaching the eutectic composition and falling back to the status of the univariant line. Another influence on the crystallization rate may be the low temperature gradient in the metallic melt. Faster crystallization rates until higher-lying regions in the ampoules are reached may be possible. Also latent heat release after a sequence with high growth rate might reduce the subsequent growth rate again. The interplay of the bad mixing, low thermal gradient and latent heat release may cause fluctuations in the growth rates, leading to the special texture in the Bridgman experiments.

---

<sup>8</sup>The Bridgman experiment failed, since the melt separated in the thin ampoule into two pieces, due to the surface tension. Therefore, the experiment was not further characterized.



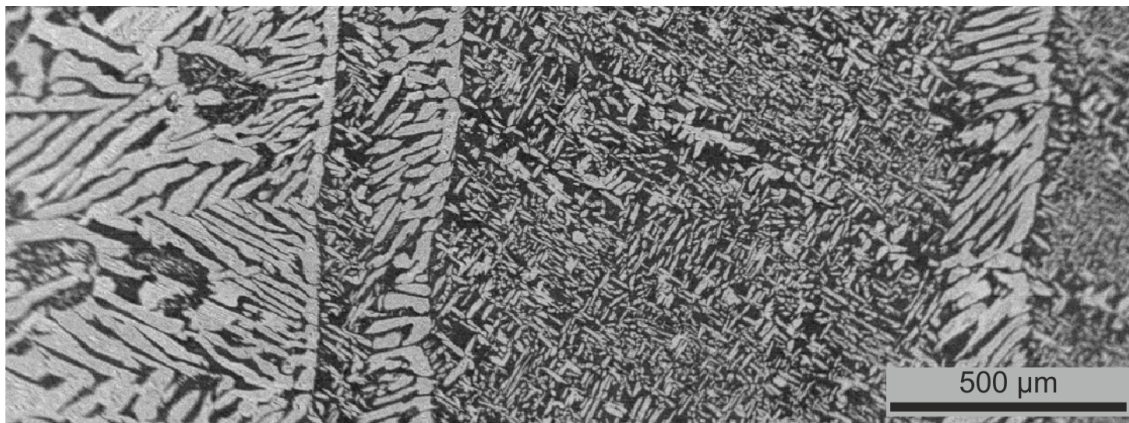


Figure 4.3: BSE image of a directionally solidified eutectic texture in a Bridgman experiment. The brighter phase is  $\text{Ga}_{2+p+q}\text{Sn}_{4-p}\text{Pd}_9$  and the darker phase mostly  $\text{Ga}_{1-x}\text{Sn}_x\text{Pd}$ .

Summarising, in experiments with compositions from the regions R3 and R7, the textures of the equilibrium-cooling experiments are less complicated, compared to that of the Bridgman experiments. They can be clearly separated into three main events: (i) primary crystallization of either the phase  $\text{Ga}_{1-x}\text{Sn}_x\text{Pd}_2$  or  $\text{Ga}_{2+p+q}\text{Sn}_{4-p}\text{Pd}_9$ , (ii) parallel crystallization of the phases  $\text{Ga}_{1-x}\text{Sn}_x\text{Pd}_2$  and  $\text{Ga}_{2+p+q}\text{Sn}_{4-p}\text{Pd}_9$  on the univariant line in an eutectic channel, and (iii) eutectic crystallization of a HT phase and the phases  $\text{Ga}_{1-x}\text{Sn}_x\text{Pd}_2$  and  $\text{Ga}_{2+p+q}\text{Sn}_{4-p}\text{Pd}_9$ . Accordingly, it can be concluded that the additional factors in the Bridgman experiment partially complicated the spatial sequence of crystallization. Nevertheless, their necessity for decoding the crystallization paths cannot be neglected, since the rough order of the three main events in the crystallization paths could be clearly determined only by transferring a time sequence into a spatial sequence.

Experiments with the initial Sn contents of  $0.5 \leq x_L \leq 0.6$ , where  $\text{Ga}_{1-x}\text{Sn}_x\text{Pd}_2$  crystallizes primarily (this corresponds to region R4 in fig. 3.2), have an additional, previous stage of the above-mentioned crystallization path of the regions R3, R5 and R7 (compare the Bridgman experiments QX689-A, fig. 3.18 and QX689-B, fig. 3.11). In that previous stage of the crystallization path, a HT phase is adjacent to the primary crystallization area of  $\text{Ga}_{1-x}\text{Sn}_x\text{Pd}_2$ . After the primary crystallization of phase  $\text{Ga}_{1-x}\text{Sn}_x\text{Pd}_2$  the eutectic channel is entered and parallel crystallization of the phases  $\text{Ga}_{1-x}\text{Sn}_x\text{Pd}_2$  and the HT phase occurs. The HT phase is later decomposed into the phases  $\text{Ga}_{1-x}\text{Sn}_x\text{Pd}_2$ ,  $\text{Pd}_{20}\text{Sn}_{13-x}\text{Ga}_x$  and  $\text{Ga}_{2+p+q}\text{Sn}_{4-p}\text{Pd}_9$ , that form a decomposition texture of lamellae (fig. 3.14, b). In the binary Pd-Sn system the HT phase  $\gamma$  occurs neighbouring to the Pd-rich side of  $\text{SnPd}_2$ . It decomposes into an eutectoid structure of  $\text{SnPd}_2$  and  $\text{Pd}_{20}\text{Sn}_{13}$  [39]. Within the scope of this study, it could not be specified, whether the ternary HT phase is an extension of the binary  $\gamma$  phase or if there is an independent ternary HT phase. In the further crystallization path,  $\text{Pd}_{20}\text{Sn}_{13-x}\text{Ga}_x$  is no longer present and the texture is the same, as described above in the regions R3, R5 and R7. Accordingly, the crystallization path passes a

ternary quasi-peritectic point (P' in fig. 4.1)<sup>9</sup> and continues on the same univariant line between the phases  $\text{Ga}_{1-x}\text{Sn}_x\text{Pd}_2$  and  $\text{Ga}_{2+p+q}\text{Sn}_{4-p}\text{Pd}_9$ . As a result the HT phase is replaced by  $\text{Ga}_{2+p+q}\text{Sn}_{4-p}\text{Pd}_9$  and continues to crystallize parallel with  $\text{Ga}_{1-x}\text{Sn}_x\text{Pd}_2$ . Like in the regions R3, R5 and R7, finally the eutectic,  $E_2$ , is reached.

The phase  $\text{Pd}_{20}\text{Sn}_{13-x}\text{Ga}_x$  was found in the XPD measurement (2 wt.%) of the very end of the Bridgman experiment (where the eutectic,  $E_2$ , is expected) but neither in the equilibrium-cooling experiments with the same starting composition, nor in the equilibrium-cooling experiments of the regions R3, R5 and R7 that are expected to end in the same eutectic,  $E_2$ . Here, further clarification is necessary.

Experiments with initial compositions according to region R8, crystallize in the primary crystallization region of  $\text{Ga}_{2+p+q}\text{Sn}_{4-p}\text{Pd}_9$ . However, in contrast to the experiments from region R7 (sharing an univariant line with  $\text{Ga}_{1-x}\text{Sn}_x\text{Pd}_2$ ), crystallization paths of these experiments proceed to lower Pd contents and are not related to the above-mentioned paths. Experiments with initial compositions in region R8 do not contain  $\text{Ga}_{1-x}\text{Sn}_x\text{Pd}_2$  and, as shown in fig. 3.44, a, section 3.1.4.3, they contain the secondarily formed phase  $\text{Ga}_{1-x}\text{Sn}_x\text{Pd}$  with a Sn-rich composition,  $\text{Ga}_{0.89(2)}\text{Sn}_{0.11(2)}\text{Pd}$  (in the regions R2-R7 the phase always has the composition  $\text{Ga}_{0.93(2)}\text{Sn}_{0.07(2)}\text{Pd}$ ).

### 4.1.3 Sn substitution in the phase $\text{GaPd}_2$

Regarding the influence of the Sn substitution in the phase  $\text{GaPd}_2$ , the Sn content,  $x$ , in  $\text{Ga}_{1-x}\text{Sn}_x\text{Pd}_2$ , increases with increasing Sn content in the melt,  $x_L$ <sup>10</sup>. Accordingly, the pseudobinary segregation coefficient,  $k^*$ , is close to 1, meaning that the same proportion of Ga, that is replaced by Sn in the melt, is also substituted in the crystal. This was the basis for estimating the initial Sn contents for the Czochralski experiments, in order to grow the desired compositions. Data gained from the Czochralski-grown single crystals, i.e. obtained from very close-to-equilibrium conditions, give more detailed information about segregation, discussed in section 4.2.5.

The measured lattice parameters in the phase  $\text{Ga}_{1-x}\text{Sn}_x\text{Pd}_2$  clearly increase with increasing Sn content,  $x$ . Figs. 3.37 and 3.60 show that the increase is not linear, which was confirmed by [18]. In the region of  $x \leq 0.4$ , very precise data could be collected from homogeneously grown Czochralski crystals by XPD. The data gained from Rietveld refinement are tabled in tab. 3.15. In most experiments secondarily formed  $\text{Ga}_{1-x}\text{Sn}_x\text{Pd}_2$  has similar lattice parameters (fig. 3.41). This is a clear hint that these secondarily formed grains have all the same origin, i.e. as discussed above, predominantly an eutectic origin. The only exceptions are experiments from compositions of  $x_L \leq 0.2$  and of  $x_L = 0.7$ . For the latter, the compositions were calculated as  $\text{Ga}_{0.53(5)}\text{Sn}_{0.47(5)}\text{Pd}_2$  from the refined lattice parameters.

Regarding crystals, grown from melts with similar Pd contents,  $y_L$ , the respective Sn content of the resulting crystals has a significant influence on the liquidus temperature of the crystal (fig. 3.58). In the case of  $\text{Ga}_{1-x}\text{Sn}_x\text{Pd}_2$ , grown from melts with a Pd content of  $61 \leq y_L \leq 61.5$ , the liquidus temperatures decreased by

<sup>9</sup>A ternary quasi-peritectic point in a ternary phase diagram is an invariant point, where three univariant lines meet. In contrast to a ternary peritectic point, where one crystallization path enters the point and two leave, in the quasi-peritectic point two paths enter the point and one path leaves the point (always to lower temperatures) [42].

<sup>10</sup>According to the description  $(\text{Ga}_{1-x_L}\text{Sn}_{x_L})_{100-y_L}\text{Pd}_{y_L}$ .

60 K within the range of  $x = 0$  to  $x = 0.4$ . However, the initial Pd content has the higher influence on the slope of the liquidus surface (fig. 3.32), what could already be expected from the binary Ga-Pd system. EPMA measurements indicate that Sn substitution for Ga causes slight deviations from the exact 1:2 stoichiometry, i.e. an increase of  $y$  with  $x$  in the crystal (fig. 3.55). This means that  $\text{Ga}_{1-x}\text{Sn}_x\text{Pd}_2$  has either Ga sites occupied by Pd, or vacancies on the Ga positions at higher Sn contents,  $x$ . However, single crystal X-ray diffraction (XSD) results of these crystals did not confirm this, yet [80].

In the investigated phase diagram region, the miscibility of the phases  $\text{GaPd}_2$  and  $\text{SnPd}_2$ , published by [18] for 500°C, could be confirmed by the equilibrium-cooling experiments, also down to room temperature. Accordingly, effects, such as spinodal decomposition due to retrograde solubility of Ga in  $\text{GaPd}_2$  with decreasing temperatures, as discussed in binary  $\text{GaPd}_2$  [11, 81], could be excluded. In few grains of the phase  $\text{Ga}_{1-x}\text{Sn}_x\text{Pd}_2$ , grown in equilibrium-cooling experiments, lamellae of  $\text{Ga}_{2+p+q}\text{Sn}_{4-p}\text{Pd}_9$  can be found (fig. 3.9, d), which could be interpreted as decomposition effects. However, these occurred only in experiments with initial compositions, located next to the outer rim of the primary crystallization field of  $\text{Ga}_{1-x}\text{Sn}_x\text{Pd}_2$ .

No signs of decomposition could be found in any Czochralski-grown single crystal.

#### 4.1.4 Sn substitution in further phases

Having a look at the ternary phase  $\text{Ga}_{2+p+q}\text{Sn}_{4-p}\text{Pd}_9$ , it stands out that the measured stability region is larger, compared to the data published by [18] (fig. 4.1). Ga contents of up to  $n_{\text{Ga}} 23$  at.% could be measured, meaning that  $n_{\text{Ga}}$  and  $n_{\text{Sn}}$  are almost equal, while published Ga contents are lower, in the range of  $13 \leq n_{\text{Ga}} \leq 18$  [18]. In the present study, solidification was equilibrium-close. However, the applied cooling rates may be still too high for solid-solid phase transitions, like the peritectoid decomposition of  $\text{Ga}_{2+p+q}\text{Sn}_{4-p}\text{Pd}_9$ . In the present study decomposition of  $\text{Ga}_{2+p+q}\text{Sn}_{4-p}\text{Pd}_9$  could be proven and the precipitation of Ga-rich phases shows a retrograde solubility of Ga in  $\text{Ga}_{2+p+q}\text{Sn}_{4-p}\text{Pd}_9$  with decreasing temperatures. However, the peritectoid decomposition may be inhibited kinetically or at least not completed at temperatures higher than 500°C. As a result, the measured compositions of  $\text{Ga}_{2+p+q}\text{Sn}_{4-p}\text{Pd}_9$  represent the stability range at higher temperatures than 500°C. In contrast, Matselko et al. [18] annealed the constituents at 500°C for weeks to months creating an equilibrium-close composition range of  $\text{Ga}_{2+p+q}\text{Sn}_{4-p}\text{Pd}_9$  for 500°C. Accordingly, the present study shows that  $\text{Ga}_{2+p+q}\text{Sn}_{4-p}\text{Pd}_9$  has a higher stability range, i.e. a higher Ga solubility at higher temperatures than 500°C.

The Pd contents have always been measured in the range of 59-62 at.% and in contrast to Ga and Sn, there are no significant differences in the whole composition range. The lattice parameter,  $a$ , depends on the Ga-Sn ratio and increases with increasing  $n_{\text{Sn}}$  and decreasing  $n_{\text{Ga}}$  (fig. 3.43).

Regarding the phase  $\text{Pd}_{20}\text{Sn}_{13-x}\text{Ga}_x$ , analogue to the phase  $\text{Ga}_{2+p+q}\text{Sn}_{4-p}\text{Pd}_9$ , a dependence of the lattice parameters from the Ga and the Sn contents could be established, however based on a small data base (fig. 3.48). Both lattice parameters  $a$  and  $c$  increase with increasing Sn contents and decreasing Ga contents, while the Pd contents do not influence the unit cell. Lattice parameter  $c$  increases stronger than  $a$  (figs. 3.48 and 3.47).

Regarding  $\text{Ga}_{3-x}\text{Sn}_x\text{Pd}_5$ , the largest measured composition was  $\text{Ga}_{2.81(3)}\text{Sn}_{0.16(3)}\text{Pd}_{5.03(3)}$ . Hence, comparable to  $\text{Ga}_{1-x}\text{Sn}_x\text{Pd}$ , the substitution limit is low.

## 4.2 Single crystal growth of $\text{Ga}_{1-x}\text{Sn}_x\text{Pd}_2$

### 4.2.1 Crystal growth and growth parameters

Single crystals of  $\text{Ga}_{1-x}\text{Sn}_x\text{Pd}_2$ , with  $x = 0.1, 0.2, 0.3$  and  $0.4$ , could be grown from (Ga,Sn)-rich solution. According to the phase diagram studies, single crystal growth from solution would be possible with Sn substitution up to  $x = 0.54$ . However, since the maximum catalytic activity depending on the respective Sn content of the solid solution  $\text{Ga}_{1-x}\text{Sn}_x\text{Pd}_2$  has been reported to be at  $x = 0.28$ , the aim to grow crystals with all interesting compositions for this research project, in the vicinity of  $x = 0.28$ , could be achieved.

During the first stages after seeding, it was observed that all crystals behaved relatively stable and reacted slowly to temperature changes. This can be explained by a steep liquidus surface being confirmed by the DTA experiments. Those experiments display a liquidus temperature change of 200 K in a composition range of 58–62 at.% Pd. That also corresponds to the observed working setpoint (WSP) temperatures of the growth experiments. However, the absolute WSP temperature differences between the beginning and the end of the crystal growth are not significant. Since the crystal-melt volume ratio changes during the experiments, the heat transport in the system is changed and the position of the growth interface changes in relation to the position of the heater. Some smaller effects may also play a role. It was mentioned that in few cases a separation between the melt and the crystal took place, since changes of the diameter and the crystallization progress were very slow. This should not be confused with the separation of the melt and crystal due to unstable crystal growth, as reported in section 3.2.2 and discussed in section 4.5, in the case of  $\text{Ga}_{1-x}\text{Sn}_x\text{Pd}$ . In contrast, the separation of  $\text{Ga}_{1-x}\text{Sn}_x\text{Pd}_2$  from the melt did not take place by partial dissolution of the seed, but occurred because the crystallization rate was lower than the pulling rate, due to too moderate cooling programs. This was obvious because the grown crystal was usually longer than the initial seed after the separation. Also, first diameter increase and later decrease (sometimes even with growth facets) indicated that the crystal did not dissolve, but a decrease in diameter (not visible by the operator) led to a separation from the melt. This result was considered for later growth experiments and by stronger cooling programs stable diameter increase was achieved also during the first millimeters.

After seeding, during the growth of the shoulder, it seemed like the crystal was completely wetted, even when it had already reached 5–6 mm in diameter. This phenomenon was reported in Czochralski growth of intermetallics at similar conditions in the case of InPd where the good wetting properties of the melt in combination with evaporation (due to the higher vapour pressure of In) caused dendrite-like roughness on the crystal surface [82]. Also, in the solid solution  $\text{Si}_x\text{Ge}_{1-x}$  a melt layer wetting the crystal 10–12 mm above the melt surface was reported [83]. If the crystal has a tangential contact to the melt in the microscopic scale, the contact angle approaches zero. In such a case, the consequence would be a total wetting of the

crystal [84]. However, in the case of  $\text{Si}_x\text{Ge}_{1-x}$  the layer was reported to partly dissolve the seed and the already grown crystal, forming a polycrystalline surface layer [83]. No evidence for such a process could be observed here. A simpler explanation might be that the shiny metallic surface of the crystal and the metallic surface of the melt could not be distinguished visually. Especially during the growth of the shoulder, i.e. during the diameter increase, the angle at the three-phase boundary between crystal and the meniscus is very large. In such a case no remarkable change between crystal and melt might be visible. In addition, the bad optical conditions at high temperatures increase the difficulties of observation. According to Planck's radiation law, at the applied growth temperatures of approx.  $1000^\circ\text{C}$ – $1250^\circ\text{C}$  higher wavelengths of the visible light such as yellow and red are disproportionately represented [46]. The attempt to cut off these high-intensity wavelengths with shortpass filters and thus, make the contrasts in the growth chamber more visible, proved to be successful.

### 4.2.2 Inclusion formation

The very first Czochralski-grown crystal showed mother liquid inclusions (fig. 3.51). Due to the incongruent crystal growth, i.e. the crystal being richer in Pd than the melt, the solvents Ga and Sn are enriched as excess components, while the solute Pd is depleted in the region below the growth interface. Accordingly, excess Ga and Sn need to be removed from the growth interface, in order to continue the crystal growth. The usual principle in Czochralski growth for homogenizing the melt is the rotation of the growing crystal with respect to the melt. However, while the forced convection by rotation works in the bulk melt, the layer next to the crystal is diffusion-dominated, meaning the transport of the solvents away from the phase boundary is slow [55]. Accordingly, the danger of constitutional supercooling as described in section 2.2.5 is present, since the melt right next to the crystal has a higher solvent concentration,  $C_L$ , than the bulk melt,  $C_0$  (fig. 2.4). Constitutional supercooling means that the solution with higher solvent concentration,  $C_L$ , has a lower liquidus temperature. As a result, the Ga- and Sn-enriched layer solidifies later than the bulk melt and the melt tends to an unstable growth interface, leading to dendritic growth, cellular growth, or trapping of liquid [55–57]. Tiller's equation (equation 2.1, section 2.2.5) shows that in the case of constitutional supercooling the risk of an unstable growth interface is large with either a low temperature gradient in the melt or a high growth or pulling rate, respectively. Since metallic melts are known to have a high thermal conductivity and accordingly a low thermal gradient, inclusion formation in Czochralski growth of intermetallics is likely to occur, if the pulling rates are not low enough. Recognising the theory, all later crystals, except the first one, have been grown with lower pulling rates and resulted in inclusion-free crystals. The resulting time-consuming growth process is challenging since the growth apparatus needs to be kept stable for weeks.

The inclusions in QX649-II (fig. 3.51) show dendrites of  $\text{Ga}_{1-x}\text{Sn}_x\text{Pd}_2$  and  $\text{Ga}_{3-x}\text{Sn}_x\text{Pd}_5$ . During further cooling the material in the liquid inclusion crystallizes continuously. The Czochralski growth was terminated before the crystallization path reached the edge of the primary crystallization region of  $\text{Ga}_{1-x}\text{Sn}_x\text{Pd}_2$ , i.e. before crystallization of two phases starts in the eutectic channel. Subsequently, it is expected that in the liquid droplet  $\text{Ga}_{1-x}\text{Sn}_x\text{Pd}_2$  at first grew according to the lattice

of the surrounding single crystal and at the end of the experiment when the crystal was separated from the melt and then cooled to room temperature, with 200 K/h, the rate was too high for stable growth and the remaining liquid grew dendritically. (First  $\text{Ga}_{1-x}\text{Sn}_x\text{Pd}_2$  and  $\text{Ga}_{3-x}\text{Sn}_x\text{Pd}_5$  grew simultaneously in the eutectic channel and later the eutectic solidified.)

### 4.2.3 Growth interface

When considering the risk of inclusion formation, the shape of the growth interface must also be considered. The grown crystals showed that both concave<sup>11</sup> and convex interfaces occur in this system (fig. 3.56 and tab. 3.13). Furthermore, sometimes features of both shapes are combined. The reason for the respective shape is not entirely clear. The shape of the phase boundary is preserved only in the state, in which the crystals were separated from the melt. Therefore, based on the available data, it cannot be evaluated how the state of the phase boundary changes during growth. The results show that neither the Sn content nor the pulling direction influence the shape of the phase boundary. The only systematic correlation that was found, is the phase boundary being concave if the diameter of the crystal was in a decreasing state in the moment when the melt and the crystal were separated. Vice versa, the growth interface was found to be convex if the diameter was in an increasing state in the moment of separation from the melt. An explanation might be that thermal radiation from the crystal has a large effect in Czochralski growth at high temperatures [85]. At high temperatures, (in this case more than 1250°C) heat transfer is dominated by radiation, according to Planck's radiation law [46]. Hence, conductive heat transport becomes less important but the importance of radiation from the crystal to the environment increases. In silicon crystal growth it is assumed that the heat, passing the growth interface, is completely dissipated by radiation from the crystal's surface during the first centimeters above the melt [85]. In the present system where crystal and melt volume and the crystallization rates are significantly smaller, the radiation might even play a larger role in the temperature balance, especially since conduction as transport mechanism is limited. The crystals are only 1–3 cm<sup>3</sup> in size and further heat transport is limited by the alumina seed holder which has poor thermal conductivity. The thermal radiation is usually reduced by the construction items of the growth apparatus. In this case the crystal is directly surrounded by the crucible wall and the heater (fig. 2.2). If the diameter increases, i.e. the crystal deviates from its cylindrical shape, the radiation is directed more towards the upper part of the apparatus and is therefore less reflected. Accordingly, a heat loss towards the upper, colder part of the apparatus is enabled. Even though heat deflection shields are placed above the crystal, radiation towards the upper part of the apparatus is the most effective way to remove heat from the growth chamber. Meaning when the crystal increases its diameter, heat from the side where the meander heater is placed is increasingly removed upwards by radiation. As a result, upwards heat flow at the solid-liquid interface is increased and the isotherms tend to be curved downwards leading to a convex growth interface. Vice versa, in an decreasing diameter state heat radiation towards the upper part of the growth chamber is reduced by the crystal itself. Consequently, the up-

---

<sup>11</sup>In crystal growth, the terms concave and convex are always used from the perspective of the crystal.

wards heat flow is reduced, and heat accumulates below the crystal. As a result, the isotherms are curved towards the crystal and create a concave growth interface. A concave phase boundary might increase the risk of trapping inclusions, especially in the case of (Ga,Sn)-rich growth of  $\text{Ga}_{1-x}\text{Sn}_x\text{Pd}_2$ , where the solution below the growth interface is enriched by the excess components Ga and Sn and therefore has a lower density than the bulk solution. Being trapped beneath the concave crystal, would hinder the excess components to be removed from the interface and thus, increase the risk of constitutional supercooling. However, the results of the crystal growth show that the growth rates were low enough. Additionally, simulations on closely related systems with exactly the same scale and crucible shape (however with far higher rotation rates) have shown that a concave phase boundary might even increase the mass flow towards the growth interface and accordingly mixing of the melt could be even improved, compared to a convex growth interface [86]. Therefore, it cannot be generally assumed that a concave growth boundary has a negative effect.

#### 4.2.4 Low-angle grain boundaries

Several investigations, i.e. BSE images, X-ray topography (XRT), Laue scans, electron backscatter diffraction (EBSD) and rocking curve analysis, have shown that Czochralski-grown  $\text{Ga}_{1-x}\text{Sn}_x\text{Pd}_2$  crystals exhibit subgrains. As no tilt angles between the grains exceed  $2.5^\circ$ , the boundaries are low-angle grain boundaries (LAGB). LAGB are a planar array of dislocations. They usually consist of a network of both components, edge and screw dislocations. Since dislocations are able to move, they may merge into two-dimensional arrangements that are favourable in terms of the resulting elastic stresses [87]. The origin for the formation of LAGB is similar to the origin of dislocations and accordingly if the origin for the formation of LAGB is discussed, the sources of dislocations must be regarded. The most abundant sources for dislocations in crystal growth are mismatches between the seed (or the substrate) and the crystal resulting in internal stress. Furthermore, condensation of point defects, inclusions (melt trapping) and thermal stresses lead to dislocations [87]. In Czochralski growth it is well known that dislocations result from residual dislocations of the seed or especially from the thermal shock, when the seed touches the melt for the first time [53, 88].

LAGB have already been observed in Czochralski-grown intermetallics under comparable conditions [89]. There, the formation of LAGB was caused by the formation of inclusions and by thermal tensions due to thermal radiation from the crystals shoulder to the surrounding. In contrast, in the present study the XRT  $\omega$  scan shows in the case of the crystal QX684 (fig. 3.66) the subgrains originate from the seed and then propagate parallel to the growth direction. Only few LAGB propagate inclined to the growth axis. Some subgrains vanish at the side of the shoulder, meaning that the shoulder is no source region for LAGB, like observed in other intermetallic systems due to thermal stresses [89]. Accordingly, the thermal shock when the crystal touches the melt surface for the first time is expected to be the main reason for dislocation formation here. The  $\omega$  scan shows the seed being finely sub-grained. A change of the lattice parameters from the pure  $\text{GaPd}_2$  seed to the  $\text{Ga}_{0.6}\text{Sn}_{0.4}\text{Pd}_2$  crystal, according to section 3.3.2, may be considered as reason for tensions, too. Fig. 3.66 shows that the first millimeters of the crystal,



directly after the seed, are strongly disrupted, with numerous small subgrains and tilts. Regarding the analysed crystal, shown in fig. 3.66 ( $x = 0.4$ ), the calculated mismatch,  $m = \frac{m_{\text{crystal}} - m_{\text{seed}}}{m_{\text{seed}}}$ , between seed and crystal is 1.7 % in the case of lattice parameter  $a$ , and 2.4 % in the case of  $c$ . Hence, the LAGB observed in the crystal QX684 may result on the one hand from the thermal shock during seeding and on the other hand from tensions, formed by the lattice mismatch of the shared (010) interface between the seed and the chemically different crystal.

The common method to remove dislocations and to avoid their propagation into the growing crystal is the so-called Dash necking, i.e. a diameter reduction after seeding in order to increase the probability of dislocations gliding outwards the crystal [53]. The choice of a proper growth direction in order to encourage the outgrowth along a preferred crystallographic plane is necessary. In the most common industrial Czochralski-grown materials, like Si and Ge, the  $\langle 100 \rangle$  directions are chosen as growth directions, since dislocations glide preferentially in the  $\{111\}$  planes of the cubic phase and accordingly glide out of the crystal [90]. However, LAGB were observed for the first time in Czochralski-grown  $\text{Ga}_{1-x}\text{Sn}_x\text{Pd}_2$  and thus their favourable growth (or preferred dislocation glide planes) are unknown in  $\text{Ga}_{1-x}\text{Sn}_x\text{Pd}_2$ . In the present growth experiments Dash necking was not considered a feasible method since the dimensions of the used seeds are already very small and thinner diameters are technically hardly feasible. This is due to the challenging diameter control and the necessary mechanical stability. Additionally, Dash necking seems to be unpromising, regarding the very high typical dislocation densities for as-grown brittle metallic materials that are in the range of  $10^6 - 10^7 \text{ cm}^{-2}$  [91, 92]. The only remaining method of reducing the abundance of dislocations in the present experiments is dissolving a few millimeters of the seed, after the seeding process was successful, in order to dissolve the area of the seed, that experienced the largest thermal shock. As the results show, this method could not prevent the previously discussed origins for the LAGB. According to the XRT  $\omega$  scan (fig. 3.66), already the seed contains numerous sub grains. An investigation, whether these subgrains (or conditions that may form subgrains at high temperatures) were already present in the seed (E.g. in section 4.3 a sub-surface damage layer induced by cutting with the wire lapping saw was discussed.), or if they have formed as a result of seeding was not clarified. The lattice parameter mismatch however could have been overcome by using seeds with similar, or at least less different composition.

The initially numerous subgrains, directly below the seed, are replaced by fewer larger subgrains with larger tilts, already a few millimeters lower. This can be seen in the XRT  $\omega$  scan of QX684 (fig. 3.66). The rocking curve examination of the crystal is in good agreement with the  $\omega$  map (fig. 3.65, a). Also in the rocking curves the tilt between two measured major peaks, i.e. subgrains in the centre of the crystal, increases from  $0.25^\circ$  to  $0.50^\circ$ , from the upper, i.e. earlier grown part, to the bottom, i.e. later grown part of the crystal. Additionally, smaller additional maxima in the rocking curves, between the larger peaks in the upper part of the crystal do not appear in the measurement of the bottom part of the crystal. This shows that in the upper parts additional smaller grains were measured in the same area with tilts that are in-between the larger measured grains. In the later-grown parts the smaller peaks are not present and the tilts of the larger grains have increased. The propagation behaviour of LAGB during progressing crystal growth is complex and it is rarely addressed in the case of intermetallic phases in literature. However,

the observation that larger subgrains have larger tilts towards each other, than smaller subgrains was confirmed in the case of different metals, semimetals and salts [93–95]. Several authors distinguished between different kinds of subgrains, defined by different sizes and tilt angles. During cooling, relaxation takes place and smaller subgrains (microsubgrains and equiaxial subgrains), which exist within larger subgrains (macrosubgrains) merge, while the larger subgrains keep their size but increase their tilts. Therefore, larger subgrains, which previously contained larger amounts of dislocations and smaller subgrains, have higher tilts compared to smaller subgrains [87, 93, 94]. The tilts, observed in the present crystals ( $0.3\text{--}2^\circ$ ) are in the typical range of macrosubgrains and smaller subgrains, with tilts of only a few arc minutes, are below the investigation limit. In the figs. 3.66, 3.67 and 3.68, a, it can be seen that in the region directly below the seed the amount of subgrains is very high (with low tilts) while later few subgrains remain. This is in contrast to reports that the number of subgrains increases with increasing ingot length [95, 96]. However, while this may apply to microsubgrains and equiaxial subgrains, the amount of macrosubgrains was also observed to decrease with vanishing LAGB [96]. Furthermore, it is known that new dislocations form at the growth interface while previously formed dislocations (or subgrains) continue to grow with the growth interface, leading also to an increase of the subgrain tilt with increasing ingot length [95, 96]. All the above-mentioned reports have in common, that LAGB occur at high dislocation densities, typically above the value of  $10^5\text{ cm}^{-1}$ .

Further rocking curves on different crystals and orientations differ, but the usual shape is broadened ( $\text{FWHM} \approx 0.2\text{--}0.5^\circ$ ), partly with peaks standing out. This means more than one subgrain was measured. (An exception is one measurement in QX667 shown in fig. 3.65, c, where only one single peak was observed.) If measured with the goniometer axis perpendicular to the growth axis, the curves have a similar FWHM but with fewer or no peaks standing out. That means sharp tilts are predominantly parallel to the growth directions while the tilts perpendicular to the growth directions are either regular transitions or fine mosaicity. In the EBSD measurements on slices of the crystal QX674, larger orientation contrasts have been measured only perpendicular to the growth axis [010] (fig. 3.71) which does not match the XRT and the rocking curve results. However, the occurring tilts are in the range of the angular resolution of EBSD and identifying LAGB below  $0.5\text{--}1^\circ$  by EBSD takes high effort [97]. Regarding all applied methods, LAGB are present in all investigated orientations and occur independently of the growth directions of the crystals. Rocking curves indicate that also crystals with lower Sn contents have LAGB but here more detailed studies, e.g. on binary  $\text{GaPd}_2$ , might answer if a mismatch, due to chemically induced lattice parameter changes, is one of the reasons for the formation of LAGB.

Most of the tilts between the subgrains were observed to be below  $1^\circ$ , typically in the region  $0.5^\circ$ . As a result, it is expected that the present LAGB have no significant negative influence on the purpose of the crystals in the present project as catalytic model material. Since the prepared surfaces will be vicinal faces of the desired crystallographic planes with only few terraces, the catalytic behaviour will be dominated by aimed crystallographic surface planes.

### 4.2.5 Segregation effects

The pseudobinary segregation coefficients,  $k^* = \frac{x}{x_L}$ , of the pre-experiments are fluctuating around the value 1, while  $k^*$  of the Czochralski experiments tend to be slightly below 1. However, the deviation from the value 1 is low and with higher Sn contents,  $x$ ,  $k^*$  approaches 1, also in the Czochralski experiments. Accordingly, with higher Sn contents in the melt and the crystal, the preference of Ga over Sn decreases.

The data of the pseudobinary segregation between Ga and Sn from the first-to-freeze parts of the Czochralski-grown crystals are much more precise, compared to the data of the pre-experiments (fig. 3.54). The pseudobinary segregation coefficient,  $k^*$ , is calculated from the first-to-freeze composition of the crystals. This part can be identified clearly and measured precisely in the Czochralski crystals only. From the crystals pieces of 50–100 mg allow precise chemical analyses, carried out by the Max-Planck-Institut für Chemische Physik fester Stoffe in Dresden via digestion-assisted ICP-OES. Furthermore, the Czochralski crystals were grown under equilibrium-close conditions while the pre-experiments may be affected by supercooling due to the lack of a seed, from which crystallization may start. When supercooling collapses and accordingly sudden, fast crystallization sets in, the segregation coefficient is influenced by restricted kinetics. A segregation coefficient influenced by high crystallization rates, approaches the value 1 [98]. A complicating factor in the pre-experiments is that, due to the absence of a seed, and the resulting typical supercooling, usually many crystallites are formed. As a result, it may be experimentally complicated to identify the first-to-freeze grains in such a experiment and to analyse it chemically reliably. This is in accordance with the measured pseudobinary segregation coefficients  $k^*$  (fig. 3.54).

The pseudobinary segregation coefficient,  $k^*$ , below 1 means Sn is rejected at the growth interface and therefore enriched in the melt. Accordingly, the concentration increase of Sn in the melt leads to an increase of the Sn content along the growth axis of the Czochralski crystals as it was measured and shown in fig. 3.53. However, even though the pseudobinary segregation coefficients  $k^*$  are only slightly smaller than 1 or even 1, the Sn content increases in all crystals. That means that with decreasing Pd content in the melt  $y_L$  and decreasing growth temperatures Sn is preferably incorporated into the crystal.

The X-ray topography  $\omega$  scan showed a drift of the  $\omega$  angle in each subgrain from the upper to the bottom part of the investigated crystal (fig. 3.66; Note: the more pronounced  $\omega$  changes within the subgrains will be addressed later). This drift might not be a curvature of the lattice, but more likely represents the increase of the Sn content along the pulling direction [010], as measured and shown in fig. 3.53. According to fig. 3.15 an increase of the Sn content,  $x$ , in the crystal causes an increase of all lattice parameters. Accordingly, when investigating the slice, the increase of  $x$  along the pulling direction [010] results in a change of the position of the investigated 412 peak along the [010] direction. Hence, it is very likely the drift of  $\omega$  is not related to a curvature of the lattice but is caused by a chemical gradient.

### 4.2.6 Striations or artefacts

The X-ray topographs show stripes or band structures, approximately perpendicular to the growth direction (figs. 3.67 and 3.68). It is well known that Czochralski-grown

crystals may show effects of micro segregation, called striations. These are fluctuations in the dopant concentration of the crystal caused by unsteady convective flow, the rotation of the crystal in a temperature field that is not exactly ideally axisymmetric, mechanical vibrations or fluctuations of the power control. Striations usually follow the growth interface and can be related to the rotation periods if relevant [99–102]. Segregation effects between Ga and Sn and the subsequent influence on the lattice spacing (as established in section 3.3.2) would affect the XRT intensity since a scattered peak, previously focused on the lattice spacing of a crystal region with a certain chemical composition, will move out of focus if the chemistry changes. Accordingly, striations could explain the stripes visible in the XRT images. However, reliable statements cannot be made, as the measurement of a comparable sample from binary  $\text{GaPd}_2$  without Sn is missing.

Comparable stripes have also been observed as artefacts, discussed as special extinction effects, in XRT measurements of intermetallic phases [103]. It speaks against striations that the distances of the stripes cannot be correlated with the pulling rate (fig. 3.49, b) but have approximately constant spacings over the whole crystal. Additionally, the periodicity of the rotations is several dimensions higher than the periodicity of the stripes observed with XRT. All the usually discussed reasons for striation formation are related to the rotation of the crystal. In industrial Czochralski growth the time for one rotation is in the range of a few seconds and due to the high pulling rates distances of striations are in the range of micrometers to millimeters [104]. However, due to the extremely low pulling rate that was used in all Czochralski experiments of this study, fluctuating growth conditions would correspond to 10–15 nm regarding the typical pulling rates and rotation rates. In contrast, distances of 250–500  $\mu\text{m}$  between the stripes were observed and accordingly typical striations as the reason for the observed stripes cannot be assumed.

However, as shown in fig. 4.4 the observed stripes show exactly the same picture if measured with  $\text{Cu-}K\alpha$  on the 412 peak or with  $\text{Cr-}K\alpha$  on the 310 peak. Accordingly, measurements from different directions with different radiation result in the same image, indicating that the stripes have a crystallographic origin and are no artefacts. The origin of the stripes remains unclear.

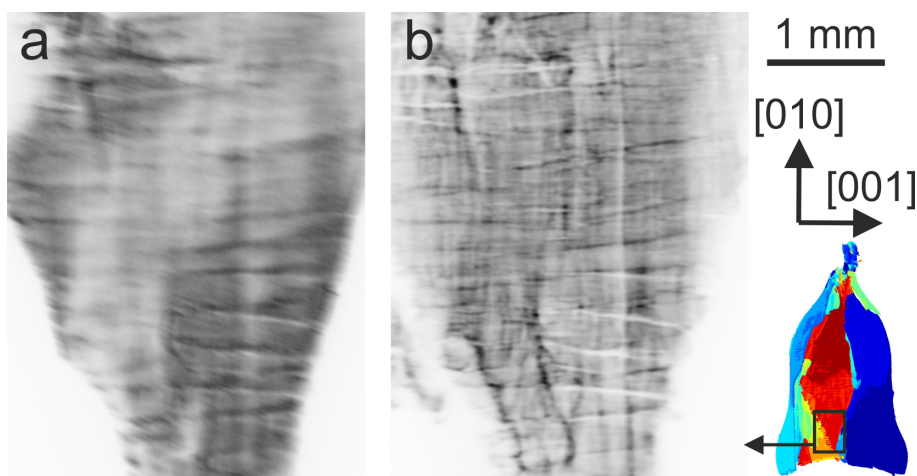


Figure 4.4: Comparison of two X-ray topographs of the same position, measured with different radiation on different reflections. a) Measured with  $\text{Cu-}K\alpha$  on the 412 peak. b) Measured with  $\text{Cr-}K\alpha$  on the 310 peak.

### 4.3 Conditions of prepared crystal slabs for catalytic experiments

First catalytic measurements on crystal slabs of different orientations showed that the tested surface planes behaved similar, regardless of their crystallographic orientation, which was not expected. Furthermore, the catalytic behaviour was different than expected from single-crystalline surface planes but rather similar to the behaviour of a powder: While a powder has high conversion due to the abundance of active sites, and low selectivity since all crystallographic planes are present, a single-crystalline surface plane ( $hkl$ ) should have low conversion and high selectivity [63]. Therefore, the results of mechanical impacts from grinding, lapping and polishing were investigated (described in section 2.4.1.2) and presented in section 3.5. Systematic surface studies are an own research topic and therefore the preparation studies made in this thesis, do not aim on a perfect understanding of the problem, but focus only on the practical preparation of suited surfaces for catalytic measurements. Therefore, the focus was on adapting the mechanical preparation of the single crystalline slabs in such a way that no surface damage could be found, in order to enable catalytic investigations on the surfaces. This aim was achieved.

As shown in the figs. A.2, A.4 and A.6 there are (i) peaks that should not appear on a  $\theta$ - $\theta$  scan of a single crystalline surface and (ii) the main peaks measured on cut and unpolished (or not sufficiently polished) single crystalline surfaces have a lower integrated intensity and a larger full-width half maximum (FWHM) compared to that of polished surfaces. The peaks that should not appear on the surface are at Bragg angles where the XPD pattern of a corresponding powder has its highest peaks. From (i) it can be concluded that there must be a polycrystalline layer on the surface of the single crystalline slabs, creating weak signals of a XPD pattern. Point (ii) indicates that the polycrystalline surface layer absorbs (or diffusely scatters) the scattered signal of the main reflections of the single crystalline surface partly and accordingly the integrated intensities are reduced. Regarding the different investigated orientations, the intensities and shapes of the measured X-ray patterns depend on the crystallographic orientation of the crystal slab. The (010) plane seems to be very sensitive to surface treatments, showing signals after lapping, being in the range of a usual XPD pattern. The (100) and (001) surfaces are far less sensitive, and showed signals only slightly higher than the background. Furthermore, the way of the surface treatment showed different levels of damage. While grinding (with embedded abrasive) and lapping (either with corundum-water suspension or cutting with  $B_4C$ -glycerine suspension) are the most surface-damaging treatments, polishing creates minor damage on the crystal surface. In the observed XPD patterns, grinding causes approximately similar signals like lapping, with the difference that the intensities of specific peaks may differ (fig A.2). Accordingly, lapping cannot be considered as the more careful abrasive method in this case. Also, the differences between an as-grown and an as-cut Laue camera image, shown in fig. 3.73, clarify that there must be a disrupted layer on the surface of the cut slabs, while the regularly grown surface has a sharp undisrupted Laue pattern. Diffuse peaks in the Laue pattern correspond to peaks with low intensity and a large FWHM.

Distorted surfaces as a result of polishing, etc., are frequently published but their state is still disputed [105] and systematic investigations are rare. Usually such layers are discussed as Beilby layers, sub-surface damage (SSD) layers or worked layers.

The differences between the terms are not clearly defined and their state may either be amorphous, fine-grained (2–100 nm) or oxidized or a combination [105–107]. However, all these studies have been carried out on different materials and there is no report of such layers on intermetallics or comparable materials present. In most discussions when the Beilby layer is addressed, layers with a thickness of a few nanometers are regarded but authors also report on layers in the range of 5–7  $\mu\text{m}$  [108]. In the present case of  $\text{Ga}_{1-x}\text{Sn}_x\text{Pd}_2$ , the signal of the damage layer is detectable with non-surface sensitive X-ray methods and therefore a thickness of several micrometers must be expected. Regarding the grain size of the polycrystalline layer, a rough grain size approximation, based on the FWHM, according to the Scherrer equation resulted in approx. 11 nm [70].

The different erosion rates of the different polishing steps, tabled in tab. 3.16, are not completely understood yet, and further parameters like the amount of lubricant seem to play a role besides polishing pressure, speed, time and abrasive size. The approach to reduce the damage layer by using very low pressure and low rotation rate is well consistent with literature [106, 107]. Still, the tangential polishing rate of 15–25 m/min could have been reduced but then polishing becomes impracticably time consuming. Having in mind that the erosion of each polishing step is far bigger than the thickness of the damage layer can be, it needs to be concluded that each step causes a new damage layer, while the preliminary one is removed. Nevertheless, a very clear result of the present polishing effort is that the thickness of the damage layer decreases with decreasing abrasive size. This is consistent with the results of other authors, who could remove the damage layer, using fine abrasives [109, 110].

Summarizing, the surfaces of insufficiently polished  $\text{Ga}_{1-x}\text{Sn}_x\text{Pd}_2$  crystals contain a polycrystalline damage layer. Even though systematic surface studies could not be carried out within the present study the polishing effort was sufficient to maintain surfaces well enough to proceed to catalytic treatments. Investigations with grazing incidence diffraction at the TU Chemnitz excluded the evidence of crystalline particles except the bulk single crystal on properly polished slabs [111].

## 4.4 The preparation of powders for X-ray powder diffraction

In section 2.4.1.1 it is anticipated that the evaluation of powders without annealing was almost impossible. Rietveld refinement of measurements of coarse powders was not feasible (section 4.3) while rough phase analyses in polycrystalline samples worked in some cases, e.g. by Le Bail fitting. Still, phases with small fractions and/or low structure factor were covered by the broad basis of larger peaks of other phases. It also became clear that the problem of peak broadening does not only affect  $\text{Ga}_{1-x}\text{Sn}_x\text{Pd}_2$ , but also most other phases of the Ga-Pd-Sn system that appeared in the present studies, i.e. all phases that have a Pd content in the range between  $\approx 49$ –68 at.%. In the case of the phases  $\text{Ga}_3\text{Pd}_5$  (section 5.3.3.2) and GaPd, this was observed also by other authors [27, 112]. Annealing was on the one hand a proper tool to achieve suitable powders for Rietveld refinement, on the other hand the temperatures and the annealing time had to be handled very carefully. In section 2.4.1.1 it is described that too high temperatures and annealing times changed the phase content. An example is shown in fig. A.10 where the peaks of

two generations of  $\text{Ga}_{1-x}\text{Sn}_x\text{Pd}_2$  with different lattice parameters merge, resulting in average lattice parameters as the annealing temperatures were too high ( $780^\circ\text{C}$ ). Obviously, at these temperatures the mobility of the atoms is high enough to allow chemical balancing by diffusion. However, for the present studies proper parameters could be established, enabling successful phase analysis and structure refinement. Due to the annealing process, only phases (and their properties) could be analysed, being in equilibrium at room temperature. None of the expected high temperature phases could be quenched to room temperature, nor analysed by XPD without annealing due to the severe peak broadening, mentioned above.

The broad peaks of the non-annealed XPD patterns are expected to have a related origin like the measured peaks on the single-crystalline slabs, discussed in section 4.3, i.e. mechanical stress causing massive peak broadening. It is well known for intermetallics that milling can cause peak broadening in XPD patterns and both, size and strain broadening is described [113, 114]. In the present study, the exact dimensions of size or strain broadening are not further clarified, since more extensive studies would go beyond the scope of this work. The brief investigations that were carried out by Rietveld refinement, including size and strain refinement according to the Thompson-Cox-Hastings method (section 3.3), still showed that size broadening is the dominant effect while strain broadening plays a minor role. Usual Rietveld refinement of non-annealed powders using the pseudo-Voigt function also indicates size broadening being dominant since the peak shape is strongly Lorentzian. The factor  $\eta^\dagger$  approaching 1, indicates size broadening (Lorentzian peak shape) while a Gaussian peak shape ( $\eta = 0$ ) would be related to strain broadening [115]. When refining the powders with respect to size broadening, the crystal domains have been found to have sizes of approx. 20 nm, and different refinement approaches (size, anisotropic size as well as size and strain combined) showed approximately similar results ( $\pm 10$  nm). The best-fitting refinement approach was splitting the phase into two fractions. One was refined without size broadening and the other one was refined with isotropic size broadening, meaning that a fraction of the same powder was treated as a nanometer-sized fraction and the other fraction as micrometer-sized. The lattice parameters and accordingly the peak positions of the two phase fractions have been set equally, i.e. were refined constrained. From that it can be concluded that the powder may have a fraction which is affected by damage of milling and a fraction that does not contain nanometer-sized crystal domains. A possible model could be a core-shell structure, where the inner parts of the grains of the milled powders are unharmed and the outer parts of the grains have a disrupted layer. The reasons may be similar to the mechanically stressed surfaces described in section 4.3. The domain size of the crystallites should not be confused with the grain size of the powder, which is in the micrometer range.

It can be excluded that the disruption, causing peak broadening is not a result of milling, since XPD measurements of shortly milled, coarse powders (approx.  $50\ \mu\text{m}$ ) show sharp peaks with only the basis of the peaks being broadened with Lorentzian peak shape. When the powder is milled finer, i.e. longer, the fraction with sharp peaks decreases. Using coarse, shortly milled powders for analysis, does not work properly since strong, complicated texture effects impede proper refinements of the powders. In such attempts even phase analysis in polycrystalline samples was too imprecise.

---

$^\dagger pV(x) = \eta L(x) + (1 - \eta)G(x)$  (section 2.4.1.1, eq. 2.3).



Summarising, milling down to grain sizes below 20  $\mu\text{m}$ , and afterwards annealing under the experimentally adjusted conditions according to section 2.4.1.1 was the method in order to achieve high-quality samples for XPD analysis. The typical processes in the annealing of metals are recovery, recrystallization, and grain growth, i.e. Ostwald ripening [116, 117].

## 4.5 Single crystal growth of $\text{Ga}_{1-x}\text{Sn}_x\text{Pd}$

According to pre-experiments and the comparable low temperatures, congruent-close growth of  $\text{Ga}_{1-x}\text{Sn}_x\text{Pd}$  is possible in principle [26, 27]. Therefore, an attempt with an almost-congruent<sup>12</sup> composition, i.e. with a Pd content of  $y_L = 50$ <sup>13</sup> was made, described in section 3.2.2. However, alternating cycles of rapid lateral growth, and subsequent separation of the seed from the melt caused the growth experiment to fail. Due to the congruent-close composition, slight changes in temperature may result in either large amounts of material crystallizing or melting, respectively. Accordingly, any limiting factor is missing for stable crystal growth. Such limiting factors are typically either the slope of the liquidus line/surface in the incongruent case, or latent-heat release by high enough pulling rates in the case of congruent growth [48]. A comparable case is the crystal growth of the phase  $\text{FeGa}_{3-x}\text{Ge}_x$ , where the liquidus surface is almost horizontal [48, 89]. The same difficulties apply here. Due to the low crystallization masses per time, automatic diameter control is not possible, and it can only be visually evaluated, and then adjusted by the operator. Accordingly, if the crystal growth is unstable, the diameter development is very difficult to control in the apparatus used. Again, the thermal radiation is estimated to be an important factor, similar as discussed in section 4.2. At high temperatures (in this case 1000°C – 1100°C) heat transfer is still dominated by thermal radiation, according to Planck’s radiation law [46]. Hence, a medium for thermal convective transport becomes less important but the importance of thermal radiation from the crystal to the environment increases. If the diameter increases, i.e. the crystal deviates from the cylindrical shape, the radiation is directed more towards the upper part of the apparatus and heat is increasingly removed by radiation into the upper, cooler part of the apparatus. Consequently, the crystal is cooled stronger and enhanced lateral growth takes place, reinforcing the effect. Since the melt is almost congruent, small temperature reductions cause a comparable large mass to freeze, and a chain reaction takes place. The observed needle-like lateral outgrowths created additional heat loss from the system, self-reinforcing their lateral expansion. To avoid uncontrolled lateral growth in such cases, heating during the growth of the shoulder and during the increase of the diameter may be necessary [48, 89]. In the case of  $\text{Ga}_{1-x}\text{Sn}_x\text{Pd}$ , heating was applied without pulling, in order to reduce the protruding lateral outgrowth. However, the longest laterally grown tips remained stable, while dissolution started at areas being closer to the centre of the crystal. This may be consistent, since the heat radiation from the lateral outgrowths may be higher than that from the centre of the crystal, since their surface points directly towards the upper, colder part of the growth chamber, while heat radiation from the centre may be reduced by the seed and the seed holder.

<sup>12</sup>A pure congruent mixture is not known since always strong segregation between Ga and Sn was observed.

<sup>13</sup>According to the description  $(\text{Ga}_{1-x_L}\text{Sn}_{x_L})_{100-y_L}\text{Pd}_{y_L}$ .

In the further process, in order to reduce the diameter to the desired size and a rounded shape, the heating power was slowly increased until the lateral outgrowths also started to dissolve. However, when the turning point was passed and the lateral outgrowths started to dissolve, suddenly the previously emitted thermal radiation from the outgrowths was missing, and as a result the temperatures at the phase boundary became too high. Typically the dissolution of the complete remaining rest of the crystal and the tip of the seed, and accordingly the separation from the melt was the consequence.

Summarizing, in the case of  $\text{Ga}_{1-x}\text{Sn}_x\text{Pd}$  a limiting factor for lateral growth was missing because of the congruent-close composition, and latent heat was neglectable due to slow pulling rates. The reason to apply slow pulling rates (especially in the case of Ga-rich solutions) is to avoid the trapping of mother liquid inclusions. As growth from an almost congruent composition was carried out here, faster pulling could have been attempted to achieve more stable crystallization. However, in the case of  $\text{Ga}_{1-x}\text{Sn}_x\text{Pd}$ , strong segregation between Sn and Ga in the melt, and a very low substitution limit of Ga by Sn in the crystal is known, and too fast pulling rates will therefore lead to the trapping of Sn-rich inclusions [26, 27]. The second growth attempt, using a solution with lower Pd-content (i.e. a more incongruent composition) and the same Ga-Sn ratio, proved to be successful because the incongruent crystal growth from (Ga,Sn)-rich solution serves as a limiting factor.

# Chapter 5

## Single crystal growth and characterization of $\text{Ga}_3\text{Pd}_5$ <sup>†</sup>

### 5.1 Introduction

Due to recent studies on Ga-Pd binary compounds and their promising properties in heterogeneous catalysis, especially in the semi-hydrogenation of acetylene [1, 6, 7, 12], efforts were made in order to achieve single crystal growth of the most promising phases. Those allow basic research and understanding of the elementary processes of catalysis, including anisotropic effects. For studying surface structures of differently oriented crystallographic faces as well as their catalytic properties, typically samples up to 1 cm<sup>2</sup> in size are needed that should be prepared from single crystals of appropriate size. For this purpose  $\text{Ga}_7\text{Pd}_3$  and GaPd (both cubic) as well as GaPd<sub>2</sub> (orthorhombic) have been grown as cm-sized single-crystals by the Czochralski technique from Ga-rich solutions [10, 11] and have been studied in detail [14, 15, 118].

During the growth of GaPd<sub>2</sub>, sometimes the peritectic to the next crystallizing phase ( $\text{Ga}_3\text{Pd}_5$ , fig. 5.1) could be observed at the end of the grown crystals. This always happened when the solid/liquid interface temperature dropped below the peritectic point where the primary crystallization region of  $\text{Ga}_3\text{Pd}_5$  starts. More interestingly, thin lamellae of  $\text{Ga}_3\text{Pd}_5$  were found in the GaPd<sub>2</sub> crystal. These lamellae are always epitaxially oriented at the shared interface<sup>1</sup>, with  $(001)_{\text{GaPd}_2}$  being parallel to  $(010)_{\text{Ga}_3\text{Pd}_5}$ , i.e. independent of the pulling direction of the GaPd<sub>2</sub> crystal. Upon cooling of the primarily crystallized GaPd<sub>2</sub> phase,  $\text{Ga}_3\text{Pd}_5$  precipitation is thermodynamically driven by the retrograde solubility of Ga in GaPd<sub>2</sub> at temperatures below approx. 1030°C. The perfect fit of the two phases results from two pairs

---

<sup>†</sup>In addition to the author of this dissertation, who is the main contributor, other authors have also contributed to the following part. Peter Gille, Sektion Kristallographie, Ludwig-Maximilians-Universität München, supervised all experimental work. Judith Schwerin, Sektion Kristallographie, Ludwig-Maximilians-Universität München, contributed preliminary work and the supply of the material from which a first  $\text{Ga}_3\text{Pd}_5$  seed could be prepared. So-Hyun Park, Sektion Kristallographie, Ludwig-Maximilians-Universität München, supervised the X-ray single crystal experiments, the structure solution and the single crystal structure refinement. Ulrich Burkhardt, Max-Planck-Institut für Chemische Physik fester Stoffe Dresden, carried out the scanning electron microscopy and EDX measurements. Wilder Carillo-Cabrera, Max-Planck-Institut für Chemische Physik fester Stoffe Dresden, carried out the transmission electron microscopy.

<sup>1</sup>The two orthorhombic phases share two lattice parameters

of almost similar lattice constants. In the case of  $\text{Ga}_3\text{Pd}_5$  the lattice parameters  $a$  and  $c$  fit to the lattice parameters  $a$  and  $b$  of  $\text{GaPd}_2$ , respectively<sup>2</sup>. Moreover, in an early paper Grin has stressed that the structural similarity of various Ga-Pd phases can be understood in terms of polymorphism with the fashion of stacking sequences of the same layers or structure sequences [24]. It has been speculated that those epitaxial lamellae may be formed by spinodal decomposition of the supersaturated  $\text{GaPd}_2$  phase [11]. According to a recent investigation by Burkhardt et al. [81], lamellae spacing within the tiny length scale of atomic distances conflicts with a stable coexistence of two phases.

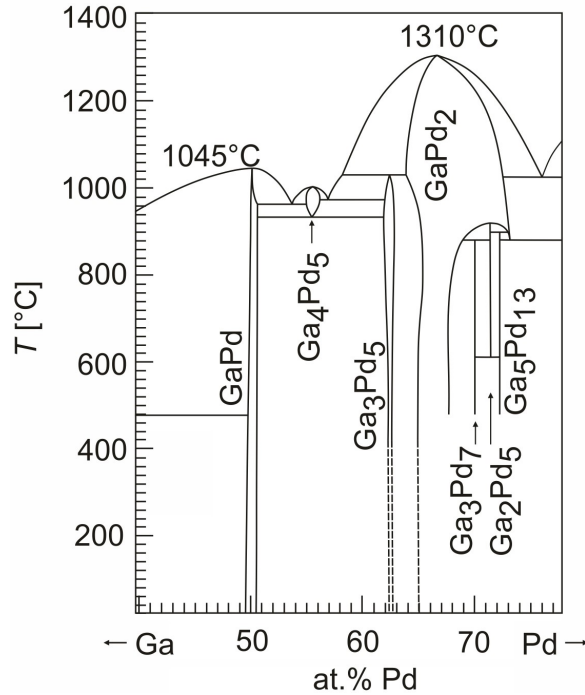


Figure 5.1: Ga-Pd phase diagram. Drawn after [23] and [120].

In order to study the intrinsic properties of phase-pure  $\text{Ga}_3\text{Pd}_5$ , it was decided to grow a single crystal with at least several millimeters in size. The difficulties of growing  $\text{Ga}_3\text{Pd}_5$  arise from the very narrow window of temperature and composition (fig. 5.1), where the compound can be grown from incongruent solution. Due to superior features of the Czochralski technique, and the long-term experience in applying this method to the growth of intermetallic compounds from incongruent melts, this technique was used here for  $\text{Ga}_3\text{Pd}_5$  as well.

## 5.2 Growth strategy

According to the Ga-Pd phase diagram (fig. 5.1),  $\text{Ga}_3\text{Pd}_5$  is stable in the region of 62–63 at.% Pd, and crystallizes from Ga-rich solution in a very narrow window between 58.3 to 57.1 at.% Pd in the temperature range of  $1030^\circ\text{C} > T > 980^\circ\text{C}$  [23]. Therefore, it can be grown incongruently below its peritectic temperature only. The

<sup>2</sup>The structures of  $\text{Ga}_3\text{Pd}_5$  [25, 51] and  $\text{GaPd}_2$  [36, 119] have been published in different setups. In this thesis for  $\text{Ga}_3\text{Pd}_5$  the setup  $a = 5.41(1) \text{ \AA}$ ,  $b = 10.49(1) \text{ \AA}$ ,  $c = 4.02(1) \text{ \AA}$  [25], and for  $\text{GaPd}_2$   $a = 5.4829(8) \text{ \AA}$ ,  $b = 4.0560(4) \text{ \AA}$ ,  $c = 7.7863(8) \text{ \AA}$ , according to [36] are used.

narrow region where the  $\text{Ga}_3\text{Pd}_5$  phase is in equilibrium with the liquid restricts the yield of the target phase, unless a re-feeding technique is applied (e.g. zone melting). In those challenging methods the problem would have been shifted to the supply of an appropriate starting material. Based on a lever rule calculation [50], a theoretical yield of a phase fraction of approx. 23 % can be expected even from a directional solidification method like Czochralski, on the other hand. Additional to good observation possibilities during the Czochralski growth process, the critical seeding can be done precisely and relatively uncomplicated, which is highly advantageous for this technique. If the experiment targets at a new phase from which no piece is available, large enough to prepare a small seed crystal, several tricks have been reported in literature how to start [49]. For the Czochralski growth of  $\text{Ga}_3\text{Pd}_5$  it was taken advantage from the side effect of previous experiments mentioned above. A well-oriented seed could be prepared from a small part of  $\text{Ga}_3\text{Pd}_5$ , epitaxially crystallized at the very end of a  $\text{GaPd}_2$  crystal, pulled in [001] direction.

The incongruent growth of  $\text{Ga}_3\text{Pd}_5$  starts just below its peritectic temperature with a melt composition of approx. 58.3 at.% Pd and ends up in an eutectic mixture of  $\text{Ga}_3\text{Pd}_5$  and  $\text{Ga}_4\text{Pd}_5$ . Growing the crystal up to the eutectic point would result in an abrupt solidification of the whole rest of the melt with the crystal being stuck in the eutectic fabric. This case leads to the grown crystal being at least partially damaged, since the crystal and the crucible rotate in opposite directions. Furthermore, the single crystal and the eutectic may have different thermal expansion coefficients, leading to tensions and cracks in the previously grown crystal. This is the reason, why crystal growth must be completed prior to reaching the eutectic temperature, which reduces again the yield possible for this experiment. As there is no thermocouple inserted into the melt, absolute temperature measurements are hard to be achieved and a setpoint (SP) temperature is measured only from a thermocouple, placed in direct contact to the graphite heater. Therefore, the end of the crystal growth needs to be estimated by observing the SP temperature difference from the SP temperature at the seeding (i.e. starting) conditions. An additional criterion for finding the suitable end of the crystal growth process is estimating the crystal's size, compared with the theoretical yield. Both methods are imprecise and, hence, the pulling should be completed by detaching the crystal from the melt early enough in order to prevent destructive forces to the grown crystal.

## 5.3 Experimental section

### 5.3.1 $\text{Ga}_3\text{Pd}_5$ single crystal growth

The starting composition  $\text{Ga}_{41.9}\text{Pd}_{58.1}$  of the Ga-rich solution was chosen according to the phase diagram and a slight difference to the reported peritectic point (fig. 5.1). The Ga pieces (5N-grade, Chempur) were reduced by heating in a glassy carbon crucible under  $\text{H}_2$  atmosphere (5.0-grade). The surfaces of the Pd ingots (3N5-grade, Degussa) were etched in aqua regia and cleaned in an ultrasonic bath with distilled water and acetone p.a.. The overall mass of the starting components was 46.46 g. From this mass, a maximum yield of approx. 10 g  $\text{Ga}_3\text{Pd}_5$  was calculated, according to the phase diagram.

For synthesis and high homogeneity of the starting solution, the metallic educts were placed in a 15 mL high-shaped alumina crucible (Alsint 99.7, Haldenwanger)

under Ar atmosphere (5.0-grade) of ambient pressure in a radio frequency generator. Slow heating was found to be critically decisive in order to reduce the speed of the strongly exothermic reaction which might cause the ceramic crucible to crack. A maximum SP temperature of approx. 1250°C was hold for an hour to achieve complete homogenization. Then, the sample was quenched to room temperature by switching off the heating power. The aim was to achieve a chemically homogeneous, fine-grained ingot, which easily dissolves in the Czochralski apparatus, where mixing is limited to the accelerated crucible rotation technique (ACRT<sup>3</sup>) [45].

The pre-synthesized ingot was transferred into a 10 mL wide-shaped alumina crucible (Alsint 99.7, Haldenwanger) and placed in the Czochralski apparatus, described in [44]. In the present study, the Czochralski apparatus was equipped with a meander-shaped graphite heater instead of the former Kanthal resistance heater. A [001]-oriented, 9 mm long, and wedge-shaped seed crystal was cut out of the epitaxially crystallized Ga<sub>3</sub>Pd<sub>5</sub> sample mentioned in the previous section. The seed was fixed in a ceramic seed holder [44] and then mounted to the pulling rod of the apparatus.

The fully metal-sealed Czochralski apparatus was evacuated to a vacuum in the 10<sup>-7</sup> mbar range, and then filled with Ar (5.0-grade) up to 545 mbar at room temperature, approximating atmospheric pressure at growth temperature. The solution was heated with a rate of 500 K/h to a SP temperature of 1100°C and then homogenized for 18 h while ACRT was applied. Since neither the exact liquidus temperature nor the exact melt temperature were known, the SP temperature appropriate for seeding was determined by slowly cooling the solution until homogeneous nucleation was observed. Then, very slow heating was applied, until the very last crystallites dissolved. The temperature where the last crystallites dissolve corresponds to the liquidus temperature of the solution, and therefore to the right seeding temperature. Seeding was carried out by slowly lowering the seed to the melt at moderate rotation of the crystal and reverse rotation of the crucible. At first contact, the seed crystal was suddenly wetted by the melt. This region was carefully re-molten later, before crystal growth was started by pulling. After successful seeding, the crystal rotation rate was increased to 40 rpm and the crucible rotation rate to reverse 15 rpm. The pulling of the crystal was started at a rate of 75 μm/h and later continuously reduced to 20 μm/h. A very low growth rate has been found to be necessary in earlier experiments from high-temperature solutions, to avoid mother liquid inclusions [49]. A temperature program with decreasing SP temperatures and a maximum cooling rate of 0.10 K/h was used to compensate the slope of the liquidus curve. In order to test if the growing crystal can be forced to get a round cross section, the crystal's rotation rate was later increased from 40 rpm to 50 rpm and to 63 rpm.

After 6 mm of pulling, the crystal was detached from the melt with an accelerated pulling rate of 20 mm/h. Finally, the crystal was cooled with a rate of 250 K/h down to room temperature within the growth apparatus.

### 5.3.2 Surface preparation

Cutting of the crystal was done in well-oriented crystallographic planes with the wire lapping saw WS 22 (KD UNIPRESS), using a 50 μm tungsten wire, and a

---

<sup>3</sup>Accelerated crucible rotation technique is a stirring method by alternating accelerating and decelerating of the crucible rotation [45].

slurry of 800 mesh boron carbide powder and glycerol. Cutting by lapping ensures a minimum surface damage and reduces material loss. The obtained crystal slabs were mechanically polished with diamond paste of decreasing grain sizes down to 0.25  $\mu\text{m}$ , followed by a chemo-mechanical polishing step with Syton OP-S (Struers).

### 5.3.3 Analysis

#### 5.3.3.1 Laue backscattering method

Laue backscattering, with a Laue camera, equipped with a Mo X-ray tube and an image plate, was used to align the crystal in the desired orientation on a goniometer head, which could be transferred to the wire saw for oriented cutting. Furthermore, raster scanning of the grown crystal allowed to prove the single-crystallinity.

#### 5.3.3.2 X-ray powder diffraction

For X-ray powder diffraction (XPD) the grown crystal samples were ground in an agate mortar and annealed under Ar atmosphere in fused silica ampoules for 12 h at 800°C to overcome grinding-induced peak broadening. High-resolution XPD data were collected on a 1D position-sensitive semiconductor detector (PSD, 1D Meteor) on a Bragg-Brentano diffractometer (GE XRD3003 TT) with Cu- $K\alpha_1$  radiation (Ge (111) monochromator). The data collection was performed with steps of  $2\theta = 0.013^\circ$  in the range of  $10^\circ \leq 2\theta \leq 130^\circ$  with an internal  $\text{LaB}_6$  standard (NIST 660c) on a zero-background quartz sample holder. Compared to these data, collected in reflection mode, preferred orientation effects on Bragg intensities could be suppressed in Debye-Scherrer geometry, using glass capillary sample holders. These transmission measurements were carried out with a phase mixture of 70 wt.% of the main phase, and 30 wt.% of  $\alpha\text{Al}_2\text{O}_3$  (corundum, NBS 674a) as standard reference material. The data acquisition was conducted on a STOE KRISTALLOFLEX diffractometer, with Mo- $K\alpha_1$  radiation (Ge (111) monochromator), and a PSD step size of  $2\theta = 0.1^\circ$  in the range of  $5^\circ \leq 2\theta \leq 70^\circ$ . Rietveld refinement and lattice parameter refinement by Le Bail fitting was done with the program package *FullProf* [61].

#### 5.3.3.3 X-ray single crystal diffraction

For the use in X-ray single crystal diffraction (XSD), a part of the single crystal was crushed, and the resulting crystallites were annealed under Ar atmosphere at 800°C for 12 hours. Measurements without annealing always showed poor results, usually Debye-Scherrer rings or reflexes with tails. The attempt to produce round grains by means of an air-flow-driven ball mill failed, since the grains obtained in this way always showed pronounced Debye-Scherrer rings in the diffraction patterns, even after annealing. Small single crystals in size of approx.  $30 \times 30 \times 30 \mu\text{m}^3$  were selected, attached on a glass fibre, and mounted onto a Nonius goniometer. Due to the anisotropic cleaving behaviour crystallites had the tendency to be elongated in the [100] direction. (Most measurements were carried out on a crystallite with the dimensions  $20 \cdot 30 \cdot 50 \mu\text{m}^3$ .) XSD data collection was performed on a four-circle single crystal diffractometer (GEMINI, Rigaku-Oxford), equipped with a charge-coupled device (CCD) detector (Atlas) using both, Mo- $K\alpha_1$  (Graphite (002) monochromator) and Cu- $K\alpha$  (mirror optic) radiation. To get a high redundancy, numbers of



frames of XSD data were collected in  $\varphi$ -scans ( $\Delta\varphi = 1^\circ$ ) at  $2\theta$ -dependent exposure times up to  $d = 0.6 \text{ \AA}$ . To check diffuse scattering an additional XSD data set was acquired with a step width of  $\Delta\varphi = 0.1^\circ$  up to  $d = 0.8 \text{ \AA}$ . Structure solutions were done with the Direct Method with the program *SHELXS* [121], and the obtained starting models were further refined with the program package *Jana2006* [122].

### 5.3.3.4 Electron microscopy

A Cameca SX-100 electron-probe microanalysis (EPMA), equipped with a  $\text{LaB}_6$  cathode was used for chemical composition measurements by wavelength-dispersive X-ray spectroscopy (WDX), and for backscattered electron imaging (BSE) at 15 keV and 40 nA. A thin slab of the crystal, cut perpendicular to the growth direction, was polished with diamond paste down to a grain size of  $0.25 \text{ }\mu\text{m}$  and then fixed on the sample holder with conductive silver lacquer. Calibration was done using a standard of binary GaPd. LPET and LiF crystals were used to measure Pd- $L\alpha$  and Ga- $K\alpha$  lines, respectively. The PAP model was applied for matrix correction [67].

For electron backscatter diffraction (EBSD) the Kikuchi patterns were acquired, using a Bruker Quantax EBSD system with a  $e^- \text{Flash}^{HR}$  detector and the software package *Esprit, version 2.2*. The resolution for the Kikuchi patterns was  $320 \times 240$  pixels, the acceleration voltage 15 kV, the sample distance 18 mm, and the samples were tilted by  $70^\circ$ . The EBSD system was mounted to a scanning electron microscope (SEM, Jeol JSM 7800 F) with an ARGUS<sup>TM</sup> imaging system, including two backscattered electron (BSE) and three foreshattered electron (FSE) detectors.

Since precipitates were found in the bulk  $\text{Ga}_3\text{Pd}_5$ , samples for transmission electron microscopy (TEM) were prepared by the focused-ion-beam (FIB) lift-out technique [123]. Thin cross-sections of the crystalline phases were extracted from a polished sample. Defined crystallographic cross-sections could be obtained by orienting the crystals prior to cutting. The FIB lift-out technique was performed on a FEI Quanta 200 3D ion/electron dual beam SEM (FEI Company, Eindhoven, the Netherlands), equipped with an Omniprobe micro-manipulator (W needle). The FEI SEM can be used both, as SEM and scanning ion microscope (SIM).

For SEM and SIM an Everhart-Thornley secondary-electron detector (ET-SED) was used for SE imaging. For back-scattered-electron (BSE) imaging a solid-state back-scattered-electron detector (SSD-BSD) was used. Before the FIB cross-section extraction, protecting Pt layers (24–28  $\mu\text{m}$  long, 3  $\mu\text{m}$  thick and 2–3  $\mu\text{m}$  high, fig. 5.2) were deposited on selected regions (perpendicular to the directions [010] and [011] of  $\text{Ga}_3\text{Pd}_5$ , using

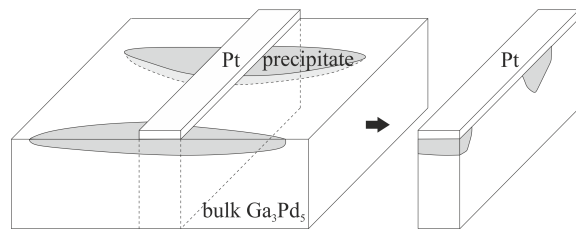


Figure 5.2: Schematic sketch, regarding the investigated section, protected by a Pt layer and then eroded from the surrounding material.

an acceleration voltage of 30 kV and a current of 0.1 nA. The initially rough cross-sections (2  $\mu\text{m}$  thick) were prepared by applying a Ga ion beam using an acceleration voltage of 30 kV and a current of 3–1 nA. Each rough-machined FIB cut was transferred onto a Mo TEM holder using the in-situ lift-out technique

[123]. Finally, each FIB cross-section was thinned to a thickness of approx. 80 nm by applying an acceleration voltage of 30 kV with currents decreasing from 0.5–0.01 nA. These FIB cuts are relatively thick and cannot be used for HRTEM but suit well for a selected area electron diffraction study. Conventional TEM and selected area electron diffraction (SAED) were performed on a FEI Tecnai F30-G2 super-twin microscope operating at 300 kV, equipped with a CCD camera (GATAN Inc.) and a standard double-tilt holder (GATAN Inc.) with a tilting range of  $\pm 40^\circ$  around the holder axis and  $\pm 30^\circ$  perpendicular to the holder axis. For the SAED images the aperture shadow on the sample had a diameter of 290 nm or 840 nm, respectively. The images were stored as files in dm3 format and were processed and analysed with Digital Micrograph (version 3.21.1374.0, GATAN Inc.). [124]

#### 5.3.3.5 Differential thermal analysis

Differential thermal analysis (DTA) was conducted with a Netzsch 404/3/F DTA system under stationary Ar atmosphere of ambient pressure. Two samples of 20 and 35 mg were measured in a 30  $\mu$ l alumina crucible with corundum powder as reference. Data acquisition was executed while heating with a rate of 2 K/min, and subsequently cooling with 2 or 1 K/min, as well as 5 K/min for both, heating and cooling. The DTA was calibrated with the melting point of Ge ( $T_m = 937.4^\circ\text{C}$ ) under equivalent conditions.

#### 5.3.3.6 Density measurements

The mass density was measured with Archimedes' principle on a single-crystalline piece of 0.8 g. Diethyl phthalate was used as buoyancy liquid, and a piece of Si as standard for calibration. An air density correction was applied regarding the actual temperature and station pressure data<sup>4</sup>.

## 5.4 Results

### 5.4.1 Single crystal growth of $\text{Ga}_3\text{Pd}_5$

During searching for the seeding temperature, it could already be observed that crystallites of  $\text{Ga}_3\text{Pd}_5$  grew in a pronounced anisotropic manner, i.e. as needles on the surface of the supercooled solution. This made the determination of the liquidus temperature easy as slow dissolving of the needles could be clearly seen. The maximum supercooling for needle formation observed in the solution was less than 2 K.

---

<sup>4</sup>Meteorologisches Institut München, Theresienstraße 37, 80333 München

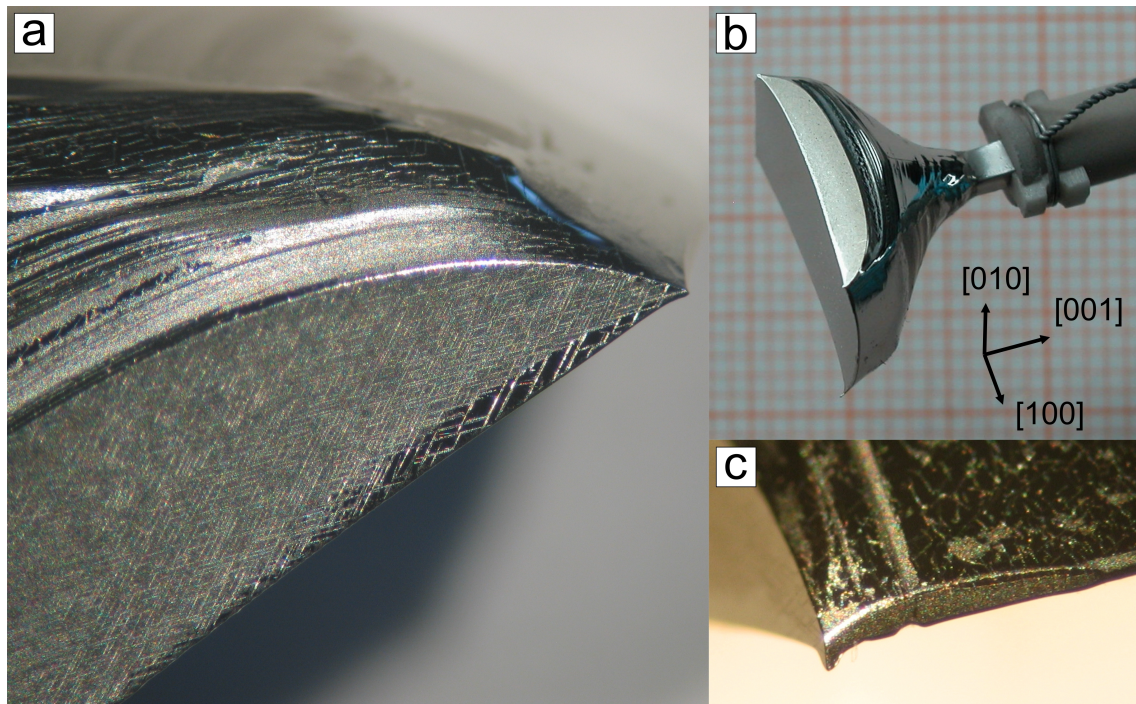


Figure 5.3: a) Czochralski-grown  $\text{Ga}_3\text{Pd}_5$  single crystal with very stable (010) faces that are macroscopically stepped, thus forming vicinal planes. b) The former solid/liquid interface is slightly concave. c)  $\{110\}$  facets, formed at the corners of the crystal.

The obtained  $\text{Ga}_3\text{Pd}_5$  single crystal (fig. 5.3) has the same orientation as the seed and is inclusion-free, with a total mass of 3.1 g. In the first two millimeters after seeding the crystal grew with an evenly rounded diameter, forming a shoulder typically for Czochralski-grown crystals. Then the cross-section perpendicular to the pulling axis evolved to an almost rectangular shape with the dimension in [100] direction being nearly twice the length of the dimension in [010] direction. Additionally, a very stable (010) plane was formed (figs. 5.3, a and b). This is very unusual since almost all Czochralski-grown intermetallic crystals exhibited a circular cross section or sometimes an elliptic shape. Still, the rectangular cross section of the  $\text{Ga}_3\text{Pd}_5$  crystal was formed at the three-phase (solid-liquid-gas) interface and did not grow below the melt level<sup>5</sup>. Having a closer look at the grown (010) face, it was found to be a vicinal face formed by microscopic steps of constant height of 3  $\mu\text{m}$ . In the main part the deviation to the (010) plane is 9°, and in the very last millimeter the amount of steps decreases, resulting in a lower tilt of 3.5°. The changes of the diameter themselves are influenced by the applied temperature-time program, as usual in incongruent Czochralski growth. The growth interface is slightly concave (fig. 5.3, b).

<sup>5</sup>This is a distinction between the Czochralski method and top-seeded solution growth, where the crystal grows below the melt surface and typically forms facets.

### 5.4.2 Thermal and chemical analyses of $\text{Ga}_3\text{Pd}_5$

WDX measurements revealed a composition of  $\text{Ga}_{37.5(2)}\text{Pd}_{62.5(2)}$  in the first-to-freeze region and  $\text{Ga}_{37.62(17)}\text{Pd}_{62.37(17)}$  at the very end. The experimentally determined density of  $\text{Ga}_3\text{Pd}_5$  was measured as  $\rho_{exp} = 10.66(2) \text{ g/cm}^3$ .

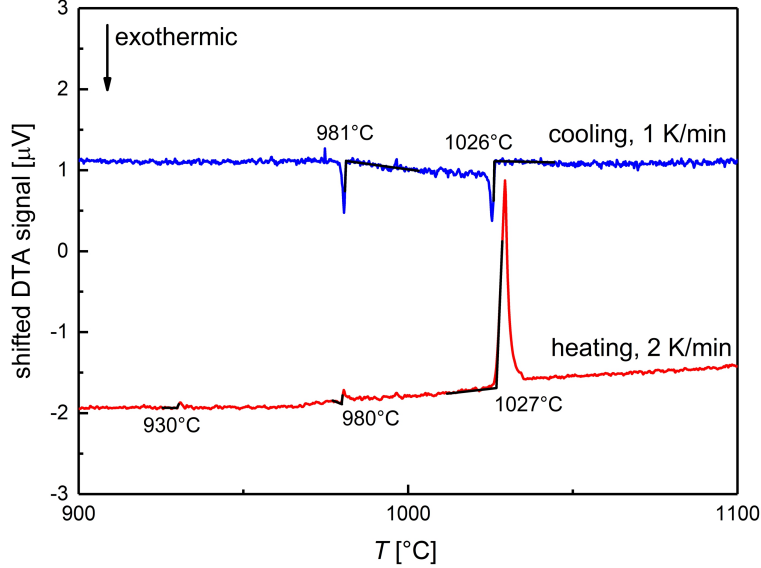


Figure 5.4: DTA heating and cooling curves of single-crystalline  $\text{Ga}_3\text{Pd}_5$ .

The measured DTA curves (fig. 5.4) are consistent with the reported phase diagram in the first instance (fig. 5.1) [23]. The heating curves show peaks at  $930^\circ\text{C}$ , at  $980^\circ\text{C}$  and at  $1027^\circ\text{C}$ . The cooling curves show peaks at  $1026^\circ\text{C}$  and  $981^\circ\text{C}$ . A certain signal occurring at  $758^\circ\text{C}$  was found in two cooling curves with a cooling ramp of  $5 \text{ K/min}$ . However, not all of the observed signals in the DTA curves can be explained by cooling or heating a single crystal, grown from liquid phase, according to the phase diagram. Possible solid-solid transitions which might be kinetically restrained could occur in the system. Therefore a slice of  $\text{Ga}_3\text{Pd}_5$  was cooled from high temperatures very slowly to room temperature in order to assist such solid-solid transitions kinetically. A (100) slab, cut parallel to the growth direction, close to the seed was chosen. The (100) slab was cooled from  $800^\circ\text{C}$  to  $500^\circ\text{C}$  with a ramp of  $0.5 \text{ K/h}$ , followed by cooling with  $200 \text{ K/h}$  to room temperature.

Fig. 5.5 shows that the  $\text{Ga}_3\text{Pd}_5$  (100) surface contains dark precipitates. Some of them are roughly elongated along  $[010]$  or  $[001]$ , but most of them show arbitrary orientations. Many precipitates also appear rounded (fig. 5.5, b), and longer precipitates sometimes are bended. On the (100) surface the precipitates show a kind of core-shell structure (fig. 5.5, b). A  $\theta$ - $\theta$  scan in Bragg-Brentano geometry on the same surface (fig. 5.6) shows that there are other peaks amongst the  $h00$  peaks of the  $\text{Ga}_3\text{Pd}_5$  crystal slab. The first remarkable observation is the presence of peaks with the indices  $h00$ :  $h = 2n - 1$  for  $\text{Ga}_3\text{Pd}_5$ , that should be extinct due to the reflection condition  $h00$ :  $h = 2n$  of the space group  $Pbam$  [125]. Furthermore, when having a closer look at the  $\theta$ - $\theta$  scan, XPD patterns of  $\text{Ga}_3\text{Pd}_5$  and GaPd are present. Texture effects occur, and the intensities cannot be fitted, but the Bragg positions of both phases fit very well. This shows the occurrence of polycrystalline  $\text{Ga}_3\text{Pd}_5$  and GaPd on the annealed surface of single-crystalline  $\text{Ga}_3\text{Pd}_5$ .



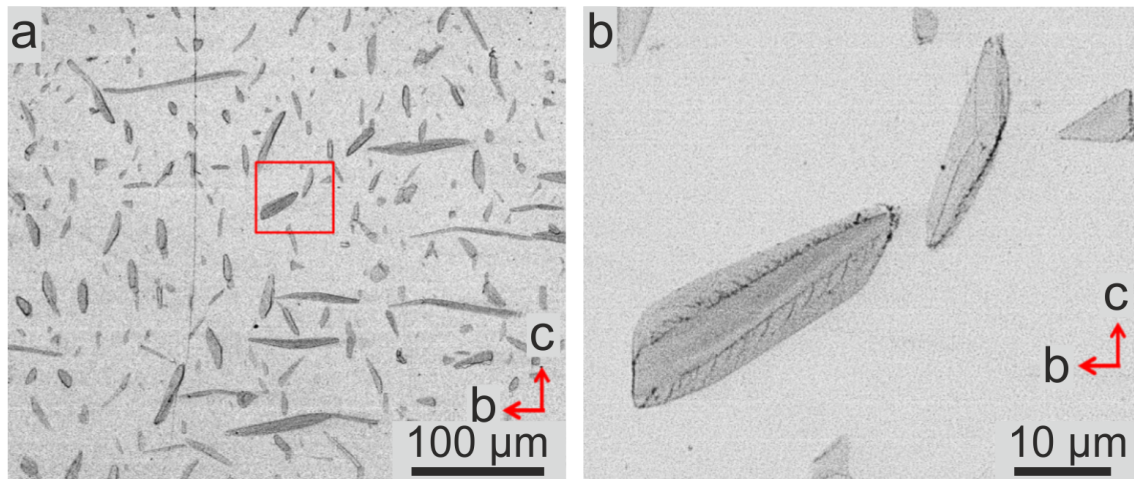


Figure 5.5: a) BSE image of a slowly cooled (100) surface of the  $\text{Ga}_3\text{Pd}_5$  crystal. b) Closer image of the precipitates framed in red. [124]

The phase maps in figs. 5.7, a and b, show that the inner core of the core-shell precipitates are GaPd grains while the outer shell is mostly composed of fine-grained GaPd with minor amounts of  $\text{Ga}_3\text{Pd}_5$ . Furthermore, not all GaPd precipitates exhibit a shell. The red arrows in fig. 5.8 show small  $\text{Ga}_3\text{Pd}_5$  grains, also being present on the surface. EBSD measurements on various grains (figs. 5.7, c, d) identified GaPd precipitates on the  $(100)_{\text{Ga}_3\text{Pd}_5}$  surface, having a tendency to be oriented with their  $[100]_{\text{GaPd}}$  axis parallel to the  $[100]_{\text{Ga}_3\text{Pd}_5}$  axis, but numerous deviations occur.

From the annealed (100) slice a perpendicular (010) cut was produced additionally, polished and investigated by EDX and EBSD in order to investigate the bulk of the annealed slice (fig. 5.9). The precipitates tend to be much smaller, less numerous and show no core-shell-like habitus as it is present on the annealed surface. Fig. 5.9, b, shows these precipitates being finely distributed throughout the entire sample. However, it cannot be easily distinguished, whether the precipitates are also present in the part which was grown earlier. Additionally, it is unclear whether or not a gradient of the amount of precipitates occurs along the growth axis. Fig. 5.9, c, shows that the orientations of the GaPd grains vary. However, there is a tendency of the GaPd main axis being parallel to the  $[100]_{\text{Ga}_3\text{Pd}_5}$  direction. In the as-grown  $\text{Ga}_3\text{Pd}_5$  single crystal no GaPd precipitates were observed.

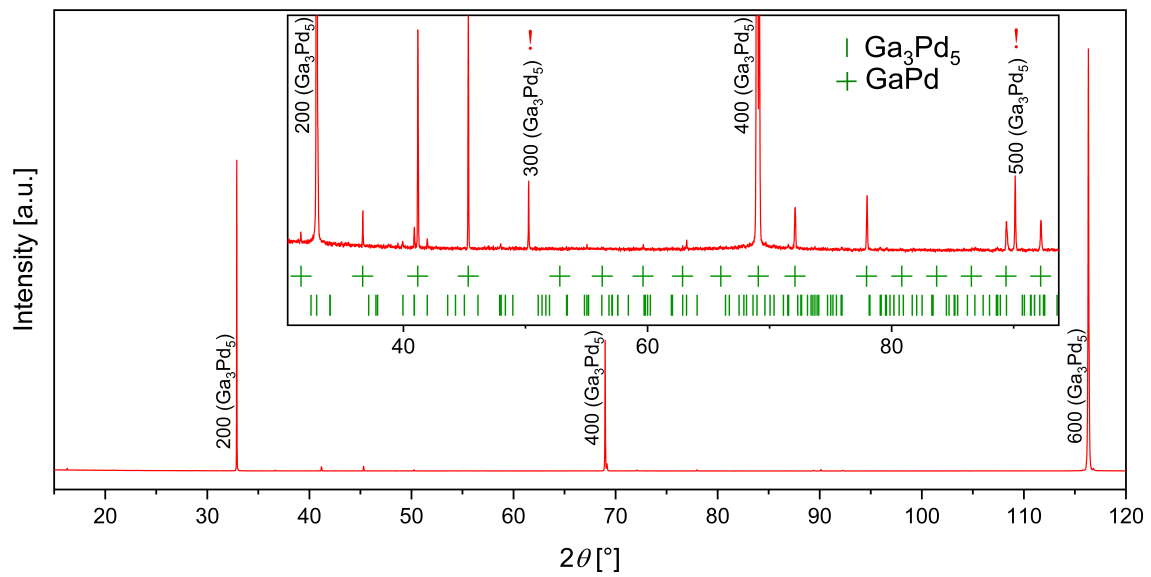


Figure 5.6:  $\theta$ - $\theta$  scan in Bragg-Brentano geometry with  $\text{Cu-K}\alpha_1$  radiation on the annealed (100) surface, shown in fig. 5.5. The inner frame represents the same measurement but enlarged at lower intensities. The green lines are the Bragg positions of  $\text{Ga}_3\text{Pd}_5$  and the green crosses are the Bragg positions of  $\text{GaPd}$ . The red exclamation marks label peaks that are fitting to uneven  $h00$  peaks, but should not appear due to extinction rules

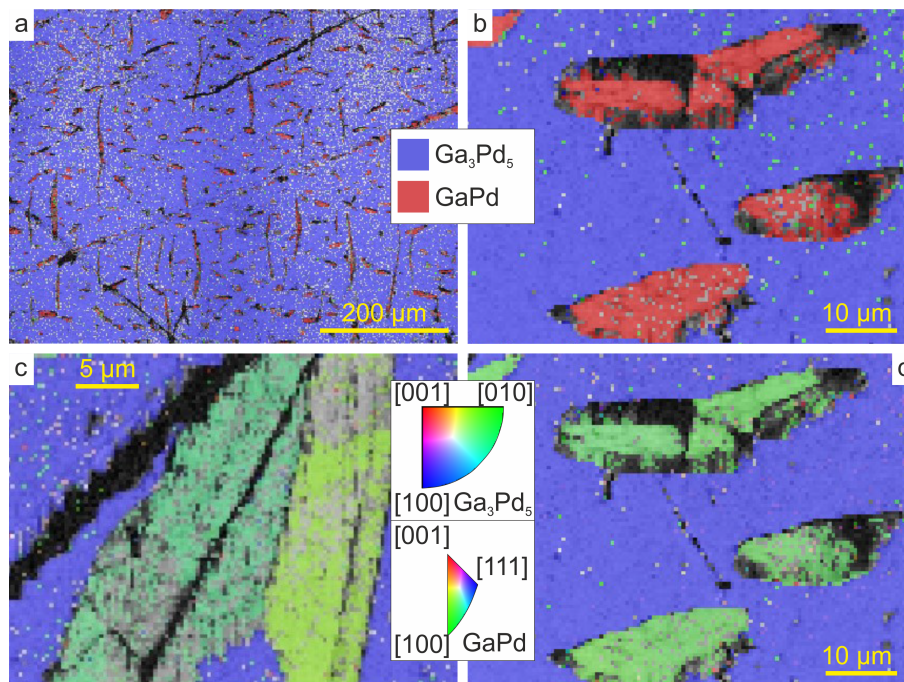


Figure 5.7: a, b) Phase map of the annealed (100) surface, created from EDX mappings. c,d) Orientation maps created from EBSD mappings [126].

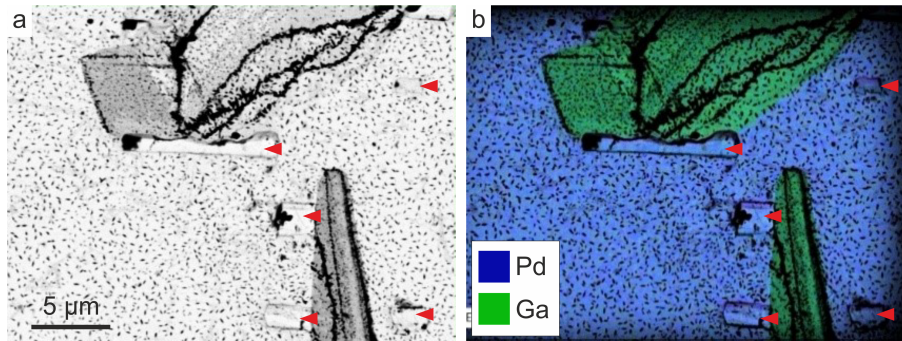


Figure 5.8: a) BSE image of various precipitates on the annealed (100) surface. b) EDX element mappings of the same section. The red arrows mark  $\text{Ga}_3\text{Pd}_5$  crystallites. The numerous black spots are present due to a certain surface roughness since the slice was not polished after annealing [126].

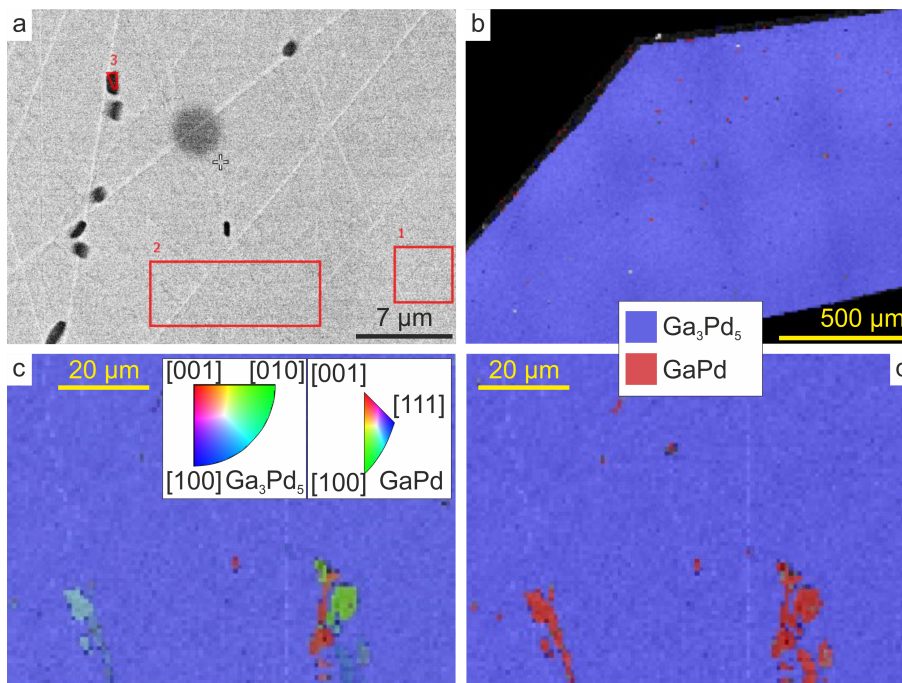


Figure 5.9: a) BSE image of a (010) plane, cut out of the annealed (100) slab (The squares mark regions where EDX spectra have been measured). b, d) Phase maps of the (010) plane created from EDX mappings. In b, the left part is grown earlier than the right part. The oblique edge on the upper left is the shoulder of the crystal. The bottom and top edges are [001] edges, formed by cuts parallel to (100). c) Orientation map of the (010) plane, created from EBSD mappings. [126]



### 5.4.3 TEM analyses

The SIM images in figs. 5.10, a and d, show the results of the FIB I and FIB II cuts, with the GaPd precipitates, chosen for TEM analyses. FIB I is a  $[010]^*_{\text{Ga}_3\text{Pd}_5}$  cross-section and FIB II is a  $[011]^*_{\text{Ga}_3\text{Pd}_5}$  cross-section. All precipitates have in common that they have straight edges in the bulk. The rounded shapes that were occasionally found on the annealed (100) surface are not present in the bulk.

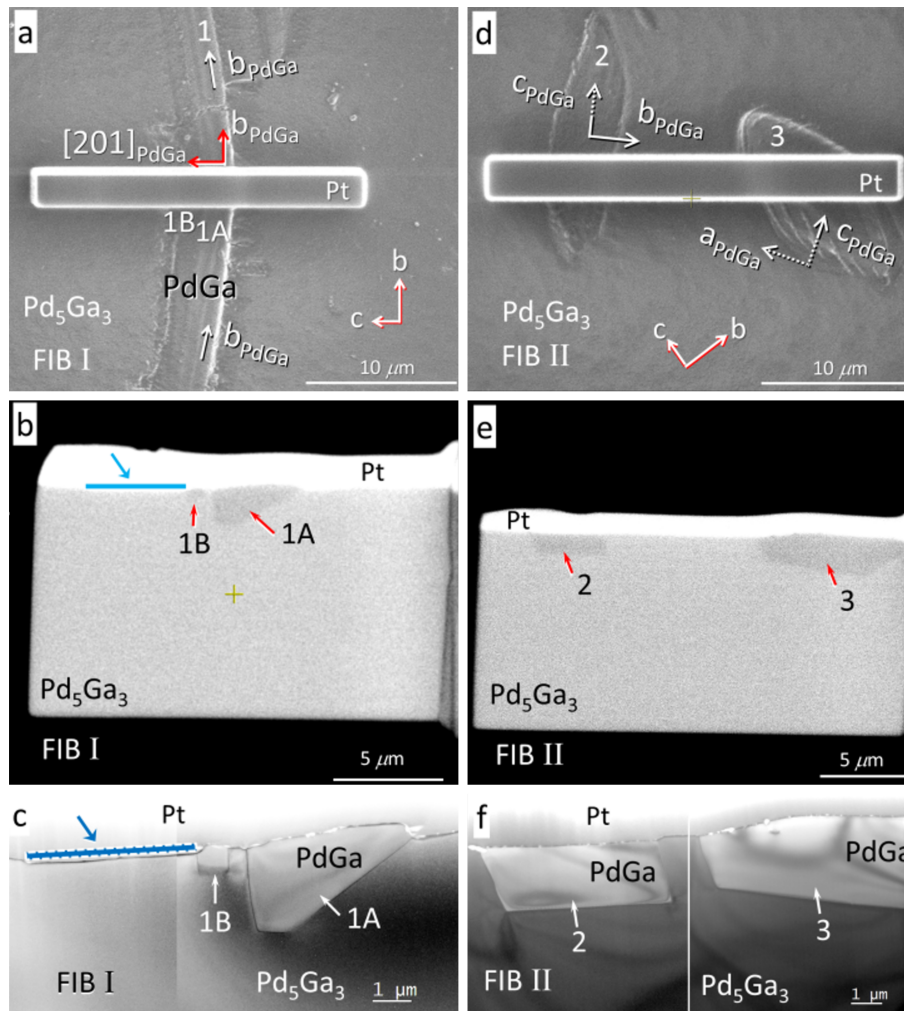


Figure 5.10: Details of the FIB cut preparation, thinning and the TEM study of the oriented FIB I (left column) and FIB II (right column) specimens. a, d) SIM images of FIB I and FIB II, after the deposition of the Pt protection layer. FIB I is a  $[010]^*_{\text{Ga}_3\text{Pd}_5}$  cross-section and FIB II is a  $[011]^*_{\text{Ga}_3\text{Pd}_5}$  cross-section. The main  $b$  axis and the  $[201]^*_{\text{GaPd}}$  direction are shown for the parallel GaPd precipitates 1A and 1B. The axis projections for 2 and 3 are also indicated. b, e) BSE-SEM images of the FIB I and the FIB II final lamellae. The GaPd precipitates 1A, 1B, 2 and 3 are indicated by red arrows. c, f) TEM images of FIB I (oriented along  $[010]^*_{\text{Ga}_3\text{Pd}_5}$ ), and FIB II ( $[011]^*_{\text{Ga}_3\text{Pd}_5}$ ) lamellae, showing the cross-section of the GaPd precipitates 1A, 1B, 2 and 3, in the single-crystalline  $\text{Ga}_3\text{Pd}_5$  matrix. The blue lines in b and c indicate a torn off small crystal. Protecting Pt layers are labelled in the figures. [124]

In the TEM studies, the precipitates could be identified as GaPd due to their

selected area electron diffraction (SAED) zone diffraction patterns and their lattice parameter (approx. 4.94 Å). Further investigations of the FIB cuts revealed the needle-like GaPd precipitates are predominantly elongated along their  $[001]^*$  direction (figs. 5.10, 5.11 and 5.13). [124]

In fig. 5.11 the TEM image of the FIB I lamella (along the  $[010]^*_{\text{Ga}_3\text{Pd}_5}$  direction) and the respective SAED patterns of the  $\text{Ga}_3\text{Pd}_5$  matrix and the 1A and 1B precipitates are presented. The 1B GaPd precipitate has a quasi-square cross-section and the 1A GaPd precipitate shows a quasi-trapezoidal cross-section, with the upper face being created by the polishing process. No further isolated precipitates appeared inside the  $24 \times 18 \mu\text{m}$  or  $28 \times 15 \mu\text{m}$  FIB cross-sections. The SAED patterns show that the  $[010]^*_{\text{GaPd}}$  axes of the 1A and 1B precipitates are parallel to the  $[010]^*_{\text{Ga}_3\text{Pd}_5}$  axis of the matrix. The 1A precipitate is tilted by  $1^\circ$  from the 1B precipitate, but the  $[010]^*_{\text{GaPd}}$  axis of the 1B precipitate is perfectly parallel to the  $[010]^*_{\text{Ga}_3\text{Pd}_5}$  axis. In the 1A precipitate, the crystallite faces are perpendicular to the  $\langle 201 \rangle^*_{\text{GaPd}}$  directions. Those are parallel to directions  $\langle 100 \rangle^*_{\text{Ga}_3\text{Pd}_5}$ ,  $\langle 001 \rangle^*_{\text{Ga}_3\text{Pd}_5}$  and  $\langle 101 \rangle^*_{\text{Ga}_3\text{Pd}_5}$  of the  $\text{Ga}_3\text{Pd}_5$  matrix. Accordingly,  $\{201\}_{\text{GaPd}}$  faces are sharing the  $\{001\}_{\text{Ga}_3\text{Pd}_5}$  and  $\{101\}_{\text{Ga}_3\text{Pd}_5}$  planes. [124]

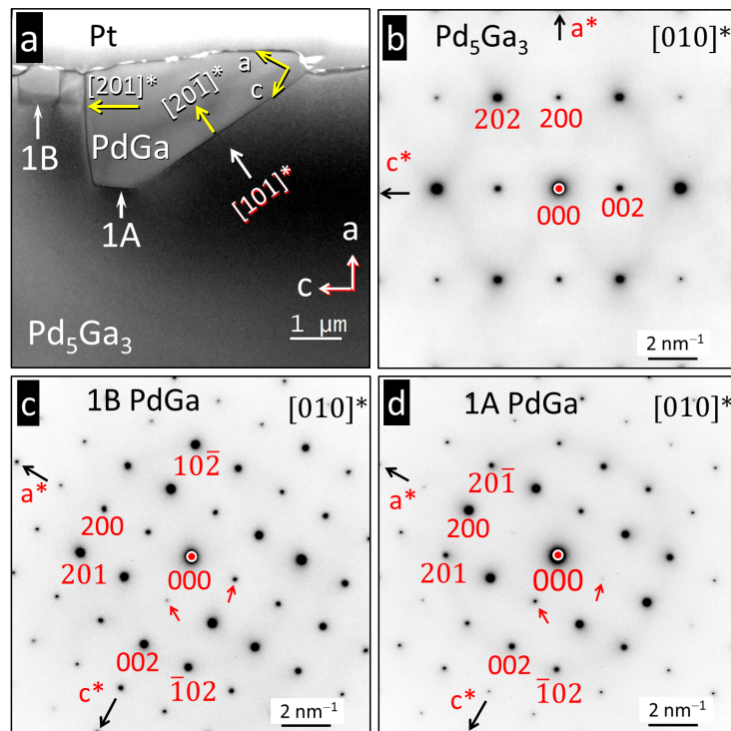


Figure 5.11: Images of the FIB I lamella. a) TEM image along the  $[010]^*_{\text{Ga}_3\text{Pd}_5}$  direction. b) SAED pattern of the  $\text{Ga}_3\text{Pd}_5$  matrix along the  $[010]^*_{\text{Ga}_3\text{Pd}_5}$  direction. c) SAED pattern of the 1B GaPd precipitate along the  $[010]^*_{\text{GaPd}}$  axis. d) SAED pattern of the 1A GaPd precipitate along the  $[010]^*_{\text{GaPd}}$  direction. In frame a, the orientation of the main axes  $a$  and  $c$  of the matrix, and the 1A precipitate are indicated. In the frames c and d, red-arrowed reflections should be extinct, but appear due to dynamical effects. [124]

In the case of the precipitate 2 in FIB II ( $[011]^*_{\text{Ga}_3\text{Pd}_5}$  cross section), it is more difficult to determine geometrical characteristics of the precipitates, since they are

grown in more general directions (figs. 5.12 and 5.13). By tilting the FIB II lamella by  $-27^\circ$  around the TEM holder axis, the  $\text{Ga}_3\text{Pd}_5$  matrix is oriented along the  $[011]^*_{\text{Ga}_3\text{Pd}_5}$  direction (fig. 5.12, c). Then the GaPd precipitate 2 (fig. 5.12, a, top) results oriented approximately along the  $[034]^*_{\text{GaPd}}$  direction (fig. 5.12, b) and the GaPd precipitate 3 (fig. 5.12, a, below) appears oriented approximately along the  $[304]^*_{\text{GaPd}}$  direction (fig. 5.12, d). No remarkable features are observed for the precipitates in this direction except one of the lateral faces of the GaPd precipitate 2, being perpendicular to the  $[160]^*_{\text{Ga}_3\text{Pd}_5}$  matrix direction. [124]

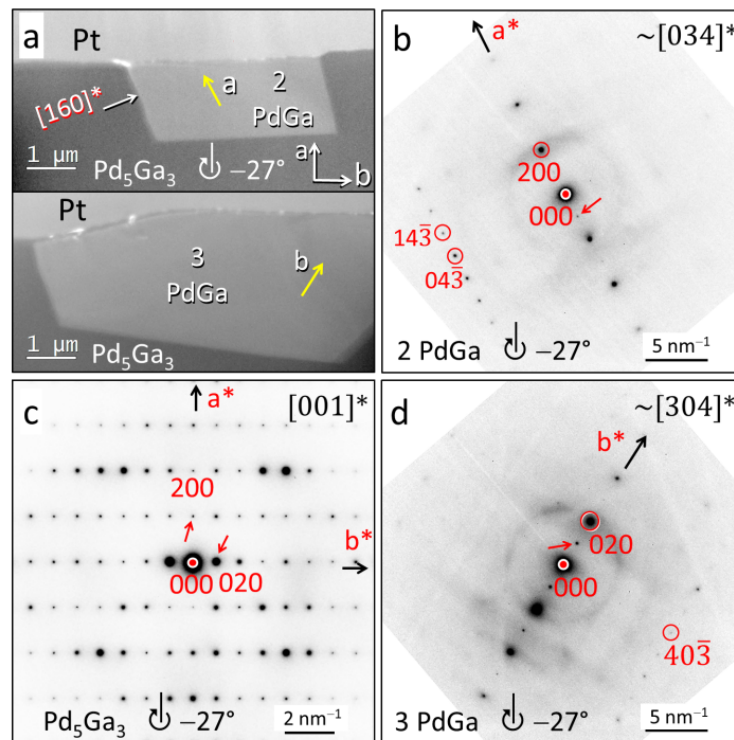


Figure 5.12: Images of the FIB II taken along  $[001]^*_{\text{Ga}_3\text{Pd}_5}$  direction by tilting  $-27^\circ$  around the TEM holder axis. a) TEM images of the GaPd precipitates 2 (top) and 3 (below). The main axes  $a$  and  $b$ , the  $[160]^*_{\text{Ga}_3\text{Pd}_5}$  matrix direction and the  $a$  axis of precipitate 2 are indicated (top). Furthermore, the  $b(=a)$  axis of precipitate 3 is indicated. b) SAED pattern of precipitate 2 along  $\approx[034]^*_{\text{GaPd}}$  direction. c)  $[001]^*_{\text{Ga}_3\text{Pd}_5}$  zone pattern of the bulk  $\text{Ga}_3\text{Pd}_5$  matrix. d)  $\approx[304]^*_{\text{GaPd}}$  pattern of precipitate 3. The red-arrowed reflections should be extinct but appear due to dynamical effects.  $\cup$  and  $\cup$  indicate rotations around the main holder axis. [124]

By tilting FIB II by  $6^\circ$  around the TEM holder axis and  $16^\circ$  perpendicular to the TEM holder axis, the GaPd precipitate 2 (fig. 5.13, a) results oriented along the  $[001]^*_{\text{GaPd}}$  direction (fig. 5.13, b) and the  $\text{Ga}_3\text{Pd}_5$  matrix appears in the  $[114]^*_{\text{Ga}_3\text{Pd}_5}$  direction (insert in (fig. 5.13, a)). Also, by tilting  $20^\circ$  around the TEM holder axis and  $-25^\circ$  perpendicular to the TEM holder axis the GaPd precipitate 3 results oriented along the  $[001]^*_{\text{GaPd}}$  direction. The  $\text{Ga}_3\text{Pd}_5$  matrix appears approx.  $5^\circ$  tilted from the  $[\bar{1}1\bar{2}]^*_{\text{Ga}_3\text{Pd}_5}$  direction, and only the approximate  $[110]^*_{\text{Ga}_3\text{Pd}_5}$  direction is shown in fig. 5.13, c. Again, no remarkable features are observed for the precipitates in this direction, only that their axes  $a$  or  $b$  are parallel to the matrix directions  $[1\bar{1}0]^*_{\text{Ga}_3\text{Pd}_5}$  or  $[110]^*_{\text{Ga}_3\text{Pd}_5}$ . Thus, the  $c$  axis of the GaPd precipitate 2 is tilted

approx.  $33^\circ$  from the  $c$  axis of the  $\text{Ga}_3\text{Pd}_5$  matrix (in the  $(100)_{\text{Ga}_3\text{Pd}_5}$  plane), but  $16^\circ$  out of the  $(100)_{\text{Ga}_3\text{Pd}_5}$  plane. Also, the  $c$  axis of the GaPd precipitate 3 is tilted approx.  $47^\circ$  from the  $c$  axis of the  $\text{Ga}_3\text{Pd}_5$  matrix (in the  $(100)_{\text{Ga}_3\text{Pd}_5}$  plane), but  $-25^\circ$  out of the  $(100)_{\text{Ga}_3\text{Pd}_5}$  plane. Furthermore, from the SEM/TEM/SAED results in the figs. 5.10, d, and 5.13, it is concluded that the GaPd precipitate 2 is elongated along its  $c$  axis while the GaPd precipitate 3 is almost equiaxial. From this study it appears that the precipitates are only elongated slightly along the  $a$  axis of the  $\text{Ga}_3\text{Pd}_5$  matrix. [124]

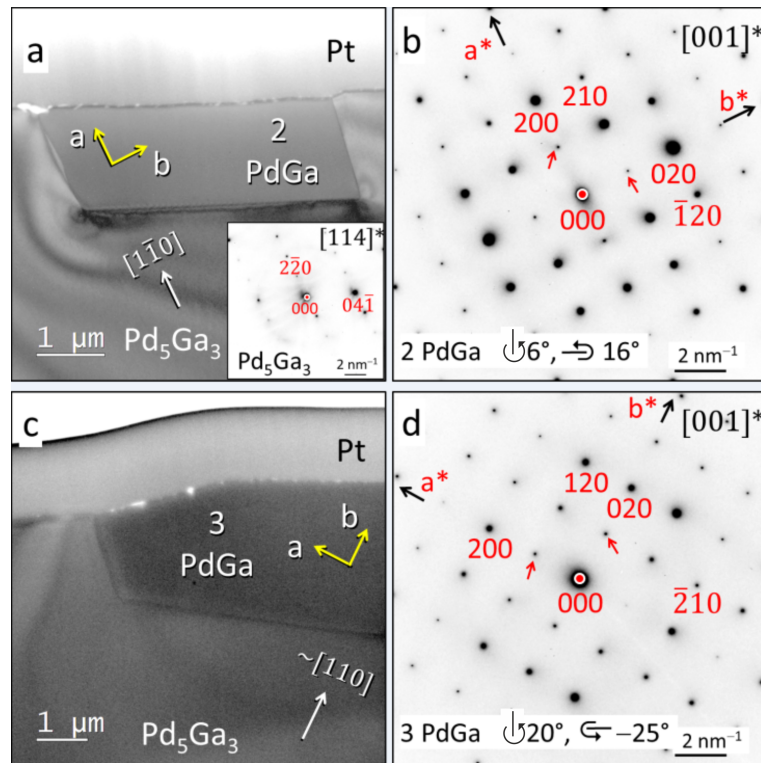


Figure 5.13: a,b) TEM image and SAED of precipitate 2 along the  $[001]^*_{\text{GaPd}}$  direction by tilting  $6^\circ$  around the TEM holder axis and  $16^\circ$  perpendicular to the TEM holder axis. Furthermore, the  $[114]^*_{\text{Ga}_3\text{Pd}_5}$  zone of the matrix is inserted. c,d) TEM image and SAED of precipitate 3 along the  $[001]^*_{\text{GaPd}}$  zone by tilting  $20^\circ$  around the TEM holder axis and  $-25^\circ$  perpendicular to the TEM holder axis. The precipitate's main axes  $a$  and  $b$ , as well as the  $[1\bar{1}0]^*_{\text{Ga}_3\text{Pd}_5}$  and  $[110]^*_{\text{Ga}_3\text{Pd}_5}$  matrix directions are indicated. Red-arrowed reflections should be extinct but appear due to dynamical effects.  $\cup$  and  $\downcup$  indicate rotations around the main holder axis and  $\curvearrowright$  and  $\curvearrowleft$  indicate rotations perpendicular to the main holder axis. [124]

The unit cell parameters for the matrix calculated from the  $[010]^*_{\text{Ga}_3\text{Pd}_5}$  zone in fig. 5.11 were  $a = 5.44 \text{ \AA}$  and  $c = 4.05 \text{ \AA}$ . Because GaPd crystallizes in a non-centrosymmetric space group ( $P2_13$ ), the choice of  $a$ ,  $b$  or  $c$  axes in the experimental SAED diffraction patterns was done by comparing with the corresponding calculated ones (*JEMS* program), where the 210, and equivalent reflections at both sides of the diagonal  $\langle 110 \rangle$  axes appear distinctly strong and weak. [124]

Even if the TEM/SAED numerical results do not have the highest accuracy, the relative magnitude or ratio of the unit cell axes found in the TEM study can be compared. A SAED pattern of the slow-cooled  $\text{Ga}_3\text{Pd}_5$  single crystal (previous



TEM study) and the SAED pattern of the same, but as-grown crystal, without further treatment (cooled with 250 K/h to room temperature) were compared. It was found that the  $b$  axis of the annealed, slow-cooled slab is 2 % larger than the  $b$  axis of the as-grown crystal (10.68 Å compared to 10.46 Å). In contrast, the  $a$  axis is approximately the same for both ( $a = 5.44$  Å). This can be observed directly in fig. 5.14 (reciprocal space  $[001]^*$  zone patterns). The horizontal reflection columns (along  $b^*$ ) in fig. 5.14, a, have a higher distance than in fig. 5.14, b (as-grown crystal), but those vertically along  $a^*$  are equal. In the as-grown  $\text{Ga}_3\text{Pd}_5$  single crystal, no  $\text{GaPd}$  precipitates or other planar defects were observed by TEM measurements. [124]

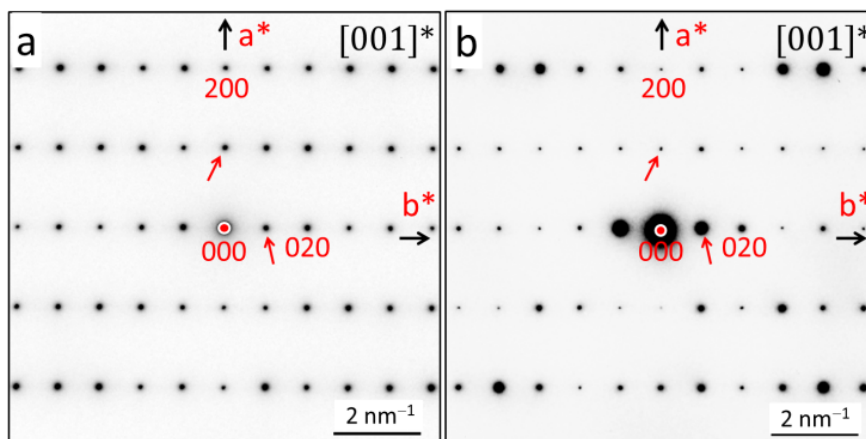


Figure 5.14: Comparison of the  $[001]^*_{\text{Ga}_3\text{Pd}_5}$  SAED patterns of the bulk  $\text{Ga}_3\text{Pd}_5$  single-crystalline matrix a) before and b) after annealing and slow cooling. Red-arrowed reflections should be extinct but appear due to dynamical effects. [124]

#### 5.4.4 Results from X-ray diffraction data analyses of $\text{Ga}_3\text{Pd}_5$

The XSD data set was reconstructed to three reciprocal lattice planes to prove the crystal quality and the lattice metric (fig. 5.15). The reconstructed reciprocal space planes of the XSD data show neither twins and diffuse streaks nor indications of symmetry lowering from the space group  $Pbam$ , known for  $\text{Ga}_3\text{Pd}_5$  [25]. Correction and integration of the XSD data set with a redundancy value of 10 were executed, using the program package *CrysAlis*, including orientation matrix refinements, peak profile analyses, Lorentz polarization, semi-empirical absorption correction, scaling, and merging. The data quality corresponds to an internal criteria value of  $R_{\text{merge}} = 0.06$ .

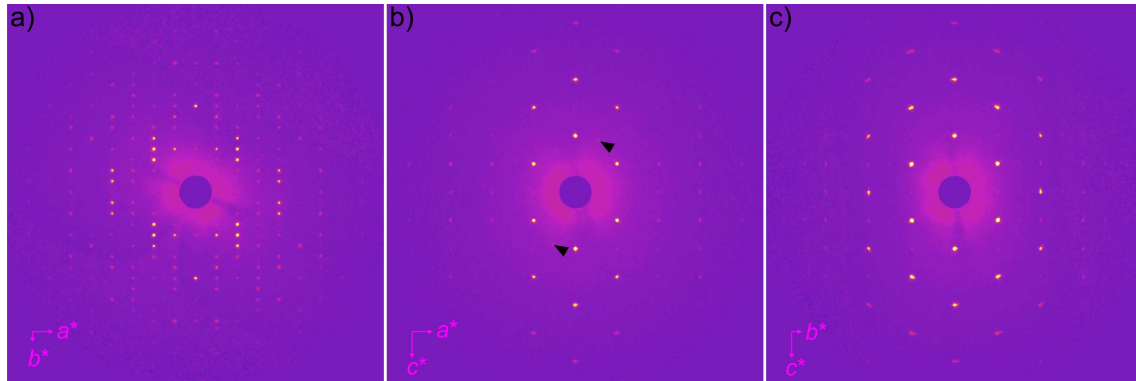


Figure 5.15: Reciprocal planes  $(hk0)$ ,  $(h0l)$  and  $(0kl)$ , reconstructed from XSD data. Black arrows in b show reflexes that do not belong to the lattice of  $\text{Ga}_3\text{Pd}_5$ .

Atom	Site	$x$	$y$	$z$	$U_{11}$ [ $\text{\AA}^2$ ]	$U_{22}$ [ $\text{\AA}^2$ ]	$U_{33}$ [ $\text{\AA}^2$ ]	$U_{12}$ [ $\text{\AA}^2$ ]	$U_{13}$ [ $\text{\AA}^2$ ]	$U_{23}$ [ $\text{\AA}^2$ ]	Oc.
Pd1	4h	0.31119(12)	0.39505(7)	1/2	0.0104(3)	0.0108(4)	0.0122(3)	0.0006(2)	0	0	1
Pd2	4g	0.09328(12)	0.23353(7)	0	0.0071(3)	0.0108(3)	0.0138(3)	-0.0016(2)	0	0	1
Pd3	2c	1/2	0	0	0.0120(4)	0.0116(5)	0.0142(4)	-0.0029(4)	0	0	1
Ga1	4h	0.3434(2)	0.14526(10)	1/2	0.0115(4)	0.0096(5)	0.0132(4)	-0.0016(3)	0	0	1
Ga2	2a	0	0	0	0.0119(6)	0.0102(7)	0.0126(6)	0.0001(5)	0	0	1

Table 5.1: Atomic positions and displacement parameters gained by Rietveld refinement of the XSD data.

The structure solution and refinements were straightforward and identified three unique sites for Pd and two for Ga atoms, based on their relatively distinctive X-ray scattering power. All anisotropic atomic displacement parameters (ADP) could be simultaneously refined without high correlations. The resulting ADP values are commonly small, near to  $0.01 \text{ \AA}^2$ , and full occupation fits best, as listed in tab. 5.1.

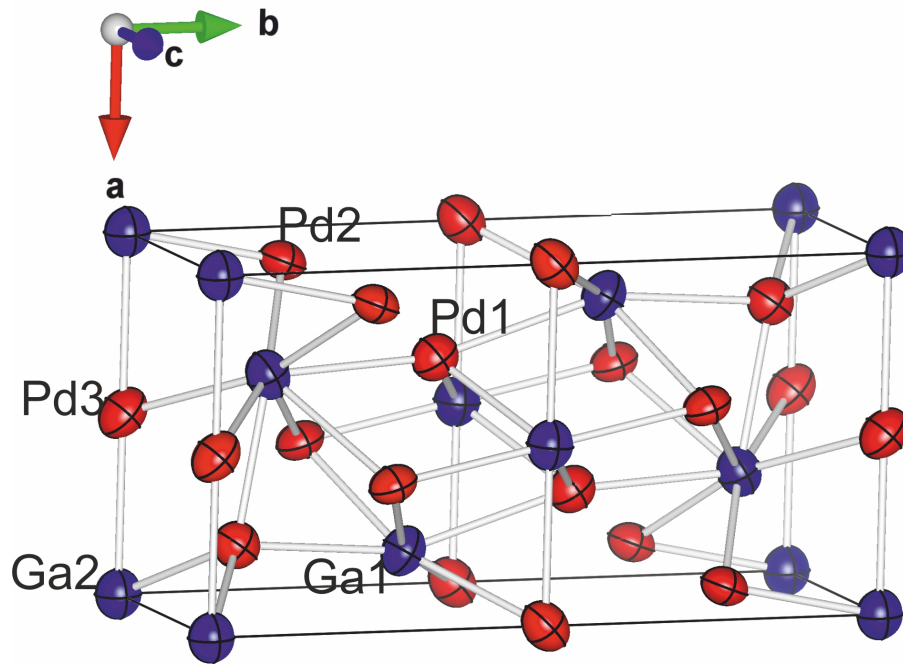


Figure 5.16: Unit cell from the refined structure data of tab. 5.1, constructed in *VESTA* [127].

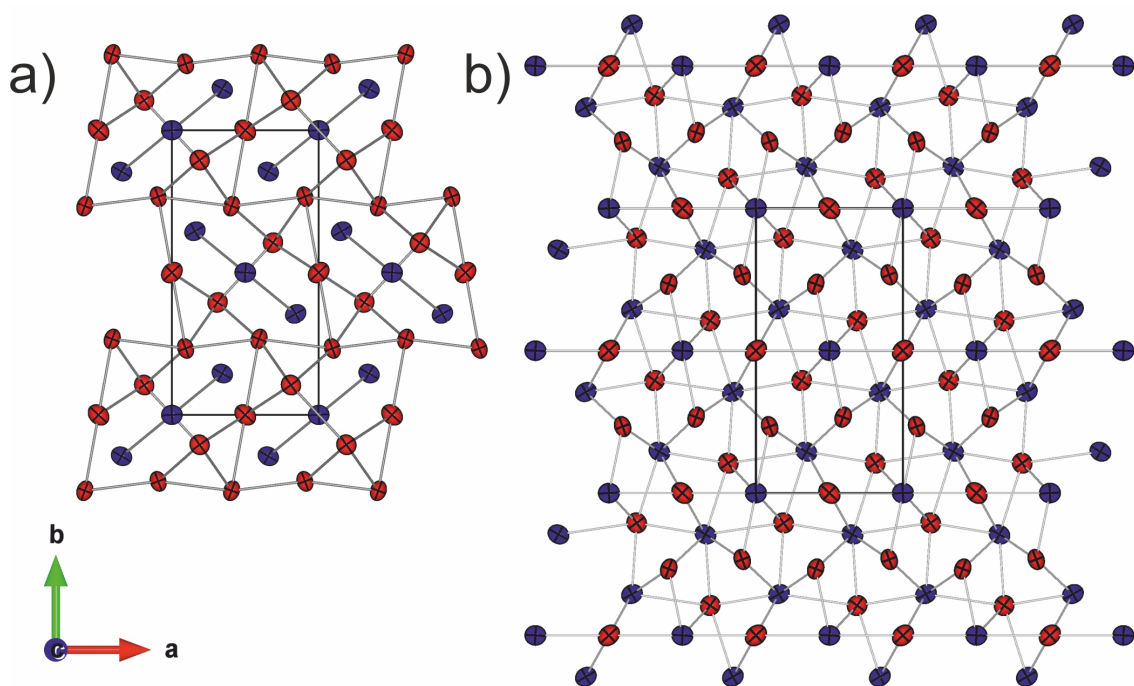


Figure 5.17: a) ABAB... sequence along  $b$ ; b) perfect straight lines of alternating Ga and Pd atoms in  $[100]$  with a bonding length of  $\frac{a}{2} = 2.72\text{\AA}$ , at  $z = 0$  and  $y = 0$  and  $0.5$ . Constructed in *VESTA* [127].



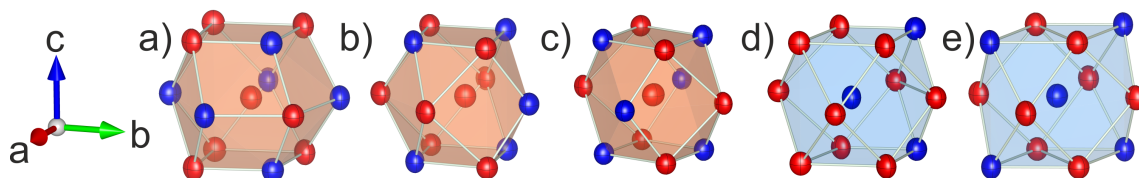


Figure 5.18: Coordination polyhedra of a) Pd1, b) Pd2, c) Pd3, d) Ga1, e) Ga2. Constructed in *VESTA* [127].

The phase shows stacking sequences of ABAB... along the  $[010]$  direction (fig. 5.17, a). Perfectly straight lines of alternating Ga and Pd atoms can be observed in direction  $[100]$ , with a bonding length of  $\frac{a}{2} = 2.72 \text{ \AA}$ , at  $z = 0$  and  $y = 0$  and  $0.5$ . Furthermore, there are layers in the  $(010)$  plane at  $y = 0.25$  and  $0.75$  built of Pd only. This distinguishes  $\text{Ga}_3\text{Pd}_5$  from the neighbouring phases  $\text{GaPd}$  and  $\text{GaPd}_2$  (fig. 5.17, b). In the  $[001]$  direction all coordination polyhedra (fig. 5.18) are framed by faces that coincide with the  $(001)$  plane. These are either at  $z = 0$  (Pd1, Ga1) or at  $z = 0.5$  (Pd2, Pd3, Ga2). Accordingly, all atoms are settled on one of the two mirror planes parallel to  $(001)$ .

The XPD measurements (fig. 5.19) show a pronounced texture of preferred orientation caused by a platy-like cracking/cleaving behaviour. There is more than one domain of preferred orientation, from which only the platy orientation parallel to the  $(010)$  plane could be specified. This has also been observed macroscopically as a pronounced cleavage parallel to  $(010)$ . Le Bail fitting using the structure model shown in tab. 5.1 and internal  $\text{LaB}_6$  standard (NIST 660c) resulted in the lattice parameters  $a = 5.438(1) \text{ \AA}$ ,  $b = 10.550(2) \text{ \AA}$ , and  $c = 4.024(1) \text{ \AA}$  ( $R_p = 2.74$ ,  $R_{wp} = 4.77$ ,  $R_{exp} = 2.73$ ,  $\chi^2 = 3.05$ ).

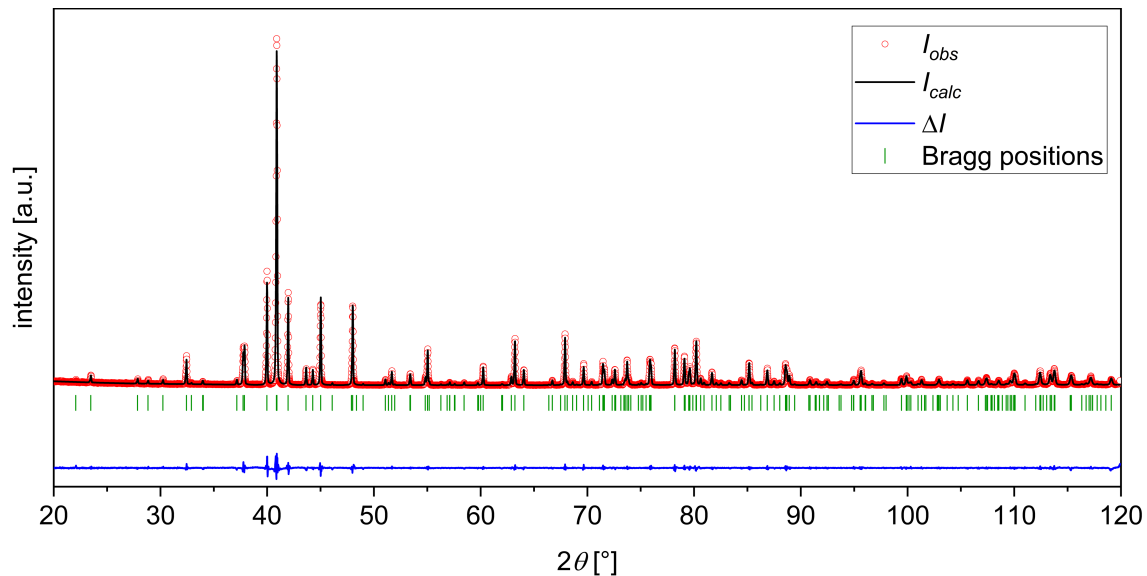


Figure 5.19: Phase-pure Le Bail-fitted XPD pattern of a milled and then annealed piece of the Czochralski-grown  $\text{Ga}_3\text{Pd}_5$  crystal, measured with  $\text{Cu-}K\alpha_1$  radiation ( $R_p = 7.32$ ,  $R_{wp} = 10.9$ ,  $R_{exp} = 7.76$ ,  $\chi^2 = 1.97$ ).  $I_{obs}$  is the measured intensity,  $I_{calc}$  is the fitted intensity and  $\Delta I$  is the difference between measured and calculated intensities. This pattern shows pronounced preferred orientation.

Rietveld refinement of the XPD data (fig. 5.20) showed slight deviations between the modelled and the measured structure factor, especially for the 002 peak, that cannot be explained with preferred orientation. If the Ga1 and the Pd1 positions are regarded (tab. 5.2), the error of the anisotropic displacement factor in  $z$  direction ( $B_{33}$ ) is almost a factor of ten higher for the lighter Ga atom even though they are both  $4h$  Wyckoff positions. Furthermore, for Pd1 the error of  $B_{33}$  in  $z$  direction is higher than the value of  $B_{33}$  itself, even though the position allows no degree of freedom in  $z$  direction.

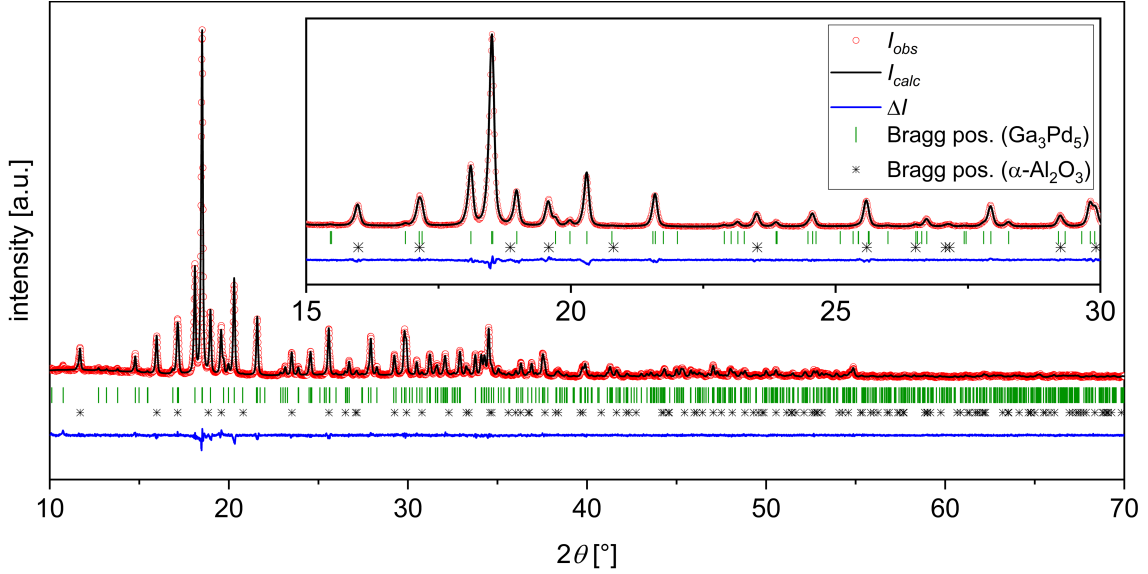


Figure 5.20: Rietveld refinement of a milled and annealed piece of the Czochralski-grown  $\text{Ga}_3\text{Pd}_5$  crystal, with internal corundum standard (NBS 674a), measured with  $\text{Mo-}K\alpha_1$  radiation ( $R_p = 9.84$ ,  $R_{wp} = 9.45$ ,  $R_{exp} = 8.59$ ,  $\chi^2 = 1.21$ ).  $I_{obs}$  is the measured intensity,  $I_{calc}$  is the fitted intensity and  $\Delta I$  is the difference between measured and calculated intensities.

Atom	Site	$x$	$y$	$z$	$B_{11}$ [ $\text{\AA}^2$ ]	$B_{22}$ [ $\text{\AA}^2$ ]	$B_{33}$ [ $\text{\AA}^2$ ]	$B_{12}$ [ $\text{\AA}^2$ ]	$B_{13}$ [ $\text{\AA}^2$ ]	$B_{23}$ [ $\text{\AA}^2$ ]	Oc.
Pd1	4h	0.3110(3)	0.39573(14)	1/2	27(5)	5(1.3)	7(11)	-5(2)	0	0	1
Pd2	4g	0.0950(3)	0.23257(14)	0	21(5)	7(1)	52(12)	-4(2)	0	0	1
Pd3	2c	1/2	0	0	32(7)	5(2)	16(52)	-6(3)	0	0	1
Ga1	4h	0.3433(4)	0.1457(2)	1/2	29(8)	10(2)	67(18)	5(3)	0	0	1
Ga2	2a	0	0	0	26(11)	5(3)	51(23)	10(5)	0	0	1

Table 5.2: Atomic positions and displacement parameters gained by Rietveld refinement of the XPD data.

This gives rise to the assumption that there is a statistical disorder in the material that cannot be stacking faults since diffuse scattering was excluded. Therefore, either point defects or a selective enrichment or depletion of one kind of element may be the reason. Both seem to be possible with respect to a certain width of the homogeneity region. Additionally, chemical measurements by EPMA gave some hint at a small gradient in the Ga-Pd ratio along the growth direction. Hence, off-stoichiometry may result in either interstitials or vacancies. Further answers might only bring diffraction studies using synchrotron radiation.

## 5.5 Discussion

### 5.5.1 Crystal growth

During the search for the seeding temperature it was striking that low supercooling of less than 2 K occurred. Compared to other Ga-rich Ga-Pd solutions, where supercooling effects up to 160 K occurred frequently, and in average at least supercooling of 20 K appeared, 2 K is noticeably low, but an experimental advantage [26]. During growth the rotation speed of the crystal was kept at higher values in order to achieve a more homogeneous circular temperature field around the crystal which might help getting a more rounded diameter. However, a round cross section of the growing crystal could not be achieved. The pronounced anisotropic crystallization rate of the fast [100], and the slow [010] direction dominated the growth process, creating a strongly elliptic, or even rectangular cross section. Regarding the stable, stepped (010) vicinal face, step formation, and thus inclination of the enveloping face, with respect to the crystallographic (010) plane, is the observed way how the growing crystal increases its radius. The radius in the [100] direction increased until the very end of the experiment (visible by the inclined shoulder). Therefore, it is expected that an even lower pulling rate might have created a more rounded diameter. However, there are experimental time limits to this. Calculating with the lever rule, the achieved 3.1 g of crystal mass corresponds to 34 % of the maximum possible yield of  $\text{Ga}_3\text{Pd}_5$ . Accordingly, the experiment could have been continued. However, in the present growth experiment no in-situ measurement method of the crystal's weight like a load cell was used and the mass could only be estimated by visual observation through the viewport. Besides this imprecise method another difficulty, regarding the end of the growth process, is the eutectic at the end of the liquidus of  $\text{Ga}_3\text{Pd}_5$ . The crystal sticking to the eutectic is an obvious risk of too long growth and cannot be taken, since it is likely that the crystal would take serious damage. The measured tiny decrease of the Pd content, from top to bottom of the crystal would correspond to the reported width of the homogeneity region in the phase diagram and a Pd decrease with decreasing growth temperature, and is further discussed in the following section, 5.5.2. Nevertheless, this small variation lies within experimental errors.

### 5.5.2 Stability of $\text{Ga}_3\text{Pd}_5$

Since several measured signals in the DTA curves could not be directly related to the phase diagram, annealing and slow-cooling experiments of a single-crystalline slice of  $\text{Ga}_3\text{Pd}_5$  were carried out. Regarding fig. 5.21, a, a crystal grown from a melt composition of  $c_0$  to a melt composition of  $c_{end}$  (which corresponds approximately to the real experimental composition range of QX658) has a crystal composition which is shifted gradually from  $c_1$  to  $c_2$ . When cooling the crystal to lower temperatures, followed by reheating in the DTA, the first visible endothermic signal should be at that temperature where the last grown part (with the composition  $c_2$ ) reaches the solidus. No part of the crystal has a solid composition left of  $c_2$ . Accordingly, the endothermic signals that were measured at the temperatures 930°C and 980°C cannot be explained, even though these transformation temperatures do occur in the phase diagram at the eutectoid decomposition temperature of  $\text{Ga}_4\text{Pd}_5$  (where  $\text{Ga}_3\text{Pd}_5$  has the Ga-richest composition), and at the eutectic temperature. The

peaks at 930°C and 980°C were observed in all measurements with different pieces of the single crystal and can also be observed in data of earlier studies on inclusion-free  $\text{Ga}_3\text{Pd}_5$  with the same thermal history, but were not further addressed [112]. Furthermore, the peak at 758°C upon cooling is difficult to explain. The peak was already observed in other studies as well (however, 10 K higher, at 768°C) and explained by the deferred eutectoid decomposition of  $\text{Ga}_4\text{Pd}_5$  [112]. This is possible since the DTA heating experiments were carried out up to temperatures where decomposition of the crystal occurred. When cooling down again, the melt follows the overall crystallization path including the formation of  $\text{Ga}_4\text{Pd}_5$  at the eutectic reaction at 981°C.

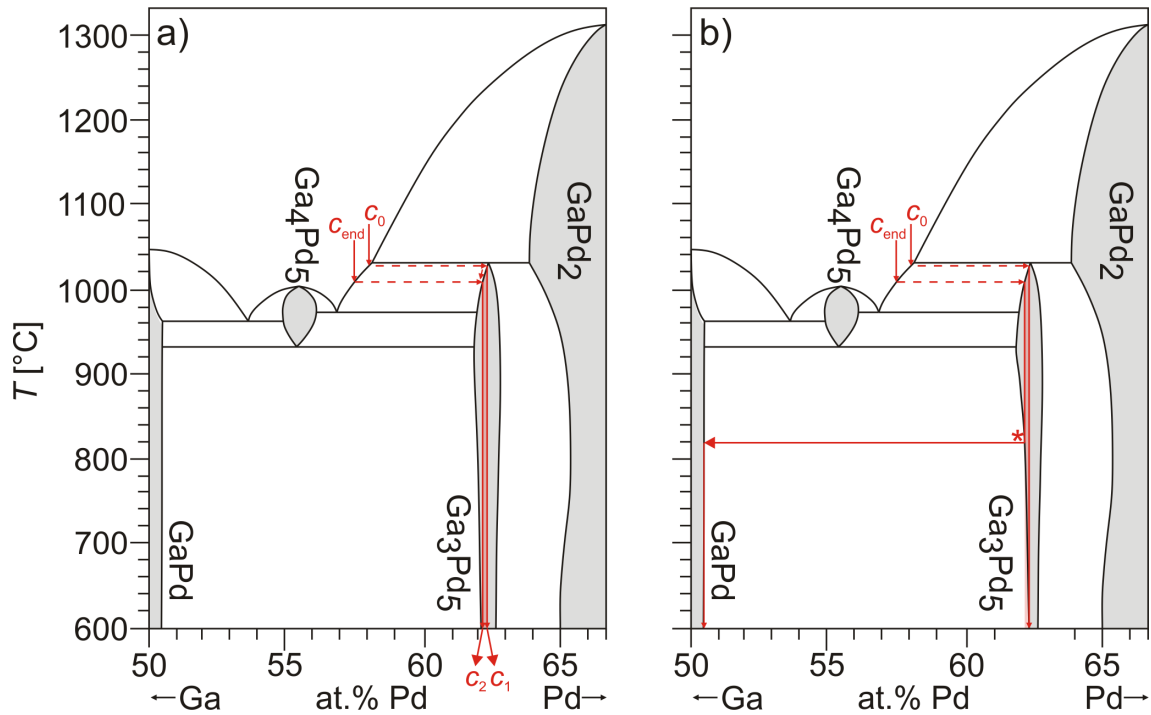


Figure 5.21: a) Ga-Pd phase diagram, changed after [23]. b) Exemplary sketch with a stronger retrograde solubility of Ga in  $\text{Ga}_3\text{Pd}_5$ . The star marks a position where the neighbouring phase GaPd would precipitate during cooling.

The only possible explanation for the peaks at 930°C and 980°C in the DTA heating curve is a narrowing of the homogeneity region of  $\text{Ga}_3\text{Pd}_5$  with lower temperatures, i.e. a retrograde solubility of Ga in  $\text{Ga}_3\text{Pd}_5$  with decreasing temperatures. This is very well consistent with the formation of the GaPd precipitates observed in the annealing and long-term cooling experiments of a single-crystalline piece. Furthermore, it is known from other phases of the Ga-Pd system, e.g.  $\text{GaPd}_2$  that such retrograde solubilities occur, e.g. a retrograde solubility of Ga in  $\text{GaPd}_2$  with decreasing temperatures [11, 112]. In the phase diagram, a decent retrograde solubility of Ga in  $\text{Ga}_3\text{Pd}_5$  is indicated (fig. 5.1 [23]), however in a dimension that is too low to explain the DTA signals and the observed precipitation of GaPd in the composition range of the grown  $\text{Ga}_3\text{Pd}_5$  crystal of this study. While slowly cooling the crystal, a retrograde solubility of Ga in  $\text{Ga}_3\text{Pd}_5$  leads to the precipitation of the neighbouring phase, in this case GaPd as sketched in fig. 5.21, b, at the position, marked with the star. The narrowing of the homogeneity region of  $\text{Ga}_3\text{Pd}_5$  must be below 930°C

since the GaPd precipitates have been found to be single-crystalline. Accordingly, if the narrowing would have taken place at temperatures above 930°C Ga<sub>4</sub>Pd<sub>5</sub> would have been formed, later decomposing in an eutectoid decay. This would have led to polycrystalline precipitates of GaPd and Ga<sub>3</sub>Pd<sub>5</sub> which cannot be observed. The fact that the constriction must be below 930°C raises the suspicion that the signals, observed around 758°C and 768°C may be the temperatures, where GaPd precipitates. However, explaining the signal with the deferred eutectoid decomposition of Ga<sub>4</sub>Pd<sub>5</sub> still cannot be excluded.

From that point of view, the observed DTA curves can be explained easier: During cooling after the growth experiment the Ga<sub>3</sub>Pd<sub>5</sub> crystal reaches a temperature where GaPd precipitates. From now on the material is a two-phase material. Heating up again, at 930°C at the interfaces between the GaPd precipitates and the Ga<sub>3</sub>Pd<sub>5</sub> matrix, Ga<sub>4</sub>Pd<sub>5</sub> is formed and the first DTA signal appears. Depending on the size of the precipitates it may be possible that GaPd completely reacts with Ga<sub>3</sub>Pd<sub>5</sub>. Heating further, at 980°C the Ga<sub>4</sub>Pd<sub>5</sub>-Ga<sub>3</sub>Pd<sub>5</sub> eutectic reaction is reached and some melt of the eutectic composition forms, leading to the weak endothermic signal. At 1027°C the crystal is completely dissolved, i.e. the solidus is passed. Cooling down again in the DTA, the whole crystallization path is passed. First (signal at 1026°C) Ga<sub>3</sub>Pd<sub>5</sub> crystallizes and then (at 981°C) the eutectic is reached. The absence of the signal at 930°C in the cooling curve may either be explained by the deferred decomposition of Ga<sub>4</sub>Pd<sub>5</sub> (see the discussion around the peaks at 758°C and 768°C above) or the exothermic energy of the decomposition of Ga<sub>4</sub>Pd<sub>5</sub> is too low to be detected. Since eutectoid decompositions are phase transitions in the solid state, it is common that these occur deferred or even are kinetically completely inhibited [128].

According to the yield calculation with the lever rule, the crystal was grown within the first third ( $58.1 \text{ at.}\% > x_{Pd} > 57.8 \text{ at.}\%$ ) of the composition range, from which the phase can be theoretically grown from the liquid phase ( $58.3 \text{ at.}\% > x_{Pd} > 57.1 \text{ at.}\%$ ). As sketched in fig. 5.21, a, the crystal was approximately grown between the starting composition  $c_0$  and the composition  $c_{end}$ . Accordingly, the crystal has a composition range, starting from  $c_1$  near the seed, and ending at  $c_2$ . If the homogeneity region would look as published ([23]) and sketched in fig. 5.21, a, a crystal with that composition range would not decompose during cooling and accordingly during heating in the DTA the first signal would appear at the temperature that corresponds to the intersect point of the solidus and  $c_2$  (i.e. also the intersect of  $c_{end}$  and the liquidus). Consequently, the constriction of the homogeneity region of Ga<sub>3</sub>Pd<sub>5</sub> must start already within the addressed range of  $58.1 \text{ at.}\% > x_{Pd} > 57.8 \text{ at.}\%$ .

Additionally, the high amount of precipitated GaPd on the surface, compared to the low amount of precipitated GaPd in the bulk of the annealed Ga<sub>3</sub>Pd<sub>5</sub> slice must be discussed. In literature, it is well known that the surface composition of bi-metallic compounds may be different from the bulk composition. This is especially the case for alloys but also known for intermetallics [129, 130]. Especially at high temperatures, it can be expected that atoms are highly mobile even in intermetallic structures. For the intermetallic compound TiAl it was shown that the mobility is significantly increased if the compound is off-stoichiometric [131], which must be expected if Ga-rich Ga<sub>3</sub>Pd<sub>5</sub> with retrograde solubility of Ga is grown from solution. For GaPd and Ga<sub>7</sub>Pd<sub>3</sub> segregation of Ga to the surface was stated [6] and accord-

ingly it is likely that the same holds for  $\text{Ga}_3\text{Pd}_5$ . A Ga-enrichment on the surface would cause stronger precipitation of GaPd on the surface compared to the bulk. Additionally, the surface nucleation of surface precipitates is significantly influenced by the surface roughness [132]. Since the crystal slice was not polished after cutting with the wire lapping saw before annealing, a certain surface roughness has to be expected. The non-annealed powders of  $\text{Ga}_3\text{Pd}_5$  for XPD showed a pronounced peak broadening, comparable to  $\text{GaPd}_2$  and  $\text{Ga}_{1-x}\text{Sn}_x\text{Pd}_2$  as reported in section 3.3.1. Furthermore, the measured, non-annealed pieces of  $\text{Ga}_3\text{Pd}_5$  for XSD always showed Debye-Scherrer rings. Accordingly, a disrupted, partially polycrystalline surface as discussed in section 4.3 is likely after cutting of  $\text{Ga}_3\text{Pd}_5$ . Long-term cooling, or rather long times at high temperatures might lead to Ostwald ripening and partial healing of the surface [117]. Hence, the recrystallization of the former surface, the growth of large GaPd grains, and the formation of  $\text{Ga}_3\text{Pd}_5$  grains as shown in fig. 5.8 at the expense of the disrupted, partly polycrystalline surface can be well explained. A comparable long-term cooling study on a polished surface might gain further information. The length of the precipitates on the surface may be up to 100  $\mu\text{m}$ . However, they also reach several micrometers (up to 4  $\mu\text{m}$ ) into the bulk. Surface diffusion is by far faster, however in metals at high temperatures, bulk diffusion by thermal fluctuations and lattice vibrations cannot be neglected, especially if the surface exhibits a different elemental concentration. Accordingly, precipitates of a depth of several micrometers are not unusual [132, 133].

The X-ray pattern of the  $\theta$ - $\theta$  scan carried out on the annealed crystal slice (fig. 5.6) correlates well with the surface texture of the surface precipitates. The main  $\text{Ga}_3\text{Pd}_5$  reflexes,  $h00$ , of the slab are present but also the XPD patterns of GaPd and  $\text{Ga}_3\text{Pd}_5$ . That fits to the core-shell structure (e.g. the two larger precipitates in fig. 5.5, b), with the outer shell being a mixed, polycrystalline material of mostly GaPd and minor amounts of  $\text{Ga}_3\text{Pd}_5$ . The uneven  $h00$  reflexes found in the pattern can be explained with the second harmonic diffraction ( $\lambda/2$ ) since the intensity, obtained from the single-crystalline slab exceeds that of usual powders by far.

The TEM studies showed a coherence between the GaPd precipitates and the  $\text{Ga}_3\text{Pd}_5$  matrix. However, the relationship is not fully understood yet. Especially precipitates, laying with their  $[001]_{\text{GaPd}}$  directions parallel or almost parallel to the directions  $[010]_{\text{Ga}_3\text{Pd}_5}$  or  $[001]_{\text{Ga}_3\text{Pd}_5}$  were observed. Additionally, a relation between the shared planes  $\{201\}_{\text{GaPd}}$  with  $\{001\}_{\text{Ga}_3\text{Pd}_5}$  and  $\{101\}_{\text{Ga}_3\text{Pd}_5}$  was found. However, for more detailed information on the coherence and whether or not all precipitates are coherent, studies on a larger number of precipitates are necessary. Furthermore, only the surface precipitates have been studied in detail and no precipitate from the bulk of the annealed slab has been investigated yet.

The crucial question arising, is whether or not the crystal is single-crystalline, and also single-phase after the growth. No precipitates were found in the as-grown crystal, neither on the surface of polished samples, nor in the TEM examinations. Also, the TEM examinations showed a different lattice parameter  $b$  between the as-grown and the slow-cooled crystal. Accordingly, it seems possible that the cooling rate of 250 K/h at the end of the growth process was fast enough to kinetically prevent the precipitation of GaPd, and the crystal was phase-purely preserved to room temperature.



### 5.5.3 Structure refinement of Ga<sub>3</sub>Pd<sub>5</sub>

It is unknown, whether the mentioned precipitation affected the XSD measurements. Fig. 5.15 shows that minor reflexes are present in the XSD pattern, that do not belong to the refined Ga<sub>3</sub>Pd<sub>5</sub> lattice. However, these reflexes appear only very rarely, and further investigations would be necessary. It has not yet been possible to assign them to GaPd. They might also originate from a tiny second grain of Ga<sub>3</sub>Pd<sub>5</sub>, oriented differently, compared to the main grain, however this assignment could not be made. If the reflexes would originate from GaPd, it should be concluded that they are highly coherent, otherwise no single reflexes but Debye-Scherrer rings would result from multiple precipitates. XSD with synchrotron radiation might address this problem.

However, the resulting atomic displacement parameters (ADP) are commonly small, close to 0.01 Å<sup>2</sup>, as listed in tab. 5.1. Hence, a static disorder of Ga and Pd over the five independent atomic sites could be tentatively excluded. For this reason, the previous report by Schubert et al., suggesting the 4*h* Ga, and the 4*h* Pd site to be exchanged [51] seems unlikely but the earlier published structure [25] is properly matching. The final structure refinement cycle in this study gave rise to a calculated density of  $\rho_{calc} = 10.66 \text{ g/cm}^3$  which is in excellent agreement to the experimentally measured density  $\rho_{exp} = 10.66(2) \text{ g/cm}^3$ .

Regarding the observed cleavage in (010), as well as the texture effects in X-ray powder diffraction patterns with platy-like habitus in the (010) plane, the stacking sequence ABAB... observed along the [010] direction offers a good explanation. Having in mind that Ga, as an excess component, is enriched at the growth interface, the pure Pd layers in the (010) plane could be the reason why the crystal shows a remarkably slow growth velocity along [010] and an extremely stable (010) vicinal face. Along the [100] direction perfectly straight aligned alternating Ga-Pd-Ga-Pd... chains might lead to a preferred growth in this direction, for the same reason.

# Chapter 6

## Conclusion

### 6.1 Phase diagram studies and single crystal growth in the Ga-Pd-Sn system

Single crystal growth in the ternary Ga-Sn-Pd system has been studied for the first time, with the background of using well oriented single-crystalline surfaces for basic research in heterogeneous catalysis. Based upon encouraging results with the binary Ga-Pd intermetallic compounds, the question came up to study the electronic contribution of a group IV element substituting for Ga in the isostructural solid solution (Ga, Sn)Pd<sub>2</sub>. In order to investigate this problem with various crystallographically oriented surfaces, successful growth of single crystals was regarded the bottleneck of the whole project.

#### 6.1.1 Phase diagram studies focussed on Ga<sub>1-x</sub>Sn<sub>x</sub>Pd<sub>2</sub>

Equilibrium-cooling and Bridgman experiments have been carried out in the Ga-Pd-Sn system for understanding the liquidus surface of the (Ga,Sn)-rich side of the primary crystallization region of Ga<sub>1-x</sub>Sn<sub>x</sub>Pd<sub>2</sub>. From these experiments the information, necessary for the Czochralski single crystal growth could be achieved. Accordingly, Ga<sub>1-x</sub>Sn<sub>x</sub>Pd<sub>2</sub> can be grown from the melt with Sn contents of  $x_L \leq 0.60$ , and Pd contents of  $56 \leq y_L \leq 62$ , according to the initial composition (Ga<sub>1-x<sub>L</sub></sub>Sn<sub>x<sub>L</sub></sub>)<sub>100-y<sub>L</sub></sub>Pd<sub>y<sub>L</sub></sub>. Larger Pd contents, above  $y_L > 62$ , have not been investigated. The pseudobinary segregation coefficient,  $k^* = \frac{x}{x_L}$ , proved to be close to the value 1 (in the range of  $x_L \leq 0.50$ ), meaning that the replacement of Ga by Sn in the starting solution, equals the substitution of Ga by Sn in the crystal. For larger Sn contents,  $x_L > 0.50$ , segregation becomes noticeable and the maximum substituted Ga by Sn in the crystal was  $x_{max} = 0.54$  (crystallized from melts with  $x_L = 0.60$ ).

First information regarding the equilibrium between the only known ternary phase Ga<sub>2+p+q</sub>Sn<sub>4-p</sub>Pd<sub>9</sub> and the liquid phase was gained. Accordingly, Ga<sub>2+p+q</sub>Sn<sub>4-p</sub>Pd<sub>9</sub> crystallizes exclusively incongruent and its primary crystallization area is adjacent to the (Ga,Sn)-rich border of the primary solidification region of Ga<sub>1-x</sub>Sn<sub>x</sub>Pd<sub>2</sub>. All primarily crystallized grains of the phase Ga<sub>2+p+q</sub>Sn<sub>4-p</sub>Pd<sub>9</sub> in the investigated equilibrium-cooling experiments, decomposed at least partially peritectoid during cooling. Accordingly the stability field of this phase is constricted at lower temperatures.

First results on full crystallization paths, mainly with the focus on the phase  $\text{Ga}_{1-x}\text{Sn}_x\text{Pd}_2$  have been achieved. However, for detailed information more experiments are necessary since the ternary Ga-Pd-Sn system contains numerous different phases within very narrow chemical composition ranges, comparable to the binary Ga-Pd and Pd-Sn systems [23, 39]. The presence of at least one high-temperature phase seems assured, but the phase could not be further specified.

### 6.1.2 Single crystal growth of $\text{Ga}_{1-x}\text{Sn}_x\text{Pd}_2$

Large  $\text{Ga}_{1-x}\text{Sn}_x\text{Pd}_2$  single crystals were grown with the Czochralski technique from (Ga,Sn)-rich solutions. For this purpose, the Czochralski method proved to be a well suited crystal growth method. Crystals with a mass of up to 18 g were grown within the pulling time of 20 – 25 days. By applying low pulling rates (partly as low as 25  $\mu\text{m}/\text{h}$ ), inclusions caused by constitutional supercooling could be successfully avoided. Difficulties that had to be handled during the crystal growth were high temperatures of up to approx. 1250°C, and enabling stable conditions during long-term experiments. Stable diameter development of the crystal was challenging since changes became noticeable within time scales of hours, meaning that the operators reactions and adaptations on the growth parameters are always late. This problem could be handled by experience since the material's parameters and behaviour became known in the course of the series of experiments.

The crystals were analysed for their chemical composition, the lattice constants and their microstructure. Segregation curves measured along the crystal axis, show a weak increase of the Sn content to later grown parts, indicating an enrichment of Sn in the melt during crystal growth. Precise chemical analysis of the single crystals revealed that the actual pseudobinary segregation coefficient,  $k^*$ , is slightly smaller than 1, explaining why segregation occurs. In order to ensure the structural consistency of the solid solution, X-ray powder diffraction data of milled crystals of all compositions have been collected. Rietveld refinement and Le Bail fitting with internal standard material resulted in precise lattice parameters of the crystals that increase with increasing Sn contents. Investigations on the microstructure of the crystals, by Laue scans, X-ray rocking curve analysis, electron backscatter diffraction, and X-ray topography show that the crystals contain low-angle grain boundaries. However, the measured tilt between the subgrains is usually far below 1°.

For catalytic studies the preparation of single-crystalline surfaces was necessary.  $\text{Ga}_{1-x}\text{Sn}_x\text{Pd}_2$  crystals came out to be very sensitive to mechanical surface treatments like cutting, lapping, grinding and polishing. Surface preparation may cause disruptions on the surface and even polycrystalline sub-surface damage layers, several micrometers in thickness could be proven by X-ray analysis. However, careful defined polishing with grinding pressure control resulted in disruption-free surfaces good enough for further surface-sensitive treatments and finally catalytic measurements.

Single crystals with the compositions  $x = 0.08, 0.18, 0.29$  and 0.40 could be provided and accordingly all necessary compositions for catalytic studies, i.e. to distinguish structural and electronic effects of the heterogeneous catalyst  $\text{Ga}_{1-x}\text{Sn}_x\text{Pd}_2$  for the semi-hydrogenation of acetylene (fig. 1.2), could be covered [19]. From these compositions single crystalline surfaces, oriented parallel to the (100), (010), (001),

(210) and (013) planes were prepared. These samples are investigated catalytically by the Institut für Chemie at the Technische Universität Chemnitz. Also, surface-physical investigations are carried out at the Institut Jean Lamour of the Université de Lorraine in Nancy. Furthermore, high-quality single crystalline samples could be achieved suitable for X-ray single crystal diffraction investigations that were recently carried out at the Max-Planck-Institut für Chemische Physik fester Stoffe in Dresden [80].

## 6.2 Single crystal growth of $\text{Ga}_3\text{Pd}_5$

The growth of a relatively large  $\text{Ga}_3\text{Pd}_5$  single crystal was achieved for the first time. A remarkably stable (010) surface of the intermetallic compound and an extremely anisotropic growth were observed, the latter being much faster in [100] compared to the [010] direction.

Annealing experiments showed that  $\text{Ga}_3\text{Pd}_5$  has a stronger retrograde solubility of Ga with lower temperatures than previously expected, leading to the risk of precipitation of the neighbouring phase GaPd. However, the precipitation is kinetically restrained and in faster cooled samples (250 K/h) no evidence for GaPd precipitates was found, while in slowly cooled  $\text{Ga}_3\text{Pd}_5$ , GaPd precipitates in coherent manner. However, further studies are necessary for more detailed statements.

The structure determination confirms the published structure and the space group  $Pbam$ .

# Bibliography

- [1] M. Armbrüster, R. Schlögl, and Yu. Grin, “Intermetallic compounds in heterogeneous catalysis - a quickly developing field,” *Sci. Technol. Adv. Mater.*, vol. 15, no. 034803, pp. 1–17, 2014.
- [2] M. Armbrüster, “Intermetallic compounds in catalysis – a versatile class of materials meets interesting challenges,” *Sci. Technol. Adv. Mater.*, vol. 21, no. 1, pp. 303–322, 2020.
- [3] W. M. H. Sachtler and R. A. Van Santen, “Surface Composition and Selectivity of Alloy Catalysts,” *Adv. Catal.*, vol. 26, pp. 69–119, 1977.
- [4] D. Zahn, F. Haarmann, and Yu. Grin, “Atomistic Simulation Study of  $\text{Cu}_{0.327}\text{Ni}_{0.673}$  Alloys: from Solid Solution to Phase Segregation,” *Z. Anorg. Allg. Chem.*, vol. 634, no. 14, pp. 2562–2566, 2008.
- [5] J. Osswald, R. Giedigkeit, R. E. Jentoft, M. Armbrüster, F. Girgsdies, K. Kovnir, T. Ressler, Yu. Grin, and R. Schlögl, “Palladium-gallium intermetallic compounds for the selective hydrogenation of acetylene: Part I: Preparation and structural investigation under reaction conditions,” *J. Catal.*, vol. 258, no. 1, pp. 210–218, 2008.
- [6] J. Osswald, K. Kovnir, M. Armbrüster, R. Giedigkeit, R. E. Jentoft, U. Wild, Yu. Grin, and R. Schlögl, “Palladium-gallium intermetallic compounds for the selective hydrogenation of acetylene: Part II: Surface characterization and catalytic performance,” *J. Catal.*, vol. 258, no. 1, pp. 219–227, 2008.
- [7] K. Kovnir, J. Osswald, M. Armbrüster, R. Giedigkeit, T. Ressler, Yu. Grin, and R. Schlögl, “PdGa and  $\text{Pd}_3\text{Ga}_7$ : Highly-Selective Catalysts for the Acetylene Partial Hydrogenation,” in *Stud. Surf. Sci. Catal.*, vol. 162, pp. 481–488, 2006.
- [8] M. Krajčí and J. Hafner, “Semihydrogenation of Acetylene on the (010) Surface of  $\text{GaPd}_2$ : Ga Enrichment Improves Selectivity,” *J. Phys. Chem. C*, vol. 118, no. 23, pp. 12285–12301, 2014.
- [9] A. Ota, M. Armbrüster, M. Behrens, D. Rosenthal, M. Friedrich, I. Kasatkin, F. Girgsdies, W. Zhang, R. Wagner, and R. Schlögl, “Intermetallic Compound  $\text{Pd}_2\text{Ga}$  as a Selective Catalyst for the Semi-Hydrogenation of Acetylene: From Model to High Performance Systems,” *J. Phys. Chem. C*, vol. 115, no. 4, pp. 1368–1374, 2011.

- [10] P. Gille, T. Ziemer, M. Schmidt, K. Kovnir, U. Burkhardt, and M. Armbrüster, "Growth of large PdGa single crystals from the melt," *Intermetallics*, vol. 18, no. 8, pp. 1663–1668, 2010.
- [11] J. Schwerin, D. Müller, S. Kiese, and P. Gille, "Single crystal growth in the Ga-Pd system," *J. Cryst. Growth*, vol. 401, pp. 613–616, 2014.
- [12] M. Armbrüster, H. Borrmann, M. Wedel, Y. Prots, R. Giedigkeit, and P. Gille, "Refinement of the crystal structure of palladium gallium (1:1), PdGa," *Z. Kristallogr.*, vol. 225, no. 4, pp. 617–618, 2010.
- [13] M. Armbrüster, K. Kovnir, M. Behrens, D. Teschner, Yu. Grin, and R. Schlögl, "Pd-Ga Intermetallic Compounds as Highly Selective Semihydrogenation Catalysts," *J. Am. Chem. Soc.*, vol. 132, no. 42, pp. 14745–14747, 2010.
- [14] J. Prinz, R. Gaspari, C. A. Pignedoli, J. Vogt, P. Gille, M. Armbrüster, H. Brune, O. Gröning, D. Passerone, and R. Widmer, "Isolated Pd Sites on the Intermetallic PdGa(111) and PdGa( $\bar{1}\bar{1}\bar{1}$ ) Model Catalyst Surfaces," *Angew. Chem. Int. Ed.*, vol. 51, no. 37, pp. 9339–9343, 2012.
- [15] D. Rosenthal, R. Widmer, R. Wagner, P. Gille, M. Armbrüster, Yu. Grin, R. Schlögl, and O. Gröning, "Surface Investigation of Intermetallic PdGa( $\bar{1}\bar{1}\bar{1}$ )," *Langmuir*, vol. 28, no. 17, pp. 6848–6856, 2012.
- [16] M. Klanjšek, A. Gradišek, A. Kocjan, M. Bobnar, P. Jeglič, M. Wencka, Z. Jagličić, P. Popčević, J. Ivkov, A. Smontara, P. Gille, M. Armbrüster, Yu. Grin, and J. Dolinšek, "PdGa intermetallic hydrogenation catalyst: An NMR and physical property study," *J. Phys. Condens. Mater.*, vol. 24, no. 8, pp. 1–9, 2012.
- [17] J. Prinz, C. A. Pignedoli, Q. S. Stöckl, M. Armbrüster, H. Brune, O. Gröning, R. Widmer, and D. Passerone, "Adsorption of Small Hydrocarbons on the Three-Fold PdGa Surfaces: The Road to Selective Hydrogenation," *J. Am. Chem. Soc.*, vol. 136, no. 33, pp. 11792–11798, 2014.
- [18] O. Matselko, Yu. Grin, R. Gladyshevskii, and U. Burkhardt, "Phase relations in the ternary system Ga-Pd-Sn at 500°C," *Mater. Charact.*, vol. 147, pp. 443–452, 2019.
- [19] O. Matselko, R. R. Zimmermann, A. Ormeci, U. Burkhardt, R. Gladyshevskii, Yu. Grin, and M. Armbrüster, "Revealing Electronic Influences in the Semihydrogenation of Acetylene," *J. Phys. Chem. C*, vol. 122, no. 38, pp. 21891–21896, 2018.
- [20] A. Borodziński and G. C. Bond, "Selective Hydrogenation of Ethyne in Ethene-Rich Streams on Palladium Catalysts. Part 1. Effect of Changes to the Catalyst During Reaction," *Catal. Rev. Sci. Eng.*, vol. 48, no. 2, pp. 91–144, 2006.
- [21] J. Czochralski, "Ein neues Verfahren zur Messung der Kristallisationsgeschwindigkeit der Metalle," *Z. Phys. Chem.*, vol. 92U, no. 1, pp. 219–221, 1918.

- [22] D. C. A. Ivarsson, I. G. Aviziotis, T. Keilhauer, and M. Armbrüster, "Fixed-bed reactor for catalytic studies on low-surface area materials," *Rev. Sci. Instrum.*, vol. 90, no. 014101, pp. 1–6, 2019.
- [23] H. Okamoto, "Ga-Pd (Gallium-Palladium)," *J. Phase Equilib. Diffus.*, vol. 29, no. 5, pp. 466–467, 2008.
- [24] Y. N. Grin, "The Intergrowth Concept as a Useful Tool to Interpret and Understand Complicated Intermetallic Structures," in *Modern Perspectives in Inorganic Crystal Chemistry. NATO ASI Series, vol. 382* (E. Parthé, ed.), pp. 77–96, Dordrecht: Springer Netherlands, 1992.
- [25] K. Schubert, H. Breimer, R. Gohle, H. L. Lukas, H. G. Meissner, and E. Stolz, "Einige strukturelle Ergebnisse an metallischen Phasen III," *Naturwissenschaften*, vol. 45, pp. 360–361, 1958.
- [26] K. Bader, A. Dorner, and P. Gille, "Single crystal growth of solid solutions from the Ga-Pd-Sn system for basic research in heterogeneous catalysis," *J. Cryst. Growth*, vol. 532, pp. 1–7, 2020.
- [27] A. Dorner, *Crystal Growth and Characterization of Ga<sub>1-x</sub>Sn<sub>x</sub>Pd*. Master's thesis, Fakultät für Geowissenschaften, Ludwig-Maximilians-Universität München, 2018.
- [28] A. Dorner, "Pre-Experiments QX 681 and investigations regarding the order of crystallization of Sn<sub>2</sub>Pd and Sn<sub>3</sub>Pd in Samples with intermediate Sn contents in the starting melt," tech. rep., Fakultät für Geowissenschaften, Ludwig-Maximilians-Universität München, 2018.
- [29] W. Reschetilowski, "Vorwort," in *Einführung in die Heterogene Katalyse*, pp. V–VII, Dresden: Springer Spektrum Berlin, Heidelberg, 2015.
- [30] W. Reschetilowski, "Begriffe und Definitionen in der heterogenen Katalyse," in *Einführung in die Heterogene Katalyse*, pp. 11–28, Dresden: Springer Spektrum Berlin, Heidelberg, 2015.
- [31] J. Osswald, *Active-Site Isolation for the Selective Hydrogenation of Acetylene: the Pd-Ga and Pd-Sn Intermetallic Compounds*. PhD thesis, Technische Universität Berlin, 2006.
- [32] Á. Molnár, A. Sárkány, and M. Varga, "Hydrogenation of carbon-carbon multiple bonds: Chemo-, regio- and stereo-selectivity," *J. Mol. Catal. A Chem.*, vol. 173, no. 1-2, pp. 185–221, 2001.
- [33] A. N. R. Bos and K. R. Westerterp, "Mechanism and kinetics of the selective hydrogenation of ethyne and ethene," *Chem. Eng. Process.: Process Intensif.*, vol. 32, no. 1, pp. 1–7, 1993.
- [34] Y. Luo, S. Alarcón Villaseca, M. Friedrich, D. Teschner, A. Knop-Gericke, and M. Armbrüster, "Addressing electronic effects in the semi-hydrogenation of ethyne by InPd<sub>2</sub> and intermetallic Ga-Pd compounds," *J. Catal.*, vol. 338, pp. 265–272, 2016.



- [35] M. Armbrüster, "Eine wissenschaftsbasierte Entwicklung selektiver Hydrierkatalysatoren," *Z. Anorg. Allg. Chem.*, vol. 636, no. 11, pp. 2043–2043, 2010.
- [36] K. Kovnir, M. Schmidt, C. Waurisch, M. Armbrüster, Y. Prots, and Yu. Grin, "Refinement of the crystal structure of dipalladium gallium, Pd<sub>2</sub>Ga," *Z. Kristallogr. N. Cryst. Struct.*, vol. 223, pp. 7–8, 2008.
- [37] F. Laufek, A. Vymazalová, F. Laufek, and J. Plášil, "Powder X-ray diffraction study of synthetic PdSn," *Powder Diffr.*, vol. 21, no. 4, pp. 307–309, 2006.
- [38] S. Püschel, *Synthesis and Characterisation of (Ga,Ge)Pd<sub>2</sub>*. Master's thesis, Fakultät für Geowissenschaften, Ludwig-Maximilians-Universität München, 2020.
- [39] H. Okamoto, "Pd-Sn (Palladium-Tin)," *J. Phase Equilib. Diffus.*, vol. 33, no. 3, pp. 253–254, 2012.
- [40] O. Matselko, U. Burkhardt, Y. Prots, R. R. Zimmermann, M. Armbrüster, R. Gladyshevskii, and Yu. Grin, "The First Ternary Phase in the Ga-Sn-Pd System: Synthesis, Crystal Structure, and Catalytic Properties of Ga<sub>2+x+y</sub>Sn<sub>4-x</sub>Pd<sub>9</sub>," *Eur. J. Inorg. Chem.*, vol. 2017, no. 29, pp. 3542–3550, 2017.
- [41] T. J. Anderson and I. Ansara, "The Ga-Sn (Gallium-Tin) System," *J. Phase Equilib.*, vol. 13, no. 2, pp. 181–189, 1992.
- [42] A. D. Pelton, "Thermodynamics and Phase Diagrams of Materials," in *Phase Transformations in Materials* (G. Kostorz, ed.), pp. 1–80, Weinheim: Wiley-VCH Verlag GmbH, 2001.
- [43] N. Eustathopoulos, M. G. Nicolas, and B. Drevet, "Wetting properties of metal/carbon systems," in *Pergamon Materials Series: Wettability at High Temperatures* (N. Eustathopoulos, M. G. Nicolas, and B. Drevet, eds.), vol. 3, pp. 317–338, Pergamon, 1999.
- [44] P. Gille and B. Bauer, "Single crystal growth of Al<sub>13</sub>Co<sub>4</sub> and Al<sub>13</sub>Fe<sub>4</sub> from Al-rich solutions by the Czochralski method," *Cryst. Res. Technol.*, vol. 43, no. 11, pp. 1161–1167, 2008.
- [45] H. J. Scheel, "Accelerated crucible rotation: a novel stirring technique in high-temperature solution growth," *J. Cryst. Growth*, vol. 13/14, pp. 560–565, 1972.
- [46] M. Planck, "Zur Theorie des Gesetzes der Energieverteilung im Normalspectrum," in *Verhandl. Dtsch. Phys. Ges. 2*, pp. 237–245, John Wiley & Sons, Ltd, 1900.
- [47] K. Khalaff and K. Schubert, "Kristallstruktur von Pd<sub>5</sub>Ga<sub>2</sub>," *J. Less-Common Met.*, vol. 37, no. 1, pp. 129–140, 1974.
- [48] K. Bader and P. Gille, "Single Crystal Growth of FeGa<sub>3</sub> and FeGa<sub>3-x</sub>Ge<sub>x</sub> from High-Temperature Solution using the Czochralski Method," *Cryst. Res. Technol.*, vol. 55, no. 2, pp. 1–8, 2020.

- [49] P. Gille, “Single crystal growth of intermetallics by the Czochralski method,” in *Crystal Growth of Intermetallics* (P. Gille and Yu. Grin, eds.), pp. 61–90, Berlin/Boston: De Gruyter, 2019.
- [50] H. Ipsier, “Phase diagrams for crystal growth of intermetallics,” in *Crystal Growth of Intermetallics* (P. Gille and Yu. Grin, eds.), pp. 21–48, Berlin/Boston: De Gruyter, 2019.
- [51] K. Schubert, H. L. Lukas, H.-G. Meissner, and S. Bhan, “Zum Aufbau der Systeme Kobalt-Gallium, Palladium-Gallium, Palladium-Zinn und verwandter Legierungen,” *Z. Metallkd.*, vol. 50, no. 9, pp. 534–540, 1959.
- [52] L. Vegard, “Die Konstitution der Mischkristalle und die Rauffüllung der Atome,” *Z. Phys. A Hadrons Nucl.*, vol. 5, no. 1, pp. 17–26, 1921.
- [53] W. C. Dash, “Growth of Silicon Crystals Free from Dislocations,” *J. Appl. Phys.*, vol. 30, no. 4, pp. 459–474, 1959.
- [54] K.-T. Wilke and J. Bohm, “Vergrößerungen, Zellularwachstum, Morphologische Stabilität,” in *Kristallzüchtung* (K.-T. Wilke and J. Bohm, eds.), pp. 349–365, Berlin: VEB Deutscher Verlag der Wissenschaften, 1988.
- [55] D. T. J. Hurle, “Morphological Stability of a Planar Rotating Interface,” in *Crystal Pulling from the Melt* (D. T. J. Hurle, ed.), ch. 9, pp. 101–124, Berlin Heidelberg: Springer-Verlag, 1993.
- [56] D. T. J. Hurle, “Constitutional supercooling during crystal growth from stirred melts-I: Theoretical,” *Solid State Electron.*, vol. 3, no. 1, pp. 37–44, 1961.
- [57] M. E. Glicksman, “Dendritic Growth,” in *Handbook of Crystal Growth (Second Edition), vol. I: Fundamentals: Part B: Transport and Stability* (T. Nishinaga, ed.), ch. 16, pp. 669–722, Boston: Elsevier, 2015.
- [58] W. A. Tiller, K. A. Jackson, J. W. Rutter, and B. Chalmers, “The redistribution of solute atoms during the solidification of metals,” *Acta Metall.*, vol. 1, no. 4, pp. 428–437, 1953.
- [59] A. Fick, “Über Diffusion,” *Ann. Phys.*, vol. 170, no. 1, pp. 59–86, 1855.
- [60] A. Einstein, “Über die von der molekularkinetischen Theorie der Wärme geforderte Bewegung von in ruhenden Flüssigkeiten suspendierten Teilchen,” *Ann. Phys.*, vol. 322, no. 8, pp. 549–560, 1905.
- [61] J. Rodríguez-Carvajal, “Recent advances in magnetic structure determination by neutron powder diffraction,” *Physica B Condens. Matter*, vol. 192, no. 1-2, pp. 55–69, 1993.
- [62] P. Thompson, D. E. Cox, and J. B. Hastings, “Rietveld refinement of Debye-Scherrer synchrotron X-ray data from  $\text{Al}_2\text{O}_3$ ,” *J. Appl. Cryst.*, vol. 20, no. 2, pp. 79–83, 1987.
- [63] S. Barth, personal communication, Technische Universität Chemnitz, 2018.

- [64] W. H. Bragg and W. L. Bragg, "The Reflection of X-rays by Crystals," *Proc. R. Soc. Lond. A*, vol. 88, no. 605, pp. 428–438, 1913.
- [65] C. Giacovazzo, "The diffraction of X-rays by crystals," in *Fundamentals of Crystallography* (C. Giacovazzo, ed.), pp. 141–228, Oxford: Oxford University Press, 1992.
- [66] Yu. Grin, unpublished report, tech. rep., Max-Planck-Institut für Chemische Physik fester Stoffe, Dresden, 2018.
- [67] J. L. Pouchou and F. Pichoir, "A new model for quantitative X-ray microanalysis. Part I: Application to the analysis of homogeneous samples," *Rech. Aerosp.*, vol. 3, pp. 167–192, 1984.
- [68] N. Sarah, K. Alasafi, and K. Schubert, "Kristallstruktur von  $\text{Pd}_{20}\text{Sn}_{13}$ ,  $\text{Pd}_6\text{AgPb}_4$  und  $\text{Ni}_{13}\text{ZnGe}_8$ ," *Z. Metallkd.*, vol. 72, no. 7, pp. 517–520, 1981.
- [69] W. Klein, H. Jin, V. Hlukhyy, and T. F. Fässler, " $\text{Pd}_{20}\text{Sn}_{13}$  revisited: crystal structure of  $\text{Pd}_{6.96}\text{Sn}_{4.31}$ ," *Acta Crystallogr. E Crystallogr. Commun.*, vol. 71, no. 7, pp. 807–809, 2015.
- [70] P. Scherrer, "Bestimmung der Größe und der inneren Struktur von Kolloidteilchen mittels Röntgenstrahlen," *Nachrichten von der Gesellschaft der Wissenschaften zu Göttingen, Mathematisch-Physikalische Klasse 1918*, pp. 98–100, 1918.
- [71] G. Liu, Q. Yang, C. Wang, Z.-h. Yu, and G.-j. Zhang, "Solidification sequence and as-cast microstructure of a model Pb-Bi-Sn alloy with quasi-peritectic reaction," *China Foundry*, vol. 16, pp. 399–405, 2019.
- [72] S. Ida, N. Sekido, and K. Yoshimi, "Solidification pathways and phase equilibria in the Mo-Ti-C ternary system," *High Temp. Mater. Process.*, vol. 39, pp. 164–170, 2020.
- [73] S. Akamatsu, S. Bottin-Rousseau, G. Faivre, and E. A. Brener, "Scaling Theory of Two-Phase Dendritic Growth in Undercooled Ternary Melts," *Phys. Rev. Lett.*, vol. 112, no. 105502, pp. 1–5, 2014.
- [74] K.-T. Wilke and J. Bohm, "Verfahren nach Bridgman-Stockbarger (Bewegen des Tiegels im Temperaturfeld)," in *Kristallzüchtung* (K.-T. Wilke and J. Bohm, eds.), pp. 609–647, Berlin: VEB Deutscher Verlag der Wissenschaften, 1988.
- [75] D. A. Porter and K. E. Easterling, "Eutectic Solidification," in *Phase Transformations in Metals and Alloys, second edition* (D. A. Porter and K. E. Easterling, eds.), ch. 4.3.2, pp. 222–229, Boca Raton: CRC Press, Taylor & Francis Group, 2004.
- [76] H. Walker, S. Liu, J. H. Lee, and R. Trivedi, "Eutectic Growth in Three Dimensions," *Metall. Mater. Trans. A*, vol. 38A, pp. 1417–1425, 2007.

- [77] K. J. Kim, Y. Furuya, K. Kamada, R. Murakami, V. V. Kochurikhin, M. Yoshino, H. Chiba, S. Kurosawa, A. Yamaji, Y. Shoji, S. Toyoda, H. Sato, Y. Yokota, Y. Ohashi, and A. Yoshikawa, "Growth and Scintillation Properties of Directionally Solidified Ce:LaBr<sub>3</sub>/AEBBr<sub>2</sub> (AE = Mg, Ca, Sr, Ba) Eutectic System," *Crystals*, vol. 10, no. 584, pp. 1–9, 2020.
- [78] S. Liu, J. H. Lee, and R. Trivedi, "Dynamic effects in the lamellar–rod eutectic transition," *Acta Mater.*, vol. 59, no. 8, pp. 3102–3115, 2011.
- [79] S. K. Aramanda, K. Chattopadhyay, and A. Choudhury, "Exotic three-phase microstructures in the ternary Ag-Cu-Sb eutectic system," *Acta Mater.*, vol. 221, no. 117400, pp. 1–18, 2021.
- [80] Yu. Grin, personal communication, Max-Planck-Institut für Chemische Physik fester Stoffe Dresden, 2020.
- [81] U. Burkhardt, to be published, Max-Planck-Institut für Chemische Physik fester Stoffe Dresden, 2021.
- [82] M. Hahne and P. Gille, "Single crystal growth of the intermetallic compound InPd," *J. Cryst. Growth*, vol. 401, pp. 622–626, 2014.
- [83] M. Kürten and J. Schilz, "Polycrystalline wetting layer on Czochralski single crystals of strongly segregating systems," *J. Cryst. Growth*, vol. 141, no. 3-4, pp. 473–475, 1994.
- [84] H. Wenzl, A. Fattah, and W. Uelhoff, "Measurements of the contact angle between melt and crystal during Czochralski growth of copper," *J. Cryst. Growth*, vol. 36, no. 2, pp. 319–322, 1976.
- [85] P. Rudolph, "Transport phenomena of crystal growth - heat and mass transfer," *AIP Conf. Proc.*, vol. 1270, pp. 107–132, 2010.
- [86] O. Harder, *Forced convection by high-speed rotation in Czochralski growth of intermetallics*. Master's thesis, Fakultät für Geowissenschaften, Ludwig-Maximilians-Universität München, 2018.
- [87] K.-T. Wilke and J. Bohm, "Korngrenzen, Subkorngrenzen, Fehlerflächen," in *Kristallzüchtung* (K.-T. Wilke and J. Bohm, eds.), pp. 380–389, Berlin: VEB Deutscher Verlag der Wissenschaften, 1988.
- [88] K.-T. Wilke and J. Bohm, "Grundlagen des Czochralskiverfahrens," in *Kristallzüchtung* (K.-T. Wilke and J. Bohm, eds.), pp. 680–701, Berlin: VEB Deutscher Verlag der Wissenschaften, 1988.
- [89] K. Bader, *Crystal growth and characterization of Fe(Ga,Ge)<sub>3</sub> grown by the Czochralski technique*. Master's thesis, Fakultät für Geowissenschaften, Ludwig-Maximilians-Universität München, 2016.
- [90] B. Depuydt, A. Theuwis, and I. Romandic, "Germanium: From the first application of Czochralski crystal growth to large diameter dislocation-free wafers," *Mater. Sci. Semicond. Process.*, vol. 9, no. 4-5, pp. 437–443, 2006.

- [91] M. Feuerbacher, C. Thomas, and S. Roitsch, "Single-crystal growth of the complex metallic alloy phase  $\text{Mg}_{32}(\text{Al,Zn})_{49}$ ," *Intermetallics*, vol. 16, no. 8, pp. 943–947, 2008.
- [92] J. H. Wernick, G. W. Hull, T. H. Geballe, J. E. Bernardini, and E. Buehler, "Czochralski growth of A15 structure intermetallic compounds," *J. Cryst. Growth*, vol. 47, no. 1, pp. 73–76, 1979.
- [93] L. A. Maslova, "Dependence of Subgrain Dimensions and Disorientation on Dislocation Density in Crystals Grown by the Bridgman, Kyropoulos, Czochralski or Stepanov Method," *Krist. Tech.*, vol. 10, no. 4, pp. 423–432, 1975.
- [94] S. V. Tsivinsky and L. A. Maslova, "Subgrain structure formation in pure crystals grown from melts," *Krist. Tech.*, vol. 15, no. 2, pp. 123–148, 1980.
- [95] D. Oriwol, E.-R. Carl, A. N. Danilewsky, L. Sylla, W. Seifert, M. Kittler, and H. S. Leipner, "Small-angle subgrain boundaries emanating from dislocation pile-ups in multicrystalline silicon studied with synchrotron white-beam X-ray topography," *Acta Mater.*, vol. 61, no. 18, pp. 6903–6910, 2013.
- [96] E.-R. Carl, A. Danilewsky, E. Meissner, and T. Geiger, "Large- and small-angle grain boundaries in multi-crystalline silicon and implications for the evolution of grain boundaries during crystal growth," *J. Appl. Cryst.*, vol. 47, no. 6, pp. 1958–1965, 2014.
- [97] L. Germain, D. Kratsch, M. Salib, and N. Gey, "Identification of sub-grains and low angle boundaries beyond the angular resolution of EBSD maps," *Mater. Charact.*, vol. 98, pp. 66–72, 2014.
- [98] K.-T. Wilke and J. Bohm, "Kinetischer Verteilungskoeffizient," in *Kristallzüchtung* (K.-T. Wilke and J. Bohm, eds.), pp. 299–303, Berlin: VEB Deutscher Verlag der Wissenschaften, 1988.
- [99] J. A. Burton, R. C. Prim, and W. P. Slichter, "The Distribution of Solute in Crystals Grown from the Melt. Part I. Theoretical," *J. Chem. Phys.*, vol. 21, no. 11, pp. 1987–1991, 1953.
- [100] J. Friedrich, W. von Ammon, and G. Müller, "Czochralski Growth of Silicon Crystals," in *Handbook of Crystal Growth (Second Edition)*, vol. IIA: Bulk Crystal Growth (P. Rudolph, ed.), ch. 2, pp. 45–104, Boston: Elsevier, 2015.
- [101] G. Müller, "Macroscopic Inhomogeneity," in *Crystal Growth from the Melt* (G. Müller, ed.), ch. 3, pp. 29–56, Berlin, Heidelberg: Springer-Verlag, 1988.
- [102] J. Barthel and M. Jurisch, "Oszillation der Erstarrungsgeschwindigkeit beim Kristallwachstum aus der Schmelze mit rotierendem Keimkristall," *Krist. Tech.*, vol. 8, no. 1-3, pp. 199–206, 1973.
- [103] B. Bauer, G. Meisterernst, J. Härtwig, T. Schenk, and P. Gille, "Czochralski growth and X-ray topographic characterization of decagonal  $\text{AlCoNi}$  quasicrystals," *Philos. Mag.*, vol. 86, no. 3-5, pp. 317–322, 2006.

- [104] A. G. Ostrogorsky and M. E. Glicksman, "Segregation and Component Distribution," in *Handbook of Crystal Growth (Second Edition)*, vol. IIB: *Growth Mechanisms and Dynamics* (P. Rudolph, ed.), ch. 25, pp. 995–1047, Boston: Elsevier, 2015.
- [105] T. M. Cuff, "Beilby Layer," tech. rep., Temple University, Philadelphia, 1993.
- [106] I. Zarudi and L. C. Zhang, "Effect of ultraprecision grinding on the microstructural change in silicon monocrystals," *J. Mater. Process. Technol.*, vol. 84, no. 1-3, pp. 149–158, 1998.
- [107] J. Xu, J. B. Luo, L. L. Wang, and X. C. Lu, "The crystallographic change in sub-surface layer of the silicon single crystal polished by chemical mechanical polishing," *Tribol. Int.*, vol. 40, no. 2, pp. 285–289, 2007.
- [108] Č. Barta Jr., V. Brožek, B. H'jek, and Č. Barta, "Properties of Surface Layers in Single Crystals of Calomel," *Cryst. Res. Technol.*, vol. 17, no. 4, pp. 439–448, 1982.
- [109] D. M. Turley and L. E. Samuels, "The nature of mechanically polished surfaces of copper," *Metallogr.*, vol. 14, no. 4, pp. 275–294, 1981.
- [110] I. Zarudi and L. Zhang, "Subsurface damage in single-crystal silicon due to grinding and polishing," *J. Mater. Sci. Lett.*, vol. 15, pp. 586–587, 1996.
- [111] S. Barth, personal communication, Technische Universität Chemnitz, 2020.
- [112] J. Schwerin, *Einkristallzüchtung und Charakterisierung intermetallischer Phasen des Ga-Pd-Systems*. Ph.D. thesis, Ludwig-Maximilians-Universität München, 2015.
- [113] L. Lutterotti and S. Gialanella, "X-ray diffraction characterization of heavily deformed metallic specimens," *Acta Mater.*, vol. 46, no. 1, pp. 101–110, 1998.
- [114] C. Patiño-Carachure, O. Téllez-Vazquez, A. Bedolla-Jacuinde, R. Esparza, C. Ángeles-Chávez, R. Perez, and G. Rosas, "Electron Microscopy Characterization of Humidity Ball-Milling AlCuFe Intermetallic Powders," *Mater. Res. Soc. Symp. Proc.*, vol. 1242, 2010.
- [115] J. I. Langford, "A rapid method for analysing the breadths of diffraction and spectral lines using the Voigt function," *J. Appl. Cryst.*, vol. 11, pp. 10–14, 1978.
- [116] W. Schatt, "Kristallerholung und Rekristallisation," in *Einführung in die Werkstoffwissenschaft* (W. Schatt, ed.), pp. 199–217, Naumburg (Saale): Deutscher Verlag für Grundstoffindustrie, Leipzig, 1973.
- [117] W. Ostwald, "Studien über die Bildung und Umwandlung fester Körper: 1. Abhandlung: Übersättigung und Überkaltung," *Z. Phys. Chem.*, vol. 22, pp. 289–330, 1897.

- [118] M. Wencka, J. Schwerin, M. Klanjšek, M. Krnel, S. Vrtnik, P. Koželj, A. Jelen, G. Kapun, Z. Jagličić, I. Sharafutdinov, I. Chorkendorff, P. Gille, and J. Dolinšek, “Intermetallics Physical properties of the GaPd<sub>2</sub> intermetallic catalyst in bulk and nanoparticle morphology,” *Intermetallics*, vol. 67, pp. 35–46, 2015.
- [119] K. Schubert, H. Breimer, W. Burkhardt, E. Günzel, R. Hauffler, H. L. Lukas, H. Vetter, J. Wegst, and M. Wilkens, “Einige strukturelle Ergebnisse an metallischen Phasen II,” *Die Naturwissenschaften*, vol. 44, no. 7, pp. 229–230, 1957.
- [120] C. Wannek and B. Harbrecht, “Phase equilibria in the palladium-rich part of the gallium-palladium system. The crystal structures of Ga<sub>3</sub>Pd<sub>7</sub> and Ga<sub>1-x</sub>Pd<sub>2+x</sub>,” *J. Alloys Compd.*, vol. 316, no. 1-2, pp. 99–106, 2001.
- [121] G. M. Sheldrick, “Phase Annealing in *SHELX-90*: Direct Methods for Larger Structures,” *Acta Cryst.*, vol. A46, pp. 467–473, 1990.
- [122] V. Petříček, M. Dušek, and L. Palatinus, “Crystallographic Computing System JANA2006: General features,” *Z. Kristallogr.*, vol. 229, no. 5, pp. 345–352, 2014.
- [123] Z. Wang, W. Wan, J. Sun, W. Carrillo-Cabrera, D. Grüner, X. Yin, S. Qiu, G. Zhu, and X. Zou, “Epitaxial growth of core-shell zeolite X-A composites,” *CrystEngComm*, vol. 14, no. 6, pp. 2204–2212, 2012.
- [124] W. Carrillo-Cabrera, “SEM/TEM study of annealed Pd<sub>5</sub>Ga<sub>3</sub> single crystal,” tech. rep., Max-Planck-Institut für Chemische Physik fester Stoffe Dresden, 2020.
- [125] *International Tables for Crystallography. Volume A: Space-Group Symmetry* (T. Hahn, ed.), vol. A, ch. Pb, pp. 282–283, Dordrecht: Springer, 5 ed., 2005.
- [126] U. Burkhardt, “EDX and EBSD investigations on annealed Ga<sub>3</sub>Pd<sub>5</sub>,” tech. rep., Max-Planck-Institut für Chemische Physik fester Stoffe Dresden, 2020.
- [127] K. Momma and F. Izumi, “*VESTA 3* for three-dimensional visualization of crystal, volumetric and morphology data,” *J. Appl. Cryst.*, vol. 44, pp. 1272–1276, 2011.
- [128] W. Schatt, “Phasenumwandlungen im festen Zustand,” in *Einführung in die Werkstoffwissenschaft* (W. Schatt, ed.), pp. 119–135, Naumburg (Saale): Deutscher Verlag für Grundstoffindustrie, Leipzig, 1973.
- [129] M. J. Kelley and V. Ponc, “Surface composition of alloys,” *Prog. Surf. Sci.*, vol. 11, no. 3, pp. 139–244, 1981.
- [130] L. Rubinovich and M. Polak, “On the surface composition of intermetallic compounds: the case of MgNi<sub>2</sub>,” *Surf. Sci.*, vol. 418, no. 2, pp. L53–L57, 1998.



- 
- [131] C. Dimitrov, N. Martin, H. Fekkar, and O. Dimitrov, "Composition dependence of atomic mobility in single phase  $\gamma$  TiAl intermetallic compounds," *Scr. Mater.*, vol. 34, no. 9, pp. 1405–1409, 1996.
- [132] Y. Chen, X. Y. Fang, Y. Brechet, and C. R. Hutchinson, "Surface precipitation on engineering alloys," *Acta Mater.*, vol. 81, pp. 291–303, 2014.
- [133] W. Schatt, "Diffusion," in *Einführung in die Werkstoffwissenschaft* (W. Schatt, ed.), pp. 193–199, Naumburg (Saale): Deutscher Verlag für Grundstoffindustrie, Leipzig, 1973.

# Appendix

## A.1 Bragg-Brentano diffraction on slices of single crystals

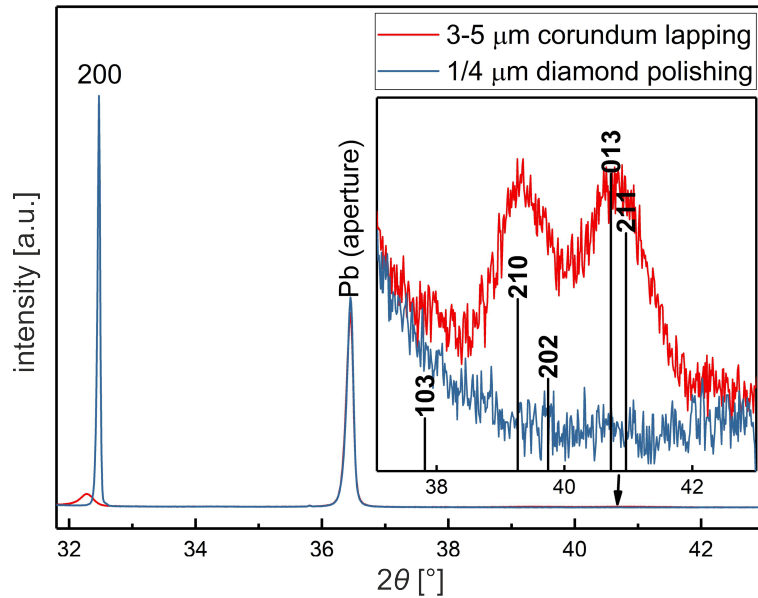


Figure A.1:  $\theta-\theta$  scans on a single-crystalline slice of a (100) surface of  $\text{Ga}_{0.8}\text{Sn}_{0.2}\text{Pd}_2$ . There are signals apart from the main surface peak and its multiples at  $38^\circ \leq 2\theta \leq 42^\circ$ , caused by mechanical surface damage. The plotted lines indicate the simulated positions and intensities of a XPD pattern of  $\text{Ga}_{0.8}\text{Sn}_{0.2}\text{Pd}_2$ . The inserted box shows a comparison between the highest surface peaks of the slice, before and after polishing. Also, it shows the very low intensities of the disruption peaks, that are only visible at closer inspection.

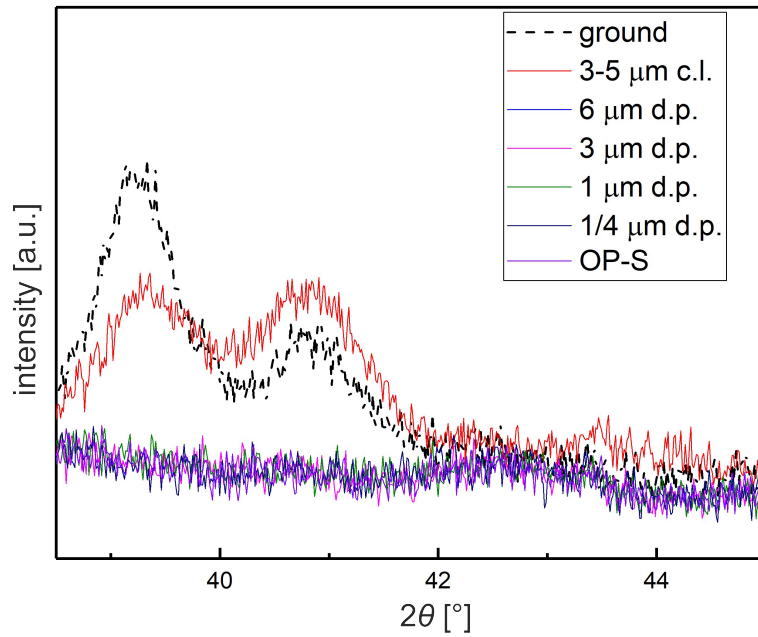


Figure A.2: Same disruption peaks as shown in fig. A.1 on a (100) surface. Here the change of the signals after different polishing steps is shown. c.l.: corundum lapping, d.p.: diamond polishing, OP-S: chemo-mechanical polishing with Syton OP-S (*Struers*).

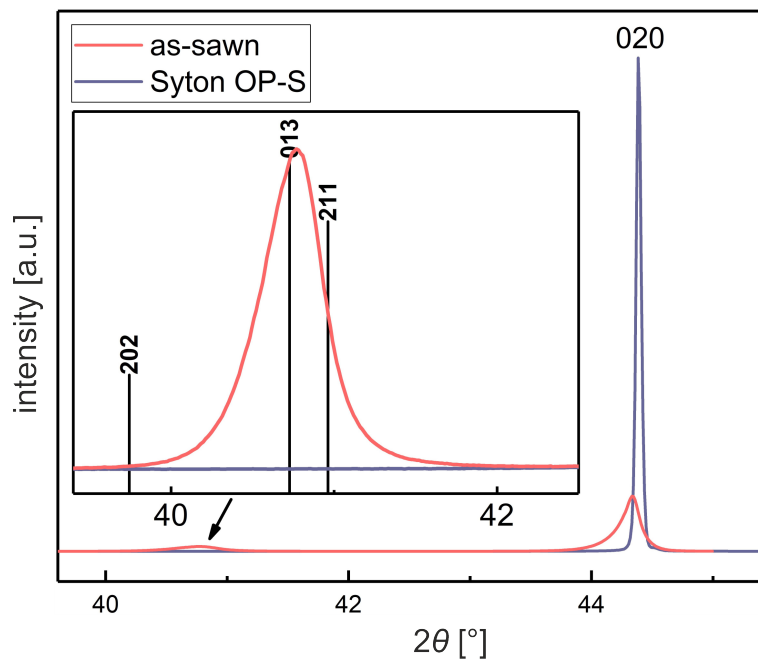


Figure A.3:  $\theta-\theta$  scans on a single-crystalline slice of a (010) surface of  $\text{Ga}_{0.8}\text{Sn}_{0.2}\text{Pd}_2$ . There are signals apart from the main surface peak and its multiples at  $38^\circ \leq 2\theta \leq 42^\circ$ , caused by mechanical surface damage. The plotted lines indicate the simulated positions and intensities of a XPD pattern of  $\text{Ga}_{0.8}\text{Sn}_{0.2}\text{Pd}_2$ . The inserted box shows a comparison between the highest surface peaks of the slice, before and after polishing. On the (010) surface the disruption peaks are more clearly visible than on the (100) and the (001) surface. They reach an intensity of a tenth of the main surface peak's intensity before any treatment after cutting.

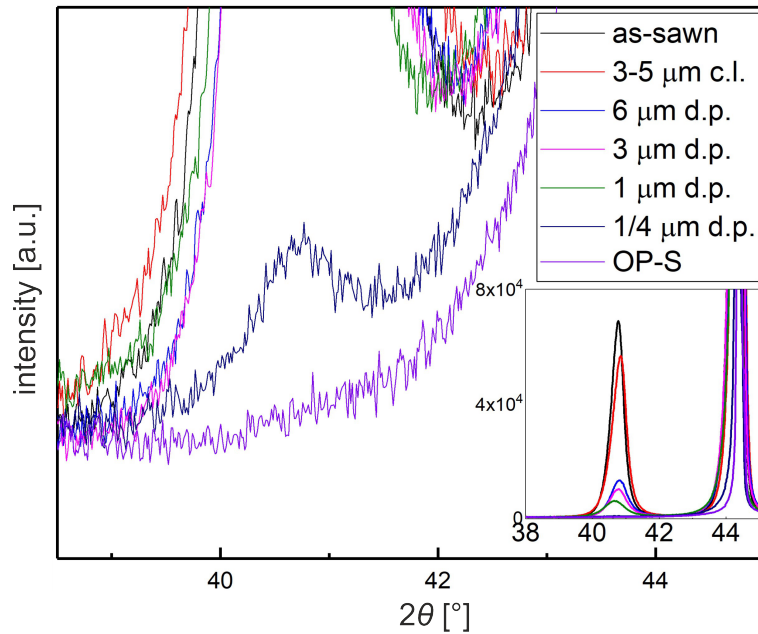


Figure A.4: Same disruption peaks as shown in fig. A.3 on a (010) surface. Here the change of the signals after different polishing steps is shown. c.l.: corundum lapping, d.p.: diamond polishing, OP-S: chemo-mechanical polishing with Syton OP-S (*Struers*).

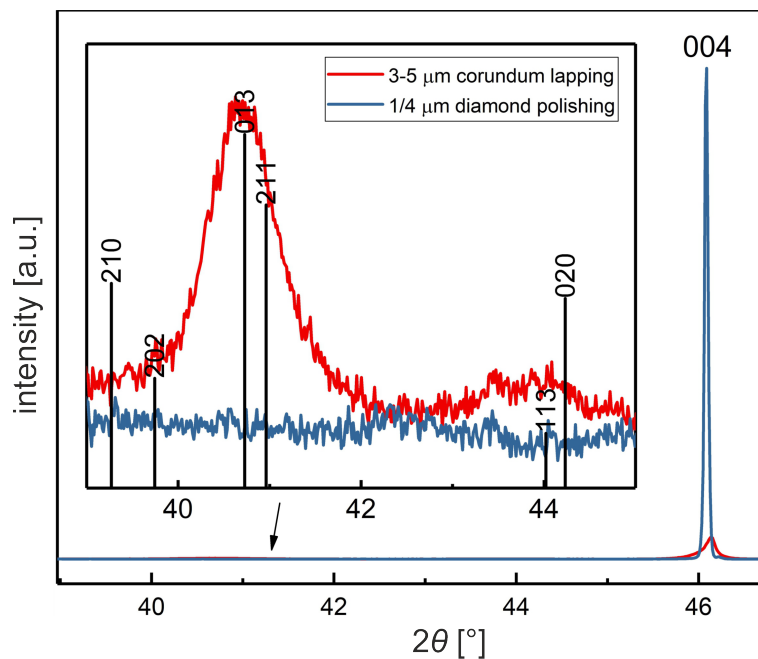


Figure A.5:  $\theta$ – $\theta$  scans on a single-crystalline slice of a (001) surface of  $\text{Ga}_{0.8}\text{Sn}_{0.2}\text{Pd}_2$ . There are signals apart from the main surface peak and its multiples at  $38^\circ \leq 2\theta \leq 42^\circ$ , caused by mechanical surface damage. The plotted lines indicate the simulated positions and intensities of a XPD pattern of  $\text{Ga}_{0.8}\text{Sn}_{0.2}\text{Pd}_2$ . The inserted box shows a comparison between the highest surface peaks of the slice, before and after polishing. Also, it shows the very low intensities of the disruption peaks, that are only visible at closer inspection.

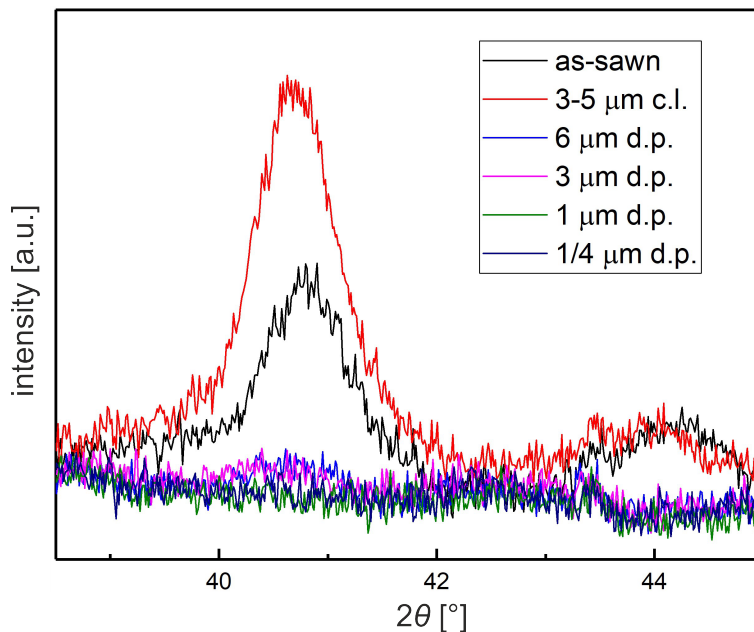


Figure A.6: Same disruption peaks as shown in fig. A.5 on a (001) surface. Here the change of the signals after different polishing steps is shown. c.l.: corundum lapping, d.p.: diamond polishing, OP-S: chemo-mechanical polishing with Syton OP-S (*Struers*).

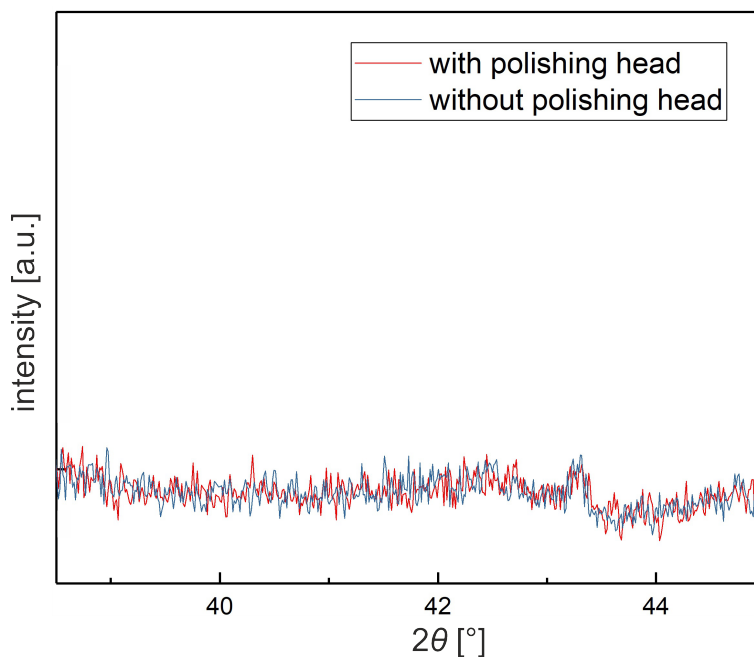


Figure A.7: Background measurement on the empty diffractometer sample holder with the Pb aperture sketched in fig. 2.5, without and with empty polishing head. The polishing head was placed 0.5 mm below the diffractometer zero plane, since the polished single-crystalline slices were thicker than 0.5 mm.

## A.2 Annealing conditions of powders for X-ray powder diffraction

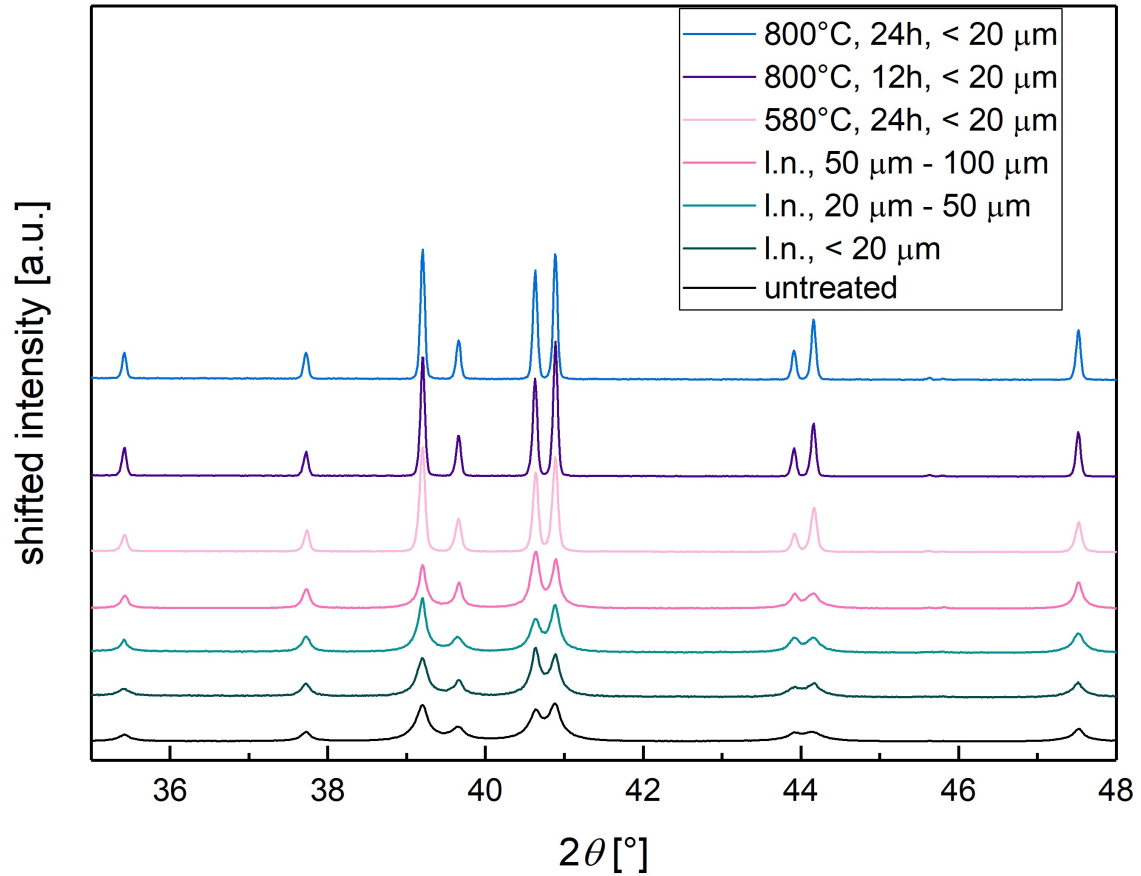


Figure A.8: Result of different treatments to reduce microstrain effects in single-crystalline powders of  $\text{Ga}_{0.7}\text{Sn}_{0.3}\text{Pd}_2$ . l.n.: the sample has been crushed in liquid nitrogen and was sieved afterwards.

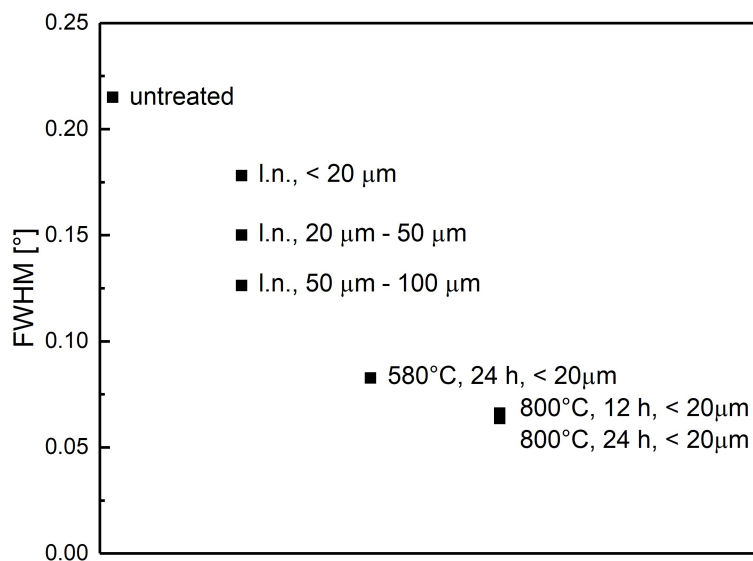


Figure A.9: Average FWHM of all peaks between  $35^\circ \leq 2\theta \leq 48^\circ$  of the XPD patterns, plotted in fig. A.8. The x-axis has no meaning here. The data point descriptions contain the treatments of the samples. l.n. means the sample was ground in liquid nitrogen. Temperatures and times indicate the annealing parameters. The size number shows how fine the sample was sieved.

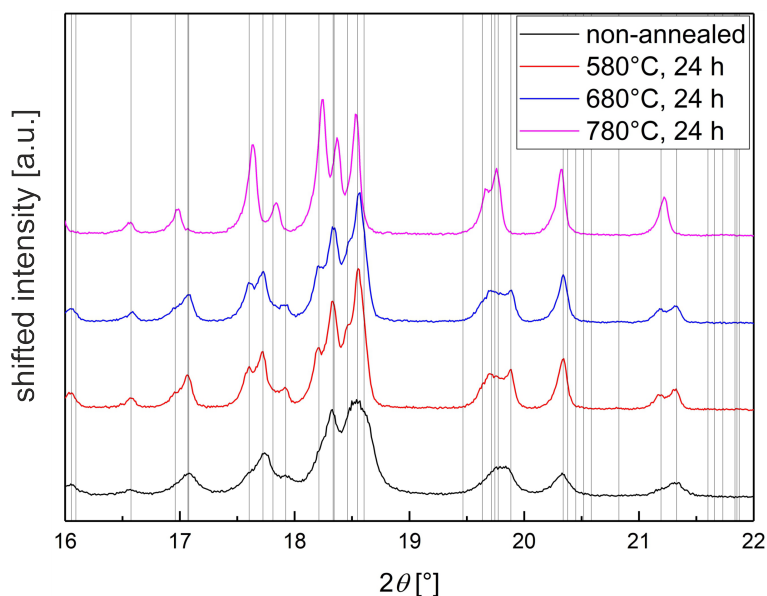


Figure A.10: XPD patterns of the same multiphase sample, but with different annealing temperatures, measured with Mo- $K\alpha_1$  radiation. The black lines indicate the Bragg positions of the peaks, according to a Rietveld refinement of the powder that was annealed at 580°C for 24 h.



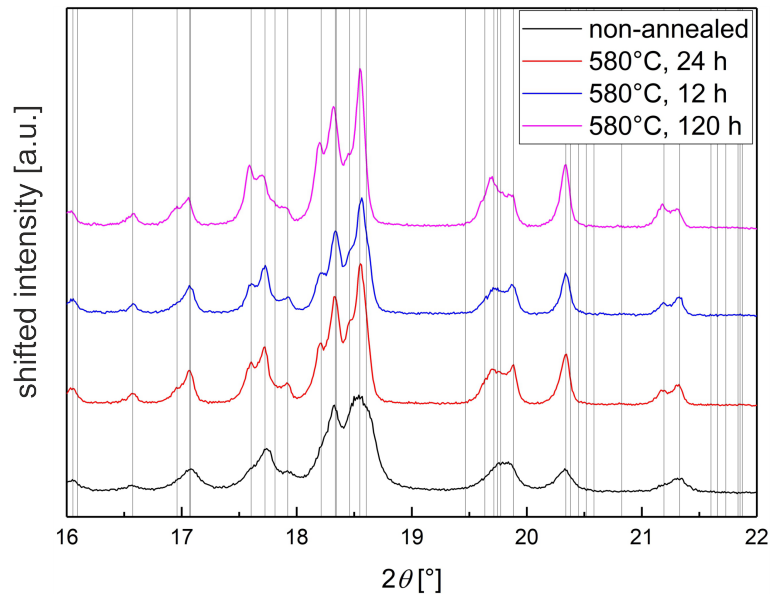


Figure A.11: XPD patterns of the same multiphase sample, but with different annealing durations, measured with Mo- $K\alpha_1$  radiation. The black lines indicate the Bragg positions of the peaks, according to a Rietveld refinement of the powder that was annealed at 580°C for 24 h.

## A.3 X-ray powder diffraction patterns

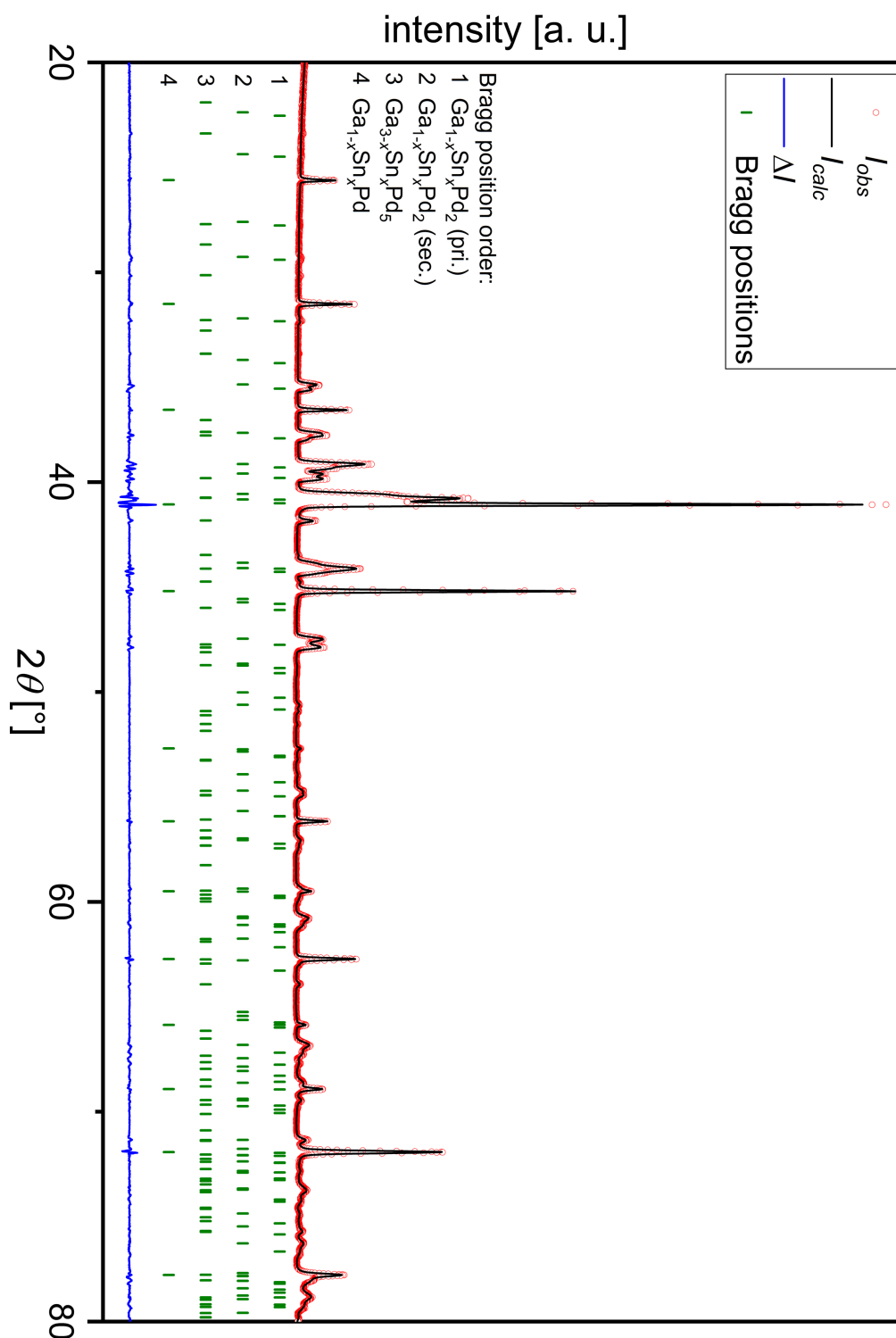


Figure A.12: QX642-A, measured in Bragg-Brentano geometry with  $\text{Cu-K}\alpha_1$  radiation. The powder was annealed at  $580^\circ\text{C}$  for 24 h and sieved to achieve a grain size below  $20\ \mu\text{m}$ . Complete measured range:  $10^\circ \leq 2\theta \leq 120^\circ$ .  $R_p = 8.33$ ,  $R_{wp} = 10.3$ ,  $R_{exp} = 6.73$ ,  $\chi^2 = 2.33$ .

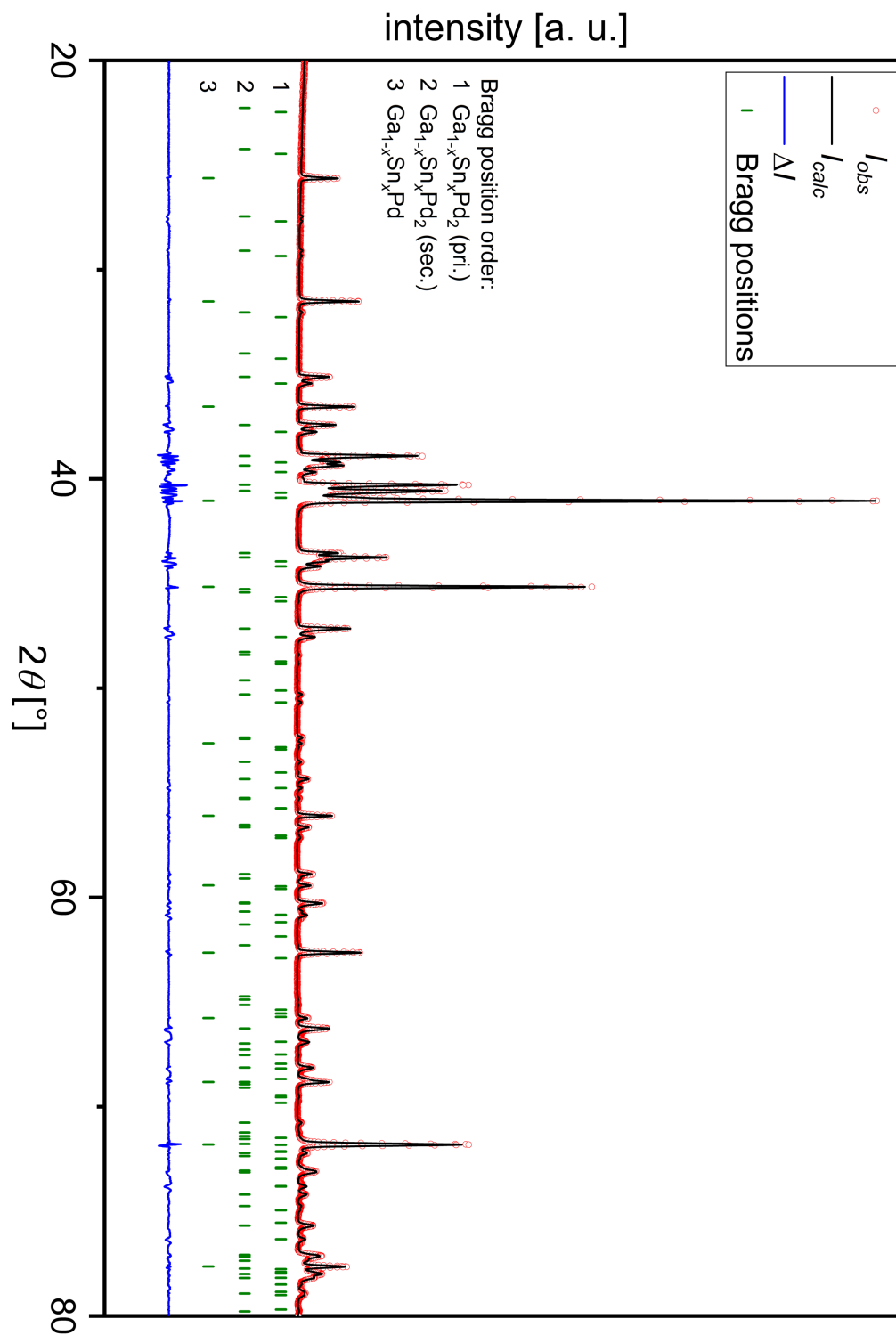


Figure A.13: QX647-A, measured in Bragg-Brentano geometry with  $\text{Cu-K}\alpha_1$  radiation. The powder was annealed at  $580^\circ\text{C}$  for 24 h and sieved to achieve a grain size below  $20\ \mu\text{m}$ . Complete measured range:  $10^\circ \leq 2\theta \leq 120^\circ$ .  $R_p = 9.95$ ,  $R_{wp} = 13.9$ ,  $R_{exp} = 6.45$ ,  $\chi^2 = 4.63$ .

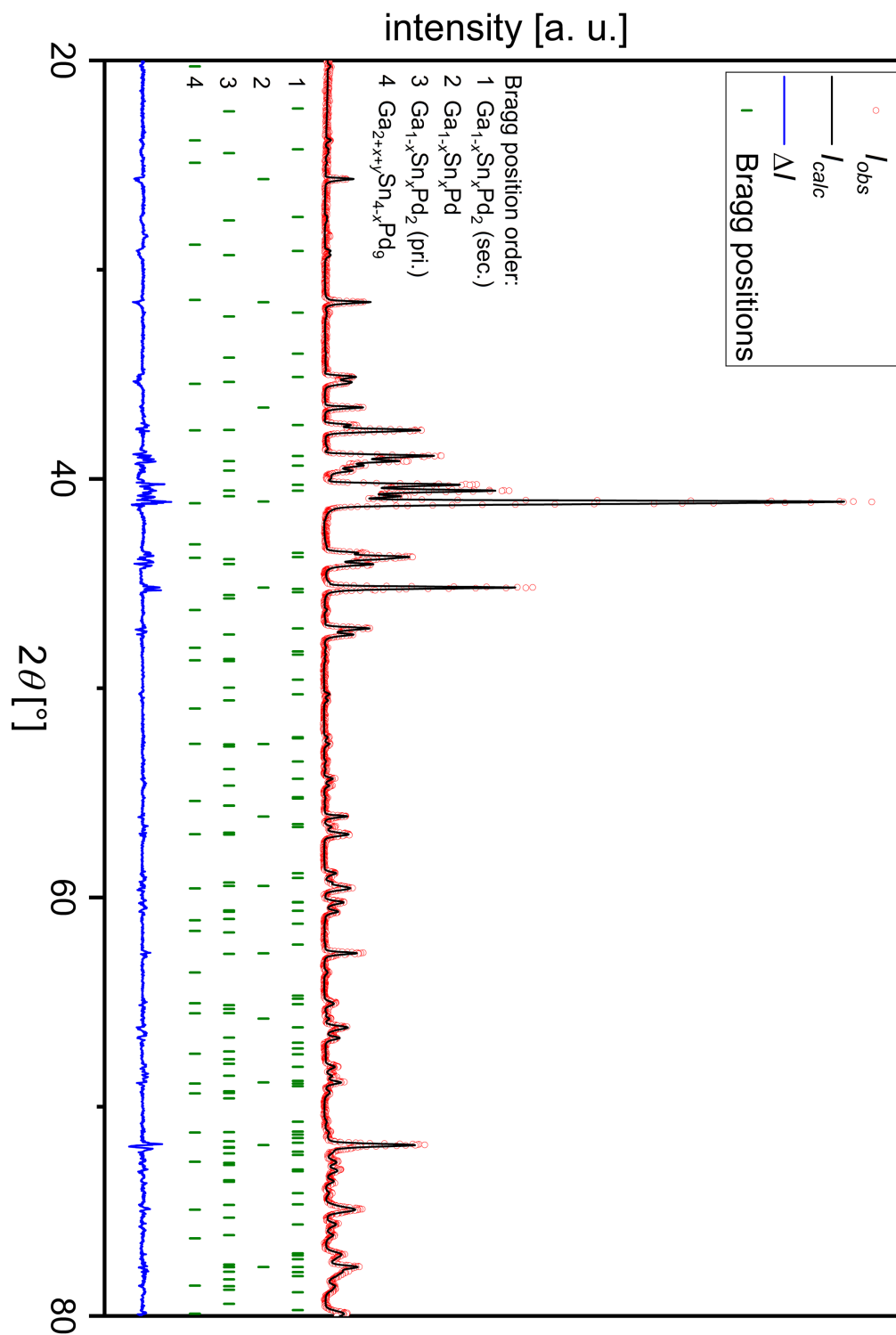


Figure A.14: QX677-A, measured in Bragg-Brentano geometry with  $Cu-K\alpha_1$  radiation. The powder was annealed at  $580^\circ C$  for 24 h and sieved to achieve a grain size below  $20 \mu m$ . Complete measured range:  $10^\circ \leq 2\theta \leq 120^\circ$ .  $R_p = 16.8$ ,  $R_{wp} = 21.9$ ,  $R_{exp} = 17.12$ ,  $\chi^2 = 1.63$ .

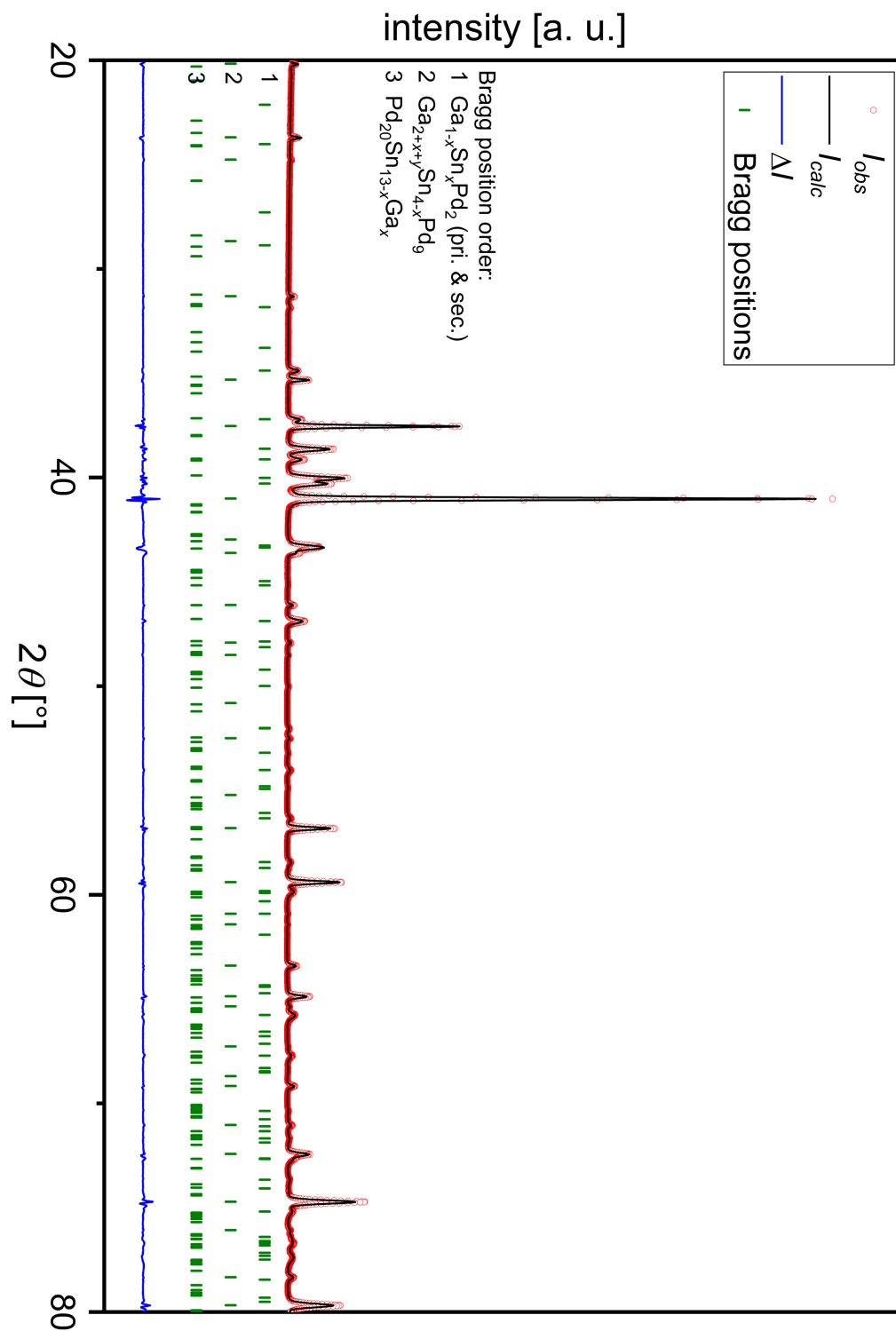


Figure A.15: QX690-C, measured in Bragg-Brentano geometry with  $Cu-K\alpha_1$  radiation. The powder was annealed at  $580^\circ C$  for 24 h and sieved to achieve a grain size below  $20 \mu m$ . Complete measured range:  $10^\circ \leq 2\theta \leq 120^\circ$ .  $R_p = 9.23$ ,  $R_{wp} = 11.4$ ,  $R_{exp} = 5.03$ ,  $\chi^2 = 5.09$ .

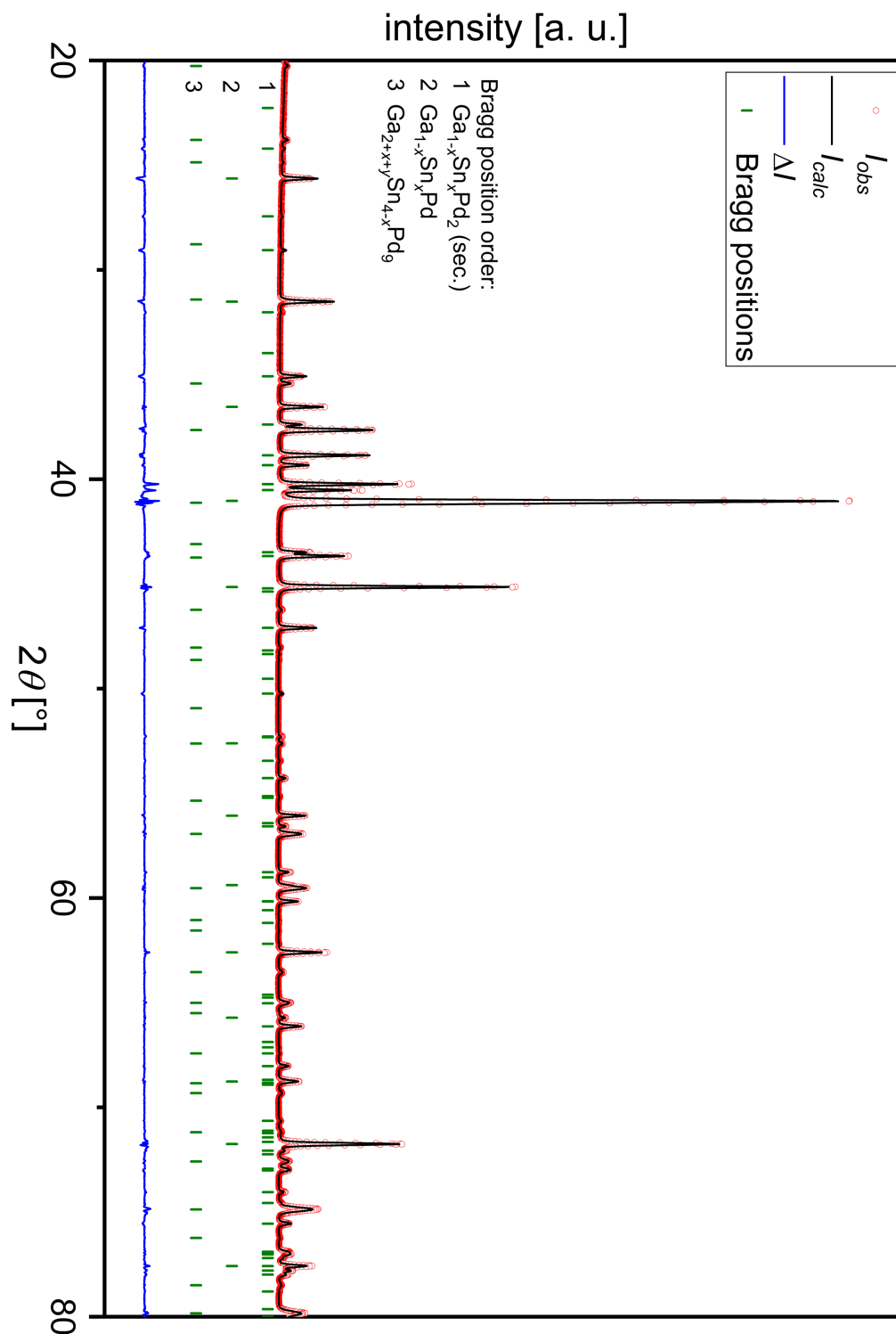


Figure A.16: QX690-B, measured in Bragg-Brentano geometry with  $Cu-K\alpha_1$  radiation. The powder was annealed at  $580^\circ C$  for 24 h and sieved to achieve a grain size below  $20 \mu m$ . Complete measured range:  $10^\circ \leq 2\theta \leq 120^\circ$ .  $R_p = 9.06$ ,  $R_{wp} = 11.5$ ,  $R_{exp} = 5.47$ ,  $\chi^2 = 4.40$ .

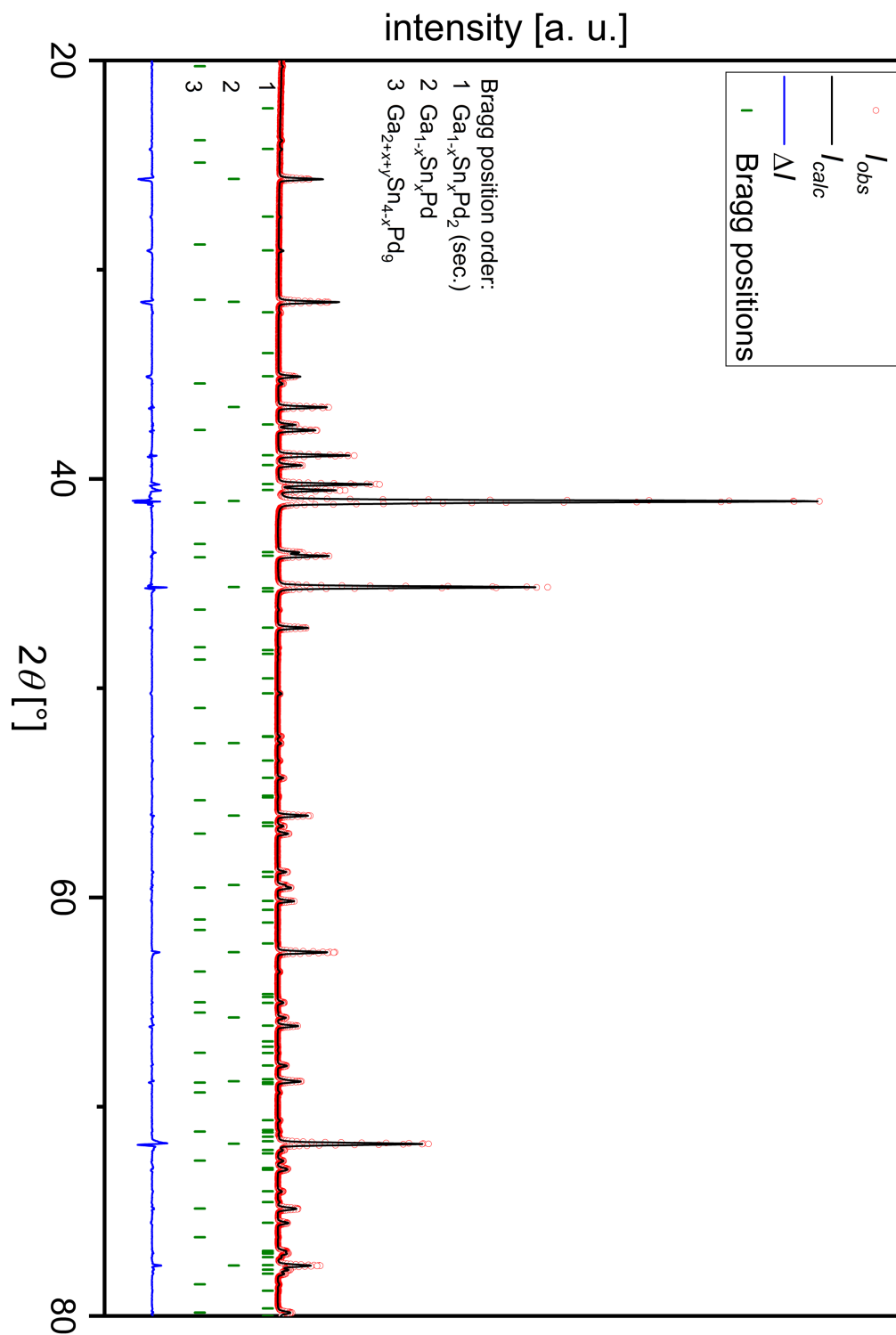


Figure A.17: QX705-A, measured in Bragg-Brentano geometry with  $Cu-K\alpha_1$  radiation. The powder was annealed at  $580^\circ C$  for 24 h and sieved to achieve a grain size below  $20 \mu m$ . Complete measured range:  $10^\circ \leq 2\theta \leq 120^\circ$ .  $R_p = 11.8$ ,  $R_{wp} = 15.1$ ,  $R_{exp} = 6.29$ ,  $\chi^2 = 5.77$ .



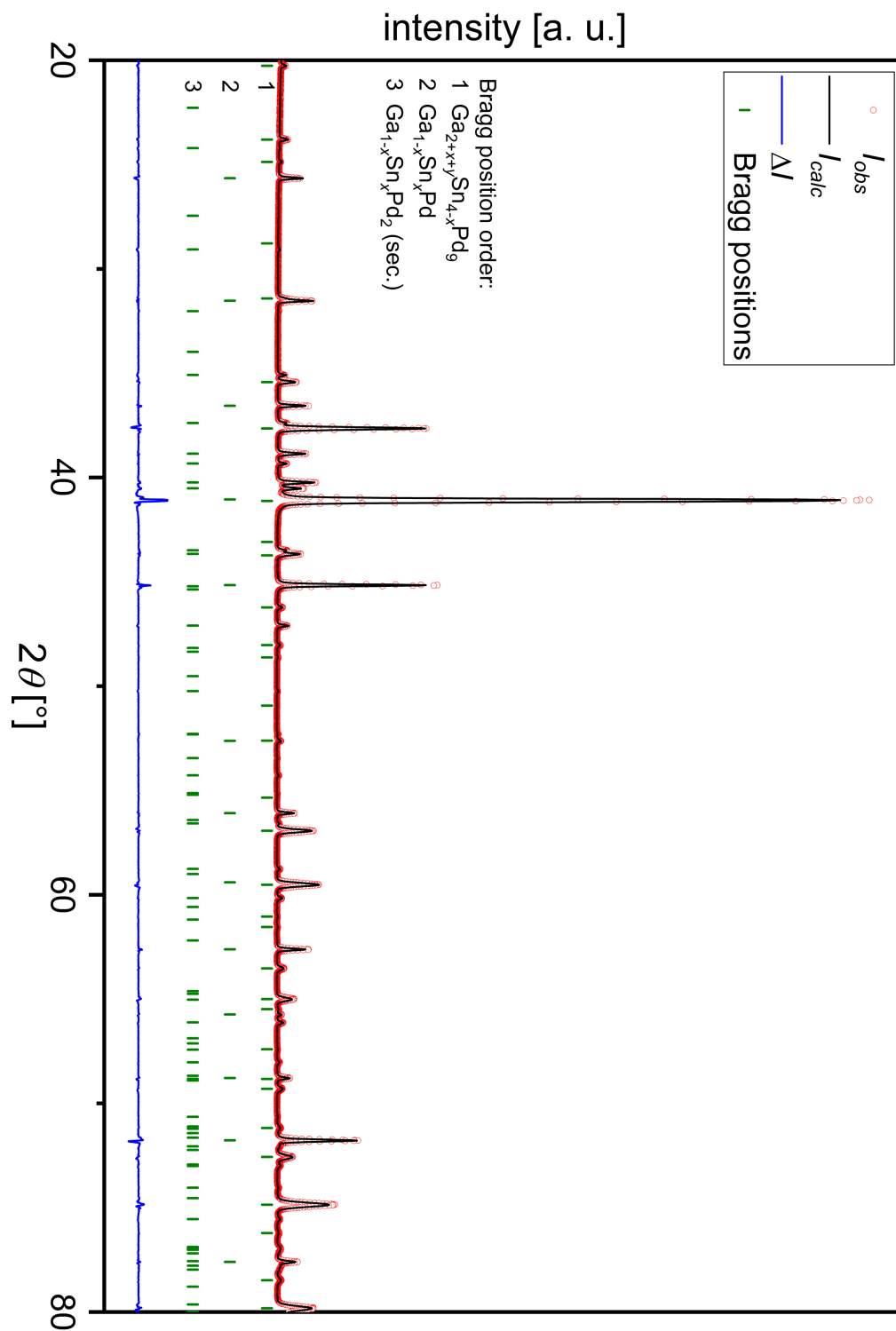


Figure A.18: QX680-A, measured in Bragg-Brentano geometry with  $\text{Cu-K}\alpha_1$  radiation. The powder was annealed at  $580^\circ\text{C}$  for 24 h and sieved to achieve a grain size below  $20\ \mu\text{m}$ . Complete measured range:  $10^\circ \leq 2\theta \leq 120^\circ$ .  $R_p = 8.50$ ,  $R_{wp} = 10.2$ ,  $R_{exp} = 6.20$ ,  $\chi^2 = 2.69$ .

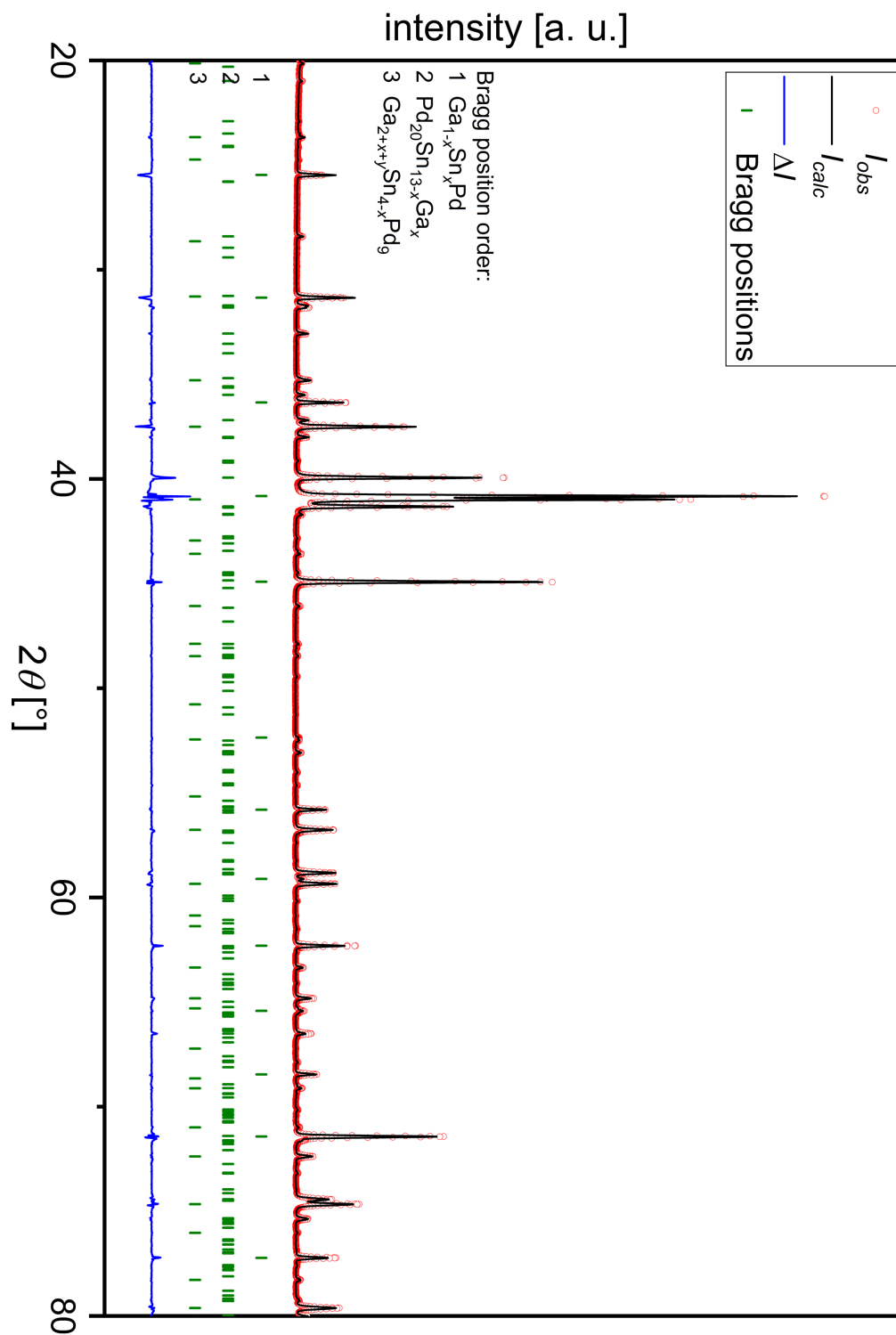


Figure A.19: QX705-C, measured in Bragg-Brentano geometry with  $Cu-K\alpha_1$  radiation. The powder was annealed at  $580^\circ C$  for 24 h and sieved to achieve a grain size below  $20 \mu m$ . Complete measured range:  $10^\circ \leq 2\theta \leq 120^\circ$ .  $R_p = 10.6$ ,  $R_{wp} = 12.9$ ,  $R_{exp} = 5.77$ ,  $\chi^2 = 5.03$ .

## A.4 Experiments overview

ID	experiment	composition	$x_0$	$m$	notes
1	QX642-A	Ga <sub>36.90</sub> Sn <sub>4.10</sub> Pd <sub>59.00</sub>	0.10	8.64 g	BM, 10 mm Ø, al
2	QX642-B	Ga <sub>36.90</sub> Sn <sub>10.00</sub> Pd <sub>53.10</sub>	0.21	7.67 g	BM, 10 mm Ø, al
3	QX647-A	Ga <sub>32.80</sub> Sn <sub>8.20</sub> Pd <sub>59.00</sub>	0.20	9.39 g	BM, 10 mm Ø, al
4	QX663-B	Ga <sub>31.20</sub> Sn <sub>7.80</sub> Pd <sub>61.00</sub>	0.20	0.59 g	EC, gs
5	QX647-B	Ga <sub>28.70</sub> Sn <sub>12.30</sub> Pd <sub>59.00</sub>	0.30	7.14 g	BM, 10 mm Ø, al
6	QX671-A	Ga <sub>24.60</sub> Sn <sub>16.40</sub> Pd <sub>59.00</sub>	0.40	0.78 g	EC, al
7	QX671-B	Ga <sub>20.50</sub> Sn <sub>20.50</sub> Pd <sub>59.00</sub>	0.50	0.82 g	EC, al
8	QX671-C	Ga <sub>16.40</sub> Sn <sub>24.60</sub> Pd <sub>59.00</sub>	0.60	0.84 g	EC, al
9	QX675-A	Ga <sub>25.35</sub> Sn <sub>13.65</sub> Pd <sub>61.00</sub>	0.35	0.76 g	EC, gs
10	QX675-B	Ga <sub>11.70</sub> Sn <sub>27.30</sub> Pd <sub>61.00</sub>	0.70	0.83 g	EC, gs
11	QX675-C	Ga <sub>22.00</sub> Sn <sub>22.00</sub> Pd <sub>56.00</sub>	0.50	0.78 g	EC, gs
12	QX677-A	Ga <sub>27.30</sub> Sn <sub>11.70</sub> Pd <sub>61.00</sub>	0.30	0.76 g	EC, gs
13	QX677-B	Ga <sub>26.65</sub> Sn <sub>14.35</sub> Pd <sub>59.00</sub>	0.35	0.79 g	EC, gs
14	QX677-C	Ga <sub>23.40</sub> Sn <sub>15.60</sub> Pd <sub>61.00</sub>	0.40	0.81 g	EC, gs
15	QX680-A	Ga <sub>27.50</sub> Sn <sub>15.50</sub> Pd <sub>57.00</sub>	0.35	0.78 g	EC, gs
16	QX680-B	Ga <sub>23.65</sub> Sn <sub>19.35</sub> Pd <sub>57.00</sub>	0.45	0.79 g	EC, gs
17	QX680-C	Ga <sub>19.50</sub> Sn <sub>19.50</sub> Pd <sub>61.00</sub>	0.50	0.79 g	EC, gs
18	QX690-A	Ga <sub>34.40</sub> Sn <sub>8.60</sub> Pd <sub>57.00</sub>	0.20	0.73 g	EC, gs
19	QX690-B	Ga <sub>30.10</sub> Sn <sub>12.90</sub> Pd <sub>57.00</sub>	0.30	0.77 g	EC, gs
20	QX690-C	Ga <sub>15.20</sub> Sn <sub>22.80</sub> Pd <sub>62.00</sub>	0.60	0.76 g	EC, gs
21	QX696-A	Ga <sub>26.65</sub> Sn <sub>14.35</sub> Pd <sub>59.00</sub>	0.35	0.75 g	EC, gs, qn
22	QX696-B	Ga <sub>20.50</sub> Sn <sub>20.50</sub> Pd <sub>59.00</sub>	0.50	0.75 g	EC, gs, qn
23	QX696-C	Ga <sub>23.65</sub> Sn <sub>19.35</sub> Pd <sub>57.00</sub>	0.45	0.63 g	EC, gs, qn
24	QX705-A	Ga <sub>36.00</sub> Sn <sub>9.00</sub> Pd <sub>55.00</sub>	0.20	0.94 g	EC, gs
25	QX705-B	Ga <sub>31.50</sub> Sn <sub>13.50</sub> Pd <sub>55.00</sub>	0.30	0.99 g	EC, gs
26	QX705-C	Ga <sub>27.00</sub> Sn <sub>18.00</sub> Pd <sub>55.00</sub>	0.40	0.94 g	EC, gs
27	QX689-A	Ga <sub>20.50</sub> Sn <sub>20.50</sub> Pd <sub>59.00</sub>	0.50	5.58 g	BM, 5 mm Ø, gs
28	QX689-B	Ga <sub>26.65</sub> Sn <sub>14.35</sub> Pd <sub>59.00</sub>	0.35	5.69 g	BM, 5 mm Ø, gs
29	QX693-A	Ga <sub>19.50</sub> Sn <sub>19.50</sub> Pd <sub>61.00</sub>	0.50	0.76 g	EC, gs, qw
30	QX693-B	Ga <sub>26.65</sub> Sn <sub>14.35</sub> Pd <sub>59.00</sub>	0.35	0.73 g	EC, gs, qw
31	QX723	Ga <sub>32.76</sub> Sn <sub>11.08</sub> Pd <sub>56.16</sub>	0.25	0.25 g	EC, gs
j	QX669-F	Ga <sub>29.98</sub> Sn <sub>19.90</sub> Pd <sub>50.12</sub>	0.40	0.74 g	EC, gs
v	QX681-F	Ga <sub>28.78</sub> Sn <sub>18.47</sub> Pd <sub>52.75</sub>	0.40	0.81 g	EC, gs

Table A.1: Compositions of experiments for phase diagram studies in the vicinity of the primary crystallisation region of Ga<sub>1-x</sub>Sn<sub>x</sub>Pd<sub>2</sub>. BM = Bridgman experiment; al = alumina crucible; gs = graphitized silica; EC = equilibrium-cooling; qw = quenched in water; qn = quenched in liquid nitrogen.

ID	experiment	composition	$x_0$	$m$	pulling direction	notes
I	QX649	Ga <sub>35.10</sub> Sn <sub>3.90</sub> Pd <sub>61.00</sub>	0.10	36.27 g	[001]	–
II	QX661	Ga <sub>31.20</sub> Sn <sub>7.80</sub> Pd <sub>61.00</sub>	0.20	50.34 g	[001]	–
III	QX667	Ga <sub>31.20</sub> Sn <sub>7.80</sub> Pd <sub>61.00</sub>	0.20	55.10 g	[010]	*
IV	QX674	Ga <sub>26.95</sub> Sn <sub>11.55</sub> Pd <sub>61.50</sub>	0.30	47.32 g	[010]	–
V	QX684	Ga <sub>23.10</sub> Sn <sub>15.40</sub> Pd <sub>61.50</sub>	0.40	54.92 g	[010]	–
VI	QX703	Ga <sub>26.95</sub> Sn <sub>11.55</sub> Pd <sub>61.50</sub>	0.30	46.81 g	[010]	–
VII	QX715	Ga <sub>26.95</sub> Sn <sub>11.55</sub> Pd <sub>61.50</sub>	0.30	51.07 g	[100]	–

Table A.2: Compositions of Ga<sub>1-x</sub>Sn<sub>x</sub>Pd<sub>2</sub> Czochralski experiments. \*residual melt of QX661, refilled.

experiment	$y_L$	$x_L$	P1, $x$ [wt.%], [ ]	P2, $x_{XPD}$ [wt.%], [ ]	P4 [wt.%]	P5 [wt.%]	P6 [wt.%]
QX642-B	53.1	0.21		3, 0.36(2)	64	33	
QX705-A	55	0.20		27, 0.48(2)	62	11	
QX705-B	55	0.30		2, 0.48(2)	49	49	
QX705-C	55	0.40			47	31	22
QX675-C	56	0.50			35	28	37
QX690-A	57	0.20	< 1, 0.272(9)	45, 0.450(15)	55		
QX690-B	57	0.30		28, 0.471(18)	46	26	
QX680-A	57	0.35		12, 0.48(2)	36	52	
QX680-B	57	0.45		2, 0.47(2)	19	79	
QX696-C	57	0.45		<< 1	29	72	
QX642-A*	59	0.10	12, 0.088(4)	34, 0.269(4)	47		
QX647-A	59	0.20	5, 0.23(2)	45, 0.453(15)	50		
QX647-B	59	0.30	28, 0.304(3)	29, 0.469(18)	31	12	
QX677-B	59	0.35	< 1, 0.340(9)	33, 0.47(2)	31	36	
QX696-A	59	0.35	39, 0.334(3)		33	29	
QX693-B	59	0.35	2, 0.325(3)	29, 0.448(14)	35	33	
QX671-A	59	0.40		25, 0.47(2)	25	50	
QX671-B	59	0.50		6, 0.47(2)	12	82	
QX696-B	59	0.50		10, 0.48(2)	13	77	
QX671-C	59	0.60			12	67	21
QX663-B	61	0.20	76, 0.196(2)	9, 0.434(14)	15		
QX677-A	61	0.30	19, 0.311(2)	35, 0.463(17)	29	17	
QX675-A	61	0.35	19, 0.345(3)	32, 0.458(14)	26	23	
QX677-C	61	0.40	18, 0.364(3)	28, 0.468(18)	21	33	
QX680-C	61	0.50	7, 0.394(8)	12, 0.449(18)	10	71	
QX693-A	61	0.50	7, 0.528(3)	20, 0.46(2)	11	62	
QX690-C	62	0.60	20, 0.537(9)			80	< 1
QX675-B	61	0.70		22, 0.64(8)		59	20

Table A.3: Phase contents of the equilibrium-cooling experiments with  $y_L > 50$ , based on Rietveld refinement.  $y_L$  and  $x_L$  relate to the initial melt according to the description (Ga<sub>1-x<sub>L</sub></sub>Sn<sub>x<sub>L</sub></sub>)<sub>100-y<sub>L</sub></sub>Pd<sub>y<sub>L</sub></sub>. P1) Ga<sub>1-x</sub>Sn<sub>x</sub>Pd<sub>2</sub> (primarily crystallized,  $x$  was measured by WDX). P2) Ga<sub>1-x</sub>Sn<sub>x</sub>Pd<sub>2</sub> (formed secondarily,  $x_{XPD}$  was calculated from the lattice parameters), P4) Ga<sub>1-x</sub>Sn<sub>x</sub>Pd, P5) Ga<sub>2+p+q</sub>Sn<sub>4-p</sub>Pd<sub>9</sub>, P6) Pd<sub>20</sub>Sn<sub>13-x</sub>Ga<sub>x</sub>. \*) The experiment QX642-A additionally contains 7 wt.% Ga<sub>3-x</sub>Sn<sub>x</sub>Pd<sub>5</sub>.

## A.5 Images of Czochralski-grown crystals

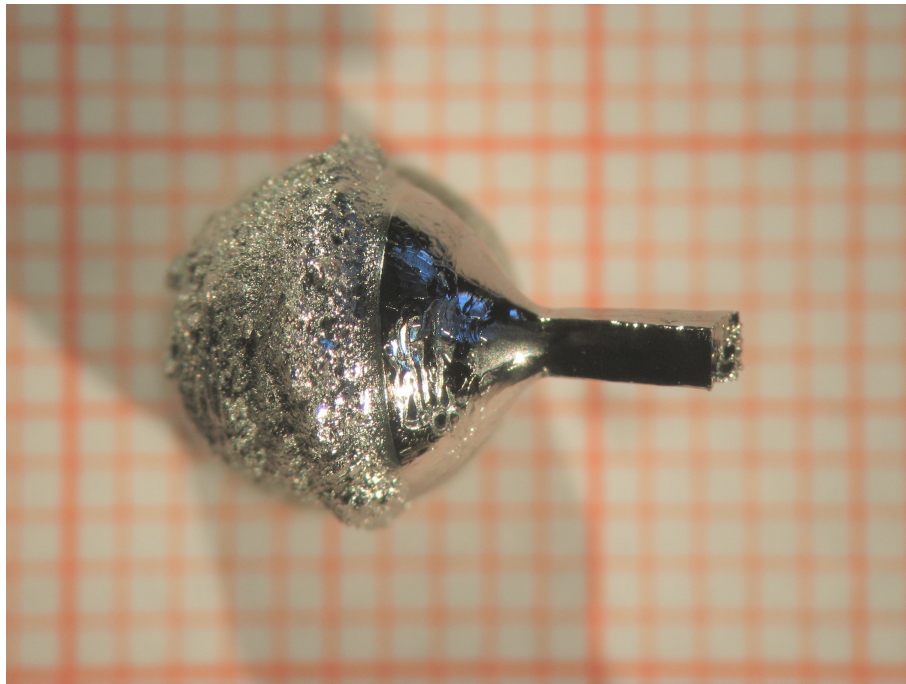


Figure A.20: QX649-II, mass = 1.6 g,  $x = 0.0757(13)$ , pulling direction [001].



Figure A.21: QX649-III, mass = 6.7 g,  $x = 0.0759(10)$ , pulling direction [001].



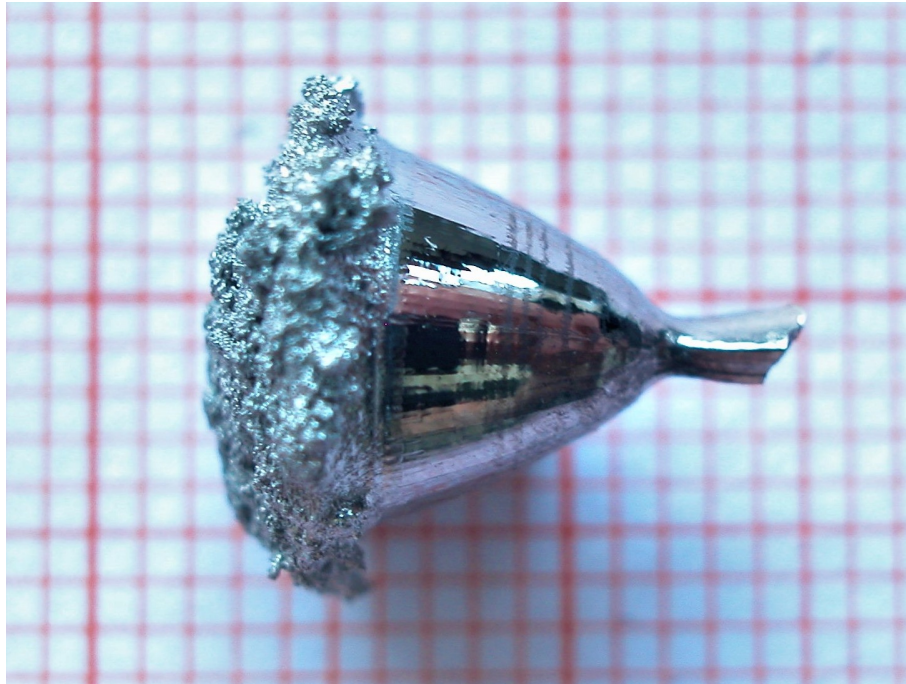


Figure A.22: QX661, mass = 2.8 g,  $x = 0.170(3)$ , pulling direction [001].

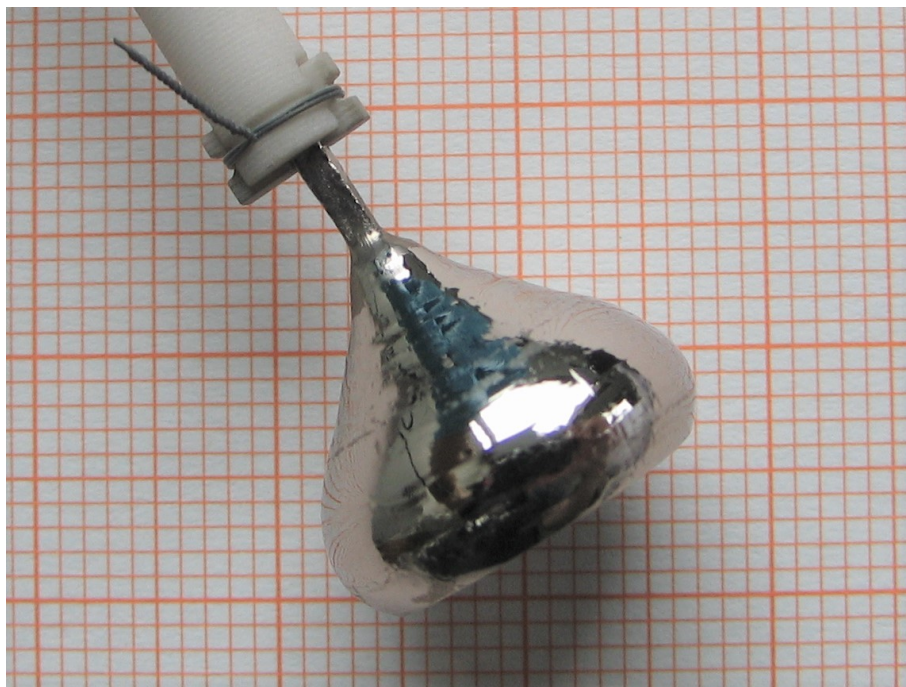


Figure A.23: QX667, mass = 11.7 g,  $x = 0.1758(14)$ , pulling direction [010].

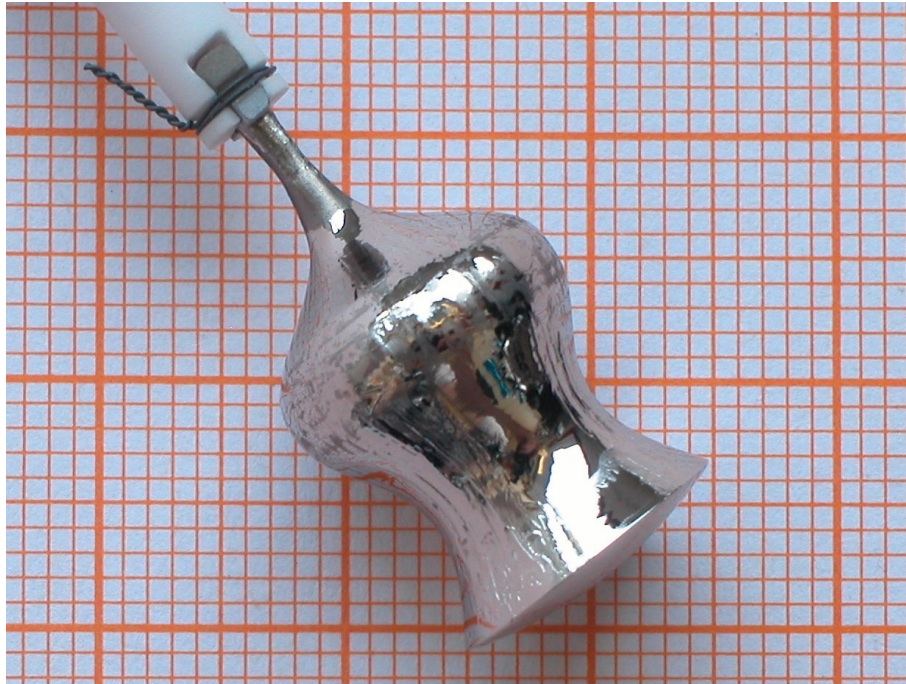


Figure A.24: QX674, mass = 14.2 g,  $x = 0.285(2)$ , pulling direction [010].



Figure A.25: QX703, mass = 14.1 g,  $x = 0.290(3)$ , pulling direction [010].



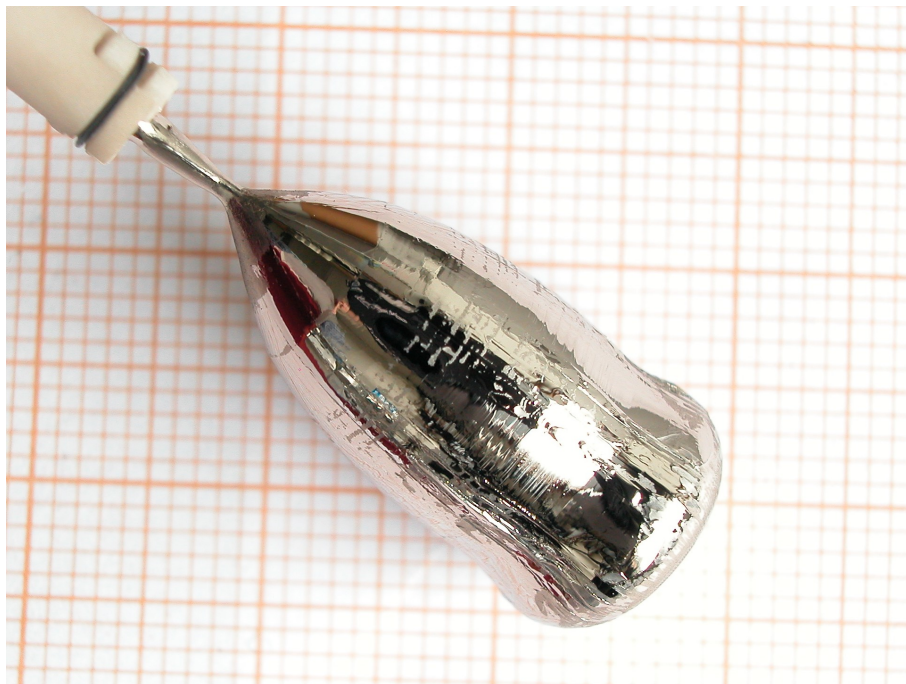


Figure A.26: QX715, mass = 15.0 g, pulling direction [100].



Figure A.27: QX684, mass = 17.8 g,  $x = 0.397(3)$ , pulling direction [010].

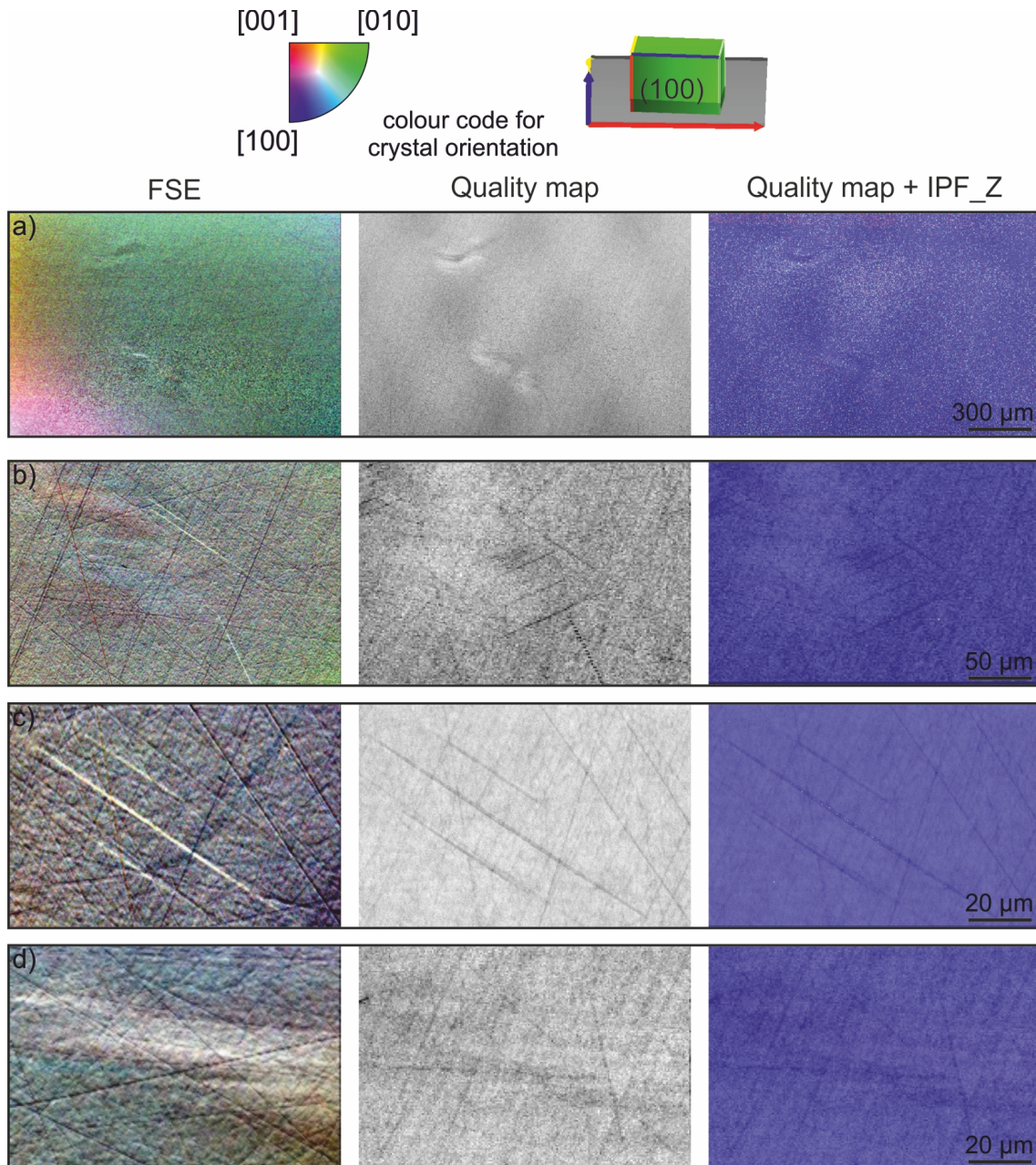


Figure A.28: FSE images (left column), quality maps (middle column) and IPF\_Z maps (right column) of different positions on a (100) slice of a  $\text{Ga}_{1-x}\text{Sn}_x\text{Pd}_2$  crystal with  $x = 0.3$  (QX674).



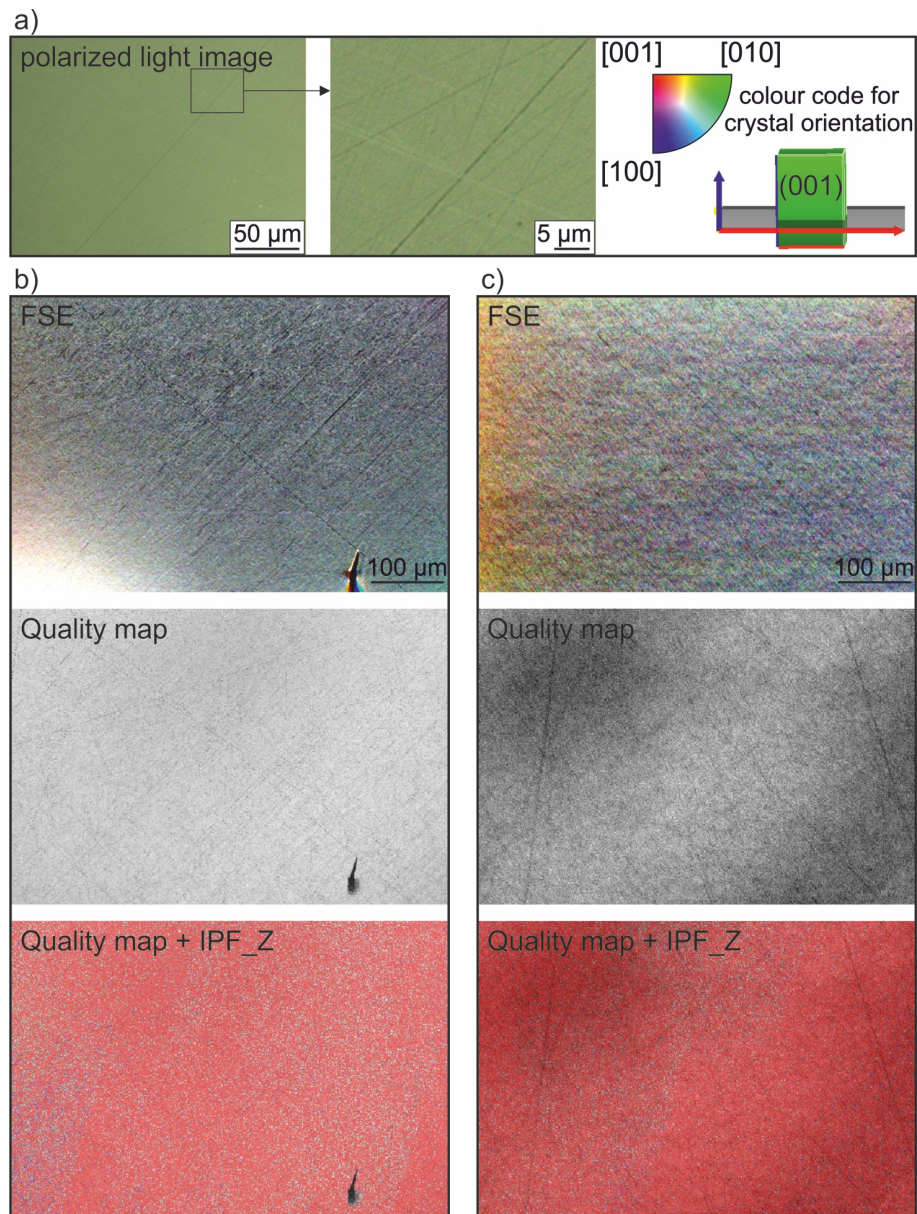


Figure A.29: a) Incident light microscope image (crossed polars) and b,c) FSE images, quality maps and IPF\_Z maps of two positions on a (001) slice of a  $\text{Ga}_{1-x}\text{Sn}_x\text{Pd}_2$  crystal with  $x = 0.3$  (QX674). The darker areas in the quality map in frame c are artefacts.

# Danksagung

Für technische Assistenz möchte ich mich bei Max Häberle, Günther Hesberg, Stefi Hoser und Moritz Zenkert bedanken. Außerdem bei meiner Arbeitsgruppe, wobei Judith Schwerin, Alicia Dorner und Stefan Püschel auch zur Arbeit beigetragen haben. Besonders Michael Hahne war öfter eine große fachliche Hilfe.

Bei den Kollegen des Instituts bedanke ich mich für fachliche Unterstützung bei Martina Greiner (Korngrößenanalyse), Dirk Müller (Mikrosonde) und besonders bei Bernd Maier und Sohyun Park, die liebenswürdige und umfangreiche fachliche Betreuung im Bereich der Röntgenbeugung geleistet haben. Auch Gunthram Jordan verdient eine persönliche Erwähnung.

Großer Dank gilt allen Beteiligten am Projekt, aus dem diese Arbeit entstanden ist. Dabei sind besonders Ulrich Burkhardt und Wilder Carillo-Cabrera für deren Untersuchungen mit dem Elektronenmikroskop zu erwähnen. Außerdem halfen in Fachgesprächen und strukturellen sowie chemischen Analysen Yuri Grin und Mark Armbrüster. Besonderer Dank gilt Stefan Barth, als Ansprechpartner und Wissensvermittler im Bereich der Katalyse.

Der Dank für röntgentopographische Aufnahmen gilt Christian Kranert und Paul Wimmer.

Ein riesen Dank geht an meine Eltern, Birgit und Toni, für bedingungslose Unterstützung.

Bei Sophie bedanke ich mich für grenzenlose Unterstützung an allen Ecken und Enden und unendliche Geduld und überhaupt.

Die letzten Worte dieser Arbeit richten sich an Peter Gille, der mich auf allen Ebenen, fachlich und menschlich, herausragend betreut hat, wie es niemand besser hätte machen können. Die letzten Jahre waren mir eine riesige Freude und ich hoffe, dass das auf Gegenseitigkeit beruht. Lieber Peter, vielen Dank!